

UNIVERSITY OF WARMIA AND MAZURY IN OLSZTYN

Technical Sciences

13



PUBLISHER UWM

EDITORIAL BOARD

Stefan Cenkowski – University of Manitoba, Canada,
Adam Chrzanowski – University of New Brunswick, Canada,
Janusz Laskowski – University of Agriculture in Lublin, Poland
Lech Tadeusz Polkowski – University of Warmia and Mazury in Olsztyn, Poland
Vladimir Tilipalov – Kaliningrad State Technical University, Russia,
Alojzy Wasilewski – University of Warmia and Mazury in Olsztyn, Poland

EDITORIAL COMMITTEE

Marek Markowski (Editor-in-Chief), Piotr Artiemjew, Ireneusz Białobrzewski,
Tomasz Lipiński, Wojciech Sobieski

Executive Editor
Mariola Jezierska

The Journal is also available in electronic form.
The online edition is hosted by MetaPress (www.metapress.com)
in partnership with Versita (www.versita.com)

The Technical Sciences is indexed and abstracted in BazTech (<http://baztech.icm.edu.pl>)

PL ISSN 1505-4675

© Copyright by Wydawnictwo UWM • Olsztyn 2010

Address

ul. Jana Heweliusza 14
10-718 Olsztyn-Kortowo, Poland
tel.: (48) (89) 523 36 61
fax: (48) (89) 523 34 38
e-mail: wydawca@uwm.edu.pl

Contents

Biosystems Engineering

O. Duber-Skwerska – <i>Mathematical Modeling of Bed Geometry in the Cultivation of Seed Potatoes</i>	1
K. Nowak, M. Markowski, E. Sztorc – <i>Modeling the Natural Convection Heating of Liquid in a Vertical Cylinder</i>	10
A. Ratajski, I. Białobrzewski, F. Dajnowiec, S. Bakier – <i>The Use of Ultrasonic Methods in the Identification of Honey Types</i>	22
E. Wachowicz, L. Woroncow – <i>Comprehensive Model of Processes Proceeding at a Mushroom-Growing Cellar</i>	30
P. Zapotoczny, T. Kawałko, S. Bakier – <i>Determination of the Physical Characteristics of Food Raw Materials by Spectrophotometry – the Example of Honey</i>	40

Civil Engineering

J. Kaczmarek, D. Leśniewska – <i>A Flood Embankment Under Changing Water Level Conditions – a Comparison of a Physical and a Numerical Model</i>	53
L.M. Kaczmarek, J. Biegowski, J.B. Skillandat – <i>Hydro- and Lithodynamic Aspects of Constructing a Navigable Canal Through the Vistula Spit – Part 2</i>	64
K. Klempka, M. Knauff – <i>Taking Subsoil Susceptibility into Account in Designing Columns in Reinforced Single-Storey Structures</i>	80
M. Zagroba – <i>Historic Spatial Layouts in Small Towns in Warmia and their Role in the Current Life of Inner Town Areas</i>	90

Environmental Engineering

P. Bogacz – <i>The Effect of the Fuel Type on the Value of Primary Energy and Emmission of Pollutants</i>	98
J.A. Pawłowicz – <i>Influence of Green Areas on Urban Landscape</i>	113

Geodesy and Cartography

K. Dawidowicz – <i>Antenna Phase Center Variations Corrections in Processing of GPS Observations with Use of Commercial Software</i>	120
A. Doskocz – <i>Initial Use of Statistical Analysis for Estimation of Horizontal Accuracy of Large-Scale Digital Maps</i>	133
A. Łyszkowicz – <i>Quasigeoid for the Area of Poland Computed by Least Squares Collocation</i>	147
A. Łyszkowicz, A. Bernatowicz – <i>Accuracy Evaluation of the Successive Campaigns of the Precise Levelling in Poland</i>	165

Mechanical Engineering

J. Dobriański, M. Duda – <i>Experimental Solar Installation with a Self-Acting Circulation Pump, Powered by Local Heat</i>	181
J. Hałacz – <i>Torque of the Operator's Upper Extremity in Relation to its Orientation within a Normal Working Space</i>	189
K. Kuś — <i>The Influence of Repeated Heating and Cooling Process on the Transformation Characteristics in Ni-Ti Alloy</i>	203
T. Lipiński, M. Bramowicz, P. Szabracki, P. Mikołajczyk, M. Cudakiewicz – <i>Abrasive Wear of the AlSi12Mg with Al-Si Alloy for Casting Machine Parts</i>	212
P. Mazur, D. Jasiukiewicz – <i>Influence of Processing Multiplicity on Values of Mass Flow Rate and Melt Volume Rate of Polycarbonate</i>	221
P. Mazur, P. Smoleński – <i>Influence of Processing Multiplicity on Values of Mass Flow Rate and Melt Volume Rate of PPS</i>	227
J. Pelc – <i>An Attempt to Improve the Axisymmetric Model of a Pneumatic Tire</i>	233
W. Sobieski – <i>Jet Pumps – Numerical Modeling Possibilities Upon the Bifurcation Phenomena</i>	240
W. Sobieski – <i>Examples of Using the Finite Volume Method for Modeling Fluid-Solid Systems</i>	256
P. Szabracki, M. Bramowicz, T. Lipiński – <i>The Computer Analysis Shape of Reflexes XRD on the Basis of X2CrNiMoN25-7-4 Steel</i>	266

Spis treści

Inżynieria rolnicza

O. Duber-Skwarska – <i>Modelowanie matematyczne geometrii zagonu w technologii uprawy ziemniaków na sadzeniaki</i>	1
K. Nowak, M. Markowski, E. Sztorc – <i>Modelowanie procesu nagrzewania cieczy w pionowym cylindrze w warunkach konwekcji naturalnej</i>	10
A. Ratajski, I. Białobrzewski, F. Dajnowiec, S. Bakier – <i>Wykorzystanie metod ultradźwiękowych do identyfikacji rodzaju miodu</i>	22
E. Wachowicz, L. Woroncow – <i>Kompleksowy model procesów występujących w pieczarkarni</i>	30
P. Zapotoczny, T. Kawałko, S. Bakier – <i>Identyfikacja fizycznych cech surowców spożywczych metodą spektrofotometryczną na przykładzie miodów</i>	40

Inżynieria lądowa i wodna

J. Kaczmarek, D. Leśniewska – <i>Wał przeciwpowodziowy w warunkach zmieniającego się poziomu wody – porównanie modeli fizycznego i numerycznego</i>	53
L.M. Kaczmarek, J. Biegowski, J.B. Skillandat – <i>Hydro- i litodynamiczne aspekty budowy kanatu żeglugowego przez Mierzę Wiślaną – część II</i>	64
K. Klempka, M. Knauff – <i>Uwzględnianie podatności podłoża w projektowaniu słupów hal żelbetowych</i>	80
M. Zagroba – <i>Historyczne układy przestrzenne małych miast Warmii i ich rola we współczesnym funkcjonowaniu obszarów śródmiejskich</i>	90

Inżynieria środowiska

P. Bogacz – Wpływ rodzaju paliwa na wartość energii pierwotnej i emisję zanieczyszczeń ..	98
J.A. Pawłowicz – Wpływ zieleni na kształtowanie krajobrazu miejskiego	113

Geodezja i kartografia

K. Dawidowicz – Poprawki do zmienności położenia centrum fazowego anteny w opracowaniu obserwacji GPS oprogramowaniem komercyjnym	120
A. Doskocz – Wstępne wykorzystanie analizy statystycznej do oceny dokładności opracowania sytuacyjnego wielkoskalowych map cyfrowych	133
A. Łyszkowicz – Wyznaczenie przebiegu quasigeoidy dla obszaru Polski metodą kolokacji najmniejszych kwadratów	147
A. Łyszkowicz, A. Bernatowicz – Ocena dokładności kolejnych kampanii niwelacji precyzyjnej w Polsce	165

Inżynieria mechaniczna

J. Dobriański, M. Duda – Eksperymentalna instalacja słoneczna z samoczynną pompą cyrkulacyjną napędzaną ciepłem lokalnym	181
J. Hałacz – Moment skręcający kończyny górnej operatora w zależności od jej położenia w normalnej przestrzeni pracy	189
K. Kuś – Wpływ procesu wielokrotnego nagrzewania i chłodzenia na charakterystyki przemian w stopie Ni-Ti	203
T. Lipiński, M. Bramowicz, P. Szabracki, P. Mikołajczyk, M. Cudakiewicz – Zużycie ściernego stopu AlSi12Mg po modyfikacji stopem Al-Si przeznaczonego na części maszyn	212
P. Mazur, D. Jasiukiewicz – Wpływ krotności przetwórstwa na wartość masowego i objętościowego wskaźnika szybkości płynięcia poliwęglanu	221
P. Mazur, P. Smoleński – Wpływ krotności przetwórstwa na wartość masowego i objętościowego wskaźnika szybkości płynięcia PPS	227
J. Pelc – Próba doskonalenia obrotowo-symetrycznego modelu opony pneumatycznej	233
W. Sobieski – Możliwości numerycznego modelowania strumienic z wykorzystaniem zjawiska bifurkacji	240
W. Sobieski – Przykłady zastosowania metody objętości skończonych do modelowania ośrodków typu fluid-solid	256
P. Szabracki, M. Bramowicz, T. Lipiński – Komputerowa analiza kształtu refleksów XRD na przykładzie stali X2CrNiMo25-7-4	266

MATHEMATICAL MODELING OF BED GEOMETRY IN THE CULTIVATION OF SEED POTATOES

Olga Duber-Skwarska

Department of Agricultural Engineering
University of Warmia and Mazury in Olsztyn

Key words: potato, bed cultivation, theoretical analysis.

Abstract

This paper investigates the effect of the working width of the bed forming unit, tractor wheel track and the inclination angle of ridger wing on the thickness of the soil layer tipped on a potato bed. The developed model was verified in a field experiment.

MODELOWANIE MATEMATYCZNE GEOMETRII ZAGONU W TECHNOLOGII UPRAWY ZIEMNIAKÓW NA SADZENIAKI

Olga Duber-Skwarska

Katedra Inżynierii Rolniczej
Uniwersytet Warmińsko-Mazurski w Olsztynie

Słowa kluczowe: ziemniak, uprawa zagonowa, analiza teoretyczna.

Abstrakt

Przeprowadzono analizę wpływu ustawienia głębokości roboczej zespołu kształtującego zagon, rozstawy kół ciągnika i kąta nachylenia skrzydeł obsypnika na grubość warstwy gleby usypanej na ukształtowanym zagonie. Oceniono teoretyczną głębokość przykrycia bulw. Opracowany model zweryfikowano.

Key

- L – rear wheel track, mm,
- L_r – width of the working path, mm,
- s_0 – width of the tractor's rear tire, mm,
- Δ_s – deformation of the tractor's rear tire, mm,
- Δ – difference between half the width of the working path and the width of the ridging body, mm,

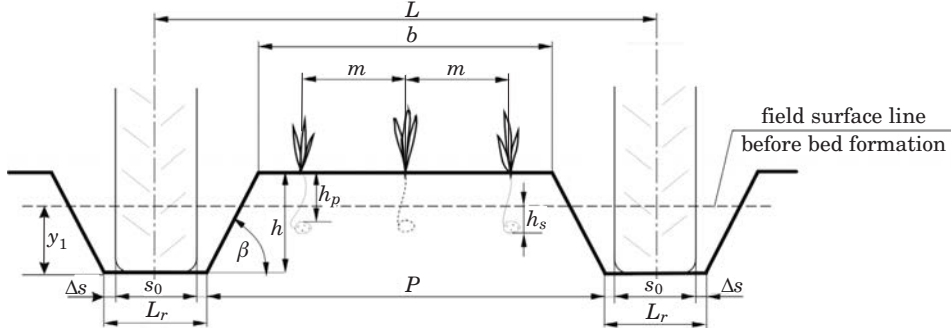
- P – width of bed base, mm,
- b – width of bed crest, mm,
- d – tuber width, mm,
- m – distance between seed potatoes in the bed, mm,
- h – height of formed bed, mm,
- h_p – thickness of soil layer covering potato tubers, mm,
- h_s – planting depth (coulters penetration depth), mm,
- s_p – working width of the ridging body, mm,
- α – angle of ridging body wing, °,
- β – angle of inclination of the formed bed's side wall, °,
- y_1 – working depth of the ridging body, mm,
- y_2 – height of the soil layer tipped on the bed, mm,
- V_1 – volume of soil lifted by the ridging body, m³,
- s_1 – cross-sectional area of soil lifted by the ridging body, m²,
- V_2 – volume of soil tipped on the bed, m³,
- s_2 – cross-sectional area of soil tipped on the bed, m²,
- x_1 – distance between the vertical wall of the working path and the side wall of the bed along the surface line of the field before bed formation, mm,
- x_1 – distance between the vertical wall of the working path and the apex of the bed crest, mm,
- k_0 – soil loosening coefficient,
- k_1 – soil sliding coefficient.

Introduction

The main aim of modern farming practices is to maximize the yield of crops characterized by specific qualitative parameters of tubers, in particular in selected areas of production, such as seed potatoes. Bed cultivation is one of such methods applied in potato farming. This technology offers a variety of advantages: the planting method improves the effectiveness of field utilization by the plant's root system, higher plant density does not lower total yield and it supports vegetation. In practice, the effectiveness of the bed cultivation technology in potato farming is determined by the performance of farming machines and working units. The three-row planter delivers optimal results in this potato cultivation technology. The setting of a planter's working units, including coulters and ridging bodies, affects bed formation.

The objective of this study was to develop a mathematical model describing the geometric parameters of a potato bed. The model has been developed based on the following simplified assumptions:

- the soil raised and shifted by the ridging body is spread across the entire bed area to ensure that all tuber rows are evenly covered;
- the width of the working path (L_r) is equal to the nominal width of the tractor's rear tire (s_0), increased by the value of tire deformation (Δ_s) (Fig. 1).



Δ_s – deformation of the tractor's rear tire, s_0 – width of the tractor's rear tire, L_r – width of the working path, L – rear wheel track, b – width of bed crest, m – distance between seed potatoes in the bed, h – height of formed bed, h_p – thickness of soil layer covering potato tubers, h_s – planting depth, β – angle of inclination of the formed bed's side wall ($\beta = 90 - \alpha$), P – width of bed base

Fig. 1. Diagram of a formed bed

Theoretical analysis

Potatoes are planted in beds using a three-row planter equipped with special ridging bodies. The setting of the planter's working units determines the shape of the formed bed, it creates a supportive environment for plant growth and it contributes to higher potato yields. The depth of the soil layer covering seed potatoes should range from 60 mm to 90 mm, while the optimal planting depth is 40 mm to 60 mm.

The bed is formed when ridging bodies lift soil from depth (y_1) and shifts it to the center of the formed bed. The geometry of the ridging body wing ensures that the side wall of the bed has the right profile, and the working width of the ridging body supports the formation of working paths.

The base of a correctly formed bed should have the optimal width (P) and height (h) to ensure the required planting depth (h_s) and thickness of the soil layer covering tubers (h_p) (Fig. 1).

The width of the working path (L_r) has to be at least equal to the nominal width of the tractor's rear tire (s_0), increased by the value of tire deformation ($2\Delta_s$). This correlation is expressed by the following formula:

$$L_r = s_0 + 2\Delta_s \quad (1)$$

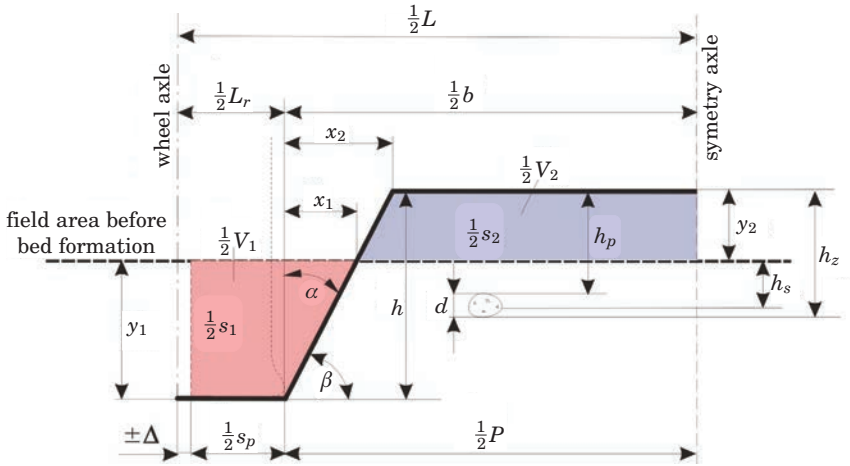
At different wheel track values ($L = 1350; 1500; 1800$ mm), the width of the bed base (P) will be equal to:

$$P = L - (s_0 + 2\Delta s) \quad (2)$$

At optimal pressure, the deformation of the rear tire will be minimal. Assuming that $\Delta_s = 0$, the width of the rear tire will be equal to the width of the working path $s_0 = L_r$, therefore:

$$P = L - L_r \quad (2a)$$

The geometric parameters of the bed in the mathematical model are presented in Figure 2.



L – wheel track, L_r – width of the working path, α – angle of ridging body wing, β – angle of inclination of the formed bed's side wall ($\beta = 90 - \alpha$), y_1 – working depth of the ridging body, y_2 – height of the soil layer on the bed, h_s – working depth of coulter (planting depth), h – height of the formed bed, h_p – thickness of soil layer covering potato tubers, d – tuber width, V_1 – volume of soil lifted by the ridging body, V_2 – volume of soil tipped on the bed, s_1 – cross-sectional area of soil lifted by the ridging body, s_2 – cross-sectional area of soil tipped on the bed, s_p – working width of the ridging body, Δ – difference between half the width of the working path and the width of the ridging body, x_1 – distance between the vertical wall of the working path and the side wall of the bed along the surface line of the field before bed formation, x_2 – distance between the vertical wall of the working path and the apex of the bed crest

Fig. 2. Geometric parameters of the bed

Ridging bodies working at depth (y_1) lift soil from a trench with volume (V_1) and spread it evenly on the bed surface to occupy volume (V_2). Soil will be loosened, and the above can be described by the following formula:

$$V_2 = k_0 \cdot V_1 \quad (3)$$

where: k_0 – soil loosening coefficient ($k_0 = 1.00 \div 1.25$).

In very long beds, changes in the volume of soil cover resulting from soil loosening will be observed only in the perpendicular direction. To account for the above, cross-sections (s_1) and (s_2) have been adopted, and formula (3) will take on the following form:

$$s_2 = k_0 \cdot s_1 \quad (4)$$

The following can be extrapolated from Figure 2:

$$s_1 = \left(\frac{2s_p + y_1 \operatorname{tg} \alpha}{2} \right) \cdot y_1 \quad (5)$$

$$s_2 = \left(\frac{L - 2s_p - 2\Delta - x_2 - x_1}{2} \right) \cdot y_2 \quad (6)$$

and

$$x_1 = y_1 \operatorname{tg} \alpha \quad (7)$$

$$x_2 = (y_1 + y_2) \operatorname{tg} \alpha \quad (8)$$

When expressions (7) and (8) are substituted for (6), the result is:

$$s_2 = \left(\frac{L - 2s_p - 2\Delta - 2y_1 \operatorname{tg} \alpha - y_2 \operatorname{tg} \alpha}{2} \right) \cdot y_2 \quad (9)$$

When expressions (5) and (9) are inserted in equation (4) and transformed, the result is:

$$y_2^2 \operatorname{tg} \alpha - y_2(L - 2s_p - 2\Delta - 2y_1 \operatorname{tg} \alpha) + k_0 y_1 (2s_p + y_1 \operatorname{tg} \alpha) = 0 \quad (10)$$

The above equation describes the correlation between the working depth of the ridging body (y_1), the angle of ridging body wing (α) and the thickness of the soil layer (y_2) covering the bed. Based on the required thickness of the soil layer covering the tuber (h_p), the height of the soil layer tipped on the bed has been determined for the set planting depth (h_s):

$$y_2 = h_p - h_s + d \quad (11)$$

and bed height:

$$h = y_1 + y_2 \quad (12)$$

In a field environment, the soil lifted by ridging bodies is shifted upwards and spread evenly over the entire bed. Expression (4) was used to calculate the theoretical cross-sectional area (s_2) and (s_1). Some soil slides away from ridging bodies, and it is returned to the working path, therefore the layer of soil that is actually tipped on the bed is thinner than the calculated layer. For this reason,

coefficient (k_1) has been introduced to determine the actual value of variable (y_2) – the height of the soil layer on the bed. Coefficient k_1 (soil sliding coefficient) is determined based on formula (13):

$$\frac{s_{1rz}}{s_t} = k_1 \quad (13)$$

where:

s_{1rz} – actual cross-sectional area of soil lifted by the ridging body;

s_t – theoretical cross-sectional area of soil lifted by the ridging body.

The actual height of the soil layer tipped on the bed will be calculated with the use of expression (14) for $k_1 \leq 1$:

$$y_{2rz} = y_2 \cdot k_1 \quad (14)$$

The mathematical model described by formulas (10), (11) and (12) describes the correlations between the geometric parameters of the bed. The above parameters constitute a basis for determining the working parameters of the planter (s_p, y^{31}, α, h_s) and the tractor (L, L_r) that affect the thickness of the soil layer covering the planted tubers.

Simulation analyses

Simulation analyses were performed on the assumption that a three-row planter will be operated with a $9 \div 14$ kN tractor. The maximum rear tire width in tractors of the above class is $241 \div 315$ mm. When formula (2a) is applied for wheel track $L = 1500$ mm, the width of the bed base is $P = 1200 \div 1300$ mm. This width of the bed base supports plant growth in line with the cultivation requirements for seed potatoes.

A computer-aided simulation of bed geometry was carried out based on the developed mathematical model. The following variable parameters were identified: working depth of the ridging body ($y_1 = 0 \div 200$ mm), angle of the ridging body wing ($\alpha = 40 \div 25^\circ$), soil loosening coefficient ($k_0 = 1.0 \div 1.2$) and planting depth ($h_s = 40 \div 70$ mm). The simulation experiment analyzed the above variables' effect on: total bed height (h), height of the soil layer forming the bed crest (y_2), height of the soil layer covering tubers (h_p).

Diagrams illustrating the results of computer-aided simulations are presented in Figure 3. An analysis of the displayed data indicates that an increase in the working depth of the ridging body (y_1) above 125 mm significantly affects the investigated parameters.

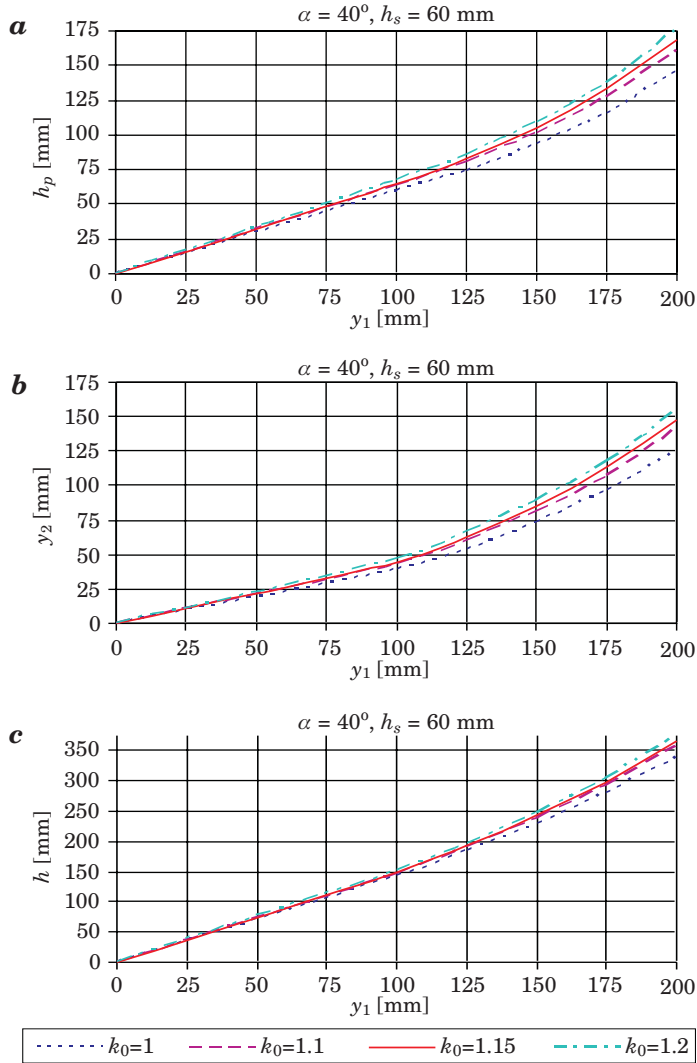


Fig. 3. Correlations between: a) thickness of the soil layer tipped on the bed (y_2), b) height of the soil layer covering tubers (h_p), c) bed height (h) and the working depth of the ridging body (y_1), angle of the ridging body wing (α) and planting depth for wheel track $L = 1500$ mm

A change in the working depth of the ridger (y_1) from 125 mm to 175 mm with planting depth (h_s) of 60 mm changes the height of the soil layer tipped on the bed (y_2) from 60 mm to 125 mm, the height of the soil layer covering tubers (h_p) from 75 mm to 140 mm, while the total increment in bed height increases from 200 mm to 300 mm.

The results of simulation analyses suggest that bed formation and tuber planting are affected by the following planter parameters: the working depth of the coulter and the working depth of the ridging body.

Model verification

A field experiment verifying the theoretical analyses of bed geometry was carried out on sandy loam with relative humidity of 25.5%.

The experimental plot had the length of 15 m. A three-row planter for bed cultivation was operated with a C-360 tractor with wheel track of 1500 mm. The planter was equipped with ridging bodies comprising skim-coulters with moldboard slats. Operating speed was constant. Seed potatoes cv. Bryza with the size of 30 ÷ 40 mm were used.

The input parameter in the mathematical model was the working depth of the ridging body (y_1) of 150 mm and planting depth (h_s) of 40 mm and 60 mm. After the planter had traveled the reference section, a profilogram was used to record the cross-sectional profiles of potato beds. Bed height and tuber depth in the bed were measured. All measurements were performed in three replications.

Profilogram data was used to determine the cross-sectional area of the soil lifted by ridging bodies and the cross-sectional area of soil tipped on the bed crest. The results of measurements and calculations are presented in Table 1.

The obtained results were used to calculate the relative error with the use of the below formula:

$$\delta_w = \frac{|x_w - x_o|}{x_o} \cdot 100\% \quad (15)$$

where: x_w – measurement result, x_o – calculation result.

Table 1
Geometric parameters of the formed bed at working depth of the ridging body $y_1 = 1500$ mm

Bed parameters	Planting depth $h_s = 40$ mm	Planting depth $h_s = 60$ mm
Width of bed base (P), mm	1350	1320
Height of formed bed (h), mm	223	220
Soil sliding coefficient (k_1)	0.9	0.9
Height of soil layer tipped on bed (y_2), mm	from 71 to 73	from 70 to 74
Thickness of soil layer covering potato tubers (h_p), mm	from 75 to 80	from 91 to 94

A comparison of the height of the soil layer tipped on the bed determined in a field experiment with the theoretical height calculated from the mathematical model produced a relative error of 2.7%. A low value of the relative error indicates that the mathematical model determines the geometric parameters of the bed with a satisfactory degree of precision.

Conclusions

The results of the study indicate that the geometric parameters of the bed are determined by the mathematical model with a satisfactory degree of precision for practical applications in the proposed potato planting technology. The height of the soil layer covering potato tubers is determined by the working depth of the ridging body and coulter penetration depth set in the planter (planting depth). In the bed cultivation system, the optimal conditions for potato farming are met when the working depth of ridging bodies is set in the range of 150 mm to 170 mm.

Accepted for print 9.07.2010

References

- BŁASZKIEWICZ Z. 2009. *Badania wpływu kół przednich i tylnych wybranych ciągników rolniczych na strukturę agregatową gleby lekkiej w koleinach*. Polska Akademia Nauk. Zeszyty Problemowe Postępów Nauk Rolniczych, 543.
- JABŁOŃSKI K. 2008. *Nowe elementy w technologii produkcji ziemniaków*. Ziemniak Polski, 1.
- MARKS N., BARAN D., BARAN P., KRZYSZTOFIK B., SOBOL Z. 1997. *Wpływ nowej techniki uprawy na powstawanie mechanicznych uszkodzeń bulw ziemniaka podczas zmechanizowanego zbioru*. Inżynieria Rolnicza, 1(1): 71–76.
- MARKS N. 1995. *Nowa technika uprawy ziemniaków*. Zeszyty Problemowe Postępów Nauk Rolniczych, 415.
- NOWAK J., KACHEL-JAKUBOWSKA M. 2009. *Postęp w technologii uprawy ziemniaków i roślin okopowych*. Technika Rolnicza Ogrodnicza i Leśna, 2.
- SKWARSKA O. *Sposób sadzenia i siewu roślin, a zwłaszcza ziemniaków*. Patent RP nr 155374.
- SKWARSKA O. 1996. *Uprawa ziemniaka w zagonach – doświadczenia i perspektywa upowszechnienia*. Materiały konferencji „Dokształcanie techniki i technologii w przemyśle i rolnictwie”, Olsztyn.

MODELING THE NATURAL CONVECTION HEATING OF LIQUID IN A VERTICAL CYLINDER

Konrad Nowak, Marek Markowski, Ewelina Sztorc

Department of Agri-Food Process Engineering
University of Warmia and Mazury in Olsztyn

Key words: natural convection, vertical cylinder, liquid food, modeling.

A b s t r a c t

Natural convection heating within a can of liquid food was simulated by solving the governing equations for continuity, momentum and energy conservation in an axisymmetric case using a commercial COMSOL Multiphysics software (Comsol). A physical experiment and computer simulations using four different models were studied. The results allowed to suggest a method of defining the properties of the material and the boundary conditions applied and to determine the usefulness of COMSOL Multiphysics package in modeling the natural convection heating of liquid food.

MODELOWANIE PROCESU NAGRZEWANIA CIECZY W PIONOWYM CYLINDRZE W WARUNKACH KONWEKCJI NATURALNEJ

Konrad Nowak, Marek Markowski, Ewelina Sztorc

Katedra Inżynierii Procesów Rolniczych
Uniwersytet Warmińsko Mazurski w Olsztynie

Słowa kluczowe: konwekcja naturalna, pionowy cylinder, żywność płynna, modelowanie.

A b s t r a k t

W pracy przeprowadzono ocenę możliwości wykorzystania pakietu Comsol Multiphysics do modelowania konwekcyjnego ogrzewania cieczy w pionowym zbiorniku w kształcie cylindra. Opisano eksperyment fizyczny oraz symulacje komputerowe procesu oparte na czterech odmiennie zdefiniowanych modelach, zrealizowanych za pomocą pakietu Comsol. Otrzymane wyniki pozwoliły na określenie przydatności pakietu Comsol Multiphysics do modelowania zjawisk konwekcji naturalnej oraz definiowania właściwości modelowanej substancji oraz zastosowanych warunków brzegowych.

Notation

$$\text{Gr} = \frac{D^3 \rho^2 g \beta (T - T_w)}{\eta^2} - \text{Grashoff number}$$

$$\text{Nu} = \frac{hD}{\lambda} - \text{Nusselt number}$$

$$\text{Pr} = \frac{c_p \eta}{\lambda} - \text{Prandtl number}$$

β – thermal expansion [1/K]

λ – thermal conductivity [W/(m K)]

ρ – actual density [kg m⁻³]

ρ_0 – initial density [kg m⁻³]

η – viscosity [Pa s]

c_p – thermal capacity [J/(kg K)]

\mathbf{g} – gravity acceleration [m s⁻²]

h – heat transfer coefficient [W/(m² K)]

n – number of measurements

p – pressure [Pa]

I – unitary matrix

Q – heat source [W]

Q_s – heat flux [W/(m² K)]

r – radial coordinate

RMSE – root mean square error [K]

T – temperature [K]

t – time [s]

T_e, T_s – measured, simulated temperature [K]

\mathbf{u} – velocity [m s⁻¹]

w – water

z – vertical coordinate

Introduction

Conventional canning processes extend the shelf life of food products and make the food safe for human consumption by destroying the pathogenic microorganisms. Natural convection induced by thermal buoyancy effects in a gravitational force field is observed in many applications. In the food industry products are thermally processed before or after packing. In the second case it is important to establish the properties of food as affected by temperature, the characteristic process parameters and to know the behavior

of the processed product in enclosure. A computational fluid dynamics (CFD) approach is a very useful tool broadly applied in the research on the behavior of liquid foods during thermal processing. GHANI *et al.* (1999) studied natural convection heating of canned liquid food using CFD methods. They detected the slowest heating zone and identified the time required to reach the sterilization temperature in this zone for vertical cylinder filled with two different liquids. GHANI *et al.* (2002) focuses on the same problems, but for a horizontal cylinder. There are also studies on effect of different shapes of enclosure on a natural convection heating of liquid food (VARMA MAHESH *et al.* 2006). RABIEY *et al.* (2007) studied transient temperature and fluid flow during natural convection heating of a cylindrical can containing large food particles. In all the studies mentioned above such commercial software as FLUENT, CFX and PHOENIX was used. Many other commercial packages enable performing CFD simulation of fluids. One of the advantages of COMSOL MULTIPHYSICS package (Comsol Co.) is its ability to work integrated with MATLAB package (MathWorks Inc.). This feature of COMSOL is not found in other engineering software packages. Therefore, the aim of this research was to study the abilities of COMSOL MULTIPHYSICS package to perform numerical simulation of heat, momentum and mass transfer in food liquid during natural convection heating of a vertical cylindrical container. The sensitivity of the model to the different values of the properties of the material and to the boundary conditions setting was also studied.

Material and experimental stand

10% water solution of sucrose was heated by natural convection in a steel can using the experimental stand shown in Figure 1. The container made of stainless steel brass with a thickness of 0.2 mm was 160 mm height and 150 mm diameter. Eight J-type thermocouples were placed on the bottom, lid, and on the wall surface of the container. Additional three thermocouples were placed inside the can: the first near the geometric centre of the can, the second and third near the bottom and the lid of the can, respectively, as can be seen in Fig. 1. Signals from thermocouples were registered by computer every 10 s. Before the beginning of the experiment, container was filled with the solution and was chilled to temperature close to 3°C. Chilled can with water was placed in steered water bath. The temperature of the water bath was maintained on the level of $40 \pm 1^\circ\text{C}$ during the experiment. Experiment was repeated 3 times.

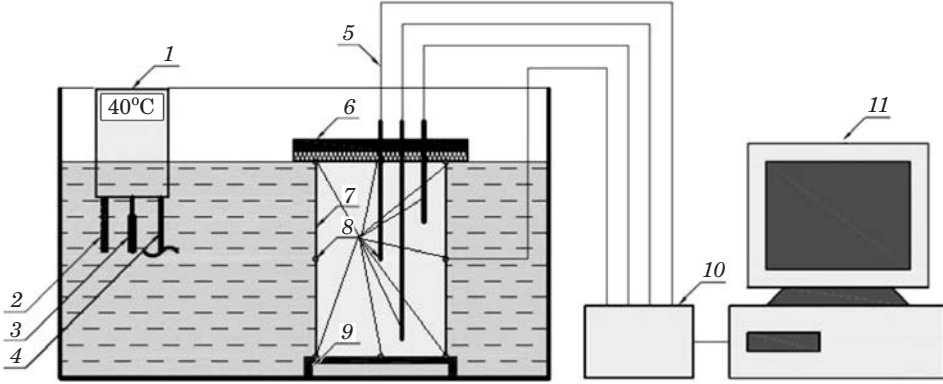


Fig. 1. The scheme of the experimental setup: 1 – thermostat, 2 – thermometer, 3 – heater, 4 – stirrer, 5 – thermocouples' wires, 6 – cover, 7 – container, 8 – thermocouples, 9 – stand, 10 – converter, 11 – PC

Mathematical model

All models were defined as two-dimension problems, with axial symmetry. Balance equations of heat (1), momentum (2) and mass transfer (3) were used as follows:

$$\rho \cdot c_p \cdot \frac{\partial T}{\partial t} + \nabla \cdot (-\lambda \cdot \nabla T) = Q + q_s \cdot T - \rho \cdot c_p \cdot \mathbf{u} \cdot \nabla T \quad (1)$$

$$\rho \cdot \frac{\partial \mathbf{u}}{\partial t} + \rho \cdot (\mathbf{u} \cdot \nabla) \cdot \mathbf{u} = \nabla \cdot [-p \cdot I + \eta \cdot (\nabla \mathbf{u} \cdot (\nabla \mathbf{u})^T)] - \frac{2}{3} \cdot \eta \cdot \nabla \mathbf{u} \cdot I + (\rho - \rho_0) \cdot \mathbf{g} \quad (2)$$

$$\frac{\partial \rho}{\partial t} + \nabla(\rho \cdot \mathbf{u}) = 0 \quad (3)$$

In order to perform the computer simulations behavior of density, viscosity, thermal conductivity, and thermal capacity of a liquid food should be known and the initial and boundary conditions should be formulated. In all the cases studied the initial temperature of the liquid was evaluated as uniformly distributed in the liquid and the initial condition was described with the following formula:

$$t = 0 \rightarrow T(r, z) = T_0 = \text{const} \quad (4)$$

Four different versions of boundary conditions, marked as M1, M2, M3 and M4, were studied. The details regarding boundary conditions applied were described underneath while the details regarding the physical properties of the liquid applied during computer simulation are set in Table 1.

Table 1

Physical properties of the water solution of the sucrose applied during simulations

Model	Coefficient
M1	$\rho(T) = (-0.004) \cdot T^2 + 2.12 \cdot T + 763.43 \text{ [kg m}^{-3}\text{]}$ $c_p = 4 \text{ 183 [J kg}^{-1} \text{ K]}$ $\lambda = 0.599 \text{ [W m}^{-1} \text{ K]}$ $\eta = 1.004 \cdot 10^{-3} \text{ [Pa s]}$
M2, M3, M4	$\rho(T) = (-0.004) \cdot T^2 + 2.12 \cdot T + 763.43 \text{ [kg m}^{-3}\text{]}$ $c_p(T) = (-0.01367) \cdot T^2 + 8.83 \cdot T + 2535.78 \text{ [J kg}^{-1} \text{ K]}$ $\lambda(T) = 4.93 \cdot 10^{-8} \cdot T^4 + (-5.84) \cdot 10^{-5} \cdot T^3 + 0.026 \cdot T^2 + (-5.12) \cdot T + 378.43 \text{ [W m}^{-1} \text{ K]}$ $\eta(T) = (-52.08 + 0.21 \cdot T)^{-2.5}$

M1. In the first case the simplest model was applied. In this model viscosity, thermal conductivity and thermal capacity of the liquid were assumed to be constant, while density was assumed to be dependent on temperature of the liquid. The temperature of a given point P on the walls, under the lid and in the bottom of the container was assumed to be constant. The boundary conditions were described with following equation:

$$t > 0 \rightarrow T|_{P \in \Omega} = T_W = \text{const} \quad (5)$$

M2. In this model viscosity, thermal conductivity, thermal capacity and density of the water solution of the sucrose were temperature dependent while similarly to the model $M1$ the boundary conditions were described with equation (5).

M3. The third model, similarly to the previous one was characterized by temperature dependent viscosity, thermal conductivity, thermal capacity and density of the water solution of the sucrose. It was assumed that Newton's law of cooling (6) can be applied to describe convection type heat transfer between surface of the cylinder and the liquid outside of the cylinder.

$$t > 0 \rightarrow -\lambda \cdot \text{grad}(T)|_{P \in \Omega} = h(t - T_W) \quad (6)$$

For this purpose the heat transfer coefficient, h , was calculated based on SERWIŃSKI (1971) on the assumption about the natural convection flow of the liquid round the vertical cylinder. Temperature dependency of the heat transfer coefficient was assumed after SERWINSKI (1971):

$$\text{Nu} = 1.18(\text{Gr} \cdot \text{Pr})^{1.125} \quad (7)$$

M4. The fourth model incorporated an artificial neural network (ANN) based on experimental data, generated by MATLAB R2009b (Mathworks Inc.). The General Regression Neural Networks (GRNN) type of ANN was used to form boundary conditions with temperature of the wall, lid and bottom varying in time. The ANN contained two layers. The number of the neurons in the first layer was equal to the size of the data set used for the teaching of ANN purpose. The number of the neurons in the second layer was 2. This approach seemed to be the most similar to real phenomenon that occurred during experiments. The boundary conditions were described with following formula:

$$t > 0 \rightarrow T|_{P \in \Omega_i} = T_i(t) \quad i = 1, 2, 3 \quad (8)$$

The values of T_i in equation (8) were generated using ANN. The values 1, 2, and 3 of index i denote wall, lid and bottom of a cylinder, respectively.

Simulations

The aim of the next stage was to simulate the natural convection heating of liquid food and calculate the changes in temperature of the liquid as monitored at measurement points shown in Figure 1. The balance equations of mass, momentum and heat (1)-(3) were used during simulations. To perform the simulations the used algorithms were implemented in COMSOL MULTIPHYSICS v.3.5a and enhanced with the Heat Transfer module. The geometry of the container used in the physical experiment was used during simulation experiments. The time range of simulations was from 0 to 300s. Solver *Direct PARADISO* was used in all simulations.

A comparison of the courses of temperature changes received from computer simulations with the results of experiments was also performed. In order to rate the differences between those results of experiments and results of the simulation root mean square error (RMSE) coefficient was used. RMSE was calculated using following formula:

$$\text{RMSE} = \frac{\sqrt{\sum_{i=1}^n (T_e^i - T_s^i)^2}}{n} \quad (9)$$

Results and discussion

The values of RMSE coefficients derived from the applied models are summarized in Table 2. The values shown in Table 2 are reflecting the correspondence of the results of the simulations to the experimental data. It can be seen in Table 2 that the results received from the models M1 and M2 are characterized by the lowest values of RMSE coefficients. The values of RMSE received from the models M3 and M4 were higher. However, the simulated values were received for the can filled only with the liquid with no thermocouple. In the case of experiment the thermocouples used for monitoring the changes in temperatures disturb the circulation of the liquid, thus temperatures and velocity of the liquid measured with and without the thermocouples poured into the liquid may be different. Figure 2 shows changes in temperature of the water solution of sucrose measured and simulated for the point near geometric centre of the cylinder during 300 s of heating. Figure 3 presents the simulated changes in average temperature of the liquid. Simulated courses of temperatures of the liquid were derived using Eqs (1)-(3) for all investigated cases of physical properties of the liquid and the boundary conditions applied. Temperature of the liquid averaged over its volume is presented in Figure 3. As can be seen in Figs 2 and 3 differences between the results received from different models are relatively small. Small values of RMSE received for all the tested models suggest that the results of simulation did not vary significantly from the experimental results. However, the least accurate results were obtained from the model M4.

Table 2

RMSE coefficients

Location of the thermocouples [m]		M1	M2	M3	M4
r	z				
0	0.08	0.111	0.111	0.270	0.340
0.025	0.05	0.221	0.221	0.282	0.312
0.005	0.11	0.078	0.078	0.124	0.164

Simulated distributions of the temperature of the liquid vs. time of heating and spatial coordinates, received for each of the applied case of the physical properties of the liquid and the boundary conditions, are shown in Figs 4–6. In case of all the courses of temperature of the liquid as derived using the method of computer simulation the period of the oscillations of the temperatures and velocities of the liquid was observed at the initial phase of the process (Fig. 2).

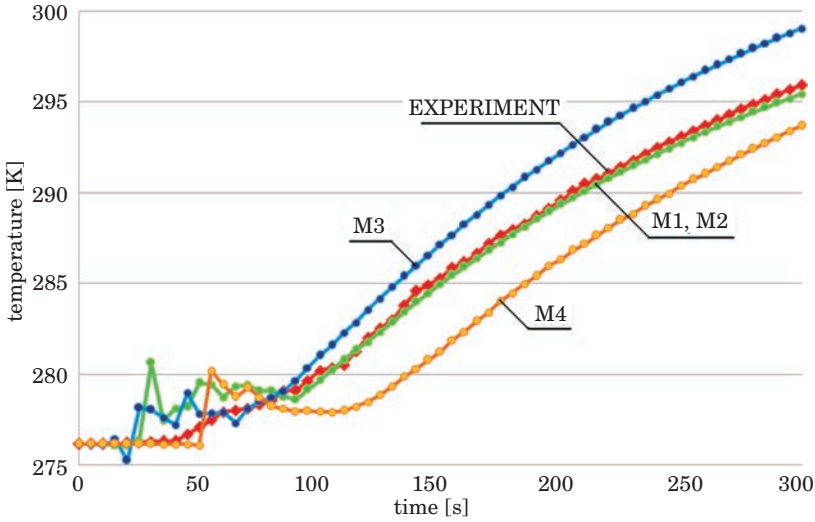


Fig. 2. Changes in the temperature of the liquid simulated at the center of the container

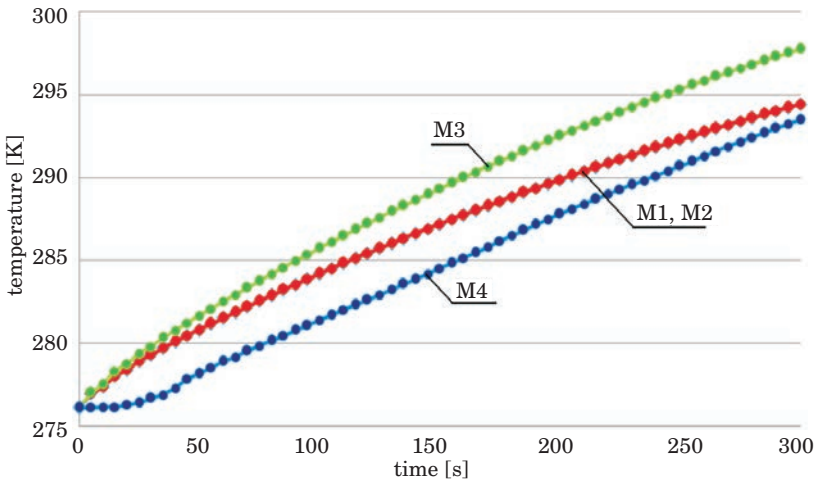


Fig. 3. Changes in average temperature of the liquid

The local oscillations in the temperature accompanied by the local whirls of the liquid gradually vanished after about 100 s of heating. The oscillations could be caused by the numerical method applied during simulation. Figure 7 presents the spatial distributions of temperature and velocity of the liquid simulated using the model M3 after 300 s of heating.

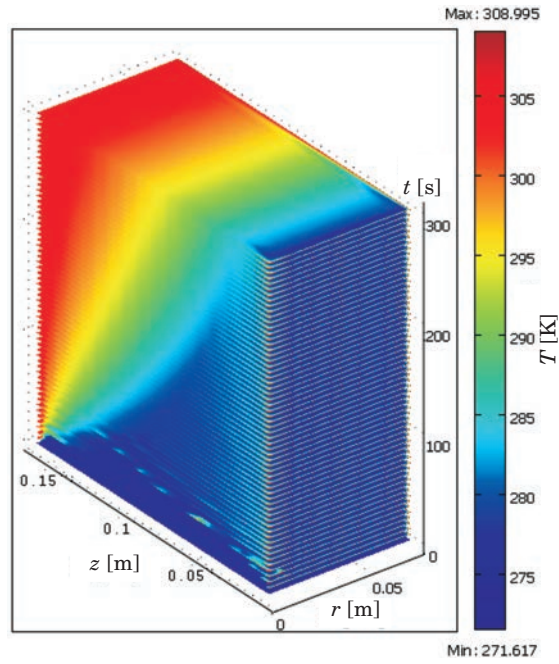


Fig. 4. Changes in temperature of the liquid simulated according to the models M1 and M2

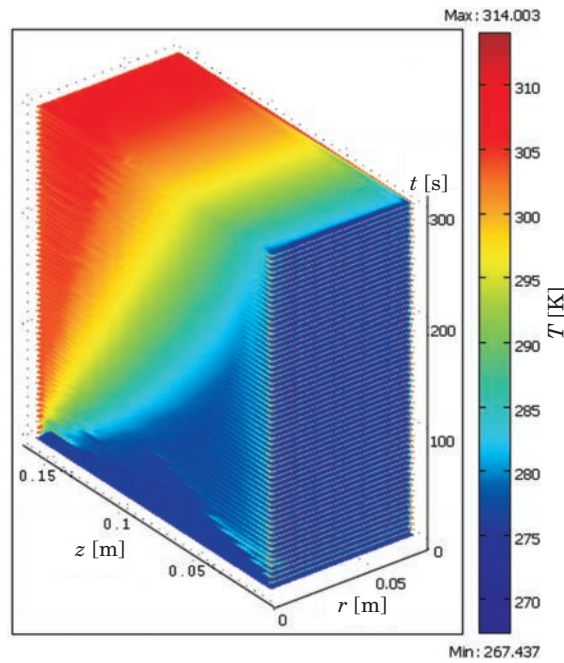


Fig. 5. Changes in temperature of the liquid simulated according to the model M3

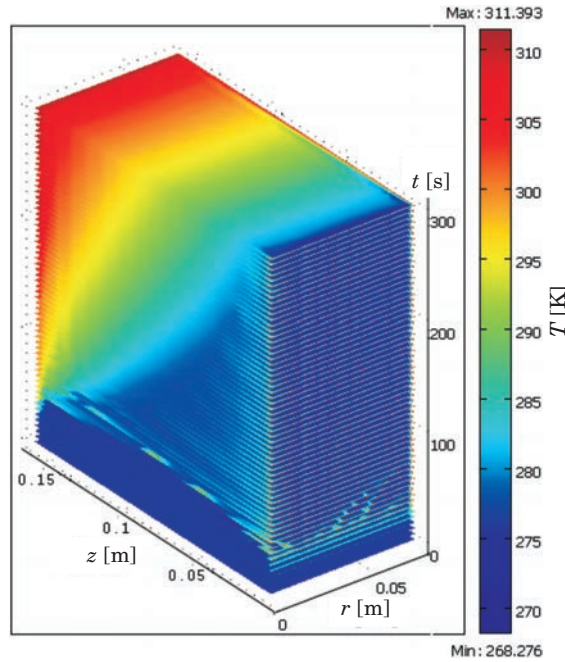


Fig. 6. Changes in temperature of the liquid simulated according to the model M4

It can be concluded from figures 2–6 that simulated courses of the local and average temperature of the liquid depend on the applied model of the physical properties of the liquid and on the type of the boundary conditions used. However, the changes in temperature of the liquid vs. time of heating simulated using models M1 and M2 are similar. This means that using thermal conductivity, thermal capacity and viscosity of liquid described as functions of the temperature do not influence significantly the results of simulation.

It should be emphasized that the method of defining the physical properties of the liquid in COMSOL MULTIPHYSICS software was important not only for the quality of the simulation model but also was important for receiving reliable results. It can be done in COMSOL by two different methods: (1) by defining an algebraic expression, (2) by using built-in data acquisition editor. It was observed that the most effective method of defining the temperature dependant physical properties of the liquid is using built-in data acquisition editor. In this case COMSOL environment uses automatically the implemented approximation procedures. The model built that way is more stable with less oscillations of the results in comparison with the model built using

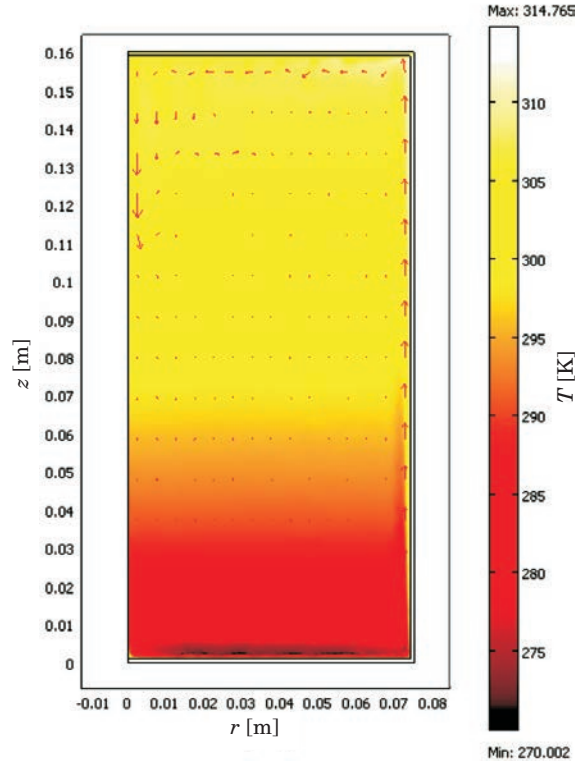


Fig. 7. Simulated spatial distributions of temperature and velocity of the liquid received using the model M3 after 300 s of heating

algebraic functions used for describing physical properties of the liquid. Also time of problem solving is reduced significantly when the built-in data acquisition editor is applied.

Conclusions

Natural convection heating within a can of liquid food was simulated by solving the governing equations for continuity, momentum and energy conservation for an axial symmetry case using a commercial COMSOL Multiphysics software (Comsol Co.). A physical experiment and computer simulations were studied using four different models. The results allowed to suggest a method of defining the properties the material and boundary conditions applied and to determine the usefulness of COMSOL Multiphysics package in modeling the natural convection heating of liquid food. Using the built-in data acquisition

editor for defining the temperature dependant physical properties of the liquid ensures receiving stable solutions with less oscillations of the results in shorter time in comparison to the model built using algebraic functions used for describing physical properties of the liquid.

Accepted for print 20.09.2010

References

- GHANI ABDUL A.G., FARID M.M., CHEN X.D., RICHARDS P. 1999. *Numerical simulation of natural convection heating of canned food by computational fluid dynamics*. Journal of Food Engineering, 41: 55–64.
- GHANI ABDUL A.G., FARID M.M., CHEN X.D. 2002. *Numerical simulation of transient temperature and velocity profiles in a horizontal can during sterilization using computational fluid dynamics*. Journal of Food Engineering, 51: 77–83.
- VARMA MAHESH N., KANNAN A. 2006. *CFD studies on natural convective heating of Canned food In conical and cylindrical containers*. Journal of Food Engineering, 77: 1024–1036.
- RABIEY L., FLICK D., DUQUENOY A. 2007. *3D simulations of heat transfer and liquid flow during sterilization of large particles in a cylindrical vertical can*. Journal of Food Engineering, 82: 409–417.
- SERWIŃSKI M. 1971. *Chemical engineering. Unit operations*. WNT, Warszawa.

THE USE OF ULTRASONIC METHODS IN THE IDENTIFICATION OF HONEY TYPES

***Arkadiusz Ratajski¹, Ireneusz Białobrzewski¹,
Fabian Dajnowiec², Sławomir Bakier³***

¹ Department of Agricultural Process Engineering

² Department of Process and Engineering Equipment

University of Warmia and Mazury in Olsztyn

³ Department of Agricultural and Food Techniques

Białystok University of Technology

Key words: ultrasound, identification, honey.

Abstract

The objective of this study was to determine the correlations between the viscosity and temperature of honey and the velocity of ultrasonic wave propagation, and to investigate the use of ultrasonic methods in the identification of different honey types. Within the analyzed temperature range, a significant correlation was found between ultrasound propagation velocity and the viscosity of honey. The results of this experiment suggest that the velocity of ultrasonic wave propagation measured at a temperature of 25°C may be a factor discriminating between different types of honey.

WYKORZYSTANIE METOD ULTRADŹWIEKOWYCH DO IDENTYFIKACJI RODZAJU MIODU

***Arkadiusz Ratajski¹, Ireneusz Białobrzewski¹, Fabian Dajnowiec²,
Sławomir Bakier³***

¹ Katedra Inżynierii Procesów Rolniczych

² Katedra Inżynierii i Aparatury Procesowej

Uniwersytet Warmińsko-Mazurski w Olsztynie

³ Zakład Techniki Rolno-Spożywczej

Politechnika Białostocka

Słowa kluczowe: ultradźwięki, identyfikacja, miód.

Abstrakt

Celem pracy było określenie zależności między lepkością miodu i temperaturą a prędkością propagacji fali ultradźwiękowej oraz zbadanie możliwości identyfikacji rodzaju miodu z wykorzystaniem metod ultradźwiękowych. W badanym zakresie zmian temperatury stwierdzono istnienie

zależności między prędkością propagacji fali ultradźwiękowej a lepkością miodu. Przeprowadzone badania pozwalają przypuszczać, że wartości prędkości propagacji fali ultradźwiękowej zmierzone w temperaturze 25°C mogą być czynnikiem dyskryminującym badane rodzaje miodu.

Symbols:

A – constant

B – activation energy [kJ mol⁻¹]

R – gas constant $R = 8.314 \text{ J mol}^{-1} \text{ K}^{-1}$

T – temperature [K]

V – velocity of ultrasonic wave propagation [m s⁻¹]

s – distance between heads [m]

t – ultrasonic wave passage time [s]

GE – global approximation error [%]

Ve – empirical value

Vm – modeled value

τ – shear stress [Pa]

γ – shear rate [s⁻¹]

μ – apparent viscosity [Pa s]

Introduction

Honey is a natural food product made by bees from flower nectar and honey-dew. The viscosity of honey is a crucial parameter in the processing and storage of honey. Viscosity is determined by the moisture content of honey, the content and type of sugars and the applied thermal processing method (ABU-JDAYIL et al. 2002).

There are various techniques for determining the viscosity of honey. According to Polish Standard PN-87/A-89291/20, the viscosity of aqueous honey solutions is determined using a Ubbelohde type viscometer. BHANDARI et al. (1999) analyzed the rheological properties of Australian honey with the application of a Brookfield viscometer featuring a spindle rotating with a set speed in the studied sample. YANNIOTIS et al. (2006) determined the viscosity of honey based on a measurement of shear forces in the gap between two coaxial cylinders. A similar technique involving a rotational viscometer and concentric cylinders was used for measuring the viscosity of honey by LAZARIDOU et al. (2004). STEFFE (1996) presented the results of honey viscosity measurements with the use of a falling sphere viscometer.

Ultrasound is increasingly often used in food tests as a nondestructive carrier of information about the analyzed material. In a series of experiments performed by MIZRACH, the velocity of ultrasonic wave propagation was

correlated with changes in the physical and chemical properties of ripening fruit and vegetables. The experimental material comprised avocados (MIZRACH 2000), plums (MIZRACH 2004) and tomatoes (MIZRACH 2007). LLULL *et al.* (2002) used ultrasound to evaluate the share of various fractions in meat stuffing. Ultrasound is also applied to test food liquids. AY *et al.* (1994) investigated the process of milk coagulation, and the measured attenuation coefficient was used to estimate process time. By relying on an empirical mathematical model, ZHAO *et al.* (2003) described the correlations between the viscosity of liquids and wave propagation velocity in the process of diluting orange juice and tomato puree.

Objective

The objective of this study was to determine the correlations between the viscosity and temperature of honey and the velocity of ultrasonic wave propagation, and to investigate the use of ultrasonic methods in the identification of different honey types.

Materials and Methods

The experimental material consisted of oilseed rape honey (H1) and mixed honey (H2) comprising multifloral honey and buckwheat honey at a 1:1 ratio. Honey was harvested in 2004 in a private apiary kept by one of the authors. To reduce the degree of crystallization, the studied honey was stored for 10 hours in an incubator at a temperature of 50°C. The rheological properties of each sample were analyzed using a Haake RheoStress1 rotational rheometer with a cone and plate system with a diameter of 35 mm and an angle of 2°. Honey samples were subjected to shear force with shear rate $\dot{\gamma}$ of 0 to 300 s⁻¹ for 180s. Measurements were performed at four honey temperatures: 25°C, 28°C, 33°C and 39°C, using a Haake DC 50 heating circulator with a water bath. The viscosity of the analyzed substances was determined using Newton's model:

$$\tau = \mu \cdot \dot{\gamma} \quad (1)$$

The application of the Arrhenius equation:

$$\mu = A \cdot e^{\frac{B}{R \cdot T}} \quad (2)$$

supported the determination of correlations between the studied samples' viscosity and temperature.

Acoustic measurements were performed using a PC equipped with the UMT-12 ultrasonic defectoscope card. Two longitudinal wave heads with a frequency of 2 MHz were applied. The heads operated in the wave transmission system, and the distance between their frontal surfaces reached 10.38 ± 0.01 mm. The time of wave passage through the analyzed material was measured when honey was cooled within the temperature range of $25 \div 45^\circ\text{C}$. The velocity of wave propagation was determined based on the below dependency:

$$V = \frac{s}{t} \quad (3)$$

The time of wave passage through the material was measured within an accuracy of $0.014 \mu\text{s}$. The distance between the frontal surfaces of ultrasound heads was determined within an accuracy of 0.01 mm. The above data were used to determine the maximum measurement error which reached $\pm 4.4 \text{ m s}^{-1}$.

The goodness of fit between the model and measuring points was evaluated with the use of the global approximation error:

$$BG = \sqrt{\frac{\sum_{i=1}^n (We_i - Wm_i)^2}{n}} \cdot 100 \quad (4)$$

Results and Discussion

The dynamic viscosity of honey was determined using Newton's fluid flow model (1) based on flow curves. Flow curves and fluid flow models are exemplified in Figure 1. In all cases, minor deviations of measuring points from a straight line could point to the presence of undissolved sugar crystals. The viscosity values produced by the applied model are presented in Table 1.

Viscosity values determined based on Newton's model

Table 1

Honey H1			Honey H2		
Temperature [°C]	Viscosity [Pa s]	GE [%]	Temperature [°C]	Viscosity [Pa s]	GE [%]
25.2	6.6	1.5	25.3	5.3	1.7
28.3	5.1	1.5	28.4	4.8	4.6
32.2	3.7	3.7	31.7	3.5	1.4
36.2	2.8	1.4	36.2	3.0	1.5

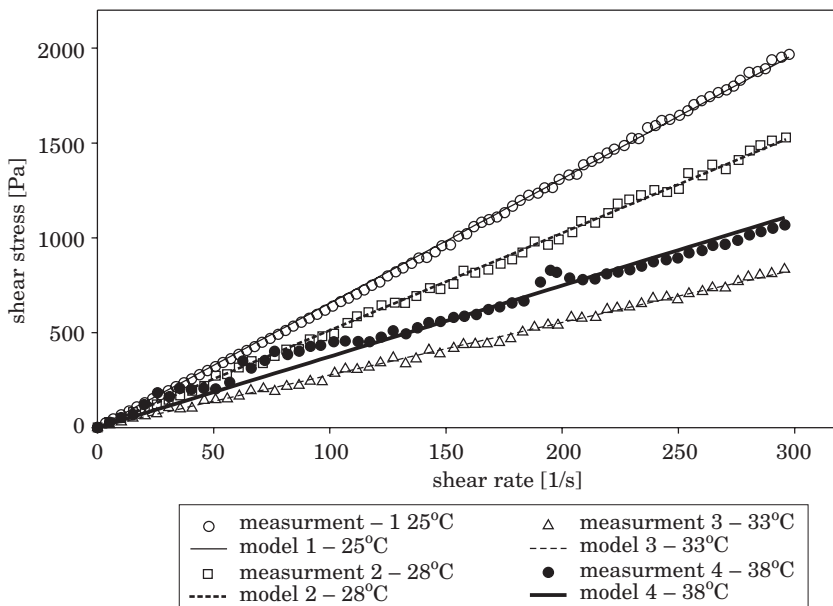


Fig. 1. Honey flow curves – experimental and model values (Newton's model [1])

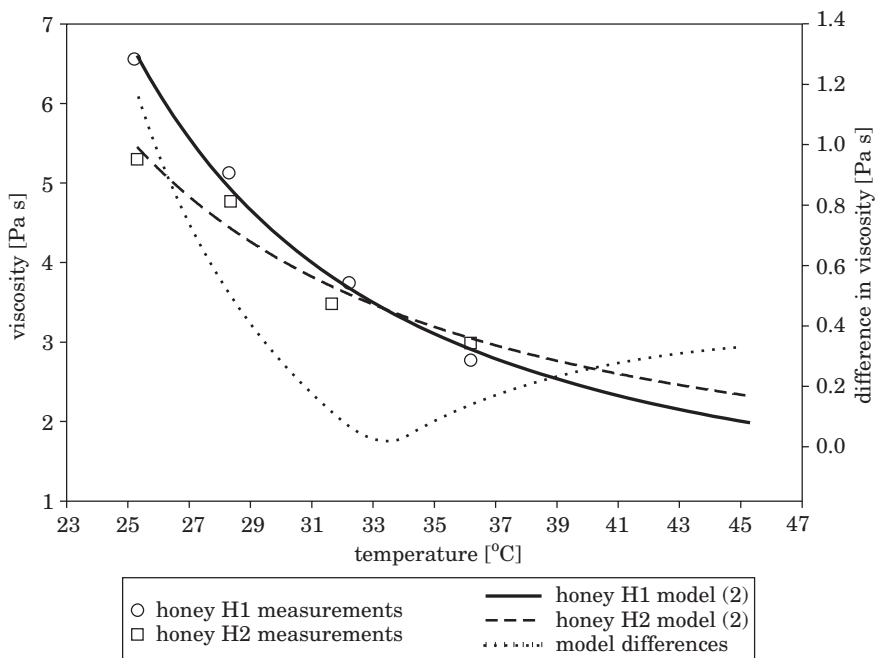


Fig. 2. The viscosity of honey as a function of temperature

The correlations between the viscosity of honey and temperature, based on experimental data and the Arrhenius-Guzman model (2), are presented in Figure 2. Although flow curves were plotted at the maximum temperature of 36.2°C, the results were extrapolated to 45°C to ensure that the temperature range is consistent with the range of ultrasonic measurements. The values of model coefficients and global approximation errors are presented in Table 2.

Table 2
Model coefficients based on the Arrhenius-
-Guzman equation

A	B	GE[%]
Honey H1		
0.434	572.8	2.1
Honey H2		
0.788	407.0	5.4

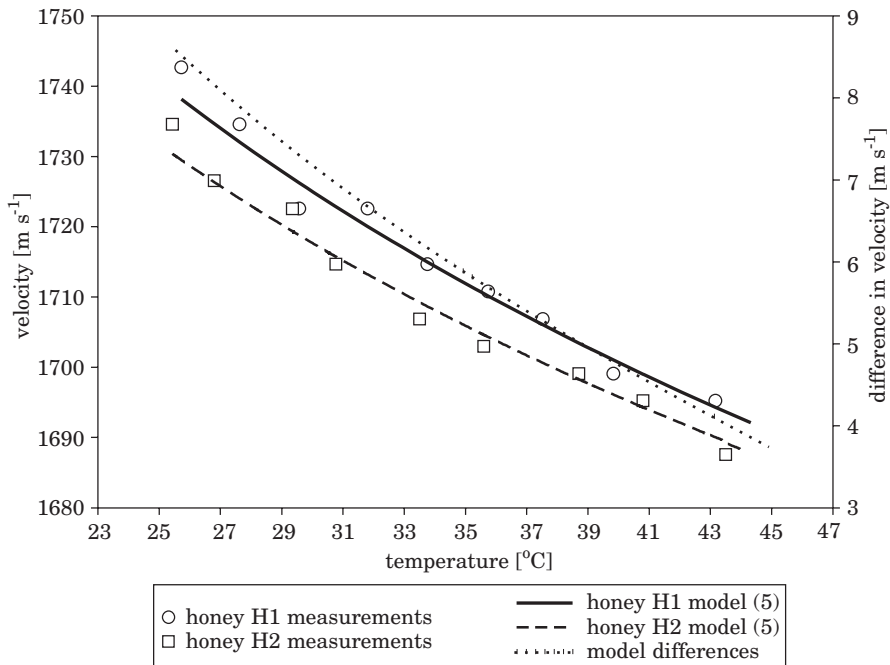


Fig. 3. Wave propagation velocity as a function of temperature and honey type

The noticeable difference in curve shapes and the values of constants A and B in the model probably resulted from variations in the composition of the studied honey due to its different origins. The modeled differences in the viscosity of honey H1 and H2 within the temperature range of 25 to 31°C reached 1.1 to 0.2 Pa s. The above differences suggest that viscosity (within the studied temperature range) could be a factor discriminating between different types of honey.

Based on ultrasonic measurements of wave propagation velocity (V) and temperature (T), a diagram illustrating the correlations between wave velocity and material temperature was developed (Fig. 3). The investigated dependency was modeled using equation (5):

$$V = c \cdot T^d \quad (5)$$

The estimated values of model coefficients are presented in Table 3.

Table 3
Model coefficients describing changes in
wave propagation velocity as a function of
temperature

c	d	GE[%]
Honey H1		
2040.3	-0.0494	0.122
Honey H2		
1998.9	-0.0446	0.111

Within the studied temperature range, the differences between the modeled wave velocity values were insignificantly below the maximum measurement error. Maximum measurement error values are unlikely to be attained, therefore, it can be assumed that significant differences in wave propagation velocity are observed at the lowest temperatures.

Conclusions

Significant correlations between the velocity of ultrasonic wave propagation and the viscosity of honey were determined within the analyzed temperature range. The results of this study suggest that if the difference in the viscosity of honey analyzed at a temperature of 25°C reaches approximately 1.1 Pa s, viscosity could be a factor discriminating between various types of honey.

The accuracy of the applied method could be improved (due to minimizing the error in velocity measurements) by increasing the distance between heads, but this approach would require larger quantities of experimental material.

Accepted for print 22.09.2010

References

- ABU-JDAYIL, BASIM, AL-MAJEED GHZAWI, ABD, AL-MALAH, KAMAL I.M., ZAITOUN, SHAHERA. 2002. *Heat effect on rheology of light- and dark-colored honey*. Journal of Food Engineering, 51: 33–38.
- AY C., GUNASEKARAN S. 1994. *Ultrasonic attenuation measurements for estimating milk coagulation time*. Transactions of the ASABE, 37(3): 857–862.
- BHANDARI B., D'ARCY B., CHOW S. 1999. *Rheology of selected Australian honeys*. Journal of Food Engineering, 41: 65–68.
- LAZARIDOU A., BILIADERIS C.G., BACANDRITSOS N., SABATINI A.G. 2004. *Composition, thermal and rheological behaviour of selected Greek honeys*. Journal of Food Engineering, 64: 9–21.
- LLULL P., SIMAL S., FEMENIA A., BENEDITO J., ROSSELLÓ C. 2002. *The use of ultrasound velocity measurement to evaluate the textural properties of sobrassada from Mallorca*, Journal of Food Engineering, 52(4).
- MIZRACH A., FLITSANOV U., AKERMAN M., ZAUBERMAN G. 2000. *Monitoring avocado softening in low-temperature storage using ultrasonic measurements*. Computers and Electronics in Agriculture, 26(2): 199–207.
- MIZRACH A. 2004. *Assessing plum fruit quality attributes with an ultrasonic method*. Food Research International, 37(6): 627–631.
- MIZRACH A. 2007. *Nondestructive ultrasonic monitoring of tomato quality during shelf-life storage*, Postharvest Biology and Technology, 46(3): 271–274.
- STEFFE J.F. 1996. *Rheological Methods in Food Process Engineering, second edition*. Freeman Press, East Lansing, MI, USA.
- YANNIOTIS S., SKALTSI S., KARABURNIOTI S. 2006. *Effect of moisture content on the viscosity of honey at different temperatures*. Journal of Food Engineering, 72: 372–377.
- ZHAO B., BASIR O.A., MITTAL G.S. 2003. *Correlation Analysis Between Beverage Apparent Viscosity and Ultrasound Velocity*. International Journal Of Food Properties, 6(3): 443–448.

COMPREHENSIVE MODEL OF PROCESSES PROCEEDING AT A MUSHROOM-GROWING CELLAR

Ewa Wachowicz, Leonard Woroncow

Department of Automation
Technical University of Koszalin

Key words: mushroom-growing cellar, modeling, simulation.

A b s t r a c t

A comprehensive, mathematical and a computer model of a mushroom-growing cellar was presented in this paper. This model includes models of a manufacturing processes occurring in a mushroom, models of air conditioning and ventilation systems, and also a control system model. The results of simulation tests on a mushroom-growing cellar carried out with the MATLAB software environment were presented in a subsequent part of the paper.

KOMPLEKSOWY MODEL PROCESÓW WYSTĘPUJĄCYCH W PIECZARKARNI

Ewa Wachowicz, Leonard Woroncow

Katedra Automatyki
Politechnika Koszalińska

Słowa kluczowe: pieczarkarnia, modelowanie, symulacja.

A b s t r a k t

W pracy omówiono kompleksowy, matematyczny i komputerowy model pieczarkarni. W jego skład wchodzi modele procesów technologicznych występujących w pieczarkarniach, a także modele układów wentylacji i klimatyzacji oraz model systemu sterowania. Przedstawiono wyniki badań symulacyjnych pieczarkarni, przeprowadzonych z wykorzystaniem środowiska programowego MATLAB.

List of symbols and signs

G – mass rate of air flow, kg s^{-1} ,
 H – mass flux density, $\text{kg s}^{-1} \text{m}^{-2}$,
 M – mass, kg ,

PP – air throttle loading, absolute,
 T – temperature, K,
 w – carbon dioxide content in air, kg kg^{-1} ,
 x – water content in air, kg kg^{-1} ,

Indices:

ch – cooler,
 CO_2 – CO_2 system,
 h – cellar,
 km – mixing chamber,
 n – air humidifier,
 na – heater,
 p – cultivated soil,
 pc – air supplied a cellar to a mixing chamber,
 ph – air supplied to a cellar,
 pw – air exhausted from a cellar to the environment,
 pz – outside air,
 s – cultivated soil sprinkler,
 skr – condenser.

Introduction

Strong market competition forces owners of mushroom-growing cellars to produce cheap, high quality mushrooms. Hence, expectations of the owners of mushroom-growing cellars directed at automation specialists include:

1. Assurance inside the cultivation halls the required runs or values of technological parameters in the form of: temperature and relative humidity of indoor air, temperature and moisture content in the cultivated soil, as well as carbon dioxide in the air inside the mushroom-growing cellars. This makes it possible to obtain high and good quality crop of mushrooms (SZUDYGA 1995). This condition is possible to meet when the mushroom-growing cellar will be equipped with air conditioning and ventilation equipment and control system for these devices.

2. Energy-efficient control of technological parameters, thereby reducing operating costs of a mushroom-growing cellar, and hence will reduce the price of mushrooms.

The above-mentioned demands are mutually incompatible. It is not the cheapest possible (i.e. without switching on the energy-consuming air conditioning and ventilation equipment), the growing of mushrooms of good quality. Therefore, in the Department of Automation at Technical University of

Koszalin the work is underway, which aims to reach a compromise between the expectations of the owners of mushroom-growing cellars. This work consists in searching for energy-saving algorithms to control the technological parameters of a mushroom-growing cellar, while ensuring the best possible quality control.

It is common knowledge that testing of new, untested proposals of mushroom-growing cellar control algorithms is associated with the possibility of the creation of material losses incurred by an owner of the mushroom-growing cellar. Therefore there was developed a comprehensive model a of mushroom-growing cellar, which allows the validation and assessment of the operation control system of ventilation and air conditioning equipment, equipped with a variety of energy-efficient control algorithms. Evaluation of algorithm control proposals will based on the results of simulation tests, carried out using a complex model a of mushroom-growing cellar.

The aim of this work was:

- formulate a comprehensive mathematical and computer model of a mushroom-growing cellar containing models of the processes of heat and transfer taking place in the hall of mushroom cultivation, models of air conditioning and ventilation equipment and a model of a control system,
- carry out simulation tests using the developed model and model validation.

Simulation model of a mushroom-growing cellar

Figure 1 illustrates a block diagram of a simulation, comprehensive model of a mushroom-growing cellar.

A simulation, comprehensive model of a mushroom-growing cellar contains the following models:

1. Control object in the form of technological processes occurring in the inside air at the hall and cultivated soil,
2. ambient or outside air,
3. processes during the operation of ventilation and air conditioning equipment, i.e. a mixing chamber, cooler, condenser, heater, humidifier, sprinkler and CO₂ system.

In addition, a model comprising the control system model for air conditioning and ventilation devices, currently implementing the control algorithm applied to the a mushroom-growing cellar in Wersk.

Comprehensive computer model of the mushroom-growing cellar is presented in Figure 2.

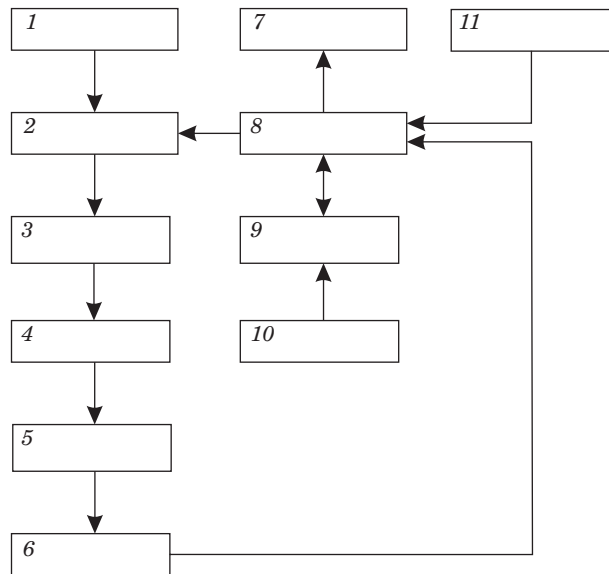


Fig. 1. Block diagram of a comprehensive model of a mushroom-growing cellar: 1 -atmospheric air, 2 - mixing chamber, 3 - cooler, 4 - condenser, 5 - heater, 6 - humidifier, 7 - outside air, 8 - inside air, 9 - cultivated soil, 10 - sprinkler, 11 - CO₂ system

Source: Own study.

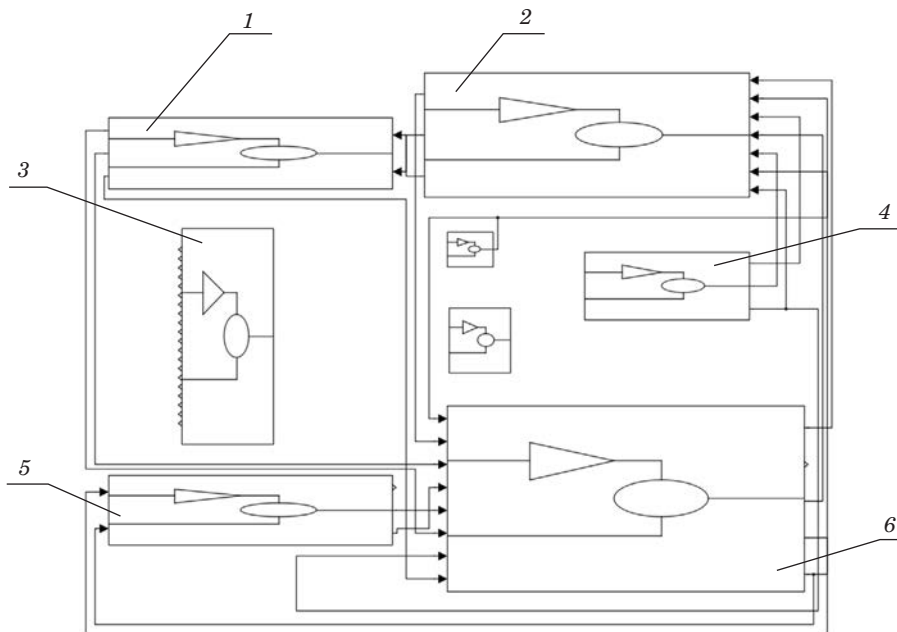


Fig. 2. Comprehensive computer model of the mushroom-growing cellar: 1 - climate control panel, 2 - mixing chamber, 3 - experimental data, 4 - outside air, 5 - cultivated soil, 6 - cultivation hall

Source: Own study.

Simulation model of processes proceeding in the mushroom-growing cellar was received after it was implemented in the MATLAB software environment Simulink toolbox (TARNOWSKI 2004) of differential equations providing a mathematical model of the heat and mass transfer processes occurring in the inside air and cultivated soil of mushrooms.

Mathematical model of processes proceeding in the mushroom-growing cellar

The mathematical model of processes proceeding in air and in cultivated soil of a mushroom-growing cellar assumes the form of a heat and mass balance equation (Equations 1–5). These equations describe changes as a function of time in:

- enthalpy of air in a plant house (Equation 1),
- water content in air in a plant house (Equation 2),
- heat of cultivated soil in a plant house (Equation 3),
- water content in a cultivated soil in a plant house (Equation 4)
- carbon dioxide content in air inside a plant house (Equation 5).

$$\underbrace{M_h \cdot c \cdot \frac{dT_h}{dt}}_{\text{Change in air enthalpy in a plant house}} = c \cdot \underbrace{(G_{ph} \cdot T_{na} \cdot K_{na})}_{\text{Heat flux from a heater}} - \underbrace{G_{ph} \cdot T_{ch} \cdot K_{ch}}_{\text{Coolness flux from a cooler}} - \underbrace{G_{pw} \cdot T_h}_{\text{Heat flux carried off with exhausted air}} + \underbrace{G_{ph} \cdot T_{km}}_{\text{Heat flux supplied to a plant house with blown-in air}} - \underbrace{G_{pc} \cdot T_h}_{\text{Heat flux supplied to a mixing chamber}} + \underbrace{\alpha \cdot S_p \cdot (T_h - T_p)}_{\text{Heat flux from cultivated soil}} \quad (1)$$

$$\underbrace{M_h \cdot \frac{dx_h}{dt}}_{\text{Change of water content in inside air}} = \underbrace{x_{pz} \cdot G_{pz}}_{\text{Water stream in atmospheric air}} - \underbrace{x_h \cdot G_{pw}}_{\text{Water stream in exhausted air}} - \underbrace{x_h \cdot G_{pc}}_{\text{Water stream supplied to a mixing chamber}} - \underbrace{H_{skr}}_{\text{Water stream collected in a condenser}} + \underbrace{H_N}_{\text{Water stream absorbed by air from a humidifier}} + \underbrace{\alpha_p \cdot S_p \cdot (x - x_{pm})}_{\text{Water stream evaporated by soil}} \quad (2)$$

$$\underbrace{M_p \cdot c_p \cdot \frac{dT_p}{dt}}_{\text{Change of heat in cultivated soil}} = \underbrace{\alpha \cdot S_p \cdot (T_h - T_p)}_{\text{Heat flux given up to air}} - \underbrace{r_{pw} \cdot \alpha_p \cdot S_p \cdot (x - x_{pm})}_{\text{Heat flux used for evaporation of water from soil}} \quad (3)$$

$$\underbrace{M_p \cdot \frac{dx_p}{dt}}_{\text{Change of water content in cultivated soil}} = \underbrace{H_S}_{\text{Stream of water obtained from a sprinkler}} - \underbrace{\alpha_p \cdot S_p \cdot (x - x_{pm})}_{\text{Stream of water evaporated by cultivated soil}} \quad (4)$$

$$\underbrace{M_h \cdot \frac{dw_h}{dt}}_{\text{Change of CO}_2 \text{ content in inside air}} = \underbrace{G_{ph} \cdot w_{km}}_{\text{Stream of CO}_2 \text{ in air supplied to a plant house}} + \underbrace{G_{CO_2} \cdot w_{CO_2}}_{\text{Stream of CO}_2 \text{ supplied from CO}_2 \text{ system}} - \underbrace{G_{pw} \cdot w_h}_{\text{Stream of CO}_2 \text{ removed from a plant house with exhausted air}} - \underbrace{G_{pc} \cdot w_h}_{\text{Stream of CO}_2 \text{ in air supplied to a fixing chamber}} \quad (5)$$

An example of a simulation model of the heat exchange process in the air inside a mushroom-growing cellar is presented in Figure 3. This model constitutes the implemented MATLAB software environment, Equation 1.

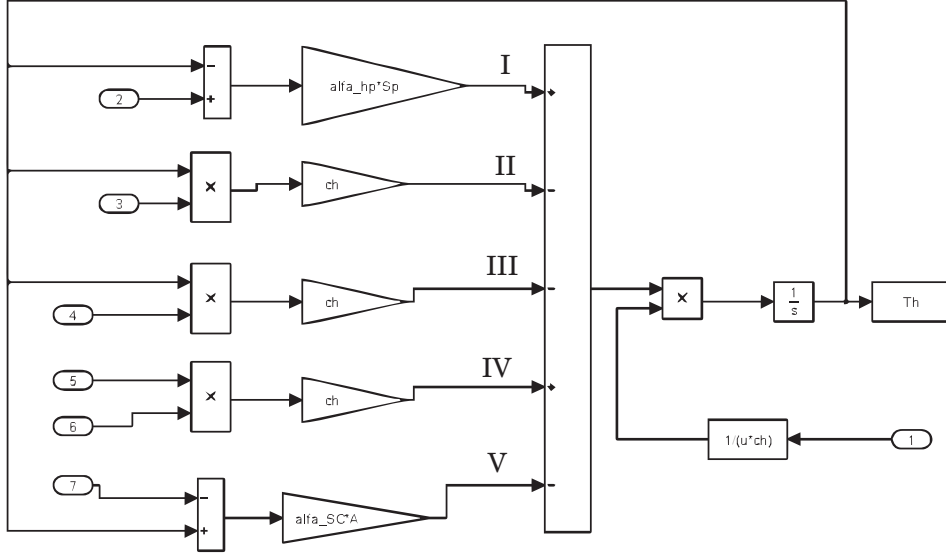


Fig. 3. Implementation of equation (1) in the MATLAB software environment forming a mathematical model of heat exchange in the air inside a mushroom-growing cellar: 1–7 – data input, I – heat flux from cultivated soil, II – heat flux removal to a mixing chamber, III – heat flux removal along with air blown out, IV – heat flux supplied to a hall along with air from a climate control panel, V – heat flux removal to environment

Source: Own study.

Mathematical models and simulation of processes proceeding during the operation of air conditioning and ventilation equipment

The processes shown in Figure 1 proceeding during the operation of air conditioning and ventilation equipment are described mathematically, using the textbook according to (MALICKI 1977). Then the equations were implemented in the MATLAB software environment. The following examples disclose equations (6 – 15), which form a mathematical model of the mixing chamber.

$$G_{ph} = G_{pz} + G_{pc} \quad (6)$$

$$G_{pz} = PP_{pz} + G_{ph} \quad (7)$$

$$G_{pc} = PP_{pc} + G_{ph} \quad (8)$$

$$PP_{pz} = 1 - PP_{pc} \quad (9)$$

$$G_{pz} = (1 - PP_{pc}) \cdot G_{ph} \quad (10)$$

$$G_{ph} \cdot w_{km} = G_{pz} \cdot w_{pz} + G_{pc} \cdot w_h \quad (11)$$

$$G_{ph} \cdot w_{km} = PP_{pz} \cdot G_{ph} \cdot w_{pz} + PP_{pc} \cdot G_{ph} \cdot w_h \quad (12)$$

$$w_{km} = PP_{pz} \cdot w_{pz} + PP_{pc} \cdot w_h \quad (13)$$

$$x_{km} = (1 - PP_{pc}) \cdot w_{pz} + PP_{pc} \cdot x_h, x_{km}(\max) = f(T_{km}) \quad (14)$$

$$T_{km} = (1 - PP_{pc}) \cdot T_{pz} + PP_{pc} \cdot T_h \quad (15)$$

A computer model of the processes proceeding in the mixing chamber, obtained after implementing the above equations in the MATLAB software environment is presented in Figure 4.

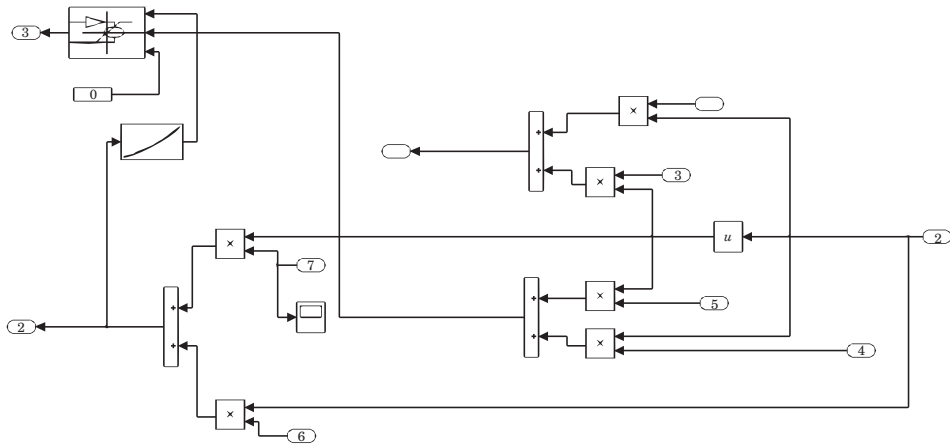


Fig. 4. Implementation of Equation (1–10), forming a mathematical model of the mixing chamber, in the MATLAB software environment: 1–6 – data ports

Source: Own study.

Sample results of simulation processes proceeding at a mushroom-growing cellar

At a mushroom-growing cellar in Wersk near Czluchow experimental investigations were conducted, during which runs of the technological parameters of a mushroom-growing cellar and operating conditions of ventilation and air conditioning equipment were simultaneously recorded. It was assumed during the simulation tests carried out based on the knowledge of a comprehensive, computer model of a mushroom-growing cellar that ventilation and air conditioning equipment was working, such as at the mushroom-growing cellar in Wersk, and then runs of the technological parameters were determined. In order to verify the correctness of a comprehensive model of a mushroom-growing cellar, it has undergone operational validation.

It was that the simulation results were compared with measurements carried out at a real mushroom-growing cellar. Simulation tests and measurements were carried out while maintaining the same reference conditions (operating conditions of ventilation and air conditioning equipment).

Figure 5 shows the examples of:

- calculated and recorded in Wersk runs of indoor air temperature obtained during the operation of an air heater (Fig. 5a),
- operating conditions of the mixing chamber, where due to the possibility of controlling the degree of throttle opening, the respective proportions of outside air were mixed with the internal (Fig. 5b). (The figure below shows the percentage of outside air in the mixed air). Moreover, the calculated and measured runs of air temperature at the outlet from the mixing chamber corresponding to the operating conditions are also presented in Figure 5b.

Analysis of the simulation test results revealed that the model was formulated properly and that it properly reflects the runs of processes proceeding at a mushroom-growing cellar.

Summary

The results of work on the development of a comprehensive model of a mushroom-growing cellar were presented in the paper. In effect, the mathematical and computer models were produced: the processes of heat and mass transfer occurring at a mushroom-growing cellar, a model of the environment, as well as models of the processes proceeding in the ventilation and air conditioning equipment and the controls. Logical and empirical analysis of the simulation test results confirmed that models were performed correctly. The comprehensive model of a mushroom-growing cellar proposed in the paper will

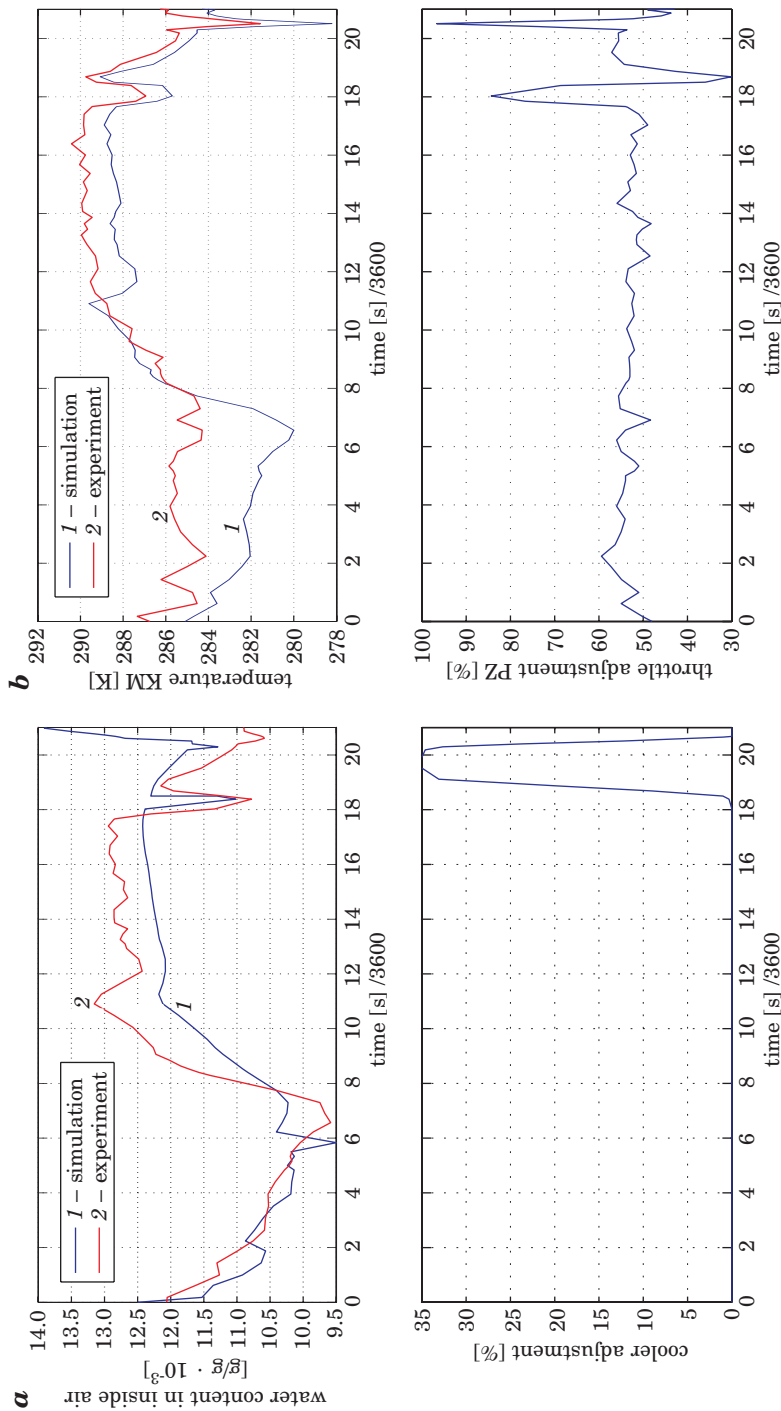


Fig. 5. Sample runs: *a* – the indoor air temperature and operating conditions of the air heater, *b* – the mixed air temperature at the outlet of the mixing chamber and the degree of opening of the outside air throttle
Source: Own study.

have application in the development and while testing the algorithms for efficient ventilation and air conditioning equipment in the building of a mushroom-growing cellar.

Translator: Leszek Kawczyński

Accepted for print 15.09.2010

References

- MALICKI M. 1977. *Ventilation and Air Conditioning*. The Polish Scientific Publishers. Warsaw.
- SZUDYGA K. 1995. *Growing mushrooms*. HORTPRESS. Warsaw. ISBN 83-86384-01-8.
- TARNOWSKI W. 2004. *Modeling of systems*. Publishers of Koszalin University of Technology. ISBN 83-7365-052-0.
- VORONTOV L., WACHOWICZ E. 2009. *Selection of aeration vent areas in the ventilating duct of a mushroom-growing cellar*. Annals of Warsaw University of Life Sciences, 54: 1977–1983.
- WACHOWICZ E., VORONTOV L. 2009. *Simulation of heat and mass exchange processes proceeding in mushroom-growing cellars*. Polish Journal of Environmental Studies, 18(4B): 216–220.

DETERMINATION OF THE PHYSICAL CHARACTERISTICS OF FOOD RAW MATERIALS BY SPECTROPHOTOMETRY – THE EXAMPLE OF HONEY

Piotr Zapotoczny¹, Tomasz Kawałko¹, Sławomir Bakier²

¹ Department of Agricultural Process Engineering
University of Warmia and Mazury in Olsztyn

² Department of Agricultural and Food Techniques
Białystok University of Technology

Key words: honey, color, $L^*a^*b^*$, storage, discrimination.

A b s t r a c t

The paper presents changes in the color of 10 selected types of honey during storage. The measurements were performed using a MiniScan XE Plus spectrophotometer (HunterLab). The color of honey was described based on $L^*a^*b^*$ coordinates. The values of hue h^* and chroma C^* were also calculated. Until day 14 of storage, no statistically significant ($p = 0.01$) changes in the color of crystallized oilseed rape honey, liquid multifloral honey and crystallized multifloral honey were noted. The color of the remaining seven honey types started to change on the first day of storage.

IDENTYFIKACJA FIZYCZNYCH CECH SUROWCÓW SPOŻYWCZYCH METODĄ SPEKTROFOTOMETRYCZNĄ NA PRZYKŁADZIE MIODÓW

Piotr Zapotoczny¹, Tomasz Kawałko¹, Sławomir Bakier²

¹ Katedra Inżynierii Procesów Rolniczych
Uniwersytet Warmińsko-Mazurski w Olsztynie

² Zakład Techniki Rolno-Spożywczej
Politechnika Białostocka

Słowa kluczowe: miody, barwa, $L^*a^*b^*$, przechowywanie, dyskryminacja.

A b s t r a k t

W pracy przedstawiono zmianę barwy dziesięciu wybranych typów miodów w czasie ich przechowywania. Pomiar wykonano z wykorzystaniem spektrofotometru MiniScan XE Plus firmy HunterLab. Barwę opisano modelem $L^*a^*b^*$. Zostały także wyliczone indeksy odcienia barwy h^* oraz

nasylenia C^* . W czasie przechowywania nie zauważono istotnie statystycznych ($p = 0,01$) zmian w barwie do 14 dnia przechowywania dla miodów rzepakowego skrzystalizowanego, wielokwiatu płynnego oraz wielokwiatu skrzystalizowanego. Barwa pozostałych siedmiu typów zmieniała się od pierwszego dnia przechowywania.

Introduction

Color is one of the key quality attributes and physical characteristics of food raw materials and products, which considerably affects their evaluation. Color provides information about the chemical composition, processing suitability and storage life of food products. Color may be described by two methods. The first method involves organoleptic evaluation, and the other – instrumental measurement. Both approaches have their advantages and disadvantages. Standardized instrumental techniques show high reproducibility and accuracy, whereas organoleptic assessment methods support color description corresponding to human visual perception. Instrumental measurements require the use of spectrophotometers and colorimeters. Based on the composition of the spectrum of radiation reflected by the studied object, a computer program calculates color coordinates in the XYZ space for a specified observer (field of view of 10° and 2°) and illuminant (e.g. D65. C. A).

Color is one of the most variable features of honey, owing to its floral origin, the applied technological process and the temperature and time of storage (SALA et al. 1993). TERRAB et al. (2004) assessed the color of 23 samples of thyme (*Thymus mastichina* and *Thymus capitatus*) honey and 13 samples of avocado (*Persea Americana*) honey, collected in Spain between 2002 and 2003. A discriminant analysis was employed to distinguish between the two types of honey. The two analyzed honey types were better characterized when lightness L^* , chroma C^* and hue angle h^* were used as variables (94% accuracy). LAZARIDOU et al. (2004) determined the color of honey with the use of a Metertech UV/VIS SP8001 spectrophotometer and a Minolta Dimage 5 digital camera. A total of 33 types of honey of different botanical origin from different geographical regions of Greece were analyzed. Honey samples were assayed for sugar composition, water content, water activity values and thermal properties. Color was measured at a wavelength of 420 nm, following honey sample dilution with distilled water at a 1:5 ratio (BATH, SINGH 1999). The images of honey samples were taken using a digital camera and a proper illumination system, according to the procedure proposed by PAPADAKIS et al. (2000). POPEK (2002) attempted to develop a new method for honey identification relying on a discriminant analysis. The author examined the physicochemical properties, quality attributes and color components of 73 honey samples, but the obtained results were unsatisfactory – the applied

procedure did not enable to classify all honey types. GONZALES *et al.* (1999) studied changes in honey color during storage in relation to honey composition and initial color. Samples of 16 floral honeys, collected in different geographical plain regions of temperate climate in Argentina, were analyzed. Honey color was measured using a Hunterlab 5100 spectrophotometer. The illuminated area had a diameter of 4.7 mm. The values of color attributes, reflecting brown pigment formation in honey, were calculated as described by BUERA *et al.* (1985) and BUERA (1989).

Objective and Scope of the Study

The objective of this study was to determine changes in the color of selected types of honey during storage. A discriminant analysis was performed to find out whether honey types can be classified based on color components. A method for color measurement was developed, and the obtained results were subjected to a statistical analysis.

Experimental Material

The measurements were performed on 10 types of honey (Tab. 1). Samples of liquid and crystallized honey were collected in 2004. Prior to color measurement, honey samples were placed in a thermostat (40°C 24 hours) for liquefaction.

Table 1

Types of honey subjected to evaluation

Honey type	Name
Honey – 1	liquid oilseed rape honey
Honey – 2	liquid buckwheat honey
Honey – 3	crystallized coniferous honeydew honey
Honey – 4	crystallized oilseed rape honey
Honey – 5	liquid multifloral honey
Honey – 6	pine honey
Honey – 7	crystallized multifloral honey
Honey – 8	liquid honeydew honey
Honey – 9	crystallized buckwheat honey
Honey – 10	mixed honey composed of honey 5 and honey 9 at a 50/50 ratio 9

Measurement Method

The color of honey was measured in reflected light, using a MiniScan™ XE Plus spectrophotometer (HunterLab) connected to a computer. Color coordinates were determined in the CIE $L^* a^* b^*$ space for the 10° standard observer and the D65 standard illuminant. The color of each honey type was measured in 30 replications, over a period of 38 days, at two-day intervals. Honey samples were placed in cube-shaped plastic containers (5x5 cm), and color was measured on each side (in five replications), at each vertex and in the middle of each side. Means were compared by a one-way analysis of variance at a significance level of $p = 0.01$ (Duncan's test). The results were verified statistically using Statistica 8.0 software. The values of whiteness index (WI E313) and yellowness index (YI E313) were calculated using Universal Software ver. 3.80 provided with the spectrophotometer. The MS Excel application was used to calculate the values of chroma C^* and hue h^* . A discriminant analysis was performed to determine whether the studied honey types could be distinguished from one another. The applied method was selected for the study since the values of the variables had a normal distribution and the variance matrix for variables in groups was homogeneous. Due to the nature of the variables, there was a minimal risk of the matrix not fulfilling the redundancy condition. The values of chroma C_{ab}^* and hue h_{ab}^* were calculated as follows:

$$C_{ab}^* = \sqrt{a^{*2} + b^{*2}} \quad (1)$$

$$h_{ab}^* = \arctan \left(\frac{b^*}{a^*} \right) \quad (2)$$

where:

a^* – redness component

b^* – yellowness component

Results and Discussion

Honey samples were divided into two groups based on the mean values of color lightness L^* (Fig. 1).

Honey 1 honey 5 and honey 4 were classified into the first group, while the second group comprised the remaining honey types. In group one, there were significant differences between honey 1 and honeys 5 and 4 while in group two – between honey 8 and honeys 7 and 10. Not all types of honey could be distinguished based on the values of color component L^* . The greatest difference in lightness was noted between oilseed rape honey and honeydew

honey. Significant differences were also observed between liquid and crystallized oilseed rape honey, and between liquid and crystallized multifloral honey.

Table 2

Mean values of color components and indices

Types of honey	L^*	a^*	b^*	WI E313	YI E313	C^*	h
	[-]	[-]	[-]	[-]	[-]	[-]	[-]
Honey – 1	24.30 ^a	0.13 ^{cd}	1.38 ^{cd}	-13.02 ^a	7.48 ^d	1.40 ^{bc}	84.73 ^a
Honey – 2	25.87 ^{cd}	0.17 ^d	1.49 ^d	-13.24 ^a	7.87 ^d	1.51 ^c	83.35 ^a
Honey – 3	25.90 ^{cd}	-0.37 ^a	0.92 ^b	-6.43 ^c	3.93 ^a	1.01 ^a	111.74 ^e
Honey – 4	24.78 ^b	0.10 ^{cd}	1.38 ^{cd}	-12.75 ^a	7.37 ^d	1.41 ^{bc}	85.73 ^a
Honey – 5	24.56 ^b	0.13 ^{cd}	1.50 ^d	-14.30 ^a	8.05 ^d	1.52 ^c	84.90 ^a
Honey – 6	26.06 ^{cd}	0.06 ^{cd}	0.90 ^b	-6.03 ^c	4.69 ^{ab}	0.93 ^a	86.00 ^b
Honey – 7	25.82 ^c	0.54 ^e	0.67 ^a	-3.36 ^d	4.54 ^{ab}	0.90 ^a	51.27 ^c
Honey – 8	26.09 ^d	-0.01 ^c	0.84 ^{ab}	-5.23 ^{cd}	4.21 ^{ab}	0.86 ^a	90.38 ^d
Honey – 9	26.02 ^{cd}	-0.20 ^b	1.25 ^c	-10.29 ^b	5.89 ^c	1.28 ^b	98.94 ^d
Honey – 10	25.82 ^c	0.21 ^d	0.92 ^b	-6.36 ^c	5.09 ^{bc}	0.96 ^a	77.28 ^a

Mean values (determined on day 1) in columns followed by different superscript letters are significantly different at $p = 0.01$.

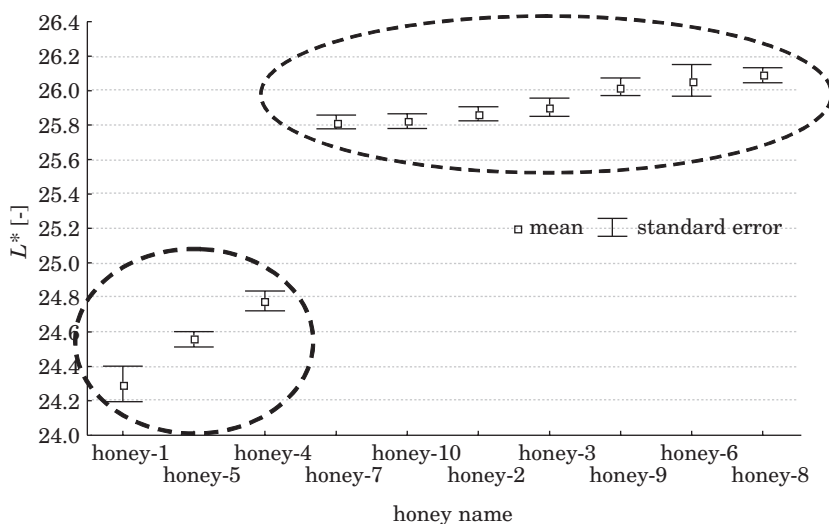


Fig. 1. Mean values of color component L^* (lightness) for each honey type on the first day of measurement

Based on the mean values of color redness a^* , the analyzed honeys were divided into four groups (Fig. 2). Honeys 3, 9 and 7 formed separate groups, while group four comprised the remaining honey types.

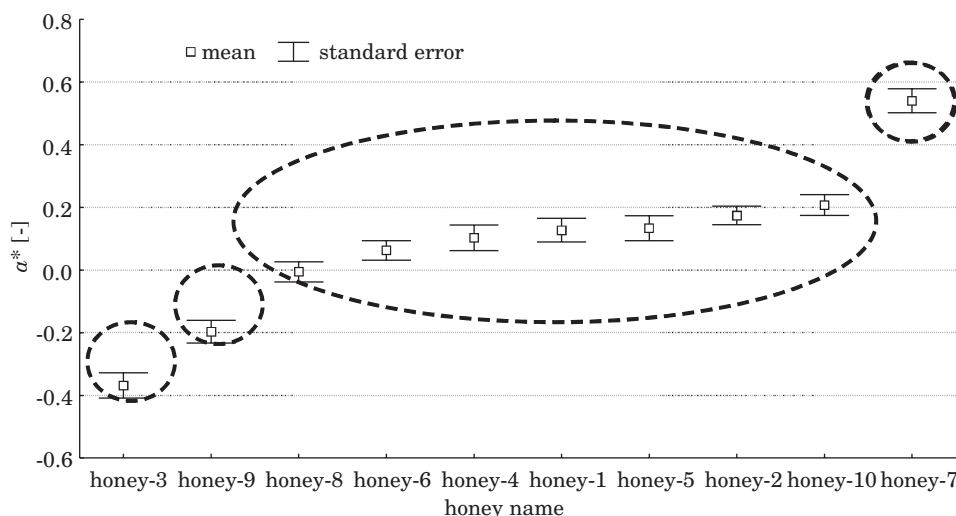


Fig. 2. Mean values of color component a^* (redness) for each honey type on the first day of measurement

In group four, there was a significant difference between honey 10 and honeys 8 and 6. Crystallization affected the values of color component a^* in the following honey pairs: honey 3 (crystallized coniferous honeydew honey) and honey 8 (liquid honeydew honey), honey 5 (liquid multifloral honey) and honey 7 (crystallized multifloral honey), honey 2 (liquid buckwheat honey) and honey 9 (crystallized buckwheat honey). The above honey types differed significantly with respect to the mean values of a^* .

The mean values of color component b^* (yellowness) supported the division of the investigated honey types into two groups (Fig. 3). The first group covered honeys 7, 8, 6, 10 and 3, and the second group – honeys 9, 1, 4, 2 and 5. There were statistically significant differences in b^* values within each of the groups. In group one, a significant difference was found between honey 7 and honey 10, while in group two – between honey 9 and honeys 5 and 2.

Similarly as in the case of redness a^* , also the values of color component b^* were affected by crystallization in the following honey pairs: honey 5 (liquid multifloral honey) and honey 7 (crystallized multifloral honey), honey 2 (liquid buckwheat honey) and honey 9 (crystallized buckwheat honey). The above honey types differed significantly with respect to the mean values of b^* .

Honey samples were divided into three groups based on the mean values of WI E313 (Fig. 4). The first group covered honeys 5, 2, 1 and 4, honey 9 formed the second group, and honeys 3, 10, 6, 8 and 7 were included in the third group. In group three, there were significant differences in WI E313 values between

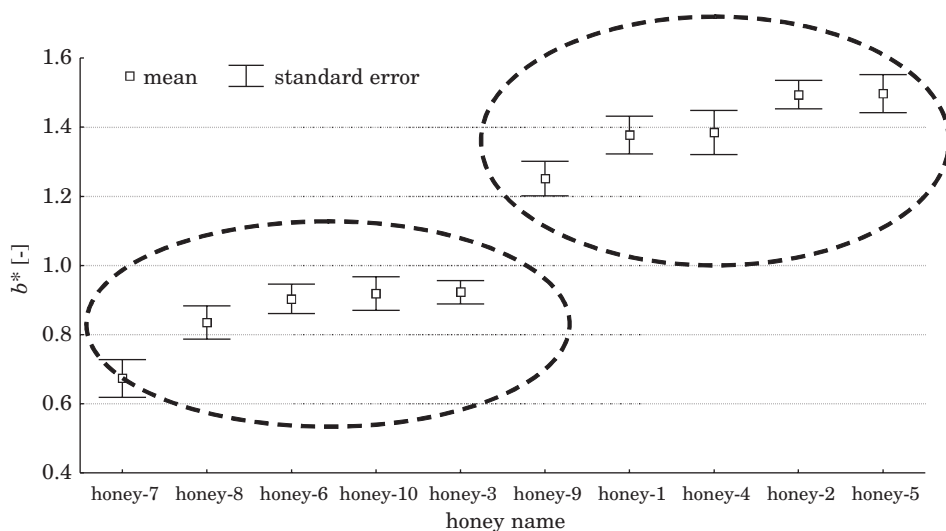


Fig. 3. Mean values of color component b^* (yellowness) for each honey type on the first day of measurement

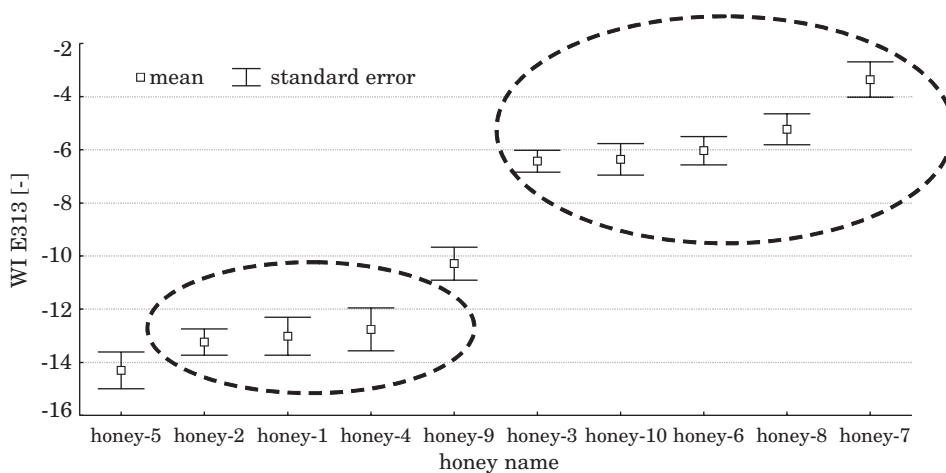


Fig. 4. Mean values of whiteness index (WI E313) for each honey type on the first day of measurement

honey 7 and the remaining honey types. Crystallization affected WI E313 values in the following honey pairs: honey 5 (liquid multifloral honey) and honey 7 (crystallized multifloral honey), honey 2 (liquid buckwheat honey) and honey 9 (crystallized buckwheat honey). Differences in WI E313 values were also noted between honey 10 (mixed honey composed of honey 5 and honey 9 at a 50/50 ratio) and honeys 5 and 9, which enabled to differentiate between mixed honey and the two honeys it was composed of.

The studied honey types differed significantly with regard to the values of yellowness index (YI E313) (Fig. 5). Coniferous honeydew honey was characterized by the lowest value of this index, whereas liquid multifloral honey and liquid buckwheat honey showed the highest YI E313 values.

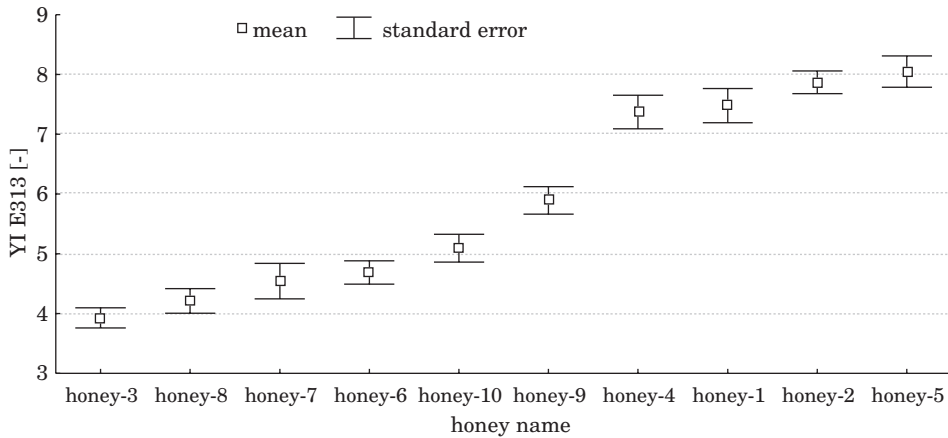


Fig. 5. Mean values of yellowness index (YI E313) for each honey type on the first day of measurement

The yellowness index allowed to discriminate between crystallized and liquid honey of the same type, including after the liquefaction of crystallized samples, which suggests that this index may be used for detecting prior crystallization.

Changes in the color of honey during storage

Figure 6 illustrates changes in the color lightness of selected honey types during 38 days of storage, and Figure 7 shows honeys 4, 5, 7 characterized by a different pattern of lightness changes. The values of color lightness decreased over storage. A rapid drop in lightness noted between day 3 and 4 in all honey types was followed by an increase and a further decrease on consecutive days until the final measurement when lightness oscillated around 24 units.

The initial color lightness of honeys 4, 5 and 7 was 25 units, and it remained unchanged until day 8 of storage. On day 8 the value of lightness started to increase, to reach 35 – 46 units on day 38. The increase in the lightness of honeys 4, 5 and 7 could be due a faster rate of crystallization accompanied by a shift in color towards whitish yellow.

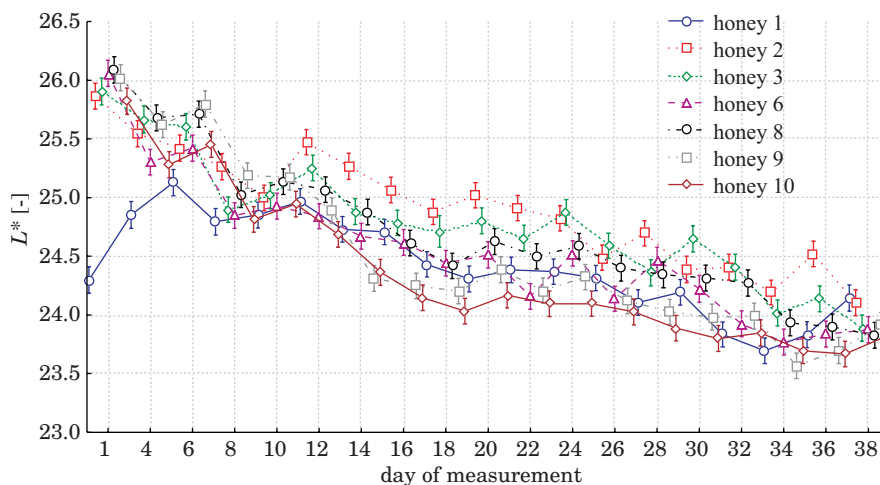


Fig. 6. Changes in the mean values of color component L^* (lightness) in selected honey types on successive days of measurement

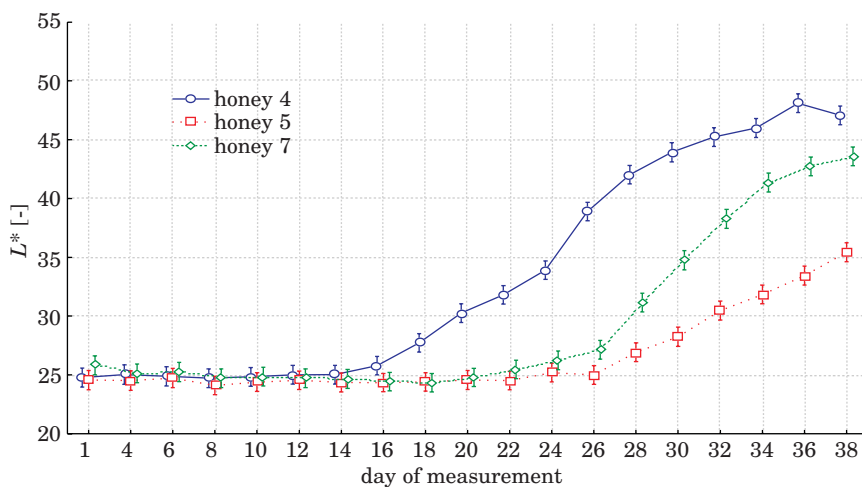


Fig. 7. Changes in the mean values of color component L^* (lightness) in honeys 4, 5 and 7 on successive days of measurement

The patterns of changes in color component a^* (redness) (Figs. 8, 9) were different in particular honey types. In the majority of cases, the value of redness was similar on the first and on the last day of measurement. An initial decrease in redness was followed by an increase in its contribution.

In honeys 4, 5 and 7, the mean value of a^* oscillated around 0.3 until day 14 of storage, and it started to increase on day 15, to reach 1 on the last day of measurement.

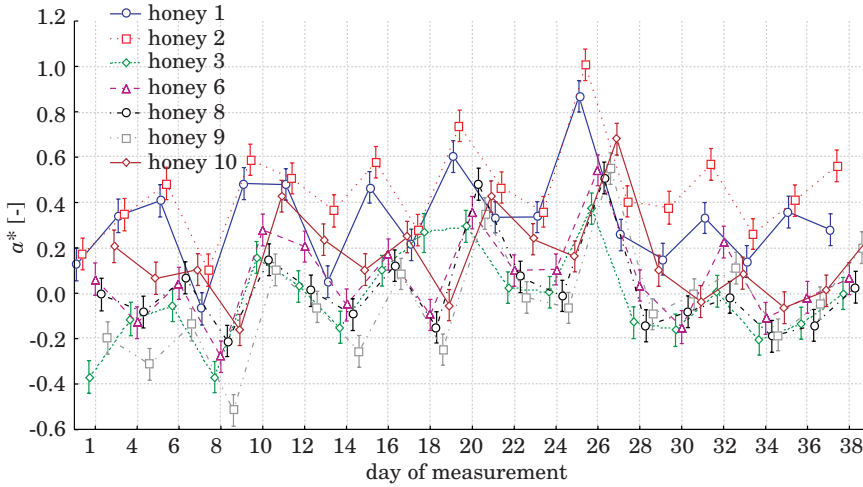


Fig. 8. Changes in the mean values of color component a^* (redness) in selected honey types on successive days of measurement

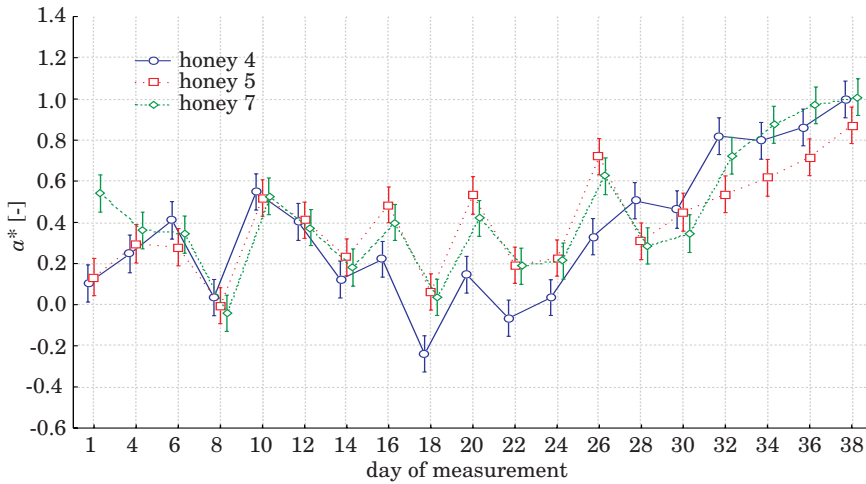


Fig. 9. Changes in the mean values of color component a^* (redness) in honeys 4, 5 and 7 on successive days of measurement

Changes in color component b^* (yellowness) (Figs. 10, 11) were similar to those observed in coordinate a^* – a decrease was followed by an increase. On the last day of storage, b^* values decreased in all honey types, ranging from 0 to 0.6 unit.

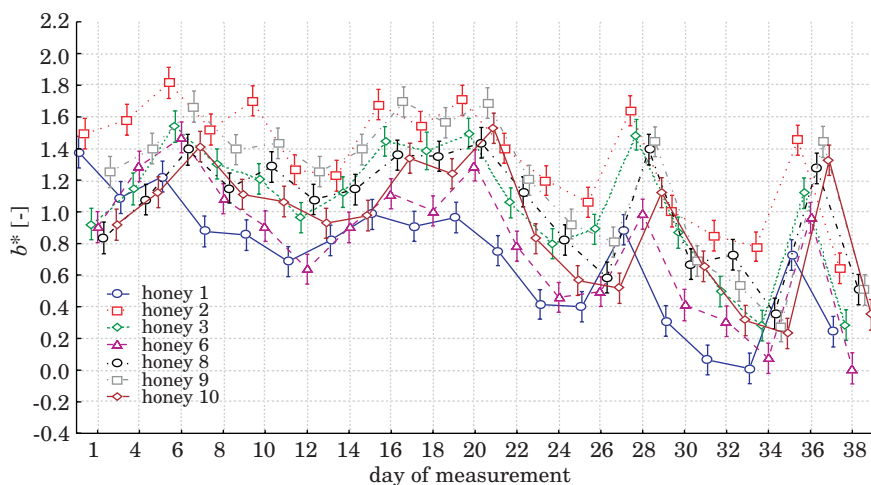


Fig. 10. Changes in the mean values of color component b^* (yellowness) in selected honey types on successive days of measurement

In crystallized oilseed rape honey, liquid multifloral honey and crystallized multifloral honey, b^* values remained unchanged until day 8 of storage in honey 4 and until day 12 in honeys 5 and 7. The final value of yellowness was 8 units in honey 4 and 12 units in honeys 5 and 7.

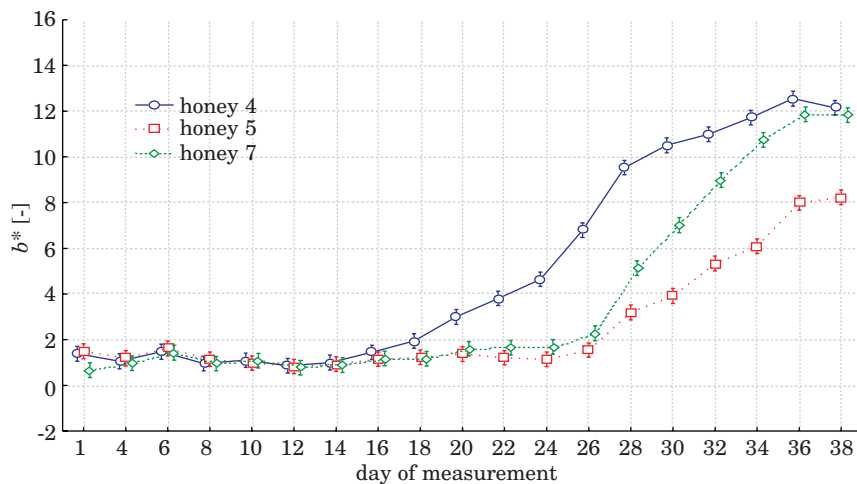


Fig. 11. Changes in the mean values of color component b^* (yellowness) in honeys 4, 5 and 7 on successive days of measurement

Results of a discriminant analysis

Table 3 presents the results of a stepwise discriminant analysis based on the values of L^* , a^* , b^* , WI 313 and YI 313, with five variables introduced successively into the model. The value of Wilks; Lambda and the F-statistic was 0.039813 and 45.13. respectively. Classification accuracy ranged from 18.8% to 84.8%. A high accuracy of classification based on color variables was obtained for liquid buckwheat honey (84.8%), crystallized multifloral honey and crystallized coniferous honeydew honey. As regards honey 5, ten samples were incorrectly classified as honey 1 and another ten samples – as honey 4, thus pointing to a high contribution of rapeseed pollen in this type of honey. The results obtained for honey 1 suggest that it is difficult to distinguish between liquid buckwheat honey and crystallized buckwheat honey based on their color, which was accomplished in buckwheat honeys. The lowest classification accuracy was reported for pine honey whose samples were erroneously classified as honeys 8, 9 and 10.

Table 3

Classification matrix for 10 honey types

Honey type	Classification accuracy [%]	1	2	3	4	5	6	7	8	9	10
1	61.3	19			10	2					
2	84.8		28							1	4
3	77.4			24	1				4	2	
4	62.5	5	1		20	4					2
5	37.5	10			10	12					
6	18.8	1		2	1		6	1	10	5	6
7	78.1		2	0				25			5
8	41.9			2			5	3	13	7	1
9	68.8		3	2			2		2	22	1
10	46.9		2				3	6	5	1	15

Conclusions

1. There exist homogenous groups of honey types that can be discriminated based on a single color component or index.

2. Crystallized honey may be distinguished from liquid honey with the use of a single color component or index.

3. The values of color component b^* (yellowness) and whiteness index

WI E313 enable to differentiate between mixed honey and the honeys it was composed of.

4. It was found, based on the values of color components L^* , a^* and b^* , that earlier crystallization affected the rate of later crystallization of honey.

5. Classification accuracy ranged from 18.8% to 84.8%. depending on honey type.

Accepted for print 4.10.2010

Reference

- BATH P.K., SINGH N. 1999. *A comparison between Helianthusannuus and Eucalyptus lanceolatus honey*. Food Chemistry, 67: 389–397.
- BUERA M.P., PETRIELLA C., LOZANO R.D. 1985. *Definition of colour in the non-enzymatic browning*. Die Farbe, 33: 316–326.
- BUERA M.P., RESNIK S. 1989. *Colorimetric measurements in a turbid medium: hydrolyzed concentrated cheese whey*. Die Farbe, 36: 201–213.
- GONZALES PEREYRA A., BURIN L., PILAR BUERA M. 1999. *Color changes during storage of honeys in relation to their composition and initial color*. Food Research International, 32: 185–191.
- LAZARIDOU A., BILIADERIS C.G., BACANDRITSOS N., SABATINI A.G. 2004. *Composition, thermal and rheological behaviour of selected Greek honeys*. Journal of Food Engineering, 64: 9–21.
- PAPADAKIS S.E., ABDUL-MALEK S., KAMDEM R.E., YAM K.L. 2000. *A versatile and inexpensive technique for measuring color of foods*. Food Technology, 54(12). 48–51.
- POPEK S. 2002. *A procedure to identify a honey type*. Food Chemistry, 79: 401–406.
- SALAS J.P., ECHÁVARRI J.F., NEGUERUELA A.I. 1993. *Influencia de la temperatura en el color de la miel*. Óptica Pura y Aplicada, 26: 549–557.
- TERRAB A., GONZALEZ-MIRET L., HEREDIA F.J. 2004. *Colour characterization of thyme and avocado honeys by diffuse reflectance spectrophotometry and spectroradiometry*. Eur Food Res Technol., 218: 488–492.

A FLOOD EMBANKMENT UNDER CHANGING WATER LEVEL CONDITIONS – A COMPARISON OF A PHYSICAL AND A NUMERICAL MODEL

Jarosław Kaczmarek¹, Danuta Leśniewska²

¹ Chair of Civil Engineering and Building Constructions
University of Warmia and Mazury in Olsztyn

² Institute of Hydroengineering, Polish Academy of Sciences in Gdańsk
University of Technology in Koszalin

Key words: flood embankments, changes in the water level, modeling, FEM calculations, PIV method.

Abstract

The paper compares the results of a study on a plane physical model of a flood embankment with the outcome of a numerical modeling using the finite element method (FEM). The numerical modeling was performed with the PLAXIS software package while the empirical data were processed with the geoPIV programme. Two types of model studies were completed, consisting of alternately raising (up to complete flooding) and lowering (to complete desiccation) the water table which affected the flood embankment model. The objective of the study was to assess the applicability of the particle image velocimetry (PIV) method to analyzing deformations of a flood embankment under changeable hydrological conditions. Qualitative agreement was found between the empirical and numerical displacement fields in the body of a flood embankment.

WAŁ PRZECIWPOWODZIOWY W WARUNKACH ZMIENIAJĄCEGO SIĘ POZIOMU WODY – PORÓWNANIE MODELI FIZYCZNEGO I NUMERYCZNEGO

Jarosław Kaczmarek¹, Danuta Leśniewska²

¹ Katedra Budownictwa i Konstrukcji Budowlanych
Uniwersytet Warmińsko-Mazurski w Olsztynie

² Instytut Budownictwa Wodnego PAN w Gdańsku,
Politechnika Koszalińska

Słowa kluczowe: wały przeciwpowodziowe, zmiany poziomu wody, modelowanie, obliczenia MES, analiza obrazu, metoda PIV.

Abstract

W pracy przedstawiono porównanie wyników badań na płaskim fizycznym modelu wału przeciwpowodziowego z wynikami modelowania numerycznego metodą elementów skończonych (MES). Modelowanie numeryczne przeprowadzono z zastosowaniem programu PLAXIS, dane z doświadczeń opracowano za pomocą programu geoPIV. Wykonano dwa typy badań modelowych, które polegały na naprzemiennym podnoszeniu (do całkowitego zalania) i obniżaniu (do całkowitego osuszenia) zwier-

ciadła wody oddziałującego na model wału przeciwpowodziowego. Celem pracy było stwierdzenie przydatności metody analizy obrazu (PIV) do badania deformacji wału przeciwpowodziowego w zmiennych warunkach hydrologicznych. Otrzymano jakościową zgodność między doświadczalnymi i obliczeniowymi polami przemieszczeń w korpusie wału.

Introduction

Nowadays, with predicted changes in the global climate leading to more frequent incidents of intensive hydro-meteorological events which will threaten human life and material possessions, it seems essential to analyze changes that occur in flood embankments under different ambient conditions (LEŚNIEWSKA et al. 2007, BOGACZ et al. 2008, MORRIS et al. 2008). Flood embankments are typically the first line of defence against flooding water, therefore any changes caused by a rising water level within the body of an embankment should be thoroughly analyzed (LEŚNIEWSKA et al. 2008, SCHNELLMANN et al. 2010, ZARADNY 2008).

Under the TROIAnet Science Network, financed by the Ministry of Science and Higher Education, laboratory tests were carried out in 2008 to analyze changes in a flood embankment body which appeared due to changing levels of the groundwater table.

Some preliminary results of these analyses, conducted using the geoPIV method, revealed that even minor changes in the position of the groundwater table led to measurable deformations in the body of a flood embankment (KACZMAREK et al. 2009).

This paper compares the results of tests completed on a flat physical model of a flood embankment with the results of numerical modeling using the finite element method (FEM). The numerical modeling was conducted with an aid of the PLAXIS software package while the empirical data were processed using the geoPIV programme.

The experiments

Two types of tests were performed, each consisting of alternately raising (up to complete flooding) and lowering (to complete desiccation) of a water table affecting a model of a flood embankment. Each test was run for 1.5 to 2 months. The types of the tests were different in the velocity of raising the water level: type I – slow changes and type II – rapid changes in the position of groundwater.

For the analysis presented in this paper, phase I of type II tests was examined, i.e. rapid raising of the water table up to complete flooding of the body of a flood embankment. Five stages of the experiment were analyzed,

corresponding to the water level $h_0 = 0$ cm (dry embankment), $h_1 = 20$ cm, $h_2 = 40$ cm, $h_3 = 60$ cm, $h_4 = 80$ cm and $h_5 = 100$ cm (the embankment completely flooded). The geoPIV software package (WHITE, TAKE 2002) was used to analyze digital photographs documenting each stage of the tests in order to obtain the corresponding displacement fields and deformations.

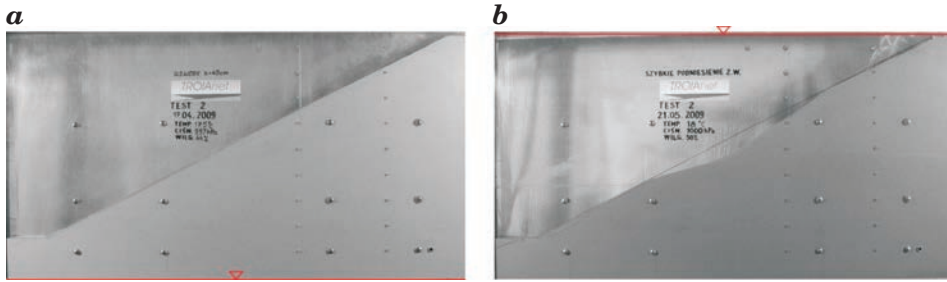


Fig. 1. The initial and final stage of phase I test II, red line – position of water table: a) $h_0 = 0$ cm, b) $h_5 = 100$ cm

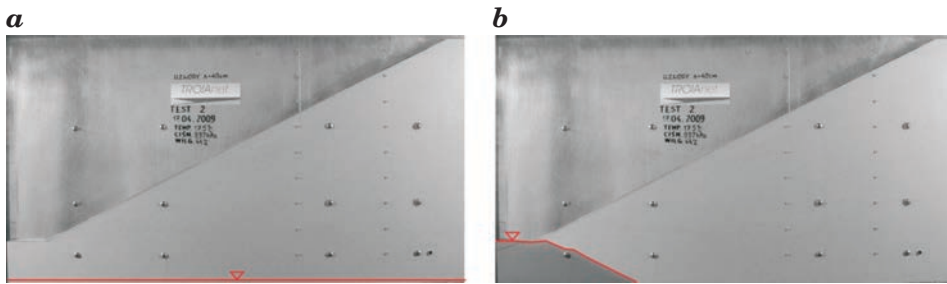


Fig. 2. Stage I of the analysis – the groundwater table at the height of: a) $h_0 = 0$ cm, b) $h_1 = 20$ cm (red lines)

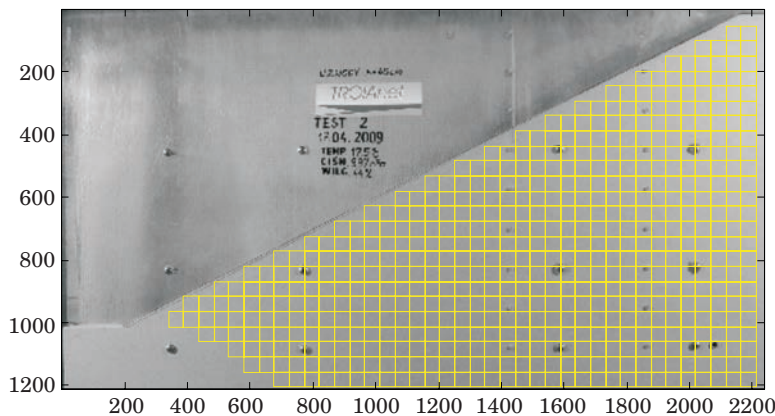


Fig. 3. geoPIV – the mesh adapted for the calculations (division of a photograph into elements)

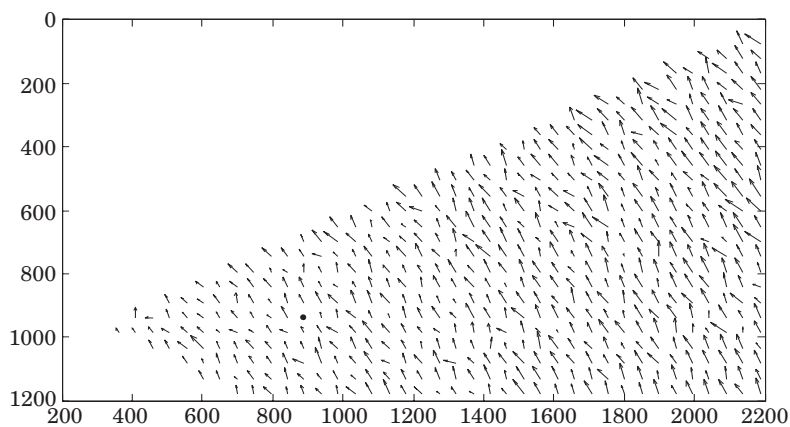


Fig. 4. Experimental fields of displacements (scaled 50 times)

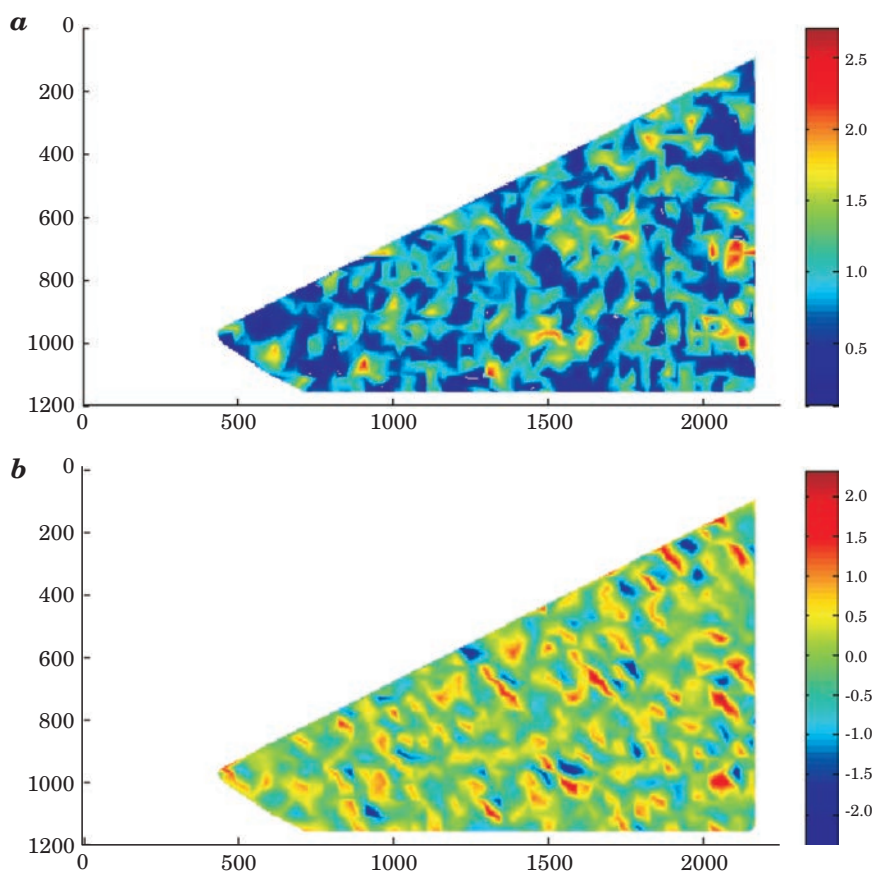


Fig. 5. shear (a), volumetric strains [%] (b) obtained from experimental field of displacements

Modeling with the finite element method (FEM)

The modeling of deformations in the body of a flood embankment caused by changes in the position of the water table based on the finite element method (FEM) was run with the PLAXIS (v. 8) software programme.

A geometrical model of the problem

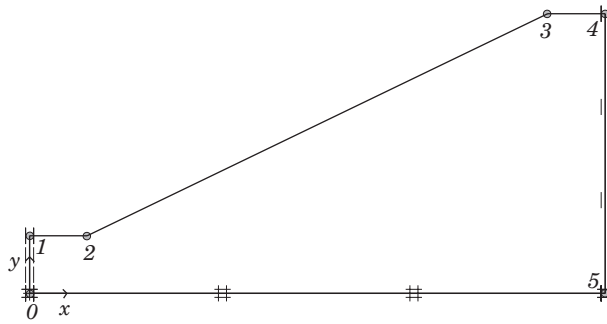


Fig. 6. The geometrical model of a flood embankment

The dimensions of the model were taken like in the experimental tests: $200 \text{ cm} \times 97.5 \text{ cm}$. The distances between the points marked in Fig. 6 are 0–1: 20 cm, 1–2: 20 cm, 3–4: 20 cm, 4–5: 97.5 cm and 0–5: 200 cm, respectively.

Computational parameters of the soil

The laboratory model of a flood embankment was made of fine-grain ($d_{50} = 0.25 \text{ mm}$), very well sorted, natural beach sand collected from a beach lying on the open coast of the Baltic Sea near the IBW PAN Seashore Laboratory in Lubiato, situated about 70 km west of Gdańsk.

For the mathematical modeling, parameters of Lubiato sand in a moderate density state were chosen: Young module $E = 50\,000 \text{ kN m}^{-2}$, Poisson's ratio $\nu = 0.3$, internal friction angle $\varphi = 26^\circ$ and cohesion $c = 0.1 \text{ kPa m}^{-2}$.

Calculation mesh

For the calculations, 15 triangular node elements offered in PLAXIS programme were chosen. Finite elements mesh was generated using a fine mesh option available in the package.

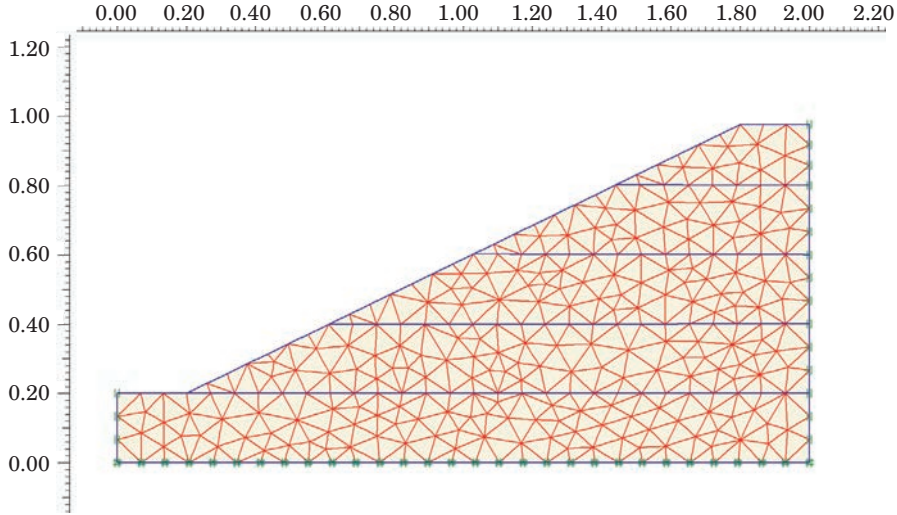


Fig. 7. The FEM calculation mesh

Soil model

For the soil (Lubiatowo sand) model, the classical Coulomb-Mohr model was selected with the associated flow law. The Coulomb-Mohr plasticity condition is an extension of Coulomb's law of friction which involves the general state of tension. This condition ensures that Coulomb's law of friction is fulfilled in every external plane of the element of the material. The full Coulomb-Mohr border condition can be defined via three border functions representing the principal stresses:

$$f_1 = \frac{1}{2} |\sigma'_2 - \sigma'_3| + \frac{1}{2} (\sigma'_2 - \sigma'_3) \sin \varphi - c \cdot \cos \varphi \leq 0 \quad (1a)$$

$$f_2 = \frac{1}{2} |\sigma'_3 - \sigma'_1| + \frac{1}{2} (\sigma'_3 - \sigma'_1) \sin \varphi - c \cdot \cos \varphi \leq 0 \quad (1b)$$

$$f_3 = \frac{1}{2} |\sigma'_1 - \sigma'_2| + \frac{1}{2} (\sigma'_1 - \sigma'_2) \sin \varphi - c \cdot \cos \varphi \leq 0 \quad (1c)$$

The two parameters of the model are internal friction angle φ and cohesion c .

Results of the FEM modeling

The phenomenon of raising a water table (every 20 cm higher until complete flooding of the flood embankment body) was modeled mathematically in order to compare the resultant failure mechanisms and the experimental fields of displacement with the actual behaviour of a physical model

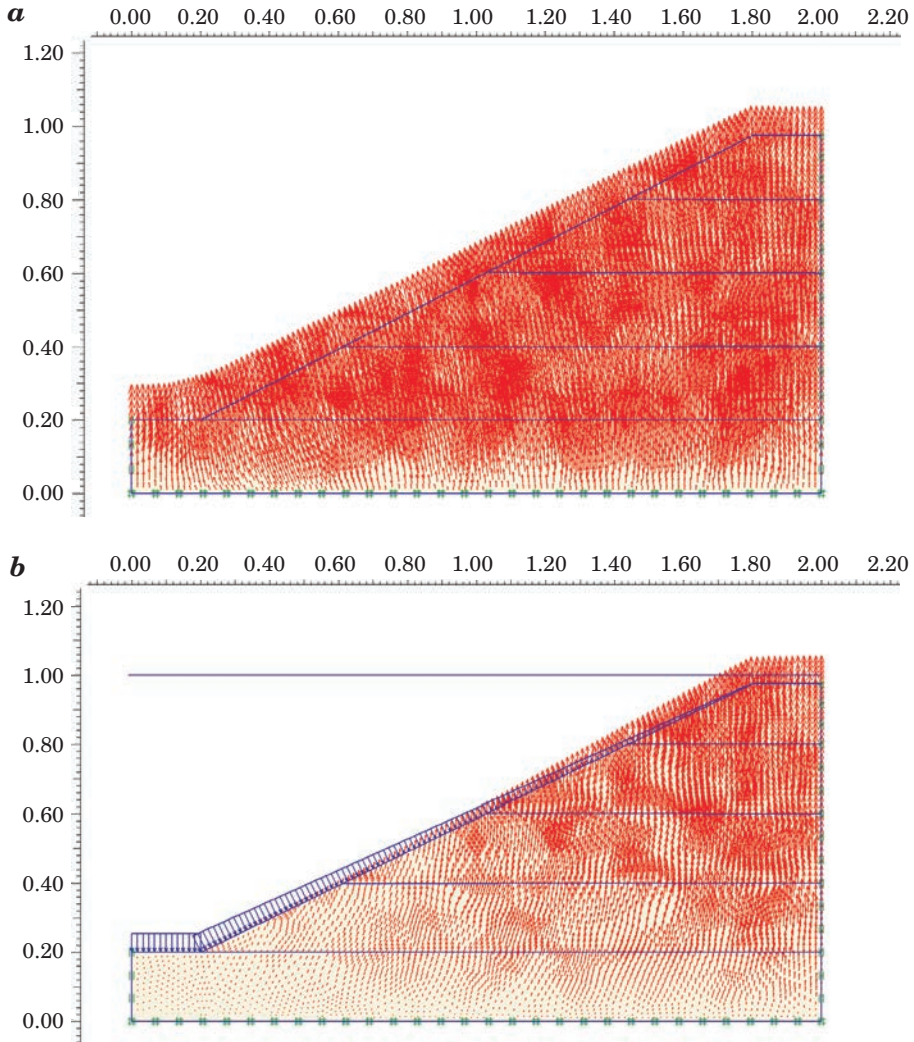
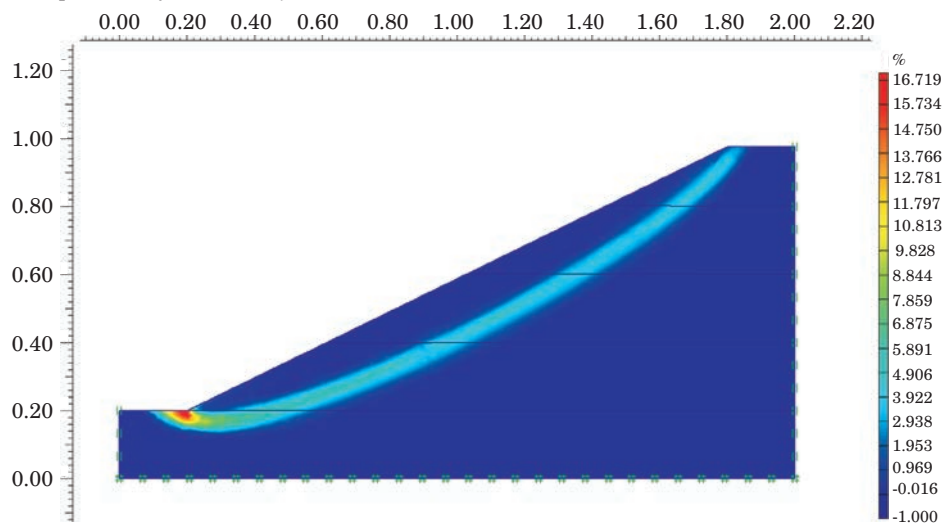


Fig. 8. Calculated fields of total displacements: *a*) $h_0 = 20$ cm, extreme calculated displacement $2.37 \cdot 10^{-6}$ m (scaled 50 000 times), *b*) $h_5 = 100$ cm extreme calculated displacement $40.77 \cdot 10^{-6}$ m, (scaled 2000 times)

of a flood embankment. The experimental (obtained by the image analysis method) and calculated fields of displacement were compared qualitatively. The results of the numerical calculations are presented in Figs. 8–10.

a slope stability coefficient $f = 1.19$



b slope stability coefficient $f = 1.26$

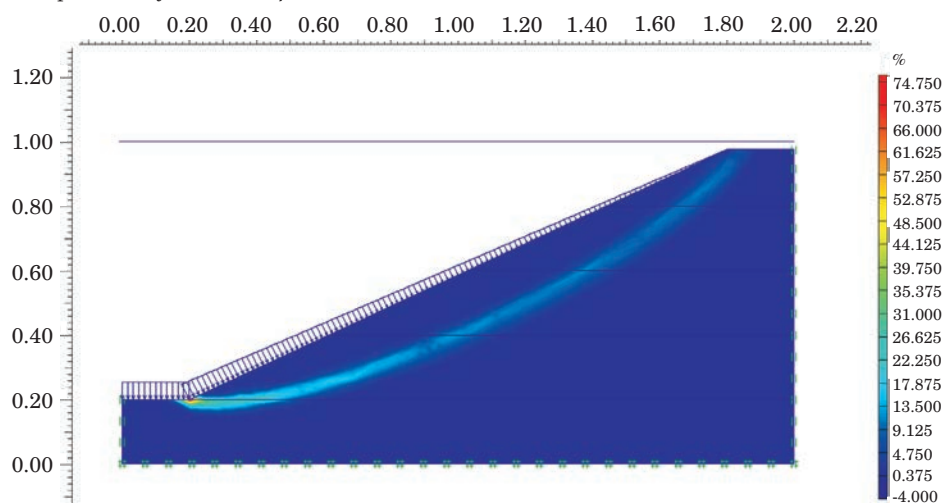


Fig. 9. Incremental shear strains (potential failure mechanism): a) $h_0 = 20$ cm, b) $h_s = 100$ cm

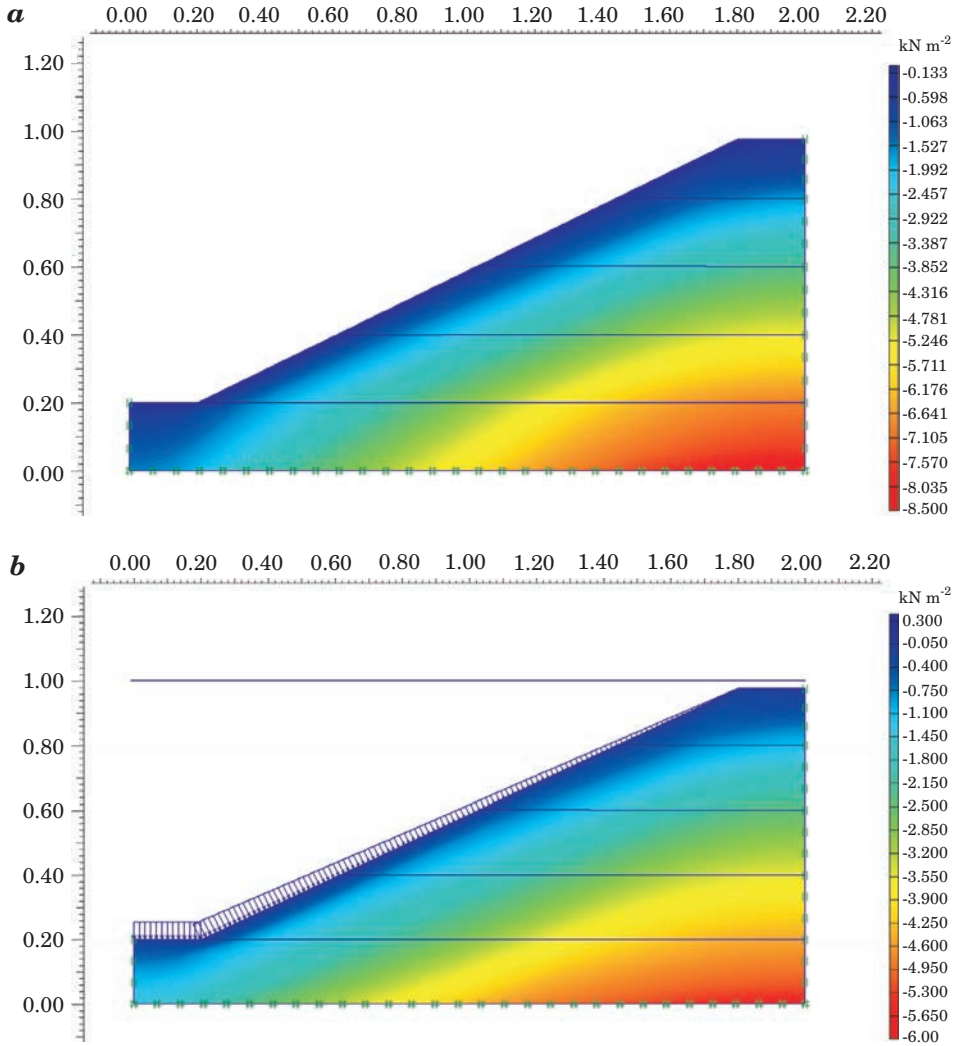


Fig. 10. Effective mean stresses in the body of a flood embankment: a) $h_0 = 20$ cm, b) $h_s = 100$ cm

Comparison of the results of the geoPIV analyses and FEM modeling

The objective of the paper has been to examine the applicability of the image analysis method (Particle Image Velocimetry, PIV) to analyzing deformations in a flood embankment under changing hydrological conditions. Figures 4 and 5 illustrate that it is possible to read, under the conditions adapted for the experiment, a full experimental field of displacement for dry

areas in a physical model. At the moment, the authors are trying to analyze areas below the groundwater table, which is difficult due to insufficient variety of the photographs taken in these areas. Vectors of displacement which make up this field are directed upwards when the water level is rising, which is in accord, qualitatively, with the results of our calculations (Fig. 8). The values of displacements, both calculated and empirical ones, are very small (in the order of 10^{-6} m). The empirical and calculated displacements show a small horizontal component.

The experimental fields of displacement, as shown in Fig. 5, demonstrate the presence of local heterogeneity of the density of the physical model, which obviously does not occur in the FEM calculations, where the soil was assumed to be homogenous. The FEM calculations generated the course of a potential mechanism of destruction of a flood embankment at every stage of the calculations, and the corresponding value of the stability coefficient. The stability coefficient for a dry flood embankment was 1.20, reaching the minimum of 1.14 for $h = 40$ cm, and then rising up to 1.26 for $h = 100$ cm. The fact that the minimum value of the stability coefficient exists explains cases of sudden loss of stability of an embankment when the water table is lowering, an event also observed in actual flood embankments.

Summary

The purpose of this study has been to test the applicability of the particle image velocimetry (PIV) method to studying deformations in a flood embankment under changing hydrological conditions. Until the present day, the authors have been successful in applying the method successfully to dry areas of a model embankment, which provides us with a useful tool for recognizing phenomena which occur in flood embankments, also under conditions which are more difficult than presented hereby.

Acknowledgement

The work described in this publication was supported by the Polish Ministry of Science and Higher Education through the grant contributed to the budget of the Scientific Network “*TROIAnet*”, Contract 57/E-84/BWSN-0114/2008.

Accepted for print 16.07.2010

References

- BOGACZ P., KACZMAREK J., LEŚNIEWSKA D. 2008. *Influence of air entrapment on flood embankment failure mechanism – model tests*. Technical Sciences, 11: 188–201.
- KACZMAREK J., BOGACZ P., LEŚNIEWSKA D. 2009. *Wpływ zmian potożenia zwierciadła wody na deformacje watu przeciwpowodziowego*. Inżynieria i Budownictwo, 12: 679–680
- LEŚNIEWSKA D., BOGACZ P., KACZMAREK J., ZARADNY H. 2007. *Air trapping phenomenon and cracking*. FLOODsite Raport T04 07.
- LEŚNIEWSKA D., ZARADNY H., BOGACZ P., KACZMAREK J. 2008. *Study of flood embankment behaviour induced by air entrapment*. Flood Risk Management: Research and Practice – Samuels et al. (eds) Taylor & Francis Group, London, ISBN 978-0-415-48507-4, pp. 655–665.
- MORRIS M.W., ALLSOP W., BUIJS F.A., KORTENHAUS A., N. DOORN N., LEŚNIEWSKA D. 2008. *Failure modes and mechanisms for flood defence structures*. Flood Risk Management. Research and Practice – Samuels et al. (eds), Taylor & Francis Group, London, ISBN 978-0-415-48507-4, pp. 693–701.
- PLAXIS (v. 8) – Users Manual
- SCHNELLMANN R., BUSSLINGER M., SCHNEIDER H.R., RAHARDJO H. 2010. *Effect of rising water table in an unsaturated slope*. Engineering Geology 114: 71–83.
- WHITE D.J., TAKE W.A. 2002. *GeoPIV: Particle Image Velocimetry (PIV) software for use in geotechnical testing*. Cambridge University Engineering, Department Technical Report, D-SOILS-TR322.
- ZARADNY H. 2008. *Modelowanie przepływu wód gruntowych w ujęciu obszarowym*. Biuletyn Państwowego Instytutu Geologicznego, 431: 275–286.

HYDRO- AND LITHODYNAMIC ASPECTS OF CONSTRUCTING A NAVIGABLE CANAL THROUGH THE VISTULA SPIT – PART 2

***Leszek M. Kaczmarek, Jarosław Biegowski,
Joanna B. Skillandat***

Institute of Hydroengineering
Polish Academy of Sciences in Gdańsk
Chair of Civil Engineering and Building Constructions
University of Warmia and Mazury in Olsztyn

Key words: the Vistula Spit, the Vistula Lagoon, cutting, navigable canal, fairway, breakwater, sediment transport, non-homogenous sediments, silting up of a fairway

A b s t r a c t

The paper discusses hydro- and lithodynamic aspects of a planned construction of a navigable canal across the Vistula Spit. The discussion is based on the results obtained under a research and development grant carried out in 2007–2008 by the Institute of Hydroengineering of the Polish Academy of Sciences in Gdańsk in collaboration with the Chair of Civil Engineering and Building Structures, the Faculty of Technical Sciences, at the University of Warmia and Mazury in Olsztyn. The analysis presented in this paper regarding the effect of the length and position of planned breakwaters on the silting up of the fairway broadens the results of the research performed under the above grant by including such aspects as the position of the fairway's axis towards the shore. All analyses were performed employing an innovative method which takes into account the changeable grain size structure of deposits (cf. KACZMAREK L.M., SAWCZYŃSKI Sz. 2007 and KACZMAREK L.M. 2008). The recommendations regarding an optimum length of planned breakwaters and depth of an approach fairway, presented previously, have found further confirmation.

HYDRO- I LITODYNAMICZNE ASPEKTY BUDOWY KANAŁU ŻEGLUGOWEGO PRZEZ MIERZEJĘ WIŚLANĄ – CZĘŚĆ 2

Leszek M. Kaczmarek, Jarosław Biegowski, Joanna B. Skillandat

Instytut Budownictwa Wodnego PAN w Gdańsku
Katedra Budownictwa i Konstrukcji Budowlanych
Uniwersytet Warmińsko-Mazurski w Olsztynie

Słowa kluczowe: Mierzeja Wiślana, Zalew Wiślany, przekop, kanał żeglugowy, tor wodny, falochrony, transport osadów, osady niejednorodne granulometrycznie, zapiaszczanie toru.

A b s t r a k t

W artykule przedstawiono aspekty hydro- i litodynamiczne planowanej budowy kanału żeglowego przez Mierzeję Wiślaną. Dyskusję wyników przeprowadzono na podstawie rezultatów uzyskanych w ramach grantu badawczego rozwojowego realizowanego w latach 2007–2008 przez Instytut Budownictwa Wodnego PAN w Gdańsku we współpracy z Katedrą Budownictwa i Konstrukcji Budowlanych Wydziału Nauk Technicznych Uniwersytetu Warmińsko-Mazurskiego w Olsztynie. Przedstawiona analiza, dotycząca wpływu długości oraz ustawienia projektowanych falochronów na zapiaszczanie toru wodnego, stanowi istotne rozszerzenie wyników badań uzyskanych w ramach grantu o aspekty związane z ustawieniem osi toru względem brzegu. Analizy wykonano, korzystając z nowatorskiej metody uwzględniającej zmienność uziarnienia osadów (por. KACZMAREK, SAWCZYŃSKI 2007 i KACZMAREK 2008). Potwierdzono zalecenia optymalizacyjne dotyczące długości projektowanych falochronów i głębokości toru podejściowego.

Introduction

This paper is a continuation of our previous article published in the last year's issue of the Technical Sciences (cf. KACZMAREK 2009), which contained the results of our studies completed as part of R&D grant no R04 017 03 called 'The analysis of hydro- and lithodynamic processes in the area of a planned cutting across the Vistula Spit and prediction of the effect of the cutting on the shore, along with the evaluation of the intensity of silting up of the fairway from the cutting to the port in Elbląg', conducted by the Institute of Hydroengineering, the Polish Academy of Sciences (KACZMAREK L.M. et al. 2008), in collaboration with the Chair of Civil Engineering and Building Structures of the University of Warmia and Mazury in Olsztyn (KACZMAREK J. et al. 2008). The concept of cutting through the Vistula Spit is not a new one and there have been many papers dealing with this idea, among which the most important ones are three expert opinions (KACZMAREK J. et al. 2008, KACZMAREK L.M. et al. 2008 and the Feasibility Study for the Construction of a Canal), which are now the basic source of information about the planned construction. In addition, other publications have appeared over the years, such as the earliest articles by GAJEWSKI et al. (1995), JEDNORAŁ (1996), DUBRAWSKI and ZACHOWICZ (1997), to the latest ones by KACZMAREK L. M. et al. (2009 a, b and c), which contain detailed results of studies and present the current state of the discussion on this construction project.

This article broadens the discussion about the planned cutting of the Vistula Spit by adding some aspects, which have been previously either neglected or taken for granted. These aspects have been analyzed as part of a master thesis (cf. SKILLANDAT 2010) completed at the Chair of Civil Engineering and Building Constructions at the UWM, under the supervision of L.M. Kaczmarek.

The article (KACZMARK L.M. 2009) contains an analysis of the influence produced by the planned breakwaters on the seaward shores of the Vistula Spit

(cf. Fig. 1) and the effect of the length of these breakwaters on sedimentation processes in and around the fairway.



Fig. 1. Location of the planned cutting across the Vistula Spit

Source: www.google.maps.pl accessed on 4 May 2010 at 4.00 p.m.

Simulations of the volume and rate of the silting-up of a fairway, in which breakwaters consisted of a single, impermeable groyne of the tested lengths of 150, 300 and 400 m and depths of the fairway of 6 and 5.5 m (Fig. 2), have proven that the optimum results are achieved when the distance between the heads of the breakwater and the coast are 400 m and the approach fairway is 5.5 m deep.

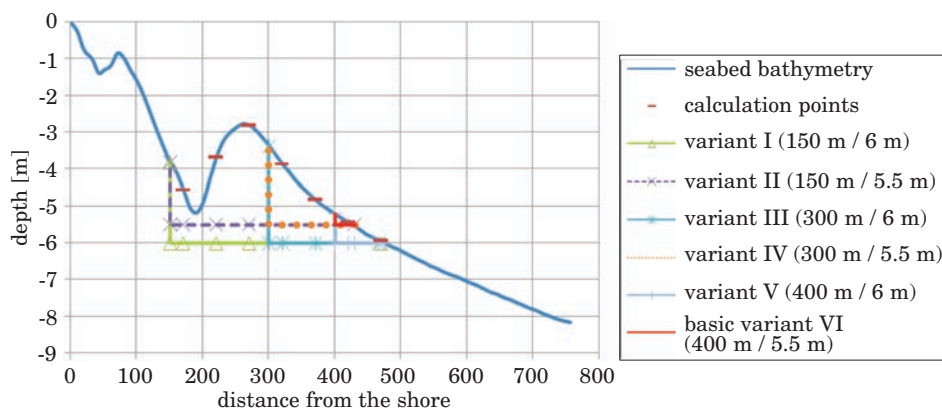


Fig. 2. Bathymetric profile in the area of the planned cutting across the Vistula Spit

All the analyses performed up to now have assumed that the fairway lies perpendicularly to the coastline. With this assumption, the forces causing the silting-up of the fairway were two of the three basic factors, i.e. wave generated sediment transport at the edges of the fairway and longshore sediment transport, in which the direction is parallel to the coastline. The volume of sediment carried by longshore transport is independent from the position of the approach fairway relative to the coastline because as the fairway diverges from the normal to the coastline, its length increases and the effective transport component, i.e. the perpendicular to its axis, decreases. The longshore transport is driven by a longshore current, generated by waves coming towards the shore which break obliquely (versus the shore). Grains of sediment are then transported in the water layers further from the bottom, where they form suspension. The wave-generated sediment transport at the edges of the fairway is the one caused by surface waves, whose direction agrees with the direction of the propagation of waves running towards the shore. This transport involves both rolling and dragging of sand grains, as well as the so-called saltation, i.e. short jumps of grains right above the bottom. Sediment grains are therefore in constant contact with one another and, in the form of a thick mixture, move in the surface layer of the bottom and a layer directly adjacent to the seabed, i.e. the contact layer (cf. KACZMAREK L.M. 2008). Silting up caused by this type of transport depends on an angle between the direction of wave propagation and the fairway, but along the winward edge of the fairway (away from the current) sediments are transported during the wave crest phase, while along the edge away from the wind (under the current), transport takes place during the wave trough phase. It is also assumed that surface wave can be described via Stokes second approximation with a steeper crest and flattened trough.

The third of the factors responsible for the silting up of a fairway, i.e. transport caused by a return current directed towards open sea, whose direction is perpendicular to the shore, does not have any influence on the volume of silting when the construction, i.e. a fairway, is situated along the normal to the shore, because the component of the transport perpendicular to the fairway's axis disappears. Analogously to the longshore transport, sediment grains are transported as suspension by the return current, generated by breaking waves.

The decision to locate the construction along the normal to the shore, which means that the estimation of potential sedimentation will only include the intensity of transport caused by waves at the edges of the fairway a longshore current, is based on the many years of experience gained by hydrotechnology engineers and the knowledge of the terrain (Fig. 1) as well as the wave climate, according to which the mean annual resultant direction of wave-generated

sediment transport at the edges at the fairway (accord. to the IBW PAN model), at a distance of 200 m and more from the shore, inclines eastward by no more than 10° from the normal to the coastline (cf. KACZMAREK *et al.* 2008). In this study, it has been decided to test the justifiability of the accepted assumption by performing additional analyses based on a changed location of the fairway relative to the coast and on measurements of the effect of the return current on the intensity of the silting up of the approach fairway.

Calculation procedure

Based on the results of bathymetric measurements and grain size composition of the sediments, as well as the calculations run according to the IBW PAN mathematical model, optimal parameters of the construction have been chosen. A model of non-homogenous sediment transport, improved by the Instituute's researchers for many years, enables us today to account for the influence produced by all fractions on the transport of rubble. This is important because in addition to the value of a median d_{50} , the shape of the distribution of grain size fractions of sediments has a significant influence on the evaluation of the transport and analysis of the silting up of a fairway (KACZMAREK L.M., SAWCZYŃSKI Sz. 2007). The model distinguishes the bedload layer, the intermediate (contact) layer and the external area, in which sediments are transported as suspension.

Some modifications and additional components introduced to the calculation model, carried out in this study, have enabled us to present additional relationships illustrating the effect of the length of breakwaters as well as the depth and position of the fairway relative to the coastline on the silting up of the fairway. With this model, it was also possible to estimate the effect of the above factors on the silting up depending on the grain size distribution of sediments. Thus, thirteen different locations of the approach fairway relative to the coast and five different groups of sediments have been tested. The fairway profile is here understood as an appropriate positioning of its axis relative to the coastline. Therefore, the fairway's axis lying along the normal to the coast was marked as angle 0° and its successive westward and eastward inclinations by 10° from the normal to the shoreline were assigned respective values of negative and positive angles. The analyzed groups of sediments consisted of three uniform sandy sediments containing grains of the diameters $d = 0.1$ mm, $d = 0.22$ mm and $d = 0.4$ mm, a grain size sediment distribution sampled at a depth of 2.2 m and designated as 31 M-7, and another one, named the actual distribution, i.e. an averaged distribution, which – depending on the depth for which the calculations were performed – was an averaged distribu-

tion from samples taken at the depths $6 \div 4$, or $4 \div 0.8$ m. The uniform sediment characterized by the smallest grain diameter, i.e. $d = 0.1$ mm, was chosen for comparative analyses, since this size of sand grains is impossible to obtain in the natural conditions present in the Baltic Sea.

In the paper, the authors have limited the discussion to re-analyzing the volume of the silting up of the fairway, excluding the effect of the breakwaters on the seaward shores of the Vistula Lagoon, as this issue was directly addressed to in the previous article (cf. KACZMAREK 2009).

The effect of the length and position of breakwaters on silting up

Waves and sea currents have the strongest influence on the transport of sediments and, consequently, on the evolution of the shores and seabed. The actual parameters of litho- and morphodynamic processes depend on the type of rubble lying on the seabed and on the vulnerability of sand fractions to the effect produced by the flow of water in the near-bottom layer. Sand fractions are transported as bedload or suspended sediment due to the effects produced by near-bottom tensions. But above all, these processes depend on the wave climate, bathymetric relations in the seabed within the shore zone and the hydrotechnical facilities built along the shore.

The volumes of rubble transported near the planned canal, calculated from van Rijn's formula for each direction of shoreward waves and by totalling (the mean annual) volume of the resultant transport, have clearly demonstrated that there would be three streams of transported rubble (cf. KACZMAREK L.M. 2009), each characterized by a different intensity depending on the distance to the shore. The main sediment transport occurred in a belt 160 m in width whereas the maximum width of a shore zone with the transport of sediments reaches about 400 m from the shore at the seaward side of the submerged bar (cf. Fig. 2). Therefore, the breakwaters should be localized about 150 m or 400 m from the shore.

Figs. 3–5 show the total mean annual volumes of sediments, divided into three grain size distributions, brought into the fairway depending on the variants of the location of the breakwaters (cf. Fig. 2) and position of the axis of the approach fairway towards the shore. Considerable influence of the length of the breakwaters on the silting up of the fairway has been verified. In variants V–VI the annual silting up reaches a few thousand square meters, but the lengths of the breakwaters being successively shortened (variants III–IV and I–II) make the volume of deposited sediment tens of fold higher than when the length of the construction is optimal (400 m). These relations have been

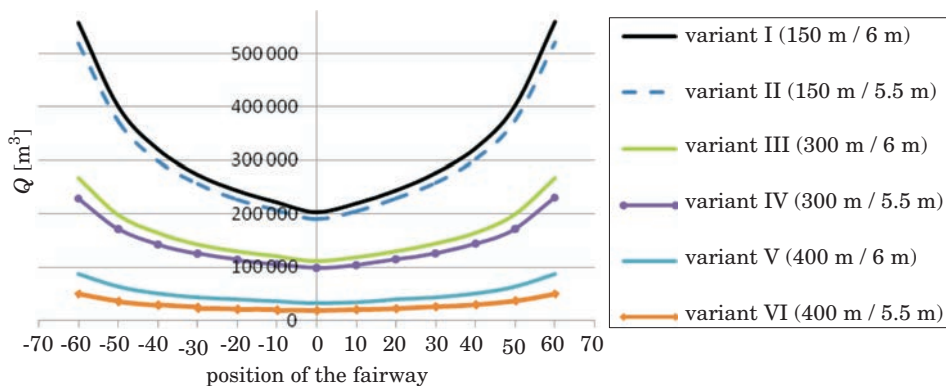


Fig. 3. The mean annual volume of the silting up of the approach fairway depending on the angle between the fairway and the normal to the shore – actual grain size distribution

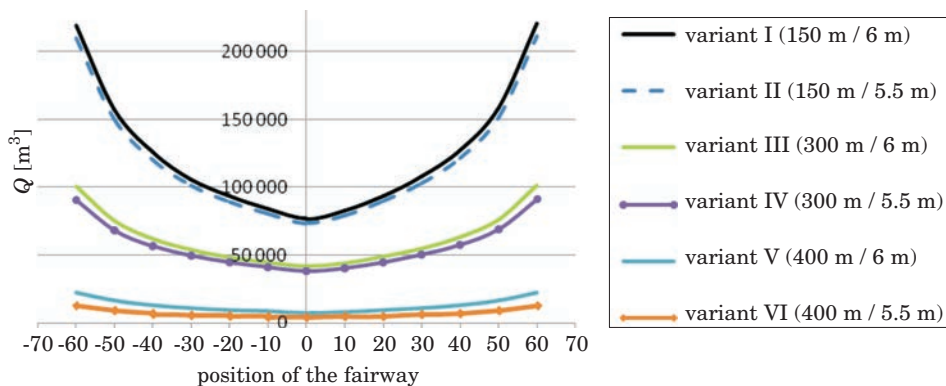


Fig. 4. The mean annual volume of the silting up of the approach fairway depending on the angle between the fairway and the normal to the shore – grain size distribution designated as 31 M-7

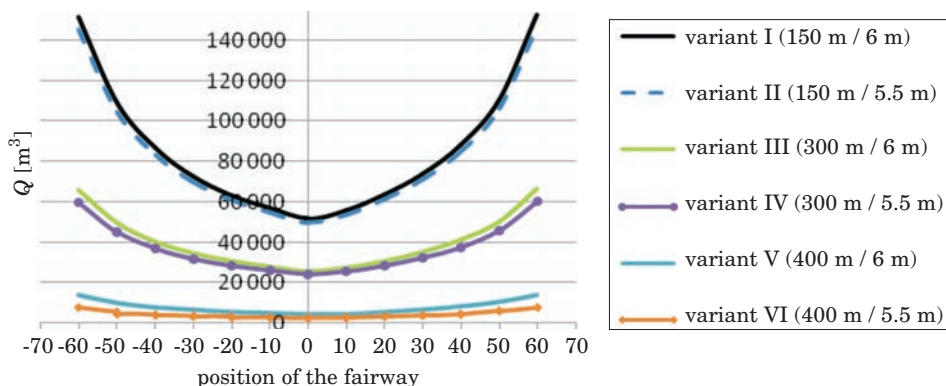


Fig. 5. The mean annual volume of the silting up of the approach fairway depending on the angle between the fairway and the normal to the shore – uniform sediment $d = 0.22$ mm

found out by totalling the mean annual volumes of the sediments deposited in the fairway due to three factors: sediment transport induced by surface waves at the edges of the fairway (Fig. 6), by longshore current (Fig. 7) and by return current (Fig. 8).

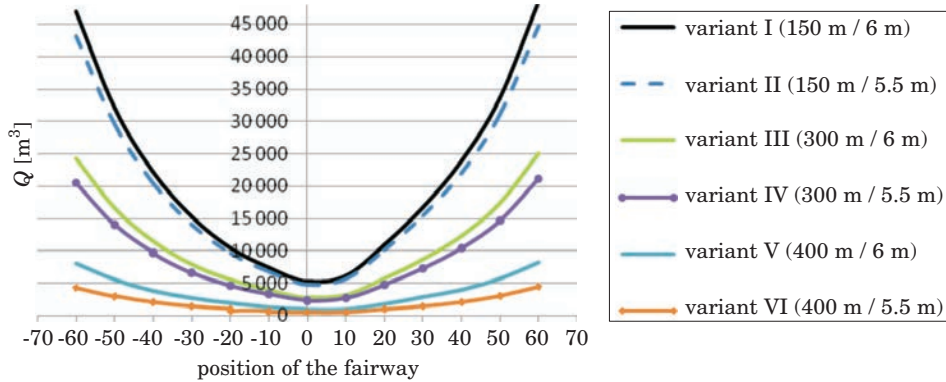


Fig. 6. Mean annual volume of the silting up of the approach fairway caused by surface waves at the edges of the fairway depending on the angle between the fairway and the normal to the shoreline – sediment designated as 31 M-7

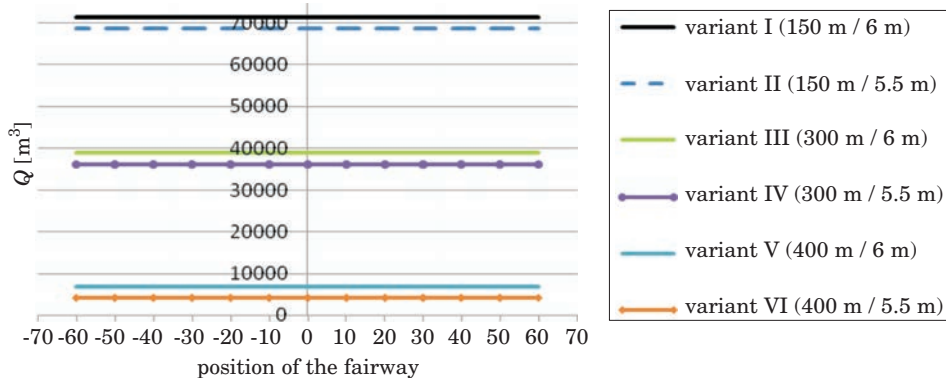


Fig. 7. Mean annual volume of the silting up of the approach fairway caused by the longshore current depending on the angle between the fairway and the normal to the shoreline – sediment designated as 31 M-7

The mean annual volume of sediments deposited in the fairway caused by the above factors have been presented for only one grain size distribution designated as 31 M-7. This grain size fraction draw our attention because it resembles in shape the fractions of sand sampled from the approach fairway to the port in Łeba (cf. KACZMAREK 2009). It can be suspected that although at present the share of small grain fractions in the averaged grain size distribu-

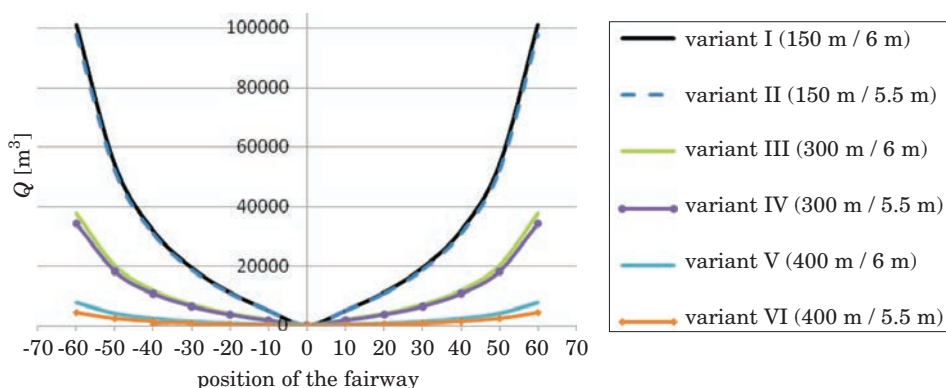


Fig. 8. Mean annual volume of the silting up of the approach fairway caused by the return current depending on the angle between the fairway and the normal to the shoreline – sediment designated as 31 M-7

tions in a transverse profile of the shore near Skowronki is larger than in the 31 M-7 distribution, once the canal is opened, the presence of fine grain fractions in the approach fairway will be stabilized after a few years on a level comparable to that in the sediments at the edges of the fairway in Łeba.

When analyzing the diagrams presented in Figs. 6–8, it can be noticed that the transport due to surface waves at the edges of the fairway (Fig. 6) is the largest for the two extreme angles of the position of the construction, whereas the smallest values are ‘located’ between the angles 0–10°. The minimum value of the mean annual silting up of the fairway shown in Fig. 6 is shifted away from the perpendicular profile by a few degrees. It is so due to the sediment transport induced by surface waves whose resultant direction, at about 200 m away from the shore (accord. to the IBW PAN model) is directed to the east and its deviation from the normal to the shore is about 10°. The volumes of the mean annual silting up caused by surface waves at the edges of the fairway, calculated for different angles between the fairway’s axis and the normal to the shore, are nearly symmetrical relative to the lower extreme value.

The silting up caused by the longshore current (Fig. 7), which moves parallel to the shoreline, is constant in each variant and independent from the position of the fairway relative to the shore. Our comparison of the orders of the volumes of sediments deposited in the fairway, shown in Figs. 6–8, proves that most of the sediment is carried by the longshore current.

The average annual volume of the sediment deposited in the fairway due to the return current, whose resultant is perpendicular to the shoreline, is symmetrical to the profile perpendicular to the shore. When the approach fairway is situated along the normal to the shore, the return transport does not

cause any silting. As the fairway inclines westward (-10° to -60°) or eastward (10° to 60°), the role of the return current transport becomes more important, reaching the maximum values for the two extreme angles.

The figures shown above illustrating the total mean annual silting up (Figs. 3–5) and the components of the volume of deposited sediment (Figs 6–8) demonstrate that the calculated values depend on both the length of the fairway and its position towards the shore. The values obtained for the breakwaters measuring 150m and 300 m are a few or even tens of fold higher than the values calculated when the breakwaters are 400 m in length.

Our computations have confirmed that the optimum location of the breakwater, which will minimize the volume of sediments deposited in the fairway, is near the profile perpendicular to the shore. In addition, figs. 3–5 show that for the breakwaters 400 m in length, the smallest mean annual silting up, independently from the particle size fractions in the sediments, occurs within the locations $\pm 20^\circ$. The shorter the breakwaters, the stronger the relation between the volume of silting up and the angle of deviation from the normal to the shore.

The final decision about the position of a fairway versus the shore is usually conditioned by the predicted volume of deposited sediments in the planned fairway and the need to ensure navigation safety when ships enter and exit the canal. Thus, wave conditions which will be created in the canal as well as in the water basin within the breakwaters, also under stormy weather, are essential. Knowing that the deviation of the approach axis from the normal to the shore within $\pm 20^\circ$ does not cause any significant change in the volume of sediments deposited in the fairway, we now have more flexibility when determining the actual position of the planned construction.

The influx of sediments caused by surface waves at the edges of the fairway, the longshore current and the return current on the total mean annual volume of sedimentation of the fairway, for the selected particle size distribution (31 M-7) and the basic variant (400 m/5.5 m) has been illustrated in figure 9. It can be seen that for the fairway whose axis is close to the normal to the shore, the largest contribution to the total mean annual silting up of the fairway is generated by the longshore transport. Any larger deviation of the fairway's axis from the profile perpendicular to the shore means that the wave – induced transport at the edges of the fairway and the return current will bring more sediments.

Noteworthy, apart from the location of the construction relative to the shore, the type of sediment lying on the seabed has a considerable effect on the contribution of particular component forces to the mean annual silting up of the fairway, as evidenced by the calculations gathered in Table 1.

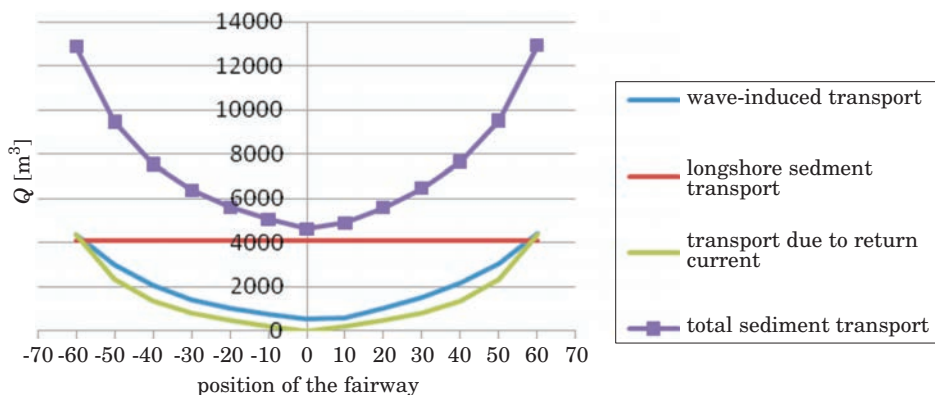


Fig. 9. Mean annual volume of the silting up of the fairway depending on the angle between the fairway and the shoreline, for variant VI – distribution 31 M-7

Table 1
Contribution of particular types of transport in the total mean annual silting up of the fairway depending on the type of sediment. Variant 400 m/5.5 m and the profile inclined by 20° from the perpendicular profile

Specification	Uniform sediment $d = 0.1 \text{ mm}$ [%]	Actual Sediment [%]	31 M-7 sediment [%]	Uniform sediment $d = 0.4 \text{ mm}$ [%]	Uniform sediment $d = 0.22 \text{ mm}$ [%]
Longshore sediment transport	81	80	73	66	20
Wave – induced sediment transport	6	8	18	27	78
Sediment transport due to return current	13	12	9	7	2

The information comprised in this table proves that if the sediment deposited on the seabed is mostly composed of fine grain fractions, then the most important factor generating the silting up of the fairway is the longshore current, whose contribution to the sedimentation process in the basic variant (400 m/5.5 m) and in a fairway deviating from the normal by 20° eastward can reach 80%. The larger the diameter of sediment particles, the lower the percentage. Likewise, the contribution to the total silting up of the return transport nearly disappears when the sediment is homogenous and particles measure 0.4 mm in diameter. It is so because both the longshore and return currents transport suspended load sediment. The transport at the edges of the fairway caused by surface waves, in contrast, involves a thick mixture of sand and water, in which grains are either dragged or more forward by making saltation jumps within the thin contact layer, right above the seabed.

The influence of grain size distribution on the total mean annual volume of sediments deposited in a fairway is shown graphically in Fig. 10. Six variants of the location of the fairway have been included in addition of five grain size distribution variants. It can be seen that the fairway in variant I, i.e. when the heads of the breakwater are 150 m away from the shoreline and the assumed depth is 6 m, will experience the most severe sedimentation during a year. By building a fairway further away from the shoreline and constructing longer breakwaters, the volume of sediments deposited in the fairway over a year decreases dramatically.

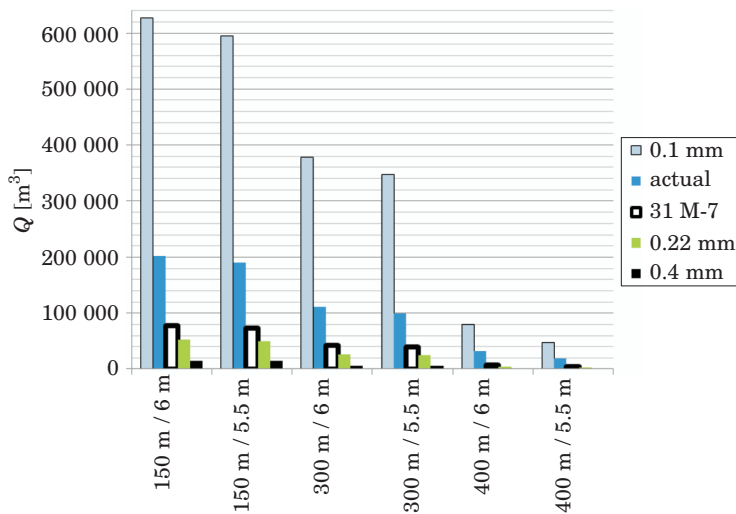


Fig. 10. Results of the calculations of sediment falling within a year into the fairway, for different types of sediment, six variants of the fairway and a profile perpendicular to the shoreline

The next diagrams (Fig. 11 and Fig. 12) show, respectively, the amount of sediment deposited during a year per length unit (L) of the fairway and the mean annual loss of depth of the fairway analysed for each of the lengths (cf. Fig. 2) and for the 60-meter width (D). Additionally, it has been assumed that the sediment trapped by fairway is evenly distributed on its bottom. It should be noticed that when predicting the amount of sediment deposited during a year per fairway length unit (Fig. 11) and the mean annual loss of depth of the fairway (Fig. 12), we obtained lower values for the deeper (6 m) approach fairway than in the variants where the fairway was 5.5 m deep. This is an effect of the bathymetry of the seabed (Fig. 2). By making the approach fairway 0.5 m deeper, from 5.5 to 6.0 m, the fairway is lengthened by 50 m (for a breakwater 400 m long, the approach fairway is 100% longer). Thus, despite

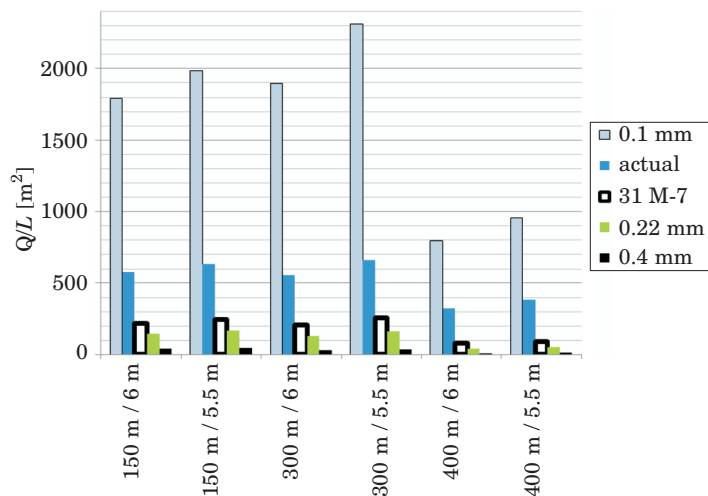


Fig. 11. Results of the calculations of the amounts of sediment deposited within a year per length unit of the fairway, for different types of sediment, six variants of the fairway and a profile perpendicular to the shoreline

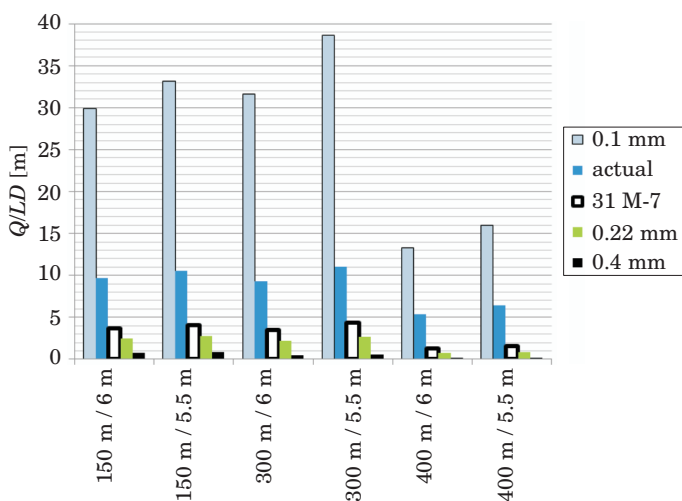


Fig. 12. Results of the calculations of the mean annual loss of depth of the fairway, for different types of sediment, six variants of the fairway and a profile perpendicular to the shoreline

the mean annual silting being almost twice as large for the deeper (6 m) fairway (Fig. 13), the loss of depth of the fairway will be nearly identical for both variants of the depth (Fig. 14).

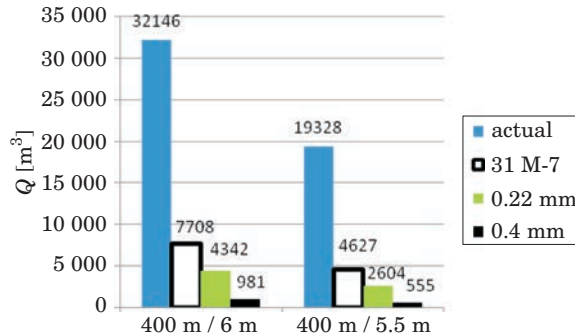


Fig. 13. Results of the calculations of the sediment falling into the fairway annually for different types of sediments – variants 400/6.0 and 400/5.5 as well as the profile perpendicular to the shoreline

A more thorough analysis of the solutions in which the heads of the breakwaters are 400 m away from the shore reveals that it is better to design a fairway that would be 5.5 m deep. In that case, the maximum amount of deposited sediment will reach about 19.5 thousand m^3 (Fig. 13) – for a considerably large fraction of small grain size in sediment – as compared to 32.1 thousand m^3 for a fairway 6 m deep. Should the amount of sediment brought into the fairway reach about 19.5 thousand m^3 annually, dredging would have to be carried out at least once a year. It is, however, highly possible that the sediment at the edges of the waterway will stabilize in time and remain at a level similar to the one found in the sediment samples taken from the edges of the fairway in Leba. Then, if the percentage of fine grain fractions in the sediment was lower (distribution 31 M-7, homogenous sediment, $d = 0.22$ mm and $d = 0.4$ mm), the annual volume of deposited sediment would be 4.6, 2.6 and 0.6 thousand m^3 respectively. The above predictions would mean that the fairway would have to be cleaned up only every 1 to 3 years, which is a satisfactory economic result.

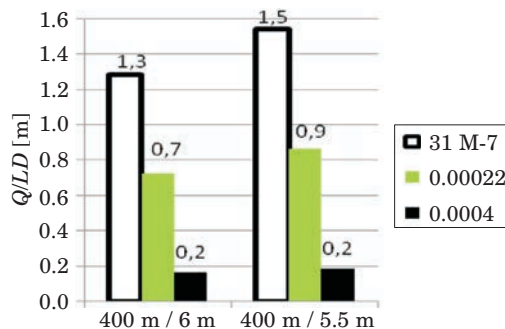


Fig. 14. Results of the calculations of the mean annual loss of depth of the fairway for different types of sediments – variants 400/6.0 and 400/5.5 as well as the profile perpendicular to the shoreline

Thus, the mean annual ranges of the fairway becoming shallower (Fig. 14) for variants V and VI, i.e. 400/6.0 and 400/5.5 (excluding the extreme value for $d = 0.1$ mm and actual distribution – with a large percentage of fine grain fractions), calculated on the assumption that the sediment in the fairway would be evenly distributed, are good prediction for the planned construction project. The values indicating the loss of depth of the fairway due to silting up confirm that the fairway would have to be cleaned up once a year at the most.

Summary

The article contains a presentation of the results of our analyses aiming at selecting the most suitable variant of the length of planned breakwaters and the depth of an approach fairway as well as its position relative to the shore so as to minimize the volume of sediment deposited in the fairway and thus reduce the frequency of dredging operations necessary in the future. The analyses included an innovative Polish calculation method called the IBW PAN, which takes into consideration the changeability of grain size distribution. For our calculations, three lengths of breakwaters (150 m, 300 m and 400 m) and two depths of an approach fairway (5.5 m and 6 m) were taken, which resulted in six different variants. Moreover, each of the variants was analyzed on the assumption involving five grain size distributions, which differed in the content of fine grain fractions. Finally, thirteen different positions of the fairway relative to the shore were examined, with the axis of the fairway situated along the normal to the shore being designated as 0° , while the successive deviations by 10° from this position, to the west and to the east, were designated as negative and positive angles.

The calculations have confirmed that the optimum solution is to situate the heads of the breakwaters 400 m from the shore and make an approach fairway that would be 5.5 m deep and to position the axis of the fairway along the normal to the shore. Then, the volume of deposited sediment shall remain on a level that will enable to reduce dredging operations to at least one-year intervals. More thorough calculations conducted for this optimum variant showed that a deviation of the water fairway from the profile perpendicular to the shore by about $15\text{--}20^\circ$ to either direction (westward or eastward) would not modify the volume of deposited sediment. However, the shorter the breakwaters, the stronger the correlation between the rate of silting up of the fairway and the angle at which the fairway's axis is positioned towards the shore.

The paper also demonstrates that when the approach fairway is deeper, from 5.5 to 6 m, it is also longer and, consequently, although the mean annual amount of deposited sediment in the deeper fairway (6 m) is almost twice as large, the loss of depth will be nearly the same for both depth variants.

However, it seems safer to design a fairway which would be 5.5 m deep (for a breakwater 400 m long) because if large amounts of fine grain fractions persisted in the sediments, the predicted volume of deposited sediments would be so large that dredging operations would have to be conducted more often than once a year.

Accepted for print 9.07.2010

References

- DUBRAWSKI R., ZACHOWICZ J. 1997. *Kanał żeglugowy na Mierzei Wiślanej – pozytywy i negatywy dla środowiska morskiego*. Inżynieria Morska i Geotechnika, 5: 301–307.
- Dynamika morza i strefy brzegowej w Zatoce Gdańskiej. Wpływ planowanego kanału żeglugowego w polskiej części Mierzei Wiślanej na zmiany morskich procesów hydrodynamicznych po odmorskiej stronie strefy brzegowej Mierzei Wiślanej. 1996. Ed. T. JEDNORAŁ. Zakład Wydawnictw Naukowych Instytutu Morskiego, Gdańsk.
- GAJEWSKI J., GAJEWSKI L., JEDNORAŁ T., LEWANDOWSKI A. 1995. *Symulacja morskich procesów lito dynamicznych wzdłuż Mierzei Wiślanej*. Inżynieria Morska i Geotechnika, 6: 284–291.
- KACZMAREK J., SAWCZYŃSKI SZ., DOMINIKOWSKI S., PAWŁOWICZ J., GRZYB G. 2008. *Podatność na zapiaszczanie i zamulanie planowanego toru wodnego z Zatoki Gdańskiej do portu w Elblągu w świetle wyników badań terenowych i analizy teoretycznej*. Raport z wykonania zlecenia wewnętrznego nr 523-0612.0301. Uniwersytet Warmińsko-Mazurski, Olsztyn.
- KACZMAREK L.M. 2008. *Modelling of the silting up of navigation channels*. Technical Sciences, 11: 175–188.
- KACZMAREK L.M. 2009. *Hydro- and lithodynamic aspects of constructing a navigable canal through the vistula spit*. Technical Sciences, 12: 40–56.
- KACZMAREK L.M., BIEGOWSKI J., GACA K., GAŚIOROWSKI D., KAŻMIERSKI J., OSTROWSKI R., PERFUMOWICZ T., PRUSZAK Z., SCHÖNHOFER J., SKAJA M., SZMYTKIEWICZ M., SZMYTKIEWICZ P. 2008. *Analiza procesów hydro- i litodynamicznych w rejonie planowanego przekopu przez Mierzę Wiślaną i predykcja wpływu przekopu na brzeg morski wraz z oceną intensywności zapiaszczania (zamułania) toru wodnego na odcinku od przekopu do portu w Elblągu*. Raport końcowy z realizacji projektu badawczego rozwojowego – na zlecenie Ministerstwa Nauki i Szkolnictwa Wyższego. IBW PAN, Gdańsk.
- KACZMAREK L.M., KACZMAREK J., BIEGOWSKI J., SAWCZYŃSKI SZ. 2009a. *Wpływ falochronów na zapiaszczanie toru wodnego z Zatoki Gdańskiej do planowanego przekopu przez Mierzę Wiślaną*. Inżynieria Morska i Geotechnika, 4.
- KACZMAREK L.M., OSTROWSKI R., SKAJA M., SZMYTKIEWICZ M. 2009b. *Wpływ falochronów osłaniających wejście do planowanego przekopu przez Mierzę Wiślaną na zmiany położenia linii brzegowej*. Inżynieria Morska i Geotechnika, 2.
- KACZMAREK L.M., OSTROWSKI R., SKAJA M., SZMYTKIEWICZ M. 2009c. *Prognoza zapiaszczania toru podejściowego prowadzącego do planowanego przekopu przez Mierzę Wiślaną*. Inżynieria Morska i Geotechnika, 3.
- KACZMAREK L.M., SAWCZYŃSKI SZ. 2007. *Zastosowanie modelu transportu osadów niejednorodnych granulometrycznie do analizy zapiaszczania toru podejściowego do portu w Łebie*. Inżynieria Morska i Geotechnika, 6: 364–374.
- RIJN L.C. VAN 1993. *Principles of sediment transport in rivers, estuaries and coastal seas*. Aqua Publications, the Netherlands.
- SKILLANDAT J.B. 2010. *Projekt koncepcyjny układu falochronów i toru wodnego w rejonie planowanego przekopu przez Mierzę Wiślaną w świetle analizy procesów hydro- i lito dynamicznych*. Praca magisterska.
- Studium wykonalności inwestycji (2007/2008): Budowa kanału żeglugowego przez Mierzę Wiślaną. Konsorcjum: Polbud Pomorze, Geosyntex Sp. z o.o. i Fundacja Naukowo-Techniczna – wykonane na zlecenie Urzędu Morskiego w Gdyni.

TAKING SUBSOIL SUSCEPTIBILITY INTO ACCOUNT IN DESIGNING COLUMNS IN REINFORCED SINGLE-STOREY STRUCTURES

Krzysztof Klempka¹, Michał Knauff²

¹ Chair of Civil Engineering and Building Constructions
University of Warmia and Mazury in Olsztyn

² The Institute of Building Structures
Warsaw University of Technology

Key words: subsoil susceptibility, effective length of columns, method based on nominal stiffness, second order effects, reinforced concrete buildings, reinforced concrete structures.

A b s t r a c t

When the Polish norm for designing concrete constructions will be replaced in 2010 by the Eurocode, its limits referring to columns' slenderness will no longer bide. While designing reinforced slender columns in single-storey buildings, it is vital to consider all the factors which may influence the bearing capacity, one of which is the increment of the bending moment caused by the rotation of foundations supported by susceptible soils. The following article presents examples of the second order calculations taking into account the influence of subsoil susceptibility and columns' nominal stiffness, as defined in the Eurocode.

UWZGLĘDNIANIE PODATNOŚCI PODŁOŻA W PROJEKTOWANIU SŁUPÓW HAL ŻELBETOWYCH

Krzysztof Klempka¹, Michał Knauff²

¹ Katedra Budownictwa i Konstrukcji Budowlanych
Uniwersytet Warmińsko-Mazurski w Olsztynie

² Instytut Konstrukcji Budowlanych
Politechnika Warszawska

Słowa kluczowe: podatność podłoża, długość obliczeniowa słupa, metoda nominalnej sztywności, efekty drugiego rzędu, hale żelbetowe, konstrukcje żelbetowe.

A b s t r a k t

Po wycofaniu (w 2010 r.) polskiej normy projektowania konstrukcji z betonu i zastąpieniu jej przez Eurokod przestaną obowiązywać zawarte w tej normie ograniczenia smukłości słupów.

Projektując smukłe żelbetowe słupy w halach, trzeba rozpatrzyć wszystkie czynniki, które mogą mieć wpływ na nośność – jednym z nich jest przyrost momentu zginającego wywołany obrotem fundamentu na podatnym podłożu. W artykule przedstawiono przykłady obliczeń według teorii II rzędu z uwzględnieniem wpływu podatności podłoża i nominalnych sztywności słupów, zdefiniowanych w Eurokodzie.

Introduction

While designing columns in reinforced concrete single-storey buildings, it is not usual to take into account the influence of subsoil susceptibility on bending moments, illustrated in Fig. 1b.

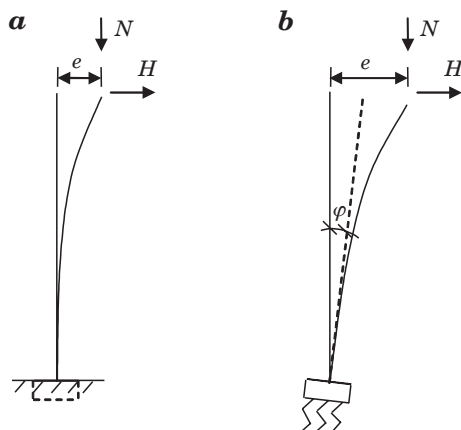


Fig. 1. Eccentricity increase: *a*) only resulting from the deflection of the column, *b*) resulting from the deflection and foundation rotation through angle φ

The PN-B-03264 norm, which still bides, recommends that the column's slenderness should not be larger than $l_0/i = 104$ ($l_0/h = 30$).

This norm is to be withdrawn in 2010 and replaced by the Eurocode, which does not contain any arbitrary limits in case of the slenderness of columns; any slenderness may be used as long as it can be proved by calculations that the bearing capacity is sufficient.

Canceling the limits of slenderness and using better materials will make it possible to design columns that are even more slender than before. According to the new general rules for designing (point 5.8.7 in Eurocode 2 (abbr. EN)), "Where relevant, soil-structure interaction should be taken into account".

As a result of the deflection of a column due to the first and second order effects (Fig. 1a), we obtain the increment of eccentricity of the applied

longitudinal force, as well as the increment of the bending moment of the column. The foundation rotation causes an additional increment of the moment as shown in Fig. 1b.

The moment increments associated with the second order effects may be calculated using two methods. The first one is a simplified method based on the concept of isolated members. To use it, it is necessary to calculate the effective length of the column being designed. EN does not give any defined effective lengths of isolated columns supported by elastic soil but only recommendations (Fig. 5.7 f, g in EN 1992-1-1) which are too general for immediate usage. The effective length of columns directly supported by foundations depends on soil susceptibility and the size of foundations. Formulae for effective lengths of isolated columns were presented in publications by KOBIĄK and STACHURSKI (1989) which had been based on the works of the German scientists FISCHER (1965) and KANY (1974).

The second method is the exact method based on the second order analysis of the whole frame structure. To use the exact method does not require calculating effective lengths – the shape of deformed elements and the associated increment of moments are determined in direct calculation. The examples of how this method may be used were presented in publications by KNAUFF and KLEMPKA in 2009.

The next part of the article will present the method of calculating the coefficient of subsoil susceptibility and shaping the foundation rotation supported by elastic soil. This will be followed by calculation results for some examples of frame structures.

Subsoil susceptibility coefficient in Winkler model

Winkler's rotation angle of foundation on soil (Fig. 2a) may be calculated using the following formula

$$\varphi = \frac{M}{C_z I_F} \quad (1)$$

where

I_F – the moment of inertia of the area of the foundation's base,

C_z – subsoil elasticity coefficient.

Coefficient C_z is not a material constant because it does not depend only on the physical characteristics of the soil but also on the dimensions of foundations. To determine its value we have to take into account uniform elastic

half-space with characteristics defined by modulus E_0 and Poisson's ratio ν . The value of the rotation angle of the foundation may be determined from formula (2) which comes from the article by GORBUNOV-POSADOV (1956).

$$\varphi = \frac{4M(1 - \nu_0^2)}{\pi E_0 b' l^2} \quad (2)$$

(1) and (2) show that the soil elasticity coefficient used in Winkler's model has to be expressed by the following dependence:

$$C_z = \frac{\pi E_0 b' l^2}{4I_F(1 - \nu_0^2)}$$

Taking into account that

$$I_F = \frac{b'(2l)^3}{12} = \frac{2}{3} b' l^3$$

We obtain

$$C_z = \frac{3\pi}{8l} \frac{E_0}{(1 - \nu_0^2)} \quad (3)$$

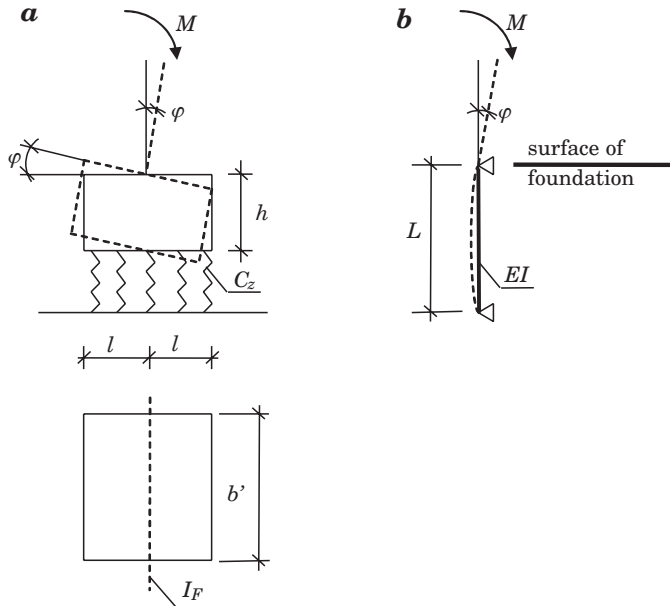


Fig. 2. Foundation supported by elastic soil (a); the way of shaping the influence of the ground in static calculations of foundations (b)

If we want to take the foundation rotation into account in static calculation of frames, we can assume that our model of a column's support will be a hypothetical bar like the one in Fig. 2b (with its length expressed by L and its stiffness by EI). The rotation angle on the bar's support, caused by moment M can be derived from formula (4):

$$\varphi = \frac{ML}{3EI} \quad (4)$$

It may be seen from (1) and (4) that length L and stiffness EI of the hypothetical bar should be selected in such a way that its flexural stiffness $3EI/L$ satisfies the following dependence

$$\frac{3EI}{L} = I_F C_z \quad (5)$$

Analysis of calculation results for examples of single-storey frames

Below we present examples of calculations of bending moments in columns of single-storey reinforced concrete buildings. For the calculations we used the exact method based on the second order analysis taking into account the nominal stiffness as described in the article by KNAUFF and KLEMPKA (2009). We analysed the case of columns fully fixed to the foundation base as well as the case of a column fixed to the foundation supported on elastic subsoil. We assumed the same foundation base – 3.0×2.0 m – for all the cases. The base is fixed on genesis-C cohesive, hard saturated plastic soil where $I_L = 0.20$, $E_0 = 20$ MPa, $\nu = 0.32$.

The moment of inertia of the area of the foundation's base is

$$I_F = \frac{2}{3} b l^3 = \frac{2}{3} 2 \cdot 1.5^3 = 4.5 \text{ m}^4$$

And the subsoil elasticity coefficient is

$$C_z = \frac{3\pi}{8l} \frac{E_0}{(1 - \nu_0^2)} = \frac{3\pi}{8 \cdot 1.5} \frac{20}{(1 - 0.32^2)} = 17.50 \text{ MN/m}^3$$

Using formula (5) we calculated the flexural stiffness of the hypothetical bars shaping the support

$$\frac{3EI}{L} = I_F C_z = 4.5 \cdot 17.50 = 78.75 \text{ MNm}$$

Example 1

Computational longitudinal forces in three-nave single-storey building (Fig. 3) are $P_1 = 450 \text{ kN}$ in the edge columns and $P_2 = 900 \text{ kN}$ in internal columns. The eccentricity resulting from cover load in edge columns is 0.15 m .

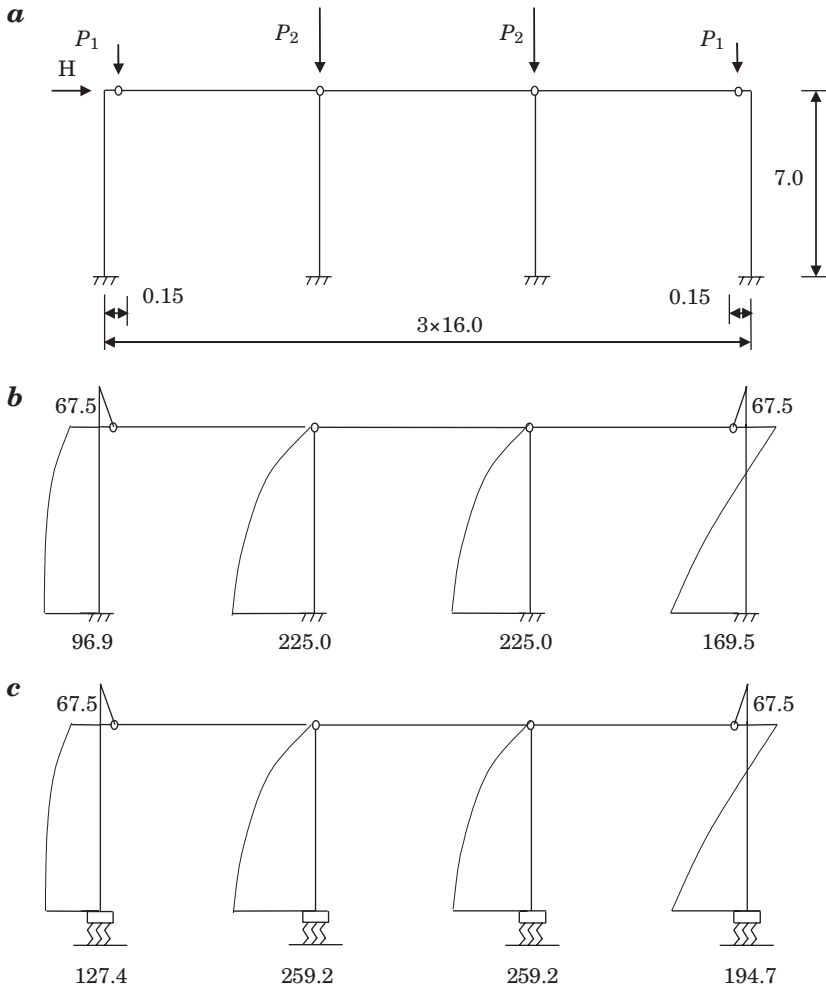


Fig. 3. Example 1. a) the diagram of the single-storey building, b) bending moments for fully fixed columns [kNm], c) moments calculated with subsoil susceptibility [kNm]

The horizontal force caused by wind pressure and suction equals $H = 36$ kN. We assumed that the stiff roof construction imposes identical horizontal shift of the top ends of all the columns. Columns (concrete C40/50, steel A-III) have identical cross sections $b = 40$ cm, $h = 45$ cm. We also assumed that the reinforcement in the edge columns is $3\phi 20$ ($A_s = 9.42$ cm²), and in the internal columns is $5\phi 20$ ($A_s = 15.71$ cm²) on each side of the cross section.

Imperfections according to point 5.2 EN equal

$$\alpha_h = \frac{2}{\sqrt{l}} = \frac{2}{\sqrt{7.0}} = 0.756, \alpha_m = \sqrt{0.5 (1 + 1/m)} = \sqrt{0.5 (1 + 1/4)} = 0.790$$

The angle of inclination is

$$\Theta_i = \Theta_0 \alpha_h \alpha_m = \frac{1}{200} 0.756 \cdot 0.790 = 0.00298$$

Horizontal forces caused by imperfections:

In edge columns $H_1 = \Theta_i P_1 = 0.00298 \cdot 450 = 1.341$ kN,

In internal columns $H_2 = \Theta_i P_2 = 0.00298 \cdot 900 = 2.682$ kN.

More details referring to the model with fully fixed columns can be found in the article by KNAUFF and KLEMPKA (2009). Bending moments are presented in Figure 3.

Example 2

We assumed that the horizontal force caused by wind pressure and suction equals $H = 30$ kN. We also assumed that the stiff roof construction imposes identical horizontal shifts of the top ends of all the columns. Columns like the ones in example 1 have on each side of their cross section reinforcement $4\phi 16$ ($A_s = 8.04$ cm²) in edge columns and $7\phi 16$ ($A_s = 14.07$ cm²) in internal columns. The calculations were conducted for two cases of loading with longitudinal forces:

Case 1

$P_1 = 200$ kN in edge columns,

$P_2 = 900$ kN in an internal column

Case 2

$P_1 = 450$ kN in edge columns,

$P_2 = 790$ kN in an internal column.

Bending moments for case 1 and 2 are presented in Figure 4 and 5 respectively.

The cases show calculations for the soil of small stiffness. Generally, the influence of subsoil susceptibility on bending moments is not very significant. The results for example 2 presented in Figure 5 are an exception. As a result of taking into account the foundation on elastic soil, the bending moments in the edge columns increased by 17% compared to the calculation results for the columns fully fixed to the foundation.

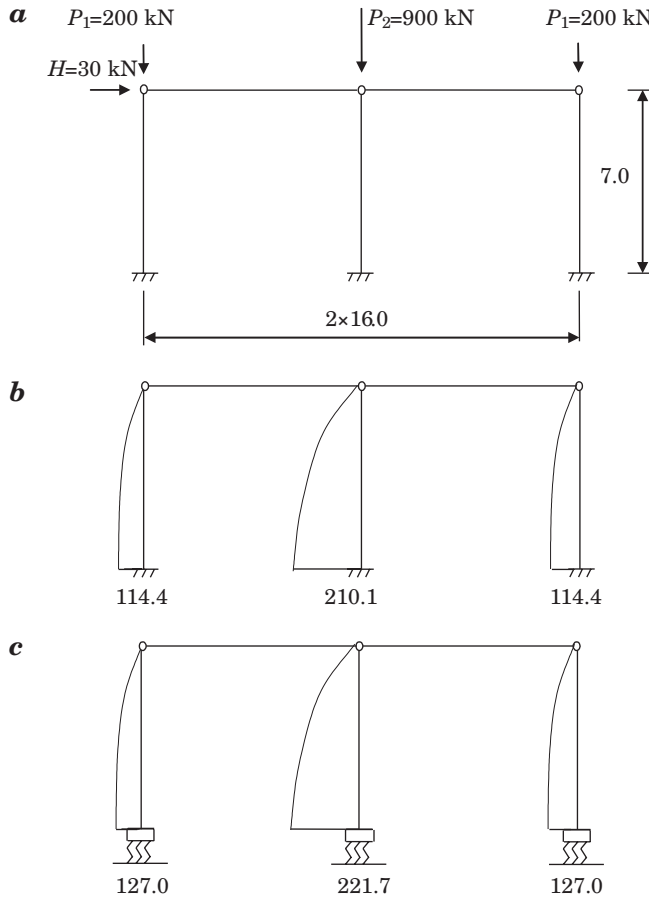


Fig. 4. Example 2- loading for case 1; a) the diagram of the single-storey building, b) bending moments for fully fixed columns [kNm], c) moments calculated with subsoil susceptibility [kNm]

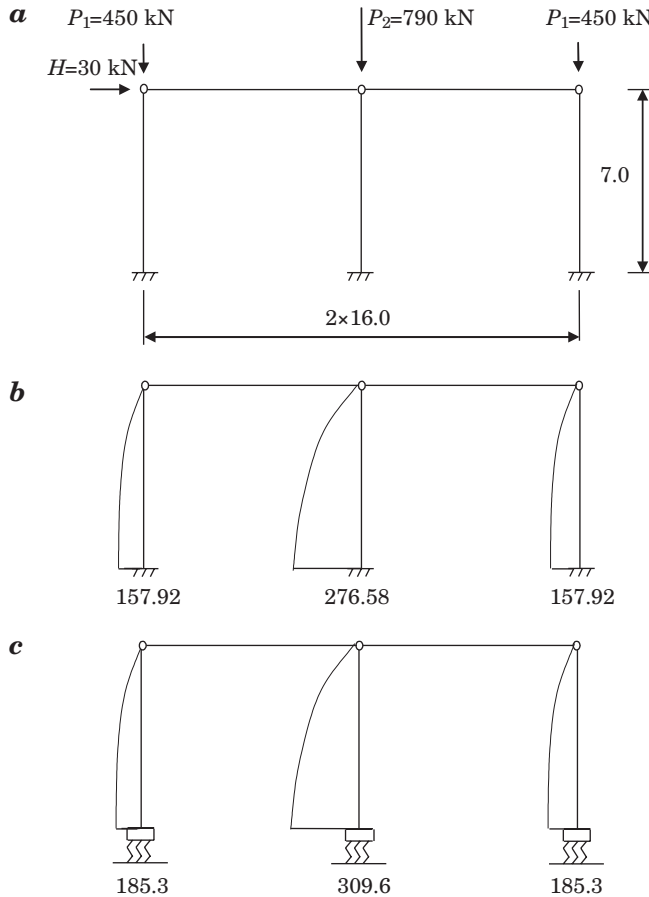


Fig. 5. Example 2 – loading for case 2. a) the diagram of the single-storey building, b) bending moments for fully fixed columns [kNm], c) moments calculated with subsoil susceptibility [kNm]

Conclusions

The article presents a method for shaping the support of a column fixed to the foundation on elastic soil. This method may be used in standard computer programmes for static calculations. We presented examples of calculations using the exact method based on the second order analysis and taking into account the nominal stiffness for frames with columns supported in the ways described in the article. Foundation rotation leads to the increase in the final values of moments in the columns, which may be of vital importance in case of fixing columns on soils of small stiffness.

References

- Eurocode 2, 2008. Design of Concrete Structures. Part 1-1. General Rules and Rules for Buildings. EN 1992-1-1.
- FISCHER K. 1965. *Beispiele zur Bodenmechanik*. Ernst u. Sohn. Berlin.
- GORBUNOW-POSADOW M.T. 1956. *Obliczanie konstrukcji na podłożu sprężystym*. Budownictwo i Architektura, Warszawa.
- KANY M. 1974. *Berechnung von Flächengründungen*. Ernst u. Sohn. Berlin.
- KNAUFF M., KLEMPKA K. 2009. *Effective lengths of reinforced concrete columns in single-storey frame structures in the light of the Eurocode*. Technical Sciences, 12, 71–82.
- KNAUFF M., KLEMPKA K. 2009. *Projektowanie smukłych słupów żelbetowych według Eurokodu 2*. Inżynieria i Budownictwo, 12: 663–665.
- KOBIĄK J., STACHURSKI W. 1989. *Konstrukcje żelbetowe*. T. 3. Arkady, Warszawa.
- LEWIŃSKI P. 2007. *Analiza współpracy żelbetowych zbiorników cylindrycznych z podłożem*. Wyd. ITB, Warszawa.
- PN-B-03264: 2002. *Konstrukcje betonowe, żelbetowe i sprężone. Obliczenia statyczne i projektowanie*.

HISTORIC SPATIAL LAYOUTS IN SMALL TOWNS IN WARMIA AND THEIR ROLE IN THE CURRENT LIFE OF INNER TOWN AREAS

Marek Zagroba

Chair of Civil Engineering and Building Constructions
University of Warmia and Mazury in Olsztyn

Key words: architecture, urbanism, renovation, revitalization, conservation of historic buildings, historic conservation zone.

A b s t r a c t

The historic layouts of streets in small towns of Warmia are mainly found in inner-town areas, which until the present day remain the town centres, giving identity to each town. Because of the complex character of the elements creating these structures, any conversion in a historic town centre should result in good exposure of the old town against the backdrop consisting of the other parts of the town. This approach, however, is possible only when many different issues, such as spatial, economic and social ones, are solved. Finding such complex solutions is a problem shared by most of the towns in Warmia.

HISTORYCZNE UKŁADY PRZESTRZENNE MAŁYCH MIAST WARMII I ICH ROLA WE WSPÓŁCZESNYM FUNKCJONOWANIU OBSZARÓW ŚRÓDMIEJSKICH

Marek Zagroba

Katedra Budownictwa i Konstrukcji Budowlanych
Uniwersytet Warmińsko-Mazurski w Olsztynie

Słowa kluczowe: architektura, urbanistyka, rewaloryzacja, rewitalizacja, konserwacja zabytków, strefa ochrony konserwatorskiej.

A b s t r a k t

Historyczne układy przestrzenne małych miast warmińskich dotyczą przede wszystkim przestrzeni śródmiejskich, pozostających do czasów obecnych centrami miast. To również przestrzenie będące przejawem tożsamości ośrodków. Złożoność elementów tworzących te struktury wymaga takich przekształceń, które powodowałyby ekspozycję zespołów staromiejskich na tle pozostałych obszarów miasta. Wymaga to rozwiązywania wielu problemów, nie tylko przestrzennych, lecz także gospodarczych i społecznych, co pozostaje obecnie wspólnym zadaniem dla większości miast regionu.

Introduction

Most towns in Warmia are small and have the original street layout similar in size. For centuries, these town centres have remained unchanged or undergone very small alterations. Most of the urban population in Warmia live in such small municipalities. However, the inner-town areas in many local towns have been badly degraded by the operations that took place in the last months of World War Two and by the post-war reconstruction efforts. Most of these inner-town areas today call for renovation. It is obvious that any remodeling should reach beyond the material component of the spatial arrangement so as to improve the living conditions of the local residents and aid the economic growth. Above all, a town is where people live.

The present state of preservation of the historic centres in the towns of Warmia – their old town areas – is quite varied. The major damage to these towns was inflicted by the Soviet Army, which demolished historic buildings on a mass scale. The spatial degradation of the towns continued after the war, when the town centres were rebuilt, often with little consideration given to the scale and character of the historic inner-town areas. In many towns, the results of this approach can be seen until today as their old towns have been nearly completely destroyed. In such towns as Biskupiec, Bisztynek, Dobre Miasto, Lidzbark Warmiński, Pieniężno, the destruction of the original layout is most clearly visible in the nearest proximity to the old town market.

The present-day view of the inner-town areas is additionally affected by the bad economic situation in the region (unemployment, migration to larger towns). This alone is an argument strong enough to prove that any renovation of the urban space should be accompanied by a search for economic and social grounds for future development. The tourism industry, whose potential economic power seems insufficiently developed (in view of the shortage of natural resources in the region), could be a possible solution. It would, however, require redesigning the revitalization programmes, which – when implemented – should pertain not only to the form of a given town but also its functions. Additionally, revitalization of the old towns in Warmia would help to preserve their historic identity and the cultural heritage of the whole region.

Spatial conditions in the towns

There are twelve towns founded in the Middle Ages in the historic region of Warmia. The specific nature of these medieval towns was shaped by the military considerations – all the towns were located at a distance of 15–30 km and had a fortified castle or a stronghold, as dictated by the policy of the

Teutonic Order towards the conquered lands of the Old Prussian tribes. This approach created a firm basis on which the towns in the whole region were founded (KAJZER 1993).

Except for Olsztyn, all the other towns in Warmia can be classified as small ones. Two of them, namely Braniewo and Frombork, have developed under different conditions, a question which could become a subject for a separate study. The remaining towns are Barczewo, Biskupiec Reszelski, Bisztynek, Dobre Miasto, Jeziorany, Lidzbark Warmiński, Orneta, Pieniężno and Reszel.

The historic layouts of the towns, in most cases, have been preserved until the present day. They consist of a regular grid of streets, which divide the town centre into square blocks and a market square in the middle. Some deviations from this regular street plan further away from the main square were due the existing watercourses and other topographic features of the terrain (CZUBIEL, DOMAGAŁA 1969).

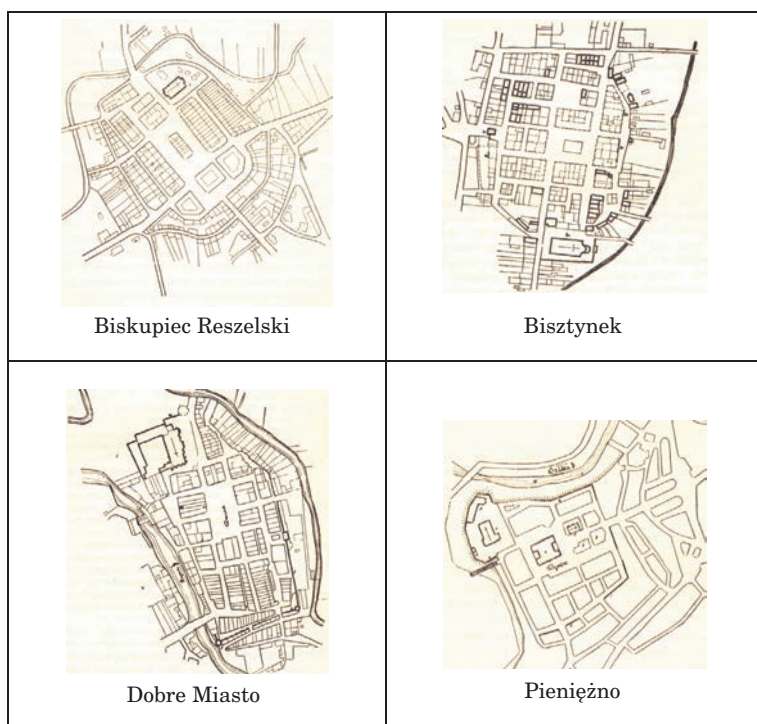


Fig. 1. Street plans of towns in Warmia in the 1950s

Source: CZUBIEL L., DOMAGAŁA T. (1969)

Among the nine towns listed above, there are the ones where certain building projects completed in the 1960s and 1970s introduced a new identity, and let us add – a weird one, to the town centres. Spatial structures of the

market squares in Dobre Miasto or Biskupiec Reszelski were filled in with roundabouts, thus becoming the main transportation hubs. Accumulating most of the road traffic in the town centre (e.g. the transit traffic passing through Dobre Miasto to the Polish-Russian border checkpoint in Bezledy) distrubs its small-town character of the main municipal square.



Fig. 2. Dobre Miasto – a roundabout in the middle of the historic market square
Photo: M. Zagroba



Fig. 3. Biskupiec Reszelski – a roundabout in the middle of the historic market square
Photo: M. Zagroba

Consequently, any action undertaken to renovate the spatial layout of any small town in Warmia should include the concept of restoring the central function of the inner-town area and building proper links with the other parts of a town. What we deal with here are small town communities, where the

bonds with one's place of residence are formed mainly by feeling attached to the inner-town area. Solutions which neglect these relationships can lead to a situation which has already appeared in some towns, for example in Pieniężno, such as depopulation of the town centre. By locating some attractive urban functions near the bus terminal in Pieniężno, e.g. services, shops, the centre of the town was shifted there away from the old town.

The buildings which today stand in the historic centres of the towns in Warmia are quite varied. Orneta and Reszel seem to be outstanding in this respect. Their spatial layouts are among the best preserved in Warmia. The urban structure as well as the architecture of these two towns are well grounded in their historic context. In both towns, the centre is dominated by a clearly visible regular pattern of the streets as well as a wealth of forms kept in a similar style including the scale, divisions, rhythms, architectural detail and light colours of walls. The accumulation of residential houses with services and trade facilities located on the ground floors defines the inner-town area as a true town centre. This in turn affects the way the town centre functions economically and socially.

The post-war reconstruction of the buildings in the historic town centres had a tragic effect on some of the towns in Warmia. Examples can be seen among the buildings raised around the market squares of Dobre Miasto, Bisztynek, Lidzbark Warmiński or Pieniężno. Buildings in an architectural style foreign to towns in Warmia or even worse – the ones lacking any style at all – do not correspond to the historically grounded patterns. The town centres lack compact complexes of small buildings, with fine lines of division, well fitted in the historical content of each town. In fact, spatial deformation has occurred over large areas of the old towns. Most of these post-war buildings were raised using means of architectural expression typical of the socialism era, thus bringing havoc to the structure which has been defined in the past centuries.

The expression of the spatial aspect of the renovation of inner-town areas should first of all serve as a means of restoring their physical image. This stage, however, contains encoded economic and social conditions, associated with the functions performed by a town. The mutual relations between these aspects are a basis for determination of the directions and ways of renovating the towns.

The spatial structure of old historic town centres to some extent defines the way other urban areas should be managed. This relationship in the analyzed small towns in Warmia is again diverse. Nonetheless, in most cases there is certain hierarchy which orders the scale and intensity of developed areas depending on the town centre. Such cohesion is particularly strongly felt in the smallest towns of Warmia, where the urban development has not been intensive.



Fig. 4. Lidzbark Warmiński – houses along the northern side of the market square
Photo: M. Zagroba



Fig. 5. Pieniężno – buildings along the eastern side of the market square – the spire of a Lutheran church and a residential house
Photo: M. Zagroba



Fig. 6. Jeziorany – fragment of a developed area in the town

Photo: M. Zagroba

The state of preservation of the spatial components in towns is largely dependent on the economic and social situation of municipalities. Statistical data such as the unemployment rate, population growth or housing stock enable us to illustrate the economic and social potential of towns, which is essential for any renovation of urban space. Based on the analysis completed by the author of this paper (statistical yearbooks) it can be concluded that the potential of the smallest towns in Warmia is weak. The situation on the labour market as well as the small population growth are particularly threatening. In the nearest future, they can lead to increased migration of the population to larger towns, depopulation of the small towns and, consequently, deteriorated management of the urban space.

Conclusions

Renovation of degraded inner-town areas in small towns is a great chance for restoring their capacity to function as historic centres of urban localities. Renovation should involve spatial issues, improvement of the quality of life for local communities and creation of opportunities for economic growth. Designing and implementing renovation programmes is a complex process planned for many years and therefore requires integrated actions undertaken by teams of people. The complex nature of town renovation means that the issue should be approached in an interdisciplinary fashion both at the preparation and implementation stages. Because the economic and social situation of the towns in Warmia is difficult, it is crucial to search for financial means and co-

financing of revitalization projects from private, municipal and external sources, e.g. structural funds, which at present offer most opportunities to co-finance revitalization programmes (SKALSKI 2002).

Accepted for print 28.06.2010

References

- CZUBIEL L., DOMAGAŁA T. 1969. *Zabytkowe ośrodki miejskie Warmii i Mazur*. Wyd. Pojezierze, Olsztyn.
- KAJZER L. 1993. *Zamki i społeczeństwo. Przemiany architektury i budownictwa obronnego w Polsce w X-XVIII wieku*. Wyd. Uniwersytetu Łódzkiego, Łódź.
- SKALSKI K.M. 2002. *O dochodzeniu do europejskich standardów finansowania rehabilitacji osiedli mieszkaniowych*. In: *Metoda rewitalizacji osiedli socjalnych Gdańska okresu dwudziestolecia międzywojennego na przykładzie wybranych osiedli*. Ed. R. Cielątkowska, Gdańsk.

THE EFFECT OF THE FUEL TYPE ON THE VALUE OF PRIMARY ENERGY AND EMISSION OF POLLUTANTS

Piotr Bogacz¹, Jacek Zabielski²

¹ Chair of Civil Engineering and Building Constructions

² Chair of Building Processes

University of Warmia and Mazury in Olsztyn

Key words: certificate of energetic characteristic, energetic audit, emission of pollutants to atmosphere, alternative sources of energy.

Abstract

The aim of this paper is to present the interdependence of the value of non-renewable primary energy and the emission of pollutants to the atmosphere depending on the type of fuel used. The analysis of the existing building object dating from 2005, in its present state using natural gas with a high methane content for the purpose of heating and preparing hot utility water. Other, alternative types of fuel have been proposed and the amounts of the primary energy index and emitted pollutants have been compared. Liquefied petroleum gas and biomass have been proved to be the most ecological fuel.

WPLYW RODZAJU PALIWA NA WARTOŚĆ ENERGII PIERWOTNEJ I EMISJĘ ZANIECZYSZCZEŃ

Piotr Bogacz¹, Jacek Zabielski²

¹ Katedra Budownictwa i Konstrukcji Budowlanych

² Katedra Inżynierii Procesów Budowlanych

Uniwersytet Warmińsko-Mazurski w Olsztynie

Słowa kluczowe: świadectwo charakterystyki energetycznej, audyt energetyczny, emisja zanieczyszczeń do atmosfery, alternatywne źródła energii.

Abstract

W pracy przedstawiono zależność wartości nakładu nieodnawialnej energii pierwotnej oraz emisji zanieczyszczeń do atmosfery w zależności od użytego rodzaju paliwa. Przeprowadzono analizę istniejącego obiektu budowlanego z 2005 roku, wykorzystującego gaz ziemny wysokometanowy na

ogrzewanie i przygotowanie ciepłej wody użytkowej. Zaproponowano inne, alternatywne rodzaje paliwa oraz porównano wartości wskaźnika EP oraz ilość emitowanych zanieczyszczeń. Wykazano, że najbardziej ekologicznym paliwem jest gaz płynny oraz biomasa.

Introduction

Starting on 01.01.2009, on the strength of the Ordinance of the Minister of Infrastructure dated 6.11.2008 concerning the methodology of calculating the energetic characteristic of a building and dwelling or part of a building constituting an independent technical and usable whole as well as the method of drawing up and the formats of certificates of their energetic characteristic (Dz.U. 2008 nr 201 poz. 1240), an obligation to draw up certificates of energetic characteristic of buildings was introduced. This practice results from the Directive of the European Parliament and the Council of the European Union 2002/91/EC (Journal of Law U. W. E. L 1/65 of 2002) concerning the energetic characteristic of buildings of 16 December 2002, which compels the community member states to reduce energy-consumption in building engineering, both in new and repaired buildings. Such a formulation is supposed to attract the attention of investors and immovable property owners to the problem of energy-consumption by building objects, and thus, a negative effect on the natural environment.

The role of the certificate of energetic characteristic

The certificate of energetic characteristic is an independent estimation of the market value and the use value of a building or quarters. This document can be issued only by an authorised specialist. The requirement for energy necessary to maintain the use comfort is determined at three levels, which are the use, final and primary ones. The requirement for energy includes: heating (in all objects), hot water (in all objects), ventilation and air conditioning (if a building is equipped with a cooling system), and also lighting in public buildings.

Use energy is energy used directly in a building, serving the purpose of heating or obtaining hot water. Its value is determined on the basis of heat loss through external partitions surrounding the regulated temperature cubature and ventilation. Final energy is balanced at the boundary of a building. It expresses the requirement for energy which should be delivered to a building including all the loss resulting from the efficiency of installation systems. The requirement for non-renewable primary energy determines the total effectiveness of a building. Apart from final energy, it includes additional inputs of non-

renewable primary energy for supplying a building boundary with every energy carrier used (e.g. coal, fuel oil, gas, electric energy, renewable energies, etc.) and support energy, necessary for auxiliary devices' drive.

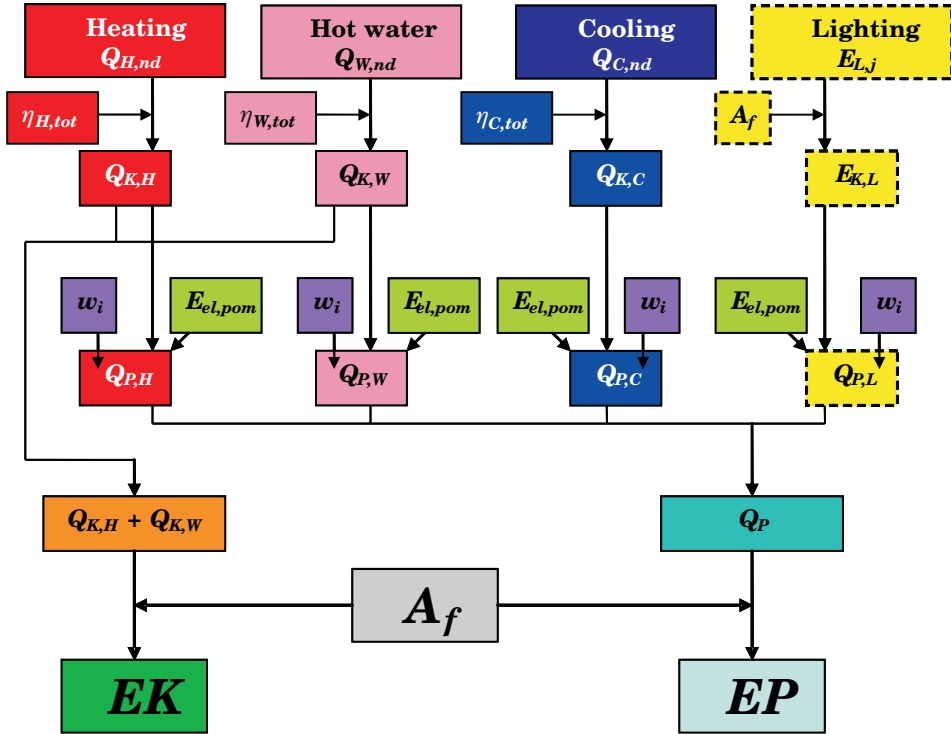


Fig. 1 Diagram for calculating the energetic characteristic

Source: authors' data

Primary energy for the heating and ventilation system is calculated according to the following equation:

$$Q_{P,H} = w_H \cdot Q_{K,H} + w_{el} \cdot E_{el,pom,H} \text{ [kWh/year]} \quad (1)$$

- $Q_{K,H}$ – annual requirement for final energy by the heating and ventilation system for heating and ventilation [kWh/year],
- w_i – coefficient of the non-renewable primary energy input for producing and delivering a final energy carrier (or energy) for an estimated building (w_{el} , w_H , w_W),

$E_{el,pom,H}$ – annual requirement for electric energy for auxiliary devices' drive of the heating and ventilation system [kWh/year].

Primary energy for the system of hot utility water preparation is calculated according to the following equation:

$$Q_{P,W} = w_w \cdot Q_{K,W} + w_{el} \cdot E_{el,pom,W} \text{ [kWh/year]} \quad (2)$$

$Q_{K,W}$ – annual requirement for final energy by the hot utility water system [kWh/year],

w_i – coefficient of the non-renewable primary energy input for producing and delivering a final energy carrier (or energy) for an estimated building (w_{el} , w_H , w_W),

$E_{el,pom,W}$ – annual requirement for electric energy for auxiliary devices' drive of the hot utility water preparation system [kWh/year].

Primary energy for the cooling system is calculated according to the following equation:

$$Q_{P,C} = w_C \cdot Q_{K,C} + w_{el} \cdot E_{el,pom,C} \text{ [kWh/year]} \quad (3)$$

$Q_{K,C}$ – annual requirement for final energy by the cooling and ventilation system for room and air cooling [kWh/year],

w_i – coefficient of the non-renewable primary energy input for producing and delivering a final energy carrier (or energy) for an estimated building (w_{el} , w_H , w_W),

$E_{el,pom,C}$ – annual requirement for electric energy for auxiliary devices' drive of the cooling and ventilation system [kWh/year].

Annual requirement for primary energy by a built-in lighting system is calculated according to the following equation:

$$Q_{P,L} = w_{el} \cdot E_{K,L} + w_{el} \cdot E_{el,pom,L} \text{ [kWh/year]} \quad (4)$$

$E_{K,L}$ – annual requirement for final energy by built-in lighting [kWh/year],

w_i – coefficient of the non-renewable primary energy input for producing and delivering a final energy carrier (or energy) for an estimated building (w_{el} , w_H , w_W),

$E_{el,pom,L}$ – annual requirement for electric energy for auxiliary devices' drive of the built-in lighting system [kWh/year].

Annual requirement for electric energy for auxiliary devices' drive includes all equipment necessary for reliable operation of heating, ventilation, hot utility water and built-in lighting systems.

The value of total primary energy is calculated according to the following equation:

$$Q_P = Q_{P,H} + Q_{P,W} + Q_{P,C} + Q_{P,L} \text{ [kWh/year]} \quad (5)$$

Two ratios are the final effect of the calculations:

– requirement for final energy EK :

$$EK = (Q_{K,H} + Q_{K,W})/A_f \text{ [kWh/m}^2\text{/year]} \quad (6)$$

– requirement for primary energy EP :

$$EP = Q_p/A_f \text{ [kWh/m}^2 \cdot \text{year]} \quad (7)$$

A_f – area of regulated temperature rooms (heated or cooled) [m^2].

Value EP , which is obtained after making a number of calculations, is compared with reference values determined according to the Ordinance of the Minister of Infrastructure of 12 April 2002 concerning technical conditions which must be complied with by buildings and their location (Dz.U. nr 75 poz. 690) and the Ordinance of the Minister of Infrastructure of 6 November 2008 amending the ordinance concerning technical conditions which must be complied with by buildings and their location (Dz.U. nr 201 poz. 1238).

The aim of energetic certificates is to stimulate the development of energy-saving building engineering supplied by renewable fuels of low emission of environmentally harmful chemical compounds. The type of fuel has an influence on the value of the non-renewable primary energy input ratio and thus on the value of indices EK and EP . The lower the EP value, the more an object is estimated as energy saving, emitting less harmful chemical substances to the atmosphere

Characterization of an object

A simulation has been carried out for a building object located in Szczecin, in a medium shaded area situated on the edge of a residential area of detached houses. It is an inner one-family segment of a terraced house. The construction

of the building is traditional, made of brick with reinforced concrete foundation, a gable roof based on a traditional rafter framing, covered with cement tiles on wooden laths. The body of the building is complemented by a one-car, heated garage, the roof over the garrage is used as a terrace. A 4-person family lives in the building. The construction of this building was started in 2003, and finished in 2005. The building was put into service in 2006.

A gas two-run furnace with an open combustion chamber of the power of 24 kW is the source of heat. It is controlled by a room controller placed on the ground floor. No hot utility water container and no circulation. Temperature of hot water at the drawing valves 55°C. Central heating and hot utility water conduits are made of plastics conducted under floors, insulated according to the requirements of the Technical Conditions. Natural gas with a high methane content ($w_i = 1,1$) constitutes fuel in actual state. The building is equipped with a natural – gravitational ventilation system, without a leak proof test.

Typical PCV windows with a double-pane pack of a declared heat-transfer coefficient of $U = 1,1 \text{ W/m}^2 \cdot \text{K}$ were used.

A layer entrance door complying with the requirement of maximum heat-transfer coefficient $U_{\max} = 2,6 \text{ W/m}^2 \cdot \text{K}$. Garage door designed for non-heated garages is improperly additionally protected from the cold.

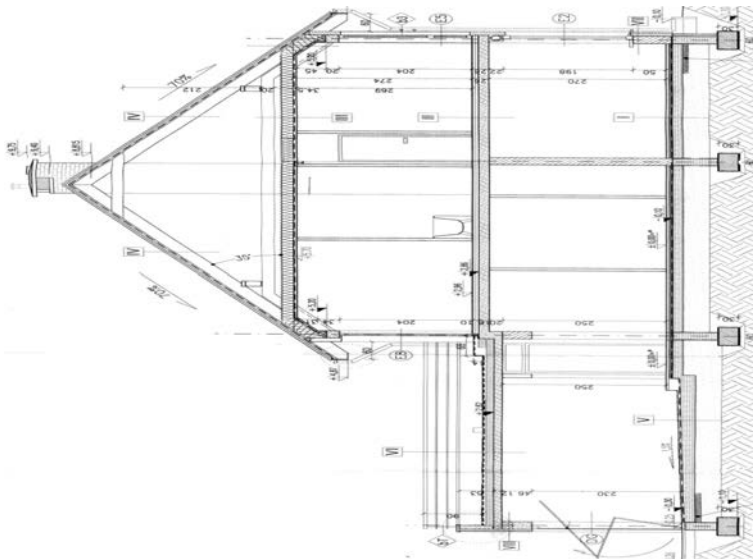


Fig. 2. Cross-section of the estimated building

Source: design documentation made available by the owner of the building

Basic technical parameters of the building

- outer cubature: 689 m³;
- ventilated cubature: 443 m³;
- heated area (with controlled temperature): 164.2 m²;
- building area: 111.4 m².

Table 1

List of rooms in the estimated building

Number/Name of room	Design temperature $\theta_{\text{int},i}$ [°C]	Room area A_i [m ²]	Inner cubature V_i [m ³]
1 WC	20.00	1.31	3.55
2 Charring room / Drying room	20.00	5.31	14.34
3 Office	20.00	12.60	34.02
4 Sitting room	20.00	30.07	81.19
5 Hall	20.00	13.93	37.62
6 Kitchen	20.00	5.43	14.66
7 Vestibule	16.00	4.54	11.34
8 Individual garage	5.00	18.45	50.92
10 Sitting room	20.00	22.70	61.06
11 Bedroom W	20.00	16.00	43.03
12 Bedroom E	20.00	13.89	37.36
13 Hall	20.00	12.01	32.32
14 Bathroom	24.00	7.99	21.50
Total		164.23	442.91

Source: authors' data

The outer walls are made of PHOROTERMU 25 on cement and lime mortar, additionally protected from cold by foamed polystyrene plates EPS 70-040 FASADA (12 cm), with a thin-layer acrylic elevation plaster outside, plastered with gypsum plaster inside.

The construction of the floor consists of: polyethylene sheeting, cement floor (4 cm), foamed polystyrene plate EPS 200-036 FLOOR (6 cm), insulating asphalt tar (2 cm), concrete of mean density of 1800 kg/m³ (15 cm) and sand bed (30 cm).

The construction of the roof over the functional attic – wooden, rafter and collar beam, additionally protected from cold by mineral wool (20 cm), covered by plane tiles.

The analysis of the present state

The collected data were introduced into the ArCadia Thermo PRO 2.4 programme, educational version. Based on the calculations, the value of the requirement for primary energy at the present state is: $EP = 153,9 \text{ kWh/m}^2 \cdot \text{year}$, with the reference value according to the Technical Conditions of 2008: $124,24 \text{ kWh/m}^2 \cdot \text{year}$ for a newly built building.

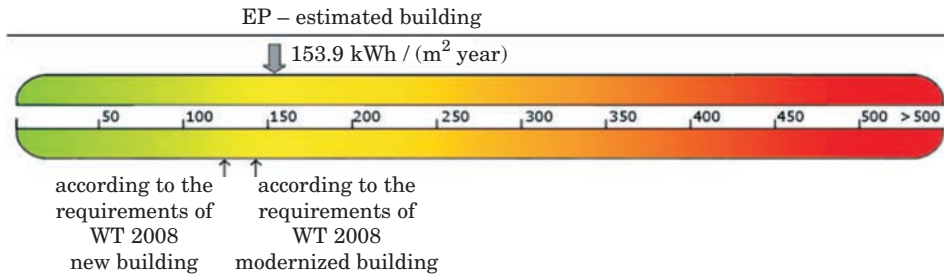


Fig. 3 Value of the non-renewable primary energy input for the estimated building
Source: ArCadia Thermo PRO, educational version, Intersoft)

The value of final energy for the present state and the amount of fuel necessary to heat and prepare hot utility water for standard assumptions is presented below.

Table 2

Value of final energy for the present state

Type of fuel – central heating	Share %	$\eta_{H,tot}$	H_u	Unit	$Q_{K,H}$ [kWh/year]	Fuel consumption B	Unit
Fuel – natural gas	100.0	0.73	9.97	kWh/m ³	15645.4	1569.2	m ³ /year
Type of fuel – hot utility water	Share %	$\eta_{W,tot}$	H_u	Unit	$Q_{K,W}$ [kWh/year]	Fuel consumption B	Unit
Fuel – natural gas	100.0	0.42	9.97	kWh/m ³	5735.1	575.2	m ³ /year

H_u – calorific value

Source: authors' data, based on ArCadia Thermo PRO, educational version, Intersoft

Alternative variants – a comparison of the EP value and the amount of fuel

- For comparison, the following have been suggested as alternative fuels:
- central heating and hot utility water – liquefied petroleum gas ($w_i = 1.1$)
 - variant I,

- central heating – hard coal ($w_i = 1.1$), hot utility water – liquefied petroleum gas ($w_i = 1.1$) – variant II,
- central heating – biomass ($w_i = 0.2$), hot utility water – liquefied petroleum gas ($w_i = 1.1$) – variant III,
- central heating and hot utility water – electric energy ($w_i = 3.0$) – variant IV.

The source of heat for heating and preparing hot utility water in variant I is a condensation boiler up to 50 kW (for central heating with parameters 70/55°C).

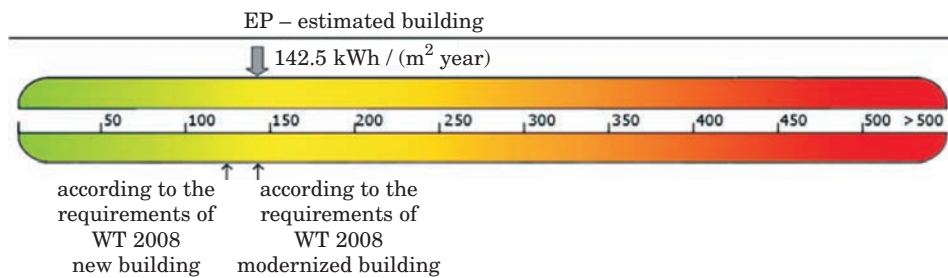


Fig. 4 Value of non-renewable primary energy input for variant I
Source: ArCadia Thermo PRO, educational version, Intersoft

Table 3

Value of final energy for variant I

Type of fuel – central heating	Share %	$\eta_{H,tot}$	H_u	Unit	$Q_{K,H}$ [kWh/year]	Fuel consumption B	Unit
Fuel – liquefied petroleum gas	100.0	0.75	6.65	kWh/m ³	15115.4	2273.0	m ³ /year
Type of fuel – hot utility water	Share %	$\eta_{W,tot}$	H_u	Unit	$Q_{K,W}$ [kWh/year]	Fuel consumption B	Unit
Fuel – liquefied petroleum gas	100.0	0.53	6.65	kWh/m ³	4562.0	686.0	m ³ /year

Source: authors' data, based on ArCadia Thermo PRO, educational version, Intersoft

In variant II, coal boiler produced after 2000 was assumed as a heat source for heating while the source of hot utility water was maintained from variant I.

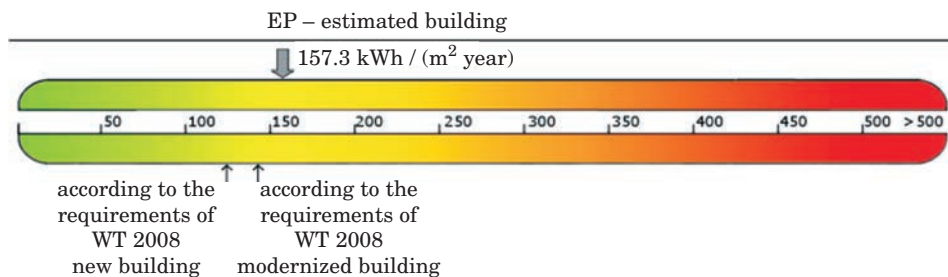


Fig. 5 Value of non-renewable primary energy input for variant II
Source: ArCadia Thermo PRO, educational version, Intersoft

Table 4

Value of final energy for variant II

Type of fuel – central heating	Share %	$\eta_{H,tot}$	H_u	Unit	$Q_{K,H}$ [kWh/year]	Fuel consumption B	Unit
Fuel – hard coal	100.0	0.66	7.70	kWh/kg	17327.4	2250.3	kg/year
Type of fuel – hot utility water	Share %	$\eta_{W,tot}$	H_u	Unit	$Q_{K,W}$ [kWh/year]	Fuel consumption B	Unit
Fuel – liquefied petroleum gas	100.0	0.53	6.65	kWh/m ³	4562.0	686.0	m ³ /year

Source: authors' data, based on ArCadia Thermo PRO,educational version, Intersoft

In variant III, biomass boiler, wood fired, with manual service of the power up to 100kW was assumed as the heat source for heating while the source of hot utility water was maintained from variant I.

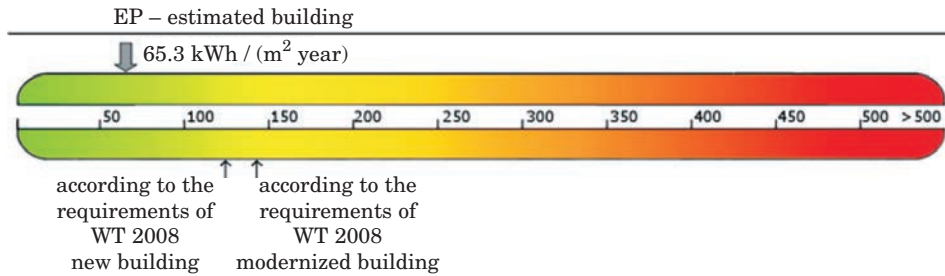


Fig. 6 Value of non-renewable primary energy input for variant III

Source: ArCadia Thermo PRO, educational version, Intersoft

Table 5

Value of final energy for variant III

Type of fuel – central heating	Share %	$\eta_{H,tot}$	H_u	Unit	$Q_{K,H}$ [kWh/year]	Fuel consumption B	Unit
Fuel – biomass	100.0	0.58	4.28	kWh/kg	19734.0	4610.8	kg/year
Type of fuel – hot utility water	Share %	$\eta_{W,tot}$	H_u	Unit	$Q_{K,W}$ [kWh/year]	Fuel consumption B	Unit
Fuel – liquefied petroleum gas	100.0	0.53	6.65	kWh/m ³	4562.0	686.0	m ³ /year

Source: authors' data, based on ArCadia Thermo PRO,educational version, Intersoft

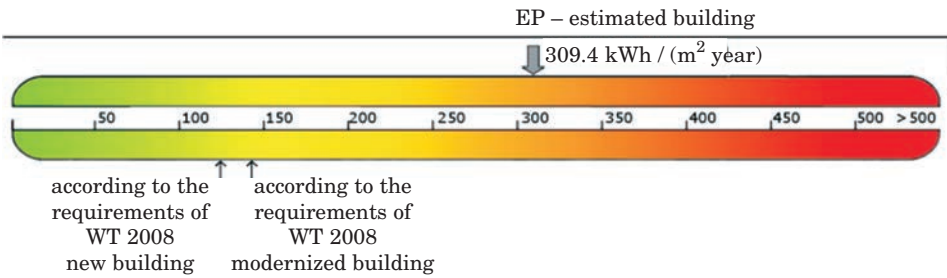


Fig. 7. Value of non-renewable primary energy input for variant IV

Source: ArCadia Thermo PRO, educational version, Intersoft

Table 6

Values of final energy for variant IV

Type of fuel – central heating	Share %	$\eta_{H,tot}$	H_u	Unit	$Q_{K,H}$ [kWh/year]	Fuel consumption B	Unit
Electric energy – mixed production	100.0	0.92	1.00	kWh/kWh	12339.1	12339.1	kWh/year
Type of fuel – hot utility water	Share %	$\eta_{W,tot}$	H_u	Unit	$Q_{K,W}$ [kWh/year]	Fuel consumption B	Unit
Electric energy – mixed production	100.0	0.60	1.00	kWh/kWh	4014.5	4014.5	kWh/year

Source: authors' data, based on ArCadia Thermo PRO,educational version, Intersoft

Thus, the value of primary energy changes depending on the fuel supplying the central heating and hot utility water systems.

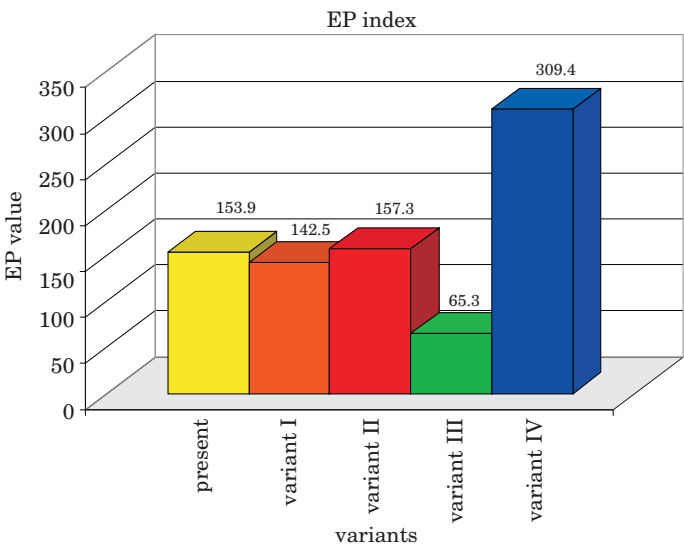


Fig. 8. Comparison of primary energy values depending on the applied combination of fuels

Source: authors' data

The influence of the fuel type on the emission of pollutants to the atmosphere

Significant changes in legal provisions concerning air protection were introduced in 2001. The basic legal act is the Environmental Protection Act of 27.04.2001 (Dz.U. nr 61, poz. 627, 2001). The guiding principle of this law is:

- Maintaining the level of substances in the air below the levels permissible for them or at least at these levels,
- Reducing the levels of substances in the air at least to the permissible ones when they are not met.

It is consistent with legal acts of the European Union expressed in Directive 96/62/EC of 27.09.1996 concerning the air quality estimation and management.

In order to simulate the amounts of pollutants emitted to the environment depending on the variant of adopted fuel supplying central heating and hot utility water, a cover plate Ecological effect of the programme ArCadia Thermo PRO educational version was used; based on introduced data, it calculates the amount of pollutants emitted to the atmosphere – SO₂, NO_x, CO, CO₂, dust, soot, B-a-P. Such an analysis is necessary when we do audit for EU subsidies or the Environmental Protection Fund. At the stage of drawing up a certificate of energetic characteristic, it makes it possible to estimate the effect of the adopted system of heating and preparing hot utility water on the environment on the basis of the amount of pollutants. The calculations of the pollutants emission are based on the information and instruction materials of the Ministry of Environmental Protection, Natural Resources and Forestry 1/96 "Indices of the emission of polluting substances introduced into the air from the processes of energetic combustion of fuels". The results below also include auxiliary electric defices necessary for the operation of the central heating and hot utility water system.

Table 7

Emission of pollutants

Total emission in the building – present state	Unit	SO ₂	NO	CO	CO ₂	DUST	SOOT	B-a-P
	kg/year	533.2464	4.0927	1.1763	4797.7392	0.9111	0.0016	0.0000
Total emission in the building – variant I	Unit	SO ₂	NO _x	CO	CO ₂	DUST	SOOT	B-a-P
	kg/year	533.2464	1.3478	0.4043	585.9850	0.8790	0.0016	0.0000
Total emission in the building – variant II	Unit	SO ₂	NO _x	CO	CO ₂	DUST	SOOT	B-a-P
	kg/year	576.4525	3,5981	101.6686	5086.6211	24.5073	0.7892	0.0315
Total emission in the building – variant III	Unit	SO ₂	NO _x	CO	CO ₂	DUST	SOOT	B-a-P
	kg/year	536.4278	93.4246	5.7989	585.9850	4.0604	0.0016	0.0000
Total emission in the building – variant IV	Unit	SO ₂	NO _x	CO	CO ₂	DUST	SOOT	B-a-P
	kg/year	15415.0895	38.9612	11.6884	16939.6588	25.4095	0.0457	0.0009

Source: authors' data, based on ArCadia Thermo PRO,educational version, Intersoft

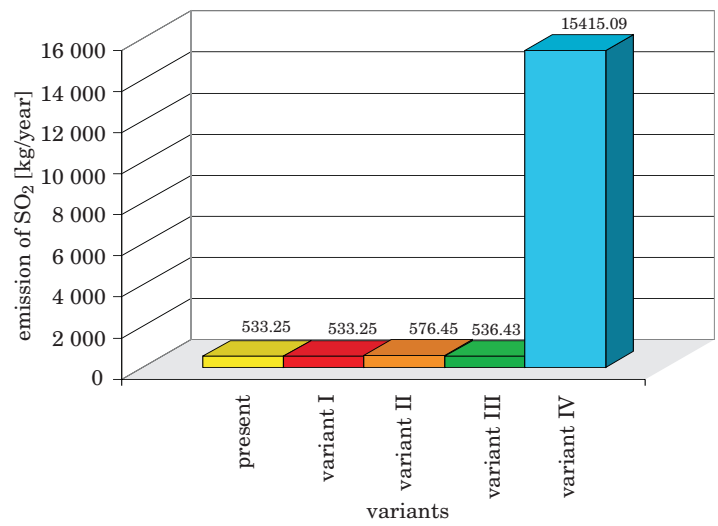


Fig. 9. Comparison of emission of SO₂ based on the data from table 7
Source: authors' data

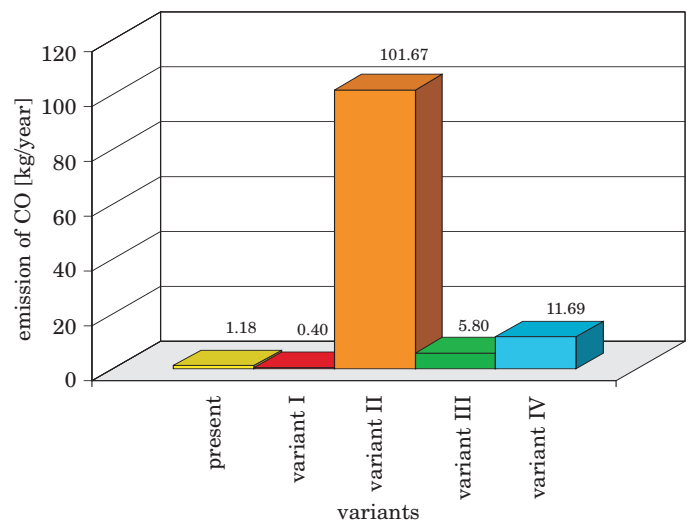


Fig. 10. Comparison of emission of CO based on the data from table 7
Source: authors' data

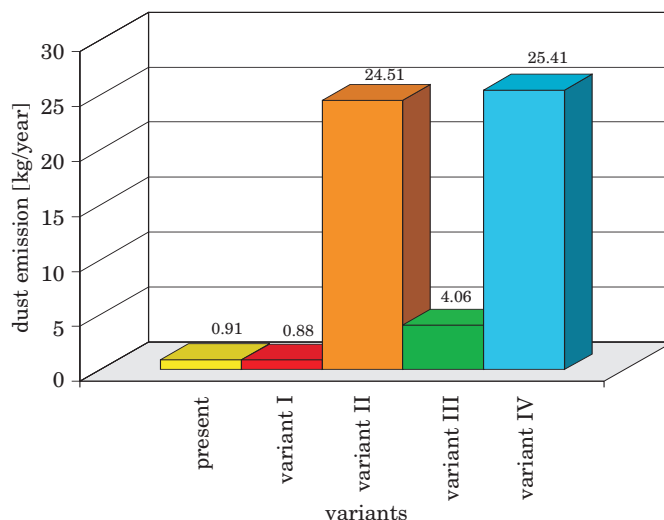


Fig. 11. Comparison of emission of dust based on the data from table 7

Source: authors' data

Conclusion

On the grounds of the analysis it can be concluded that the type of fuel has a significant effect on the value of the index of non-renewable primary energy input. The lower this value – the more energy-saving the building is. With an increase in primary energy the object becomes less attractive for the owner. The value obtained for every newly-built or modernized building should meet reference values specified in the Technical Conditions. The simulation has confirmed that the building in which electric energy from mixed production is used for heating and preparing hot utility water is the most costly in use. On the other hand, it is possible to build a house in which biomass energy is used for heating. With the application of the most frequently used fuels: liquefied petroleum gas, natural gas and hard coal, the primary energy value is maintained at a similar level.

It has been proved in the simulation that the use of electric energy from mixed production for supplying central heating and hot utility water is the least ecological one in terms of emission of pollutants to the atmosphere.

Accepted for print 15.07.2010

References

- Directive 2002/91/EC concerning the energetic characteristic of buildings of 16 December 2002.
- Directive 96/62/EC of 27.09.1996 concerning the estimation and management of air quality.
- Ustawa z dnia 7 lipca 1994 roku – Prawo budowlane (Dz.U. 1994 nr 89 poz. 414 z późn. zm.).
- Ustawa z dnia 27.04.2001 roku – Prawo ochrony środowiska (Dz.U. nr 61, poz. 627 z 2001 r. z późn. zm.).
- Rozporządzenie Ministra Infrastruktury z dnia 12 kwietnia 2002 r. w sprawie warunków technicznych, jakim powinny odpowiadać budynki i ich usytuowanie (Dz.U. 2002 nr 75 poz. 690 z późn. zm.).
- Rozporządzenie Ministra Infrastruktury z dnia 6 listopada 2008 r. w sprawie metodologii obliczania charakterystyki energetycznej budynku stanowiącej samodzielną całość techniczno-użytkową oraz sposobu sporządzania i wzorów świadectw ich charakterystyki energetycznej (Dz.U. 2008 nr 201 poz. 1240).
- Materiały informacyjno-instruktarzowe MOŚZNiL 1/96 „Wskaźniki emisji substancji zanieczyszczających wprowadzanych do powietrza z procesów energetycznego spalania paliw”.
- Materiały informacyjno-instruktażowe MOŚZNiL 1/96 „Wskaźniki emisji substancji zanieczyszczających wprowadzanych do powietrza z procesów energetycznego spalania paliw”.

INFLUENCE OF GREEN AREAS ON URBAN LANDSCAPE

Joanna Agnieszka Pawłowicz

Chair of Civil Engineering and Building Constructions
University of Warmia and Mazury in Olsztyn

Key words: urban landscape, town planning, urban green areas.

Abstract

Nature plays an important role in proper development of a town. Consequently, town planners should realise that there are certain limits which must not be crossed or else the balance between particular elements of urban space may be disturbed.

Town planners, whose aim is to maintain the equilibrium, especially at the point of contact between development – nature – quality of human life, should be interested in buildings, their purpose or street layouts as much as in green areas, which are an indispensable part of a town's design, whichever form it takes, be it a single tree, a green square, a park or a forest.

WPLYW ZIELENI NA KSZTAŁTOWANIE KRAJOBRAZU MIEJSKIEGO

Joanna Agnieszka Pawłowicz

Katedra Budownictwa i Konstrukcji Budowlanych
Uniwersytet Warmińsko-Mazurski

Słowa kluczowe: krajobraz miejski, urbanistyka, zielen miejska.

Abstrakt

Duże znaczenie w prawidłowym rozwoju miasta ma przyroda. Oznacza to, że urbanista powinien sobie zdawać sprawę z istnienia granic, których nie należy przekraczać. Ich naruszenie może się wiązać z zachwianiem równowagi między poszczególnymi elementami przestrzeni miejskiej.

Urbaniści dążący do zachowania równowagi, zwłaszcza na styku: rozwój – natura – jakość życia człowieka, powinni się zainteresować nie tylko zabudową, jej przeznaczeniem, czy układem ulic, lecz także roślinnością, która jest nieodłączną częścią kompozycji miasta, bez względu na to, w jakiej formie występuje: jako pojedyncze drzewo, skwer, park czy nawet las.

When town planners use the term “urbanised area”, they most often refer it to a town, i.e. an area where the space has been designed, buildings and other constructions have been raised alongside necessary technical infrastructure, for example streets and pavements, so as to provide local residents with the best possible conditions for life and work.

The term “urban green areas” has a broad meaning, encompassing all types of areas within a town which are naturally or artificially (i.e. planted by man) covered with plants.

Urban green areas also include groups of trees, woods and open water bodies found within the administrative borders of a town (Fig. 1).



Fig. 1. Olsztyn – the Municipal Forest and a foot path along Długie Lake. Summer 2004
Source: the author's photo.

The natural environment determines an ecologically oriented town design process, which means that when shaping the space a town planner should realise that there are certain limits not to be crossed. Breaching these limits can disturb the balance between particular elements of animate and inanimate nature.

The ecological aspect of town designing is also connected with sustaining the balance, especially at the point of contact between spatial development, nature and quality of human life. Eco-friendly civil engineering is closely connected with planning both buildings and their purpose as well as the surrounding space. When properly shaped, the surrounding space has good influence on people's well-being and life comfort; carefully designed composition of green areas, be it a single tree, a green square, a park or a forest, gives aesthetic pleasure (Fig. 2).



Fig. 2. Chelmino – a park in a former castle moat. Autumn 2009

Source: the author's photo.

Ecology in town planning manifests itself in such aspects as taking great care to ensure that a town can “breathe”. Developed town areas are composed of different types of urban fabric in a grid of roads and streets, which can cause accumulation of exhaust fumes and generation of smog (Fig. 3). A good plan of the network of streets and how they developed can create conditions for their natural airing. This effect can be achieved by creating open spaces, where air can travel freely from innertown and suburban green areas, for example forests, from which air is “pumped” into the centre of the town.

Another good solution is to plant low- and high-growing plants around buildings, squares and communication passages because such green areas can protect residents from noise and exhaust fumes. Besides, groups of trees and shrubs have a recreational function, making the urban landscape more attractive, which has great influence on the health and well-being of local communities (Fig. 4).

Reflecting on the ecological approach to the development of urban areas, one should keep in mind the fact that it is not always possible to interfere with the present plan of streets and buildings. Moreover, the existing green areas can be threatened with elimination simply because they grow in attractive sites in a town, which can attract developers interested in purchasing and developing such land plots. For the town's authorities, a prospect of selling some land



Fig. 3. Kraków – Nowa Huta. Insulating green plants along a street
Summer 2008. Source: the author's photo.



Fig. 4. Olsztyn – green areas near the Old Town. Spring 2009
Source: the author's own photo.

can also be tempting because land in the town can be expensive owing to the existing technical infrastructure. As a result, we often experience shortage of available land to create a park or at least a small green square or a lawn.



Fig. 5. A creeper on a tree. Summer 2004

Source: the author's photo.

In order to maintain proper proportions between land covered by plants and a developed area, one should first of all ensure that green areas are integrated with the town's structure, so as to preserve the symbiosis between urban tissue and elements of animate nature. A high ratio of biologically active surface area can also be attained by arranging plants in flower beds on lawns, plants on balconies and terraces, as well as growing climbing plants on walls, pillars and other elements of the urban landscape, which can support and help to exhibit plants (Fig. 5).

Climbing plants enable us to spread ecologically green plants over large areas of walls of existing buildings at low technological outlay. This eco-friendly approach to shaping urban space makes it possible to improve microclimate and enables plants and animals to grow and develop even in highly urbanised terrains (Fig. 6).



Fig. 6. Olsztyn – the university campus in Kortowo – a facade of a building overgrown with creeper
Spring 2009

Source: the author's photo.

Green plants climbing walls of buildings can also help to reduce emission of heat, the so-called oven effect, which appears when elements of a building, due to their high capacity of absorption, accumulate large amounts of heat during the daytime, then emitted in the evening.

With tree and shrub plantings it is possible to air built areas and to maintain optimum humidity conditions in a town. Plantings also help to improve soil and water conditions in a town.

Overgrown with green plants, the ground is more stable and resistant to erosion. Roots of plants maintain the stability of the ground. They also help to absorb precipitation water from the surface of land, which prevents groundwater logging and local floods, especially in land depressions.

Urbanised area undergoes transformations triggered by changes in functions of a town expected by local communities. Modern civil engineering practice has pushed nature outside the town's boundaries. Fortunately, as it is now fashionable to be eco-friendly, which means that today town residents expect the urban landscape to be formed not only of such materials as concrete, steel, glass or tarmac, but also with components of animate and inanimate nature. Moreover, the use of natural materials for constructing certain elements of urban structure is sometimes imposed by the location itself. For

example, building objects of garden architecture in parks or woods using timber logs is a natural and obvious choice (Fig. 7).



Fig. 7. Olsztyn – a recreational square in the Municipal Forest. Winter 2009
Source: the author's own photo.

It is undisputable that green areas are an important component of an eco-friendly management of urban space, and the question of how they are handled is associated with our wish to live comfortably, in accord with the natural environment and principles of aesthetics.

Accepted for print 20.08.2010

References

- CHMIELEWSKI J.M. 2001. *Teoria urbanistyki w projektowaniu i planowaniu miast*. Oficyna Wydawnicza Politechniki Warszawskiej, Warszawa.
- ŁUCZYŃSKA-BRUZDA M. 1999. *Elementy naturalne środowiska*. Politechnika Krakowska im. T. Kościuszki, Kraków.
- PEŃSKI W. 1999. *Zarządzanie zrównoważonym rozwojem miast*. Arkady, Warszawa.
- BAUMANN R. 1991. *Domy w zieleni*. Arkady, Warszawa.

ANTENNA PHASE CENTER VARIATIONS CORRECTIONS IN PROCESSING OF GPS OBSERVATIONS WITH USE OF COMMERCIAL SOFTWARE

Karol Dawidowicz

Institute of Geodesy
University of Warmia and Mazury in Olsztyn

Key words: GPS antenna, phase center variations, GNSS data processing.

A b s t r a c t

It is well known that magnitude of antenna phase center variations (PCV) can reach several centimeters. Unfortunately part of commercial GPS post-processing software does not include corrections related to antenna PCV. This paper presents a proposal of a subroutine which introduces PCV corrections to code and phase observations basing on ANTEX file and RINEX observations and navigation files. This approach has been tested using GPS data collected at four measurement points. Three different types of antenna were used in observations. Observation processing was done with Ashtech Solutions and TopconTools software. The results of calculations show, that the proposed subroutine can be successfully used in commercial software which does not include such correction algorithms. The subroutine can also serve to verify antenna PCV corrections algorithms in commercial software where there is often no possibility of looking into applied algorithms.

POPRAWKI DO ZMIENNOŚCI POŁOŻENIA CENTRUM FAZOWEGO ANTENY W OPRACOWANIU OBSERWACJI GPS OPROGRAMOWANIEM KOMERCYJNYM

Karol Dawidowicz

Instytut Geodezji
Uniwersytet Warmińsko-Mazurski w Olsztynie

S ł o w a k l u c z o w e: antena GPS, zmienność położenia centrum fazowego, opracowanie obserwacji GNSS.

A b s t r a k t

Powszechnie wiadomo, że zmiany położenia centrum fazowego anteny (phase center variations – PCV) mogą osiągać wartość kilkunastu centymetrów. Niestety, część programów komercyjnych do opracowania obserwacji GPS nie zawiera poprawek związanych z PCV. W artykule przedstawiono

propozycję podprogramu, który na podstawie pliku ANTEX oraz obserwacyjnych i nawigacyjnych plików RINEX wprowadza poprawki PCV do obserwacji kodowych i fazowych. Podejście zostało przetestowane na podstawie danych GPS zebranych w czterech punktach pomiarowych. W pomiarach wykorzystano trzy różne typy anten. Obserwacje opracowano z wykorzystaniem programu Ashtech Solutions i TopconTools. Wyniki obliczeń dowodzą, że proponowany podprogram może być skutecznie wykorzystany jako uzupełnienie programu firmowego nie mającego takich poprawek. Podprogram może również służyć do weryfikacji zastosowanych poprawek PCV w programach komercyjnych, w których często brakuje wglądu w zastosowane algorytmy.

Introduction

A fundamental role of GPS antenna is filtering, amplification and changing electromagnetic waves sent from satellites to electric current, which can be transmitted through electronic systems of the receiver. The electrical antenna phase center is the point in space where GPS signal is received. The actual location where the signal is received, however, varies depending on the direction of the incoming GPS signal. For practical needs a mean position of the electrical antenna phase center (MPC) is determined. The height above the physical network point, at which the antenna is situated, is usually measured to the antenna reference point (ARP). The IGS has defined the ARP as the intersection of antenna's vertical axis of symmetry with the bottom of the antenna. The antenna phase center offset (PCO) is defined as the difference between the ARP and the MPC. When comparing the electrical antenna phase center of an individual measurement with the mean electrical antenna phase center, a deviation arises. These deviations are referred to as antenna phase center variations (PCV). A review of the antenna phase center variations problem can be found e.g. in BRAUN et al. 1993, GEIGER 1998, HOFMANN-WELLENHOF et al. 2008, ROCKEN 1992, SCHMID et al. 2005, SCHMITZ et al. 2002, SCHUPLER, CLARK 1991.

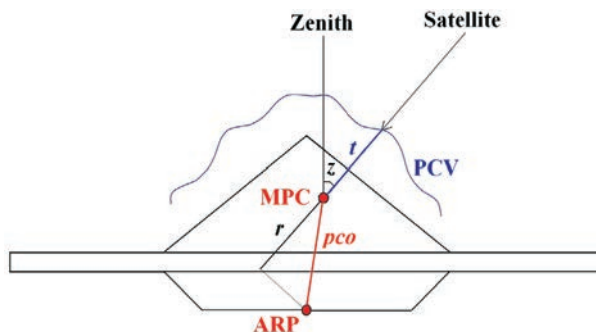


Fig. 1. Diagram of the ARP, MPC and PCV location

Spatial relations between ARP, MPC and PCV points are determined in the calibration process. Three major methods are presently used to determine variations of the phase center for GPS receiver antennas and create their models:

- relative field calibrations,
- anechoic chamber measurements,
- absolute field calibrations.

In relative field calibrations PCO and PCV of one antenna are determined with respect to another, the reference antenna. Both antennas are set up on very short baseline with accurately known coordinates. The GPS measurements are used to estimate the position of the phase center depending on the elevation (or elevation and azimuth) of the measured satellites.

Anechoic chamber measurements allow the absolute antenna phase center variations obtained by measuring how the phase of an artificial GPS signal is changed when the antenna (put into an anechoic chamber) is rotated and tilted.

Absolute field calibrations are performed using a high precision robot which rotates and tilts the antenna. In the same time the reference antenna is kept fixed.

These methods are described in detail e.g. in FALKO et al. 1998, MADER 1999, ROTHACHER 2001, ROTHACHER, MADER. 1996, WÜBBENA et al. 1997.

Antenna models are produced in several scientific centers. Well-known examples are: US National Geodetic Survey (IGS, 2008) and Geo++GmbH (Geo++, 2008). In NGS are created relative antenna calibrations models, where all antenna offsets and phase center variations are computed with respect to the AOAD/M-T antenna. Absolute NGS antenna calibrations models are created in such a way that the relative antenna offsets and phase center variations that the National Geodetic Survey has computed have been added to the absolute values for AOAD/M-T antenna defined by Geo++. Geo++ antenna calibrations models are created by the automated absolute field calibrations. There are some differences between antenna corrections files created in these two centers. For example in NGS all values are given in mm and in Geo++ in meters. Additionally PCV values in Geo++ file have an opposite sign to values in NGS file.

Antenna phase center variations can have an amplitude of several centimeters. The effect is more crucial in the elevation dependent component although azimuth dependent effects can become important over very long baselines. Ignoring these phase center variations can lead to serious (up to 10 cm) vertical errors (ROTHACHER, MADER 1996, MADER 1999).

In the last years research groups started to realize that not only the receiver, but also the satellite antennae show phase center variations. At the

moment, several IGS analysis centers are working on the generation of best possible satellite antenna correction values (ROTHACHER et al. 2002, SCHMID et al. 2005).

In some commercial post-processing software, the solution to the antenna phase center variations problem is simplified. For example in Ashtech Solutions 1.0 there is no possibility to account for the type of antenna used in measurements (*Magellan...* 1998). In Ashtech Solutions 2.0 there is only the possibility to reduce the antenna phase center offsets, but not the antenna phase center variations (*Thales...* 2002). Only the newest versions of so-called commercial software are equipped with models of antenna phase center variations corrections. An example of that is GNSS Solutions (presently replacing Ashtech Solutions) or Topcon Tools in which the US National Geodetic Survey's absolute antenna calibration models are applied by default from version 6.11 (*Topcon...* 2006). Unfortunately even these software products are not equipped with models of satellite antenna phase centers variations, which is very important when using precise orbit in observation processing. So when we use commercial software to observations processing, particularly for the determination of heights, we should pay particular attention to how the phase center variations problem was solved.

The paper presents a proposal of a subroutine which introduces PCV corrections to code and phase observations. Observations prepared in such way can be then processed with use of any commercial software. Another advantage of presented procedure is the possibility to use antenna calibration files from all scientific centers where they are created. The subroutine also lets to look into every stage of the correction process which is not guaranteed in commercial software.

The subroutine allows correction of observation by using information about the real position of antenna phase center which is a function of direction of incoming GPS signals. This information, obtained as a result of antenna calibration is available, for example, on International GNSS Service website in ANTEX format text files. In any ANTEX file, profiles of antenna are defined by three so-called offsets ("north", "east" and "up") and changes of the antenna phase center position as a function of incoming signal elevation and (at present for some antennas) also as a function of azimuth. These values are given in a five-degree interval: from 0° to 80° (90°) for elevation and from 0° to 360° for azimuth.

The proposed subroutine, written in MATLAB programming language, introduces (Fig. 2) corrections to code and phase observations basing on the antenna phase center positions and RINEX observation and navigation files. The satellites coordinates on observational epoch are calculated in the first stage. Then, elevation and azimuth of each satellite are calculated using

satellites positions data and approximate coordinates of the receiver. The next stage is reading the proper data from the antenna phase center position file. These values are then used to calculate the corrections to code and phase observations. The subroutine can make calculations using antenna calibration results from all centers where they are created. The observations can be reduced to MPC and to ARP.

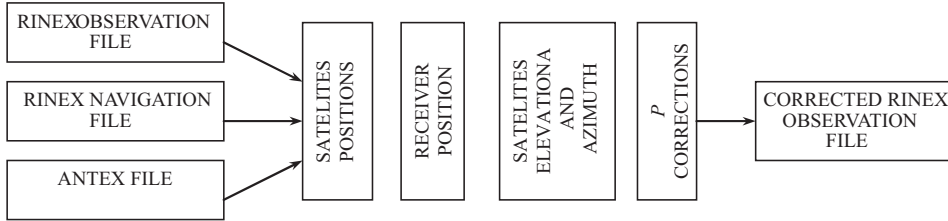


Fig. 2. Diagram of corrected RINEX observation file calculation with use of the proposed subroutine

Corrections to ARP are computed using below formula (Fig. 1):

$$p = r + t = (pco)\cos z + t \quad (1)$$

where:

p – correction to the observation; r – correction of the phase center position as function of pco and elevation of the satellite; t – correction of the phase center position as function of the satellite’s elevation or elevation and azimuth; pco – position of phase center in relation to ARP (“up” offset); z – elevation of the satellite.

In the present version of the subroutine, the estimation of r value is simplified because only the “up” offset is taken under consideration in calculations. Such approximation does not influence the results in an essential way, because comparing to “up” offset, the other two offsets are very small and their values are mostly less than 1mm and do not exceed several millimeters for any antenna. Because the value of t is expressed in five degrees interval, its proper value (for current elevation or elevation and azimuth) is calculated by a well known linear interpolation formula:

$$t = t_1 + (e - e_1) \frac{t_2 - t_1}{e_2 - e_1} \quad (2)$$

where:

t – position of the phase center as a function of current satellite’s elevation or elevation and azimuth (e); t_1, t_2 – values of phase center position for e_1, e_2 satellite’s elevations or elevations and azimuths known from the ANTEX file.

The code observations are directly adjusted with corrections calculated in such way. In order to conduct phase observations, the corrections have to be converted to phase cycles. For L1 frequency, the final value of t is calculated by dividing the result obtained from equation (1) by 0,19029, and for L2 frequency by 0,24421. When observations are reduced to the MPC, correction p simply equals t value interpolated for current satellite's elevation or elevation and azimuth.

For comparison in Bernese GPS Software Version 5.0 (DACH et al. 2007), which is a sophisticated tool meeting highest quality standards for geodetic and further applications using Global Navigation Satellite Systems, antenna phase center variation correction has the following mathematical representation:

$$\Delta\phi(\alpha, z) = \Delta\phi'(\alpha, z) + \Delta r \cdot e \quad (3)$$

where:

$\Delta\phi(\alpha, z)$ – the total phase center correction in direction; α, z , α, z – azimuth and the zenith angle of the satellite line of sight; Δr – the position of the mean antenna phase center with respect to the mechanically defined antenna reference point; e – the unit vector in the direction from the receiver antenna to the satellite; $\Delta\phi'(\alpha, z)$ – the function modeling the phase center variations (two different model functions may be used in the Bernese GPS Software: piece wise linear function or spherical harmonic function).

Similar research was performed by GÓRAL and KUDRYS 2007. Ashant subroutine, described by them, worked with Ashtech binary files (b-files), and made possible to correct observations only in function of elevation of incoming GPS signal. L2 observations were reduced to MPC of L1 frequency, differently than in the subroutine proposed by the author (L1 and L2 observations can be reduced to their MPC or both observations can be reduced to ARP). In following analyses the author proposed also use different, newer versions of software to observations processing and focuses on PCV magnitude calculation and reduction when medium baselines are measured and this causes the necessity to use linear combination of observations in processing.

Methodology of studies

Measurement points

Four points situated between 53°34' and 54°00' north latitude and 20°04' and 20°27' east longitude were selected for test measurements. The longest measured baseline has about 49 km, the shortest – 25 km. The location of

proposed points causes the necessity to use linear combination in observations processing, which causes antenna phase center variations of both frequencies to appear in final results.

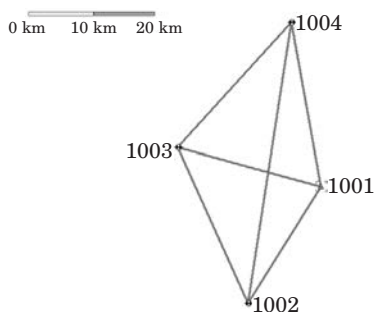


Fig. 3. Diagram of measurement points

Testing hardware and software

Three measurement sessions were conducted on the test points. The GPS observations were made by workers of Institute of Geodesy University of Warmia and Mazury in Olsztyn (research project nr 528-0302-0803). The following GPS parameters were assumed for all measurement sessions: sampling interval 10s, minimum satellite's elevation 15° , time of measurement 4 hours. Following types of antenna, presented on figure 4, were used in the measurements: ASH700228A (session 1 and 2), ASH700718A (session 2 and 3) and AOAD/M_T (session 3).



Fig. 4. Antenna used in measurements: a) ASH700228A, b) ASH700718A, c) AOAD/M_T

ASH700228A and ASH700718A are typical surveying antennas in contrast to AOAD/M_T antenna which is rather geodetic than surveying. The locations of MPC over ARP ("up" offset) for L1 and L2 frequencies for these antennas

are respectively (in millimeters): ASH700228A (61.14; 71.26); ASH700718A (68.54; 55.46); AOAD/M_T (91.24; 120.06).

Figure 5 presents comparison of the elevation dependent phase center variations for antennas used in session 2 and 3 – it is visible that they have completely different profiles.

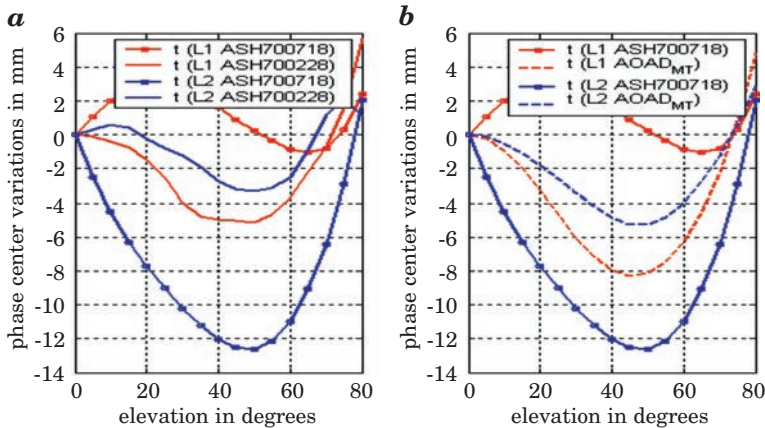


Fig. 5. Elevation dependent phase center variations: a) for antenna pair ASH700228A and ASH700718A; b) for antenna pair AOAD/M_T and ASH700718A

The aim of this paper was proposing a subroutine which, using the results of antenna phase center variation calibrations, can prepare GPS observations for processing with software which is not equipped with proper correction algorithms. An example of such software is Ashtech Solutions 1.0, which does not give any possibility of antenna type selection (*Magellan...* 1998). Topcon Tools 6.11 software was also chosen for observation processing. Topcon Tools software from version 6.11 uses the US National Geodetic Survey's absolute antenna calibration models and therefore can be used for verification of received results. The software selected assured verification of usefulness of the proposed subroutine on one hand and control of correctness of his calculations on the other.

Both chosen software types are examples of so-called commercial software. The operator has only little influence on the choice of processing options – for example processing frequency, troposphere model or ambiguity resolution strategy are beyond possibilities of selection. Automatic selection of processing frequency in chosen software looks as follows:

- 0-10 km baselines processing is L1 and L2,
- 10-30 km baselines processing is L1&L2c (ionosphere-free combination),
- 30-400 km baselines processing is wide lane.

Because using linear combination of observations causes antenna phase center variations for both frequencies to appear in final results, and processing frequency is beyond possibilities of own selection, suitable distant points locations were proposed for the measurements. The length of baselines between 25 km and 49 km causes the selection of processing frequency using linear combination.

Analysis of processing results

The GPS observations for all sessions were corrected by proposed subroutine with use of `igs_05.atx` file, which contains values of absolute elevation and azimuth dependent antenna phase center variations. Then, the corrected and the uncorrected observations were processed with two selected examples of commercial software (Ashtech Solutions 1.0 and Topcon Tools 6.11).

Point 1001 situated in Olsztyn (ASH700228A antenna on first session and ASH700718A antenna on second and third sessions), with coordinates appointed in reference to IGS LAMA station, was chosen as the reference station. Post-processing was done in the following variants:

- processing of uncorrected observations (without antenna phase center variation corrections) using Ashtech Solutions software (**AS without corrections**),
- processing of corrected observations (with antenna phase center variation corrections introduced using the proposed subroutine) using Ashtech Solutions software (**AS subroutine corrections**),
- processing uncorrected observations (without antenna phase center variation corrections) using Topcon Tools software (**TT without corrections**),
- processing corrected observations (with antenna phase center variation corrections introduced using the proposed subroutine) using Topcon Tools software (**TT subroutine corrections**),
- processing corrected observations (with use antenna phase center variation corrections available in the software) using Topcon Tools software (**TT software corrections**). Ellipsoidal heights calculated in such way were considered in further comparisons as true.

Third and fourth variants were possible because in Topcon Tools software there is an option of processing observations without using any antenna model (option “none” in the window of antenna model selection).

The ellipsoidal heights of measurement points obtained for all post-processing variants were compared on figure 6.

When the same type of antenna as on the reference station (session 1 for all points and session 2 and 3 for 1004 point) was placed on the measured point,

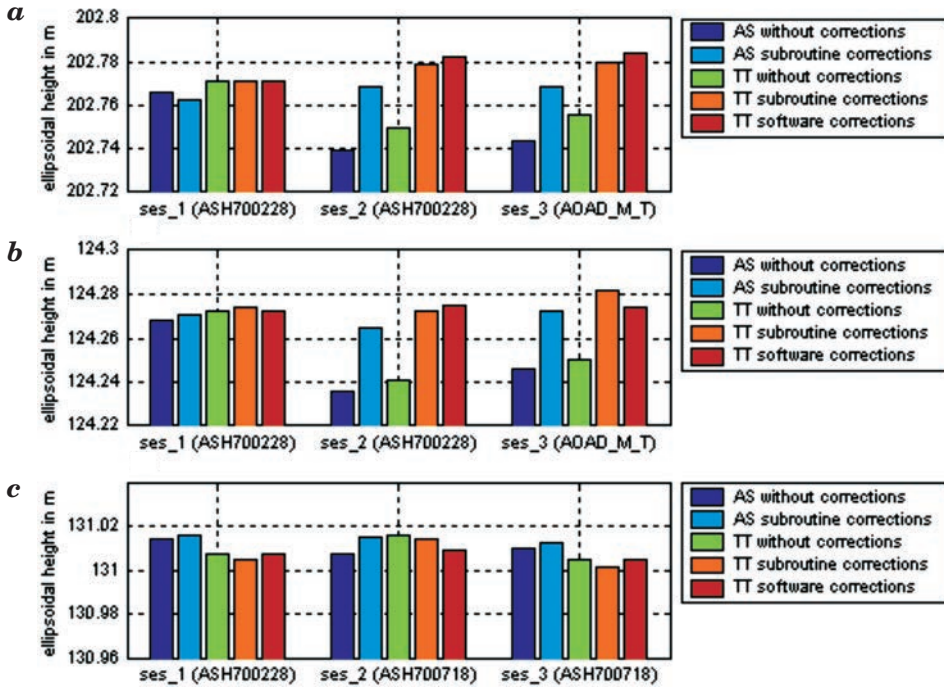


Fig. 6. Ellipsoidal height obtained for measurement points depending on the used software and used or no the antenna calibration file: a) for 1002 point; b) for 1003 point; c) for 1004 point (in brackets type of antenna used in respective sessions)

heights from all processing variants were consistent with 10 mm accuracy. Processing medium baseline, with the same type of antenna on both ends, without using PCV corrections, does not influence the results because systematic error is reduced in differential elaboration. When there was a different type of antenna on the measured point than on the reference station (session 2 and 3 for 1002 and 1003 points) it was clear that observations processing without the PCV corrections caused systematic error of about 2–3 cm. The error magnitudes are similar for antennas ASH700228A and AOAD/M_T surely because the both antennas have very similar phase center variation characteristics (Fig. 5). The heights, obtained from observations processing with use of the PCV corrections method proposed by author and with use of antenna phase center variation corrections available in Topcon Tools software, are consistent with 6mm accuracy.

In addition, preliminary analysis has been carried out concerning the effects of adoption absolute or relative antenna calibration file on height appointment. The calculations were performed again using two commercial software (Ashtech Solutions 1.0 – **AS**, Topcon Tools 6.11 – **TT**). Before

processing, GPS observations has been corrected through proposed by the author subroutine using developed by NGS (the most accessible) relative and absolute antenna calibration models. The results of these calculations are shown in Figure 7.

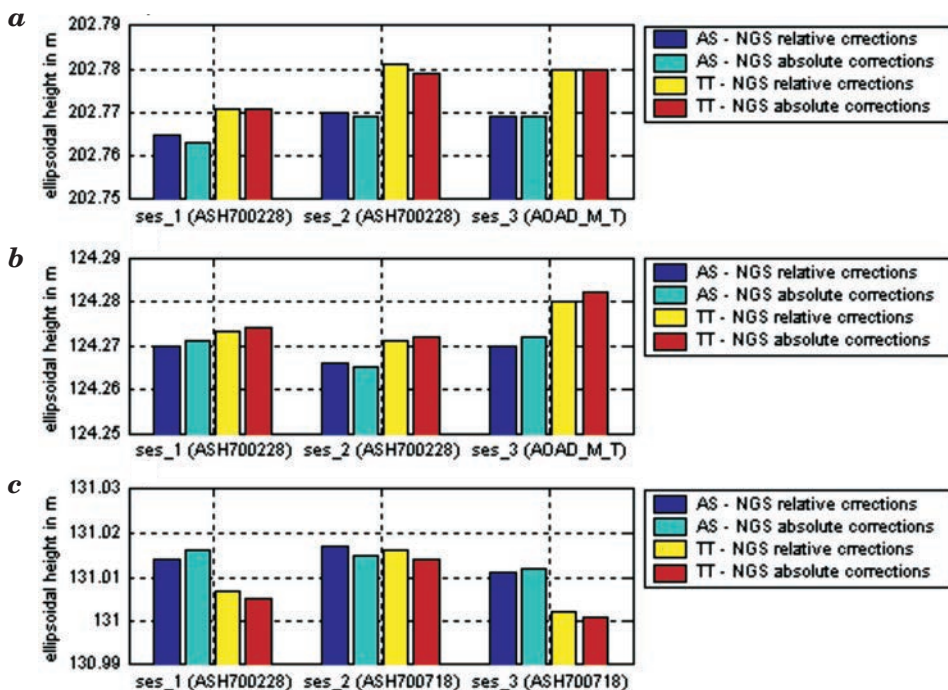


Fig. 7. Ellipsoidal height obtained for measurement points depending on the used software and the type of antenna calibration file: a) for 1002 point; b) for 1003 point; c) for 1004 point (in brackets the type of antenna used in respective sessions)

The height difference between the solution using NGS absolute and relative antenna calibration file, for the same software, in any of the cases did not exceed 2 mm. In the proposed study the use of absolute or relative antenna calibration model no effect the height appointment. Such results are not surprising because NGS absolute calibration model was created by adding the relative antenna offsets and phase center variations that the National Geodetic Survey has computed to the absolute values for AOAD/M_T antenna and all processing, presented in paper, were done with broadcast orbit.

Maybe more interesting results could give similar analyses conducted with use GPS observations on short baselines in short sessions with precise orbits and more antenna calibration models.

Conclusions

Analyses were done using GPS data collected at four measurement points with distances between them ranging from 25 km to 49 km. Such long baselines cause the necessity of conducting suitably long observational sessions. In nearest future the author plans to conduct similar analyses performed using GPS observations on short baselines in short sessions. The author also plans some modifications of the subroutine. In future the subroutine will allow corrections of observations taking satellites antenna PCV into account.

Moved analyses confirmed that the PCV problem cannot be disregarded in surveying measurement – seemingly very similar surveying antennas (ASH700228A and ASH700718A) have significantly different PCV characteristics. Using those antennas in measurements and then processing observations without PCV corrections causes a systematic vertical error of several centimeters. The results presented in this paper also show that the subroutine proposed by the author can be used in commercial software which is not equipped with PCV correction algorithms.

Accepted for print 29.06.2010

References

- Ashtech Solutions Tutorial*. Printed in USA. 1998. Magellan Corporation Ashtech Precision Products.
- Ashtech Solutions User's Guide*. Printed in USA. 2002. Thales Navigation.
- BRAUN J., ROCKEN C., MEERTENS C.M., JOHANSON J. 1993. *GPS antenna mixing and phase center corrections*. Eos Trans. AGU, Fall Meeting Supplement, p. 197.
- DACH R., HUGENTOBLE U., FRIDEZ P., MEINDL M. 2007. *Bernese GPS Software Version 5.0*. Astronomical Institute, University of Bern, p. 327–346.
- FALKO M., SEEGER G., VÖLKSEN CH., WÜBBENA G., SCHMITZ M. 1998. *Results of Absolute Field Calibration of GPS Antenna PCV*. ION GPS-98; Proceedings of the 11th International Technical Meeting of the Satellite Division of the Institute of Navigation, Nashville, TN; UNITED STATES; 15–18 Sept., p. 31–38.
- Geo++ GmbH / GeoService GmbH /. 2008. *Format of Geo++ PCV Antenna File*, <http://www.geopp.de/media/docs/pdf/>
- GEIGER A. 1998. *Modeling of Phase Center Variation and its Influence on GPS Positioning*. GPS-Techniques Applied to Geodesy and Surveying: Proceedings of the International GPS-Workshop Darmstadt, April 10 to 13, Editor: Erwin Groten, Robert Strauß, Lecture Notes in Earth Sciences, 19: 210–222.
- GÓRAL W., KUDREY J. 2007. *Obliczanie poprawek uwzględniających wpływ charakterystyk anten w pomiarach fazowych GPS*. Geomatics and Environmental Engineering, 1(1/1): 133–139.
- HOFMANN-WELLENHOF B., LICHTENEGGER H., WASLE E. 2008. *GNSS – Global Navigation Satellite Systems*, Springer-Verlag Wien, Austria.
- IGS Working Group. 2008. *IGS antenna files*. <ftp://igsceb.jpl.nasa.gov/pub/station/genereal/antenna-README.pdf>
- Instrukcja Techniczna G-2. 2001. *Szczegółowa pozioma i wysokościowa osnowa geodezyjna i przeliczanie współrzędnych między układami*. Główny Urząd Geodezji i kartografii, Warszawa.

- MADER G.L. 1999. *GPS Antenna Calibration at the National Geodetic Survey*. Journal of Geodesy, 3(1).
- ROTHACHER M. 2001. *Comparison of Absolute and Relative Antenna Phase Center Variations*. GPS Solutions, 4(4): 55-60
- ROTHACHER M., MADER G. 1996. *Combination of antenna phase center offsets and variation: antenna calibration set IGS-01*, anonymous ftp ubeclu.unibe.ch, June.
- ROCKEN C. 1992. *GPS antenna mixing problems*. UNAVACO Memo, November 12.
- SCHUPLER B., CLARK T.A. 1991. *How different antennas affect The GPS observables*. GPS World November/December.
- SCHMID R., ROTHACHER M., THALLER D., STEIGENBERGER P. 2005. *Absolute phase center corrections of satellite and receiver antennas*. GPS Solutions, 9(4).
- SCHMITZ M., WÜBBENA G., BOETTCHER G. 2002. *Tests of phase center variations of various GPS antennas, and some results*. GPS Solutions, 6: 18-27.
- Topcon Tools User's Guide*. 2006. Topcon Positioning Systems Inc, May.
- WÜBBENA G., MENGE F., SCHMITZ M., SEEGER G., VÖLKSEN CH. 1997. *A New Approach for Field Calibration of Absolute Antenna Phase Center Variations*. Presented at ION GPS-96, Kansas City, Missouri.

INITIAL USE OF STATISTICAL ANALYSIS FOR ESTIMATION OF HORIZONTAL ACCURACY OF LARGE-SCALE DIGITAL MAPS

Adam Doskocz

Chair of Surveying
University of Warmia and Mazury in Olsztyn

Key words: digital map, horizontal accuracy, statistical analysis.

Abstract

The paper presents estimation of horizontal accuracy of maps using of initial statistical analysis. Investigations have been performed for four large-scale digital maps made with different methods of producing digital map data: new total station survey (object *A*), re-calculation of previous direct measurements (orthogonal and polar surveys) (object *B*), manual vectorisation of a raster orthophotomap image (object *C*) and graphical-and-digital processing of analogue maps (object *D*).

Analysis has been performed for large statistical samples of sets of vectors of shift of control points ε_L and their components, i.e. true errors of increments of co-ordinates ε_X , ε_Y . In the case of a map produced by means of new survey with an electronic tacheometer, the true errors were represented by differences between co-ordinates of control points obtained from two separate set outs. In the case of other methods of data collection for digital map production true errors were represented by differences of co-ordinates acquired from an investigated map and co-ordinates calculated from new direct surveys.

WSTĘPNE WYKORZYSTANIE ANALIZY STATYSTYCZNEJ DO OCENY DOKŁADNOŚCI OPRACOWANIA SYTUACYJNEGO WIELKOSKALOWYCH MAP CYFROWYCH

Adam Doskocz

Katedra Geodezji Szczegółowej
Uniwersytet Warmińsko-Mazurski w Olsztynie

Słowa kluczowe: mapa cyfrowa, dokładność opracowania sytuacyjnego, analiza statystyczna.

Abstrakt

W pracy przedstawiono ocenę dokładności opracowania sytuacyjnego map numerycznych z wykorzystaniem wstępnej analizy statystycznej. Badania zrealizowano na przykładzie czterech wielkoskalowych map numerycznych wykonanych różnymi metodami pozyskiwania danych

numerycznych: nowy pomiar tachimetrem elektronicznym (obiekt *A*), przeliczenie wyników wcześniejszych pomiarów bezpośrednich (ortogonalnych i biegunowych) (obiekt *B*), manualną wektoryzację rastrowego obrazu ortofotomapy (obiekt *C*) oraz przetworzenie graficzno-numeryczne map analogowych (obiekt *D*).

Analizę wykonano na dużych próbach statystycznych zbiorów długości wektorów przesunięcia punktów kontrolnych ε_L oraz jego składowych, tj. błędach prawdziwych przyrostów współrzędnych ε_X , ε_Y . W przypadku mapy wykonanej z nowych pomiarów tachimetrem elektronicznym jako błędy prawdziwe przyjęto różnice dwukrotnie wyznaczonych współrzędnych punktów kontrolnych. W odniesieniu do pozostałych metod pozyskiwania danych do tworzenia map numerycznych błędy prawdziwe uzyskano z różnic współrzędnych pozyskanych z badanej mapy i współrzędnych wyznaczonych z nowego pomiaru bezpośredniego.

Introduction

The feature of horizontal accuracy of the digital map database is very important for state geodetic administration and surveying documentation centres, and for good relation between producers and users of digital map data (DĄBROWSKI et al. 2007).

The discussed issue is not a local problem, that occurs in Poland only. Accuracy of digital data has already been investigated by numerous researchers (e.g. HUSÁR 1996). Those investigations are also performed with the use of statistical analysis (BOLSTAD et al. 1990), as well as other, modern research methods (PODOBNIKAR 1999). They concern, however, maps produced at medium and small scales available in particular countries. In Poland, the large-scale maps exist for the entire country in the form of the base map; the investigations were thus focused on that map (in opinion author of this paper).

The aspect of direct relations between results of analysis and correctness (accuracy) of data (the GIGO principle, i.e. “Garbage In, Garbage Out”) (URBAŃSKI 1997) has been often discussed in literature. Correlations between data quality and costs of data acquisition are also stressed. Costs of survey depend, in general, on the accuracy of survey (GAŹDZICKI 1995).

The paper presents the initial use of statistical analysis for estimation of horizontal accuracy of large-scale digital maps.

Methodology of research and characteristics of investigated objects

Statistical analysis for estimation of accuracy of digital maps was executed basing on true errors ε_X , ε_Y of increments of plain coordinates of geometric details of the 1st accuracy group (of selected details of the 1st group, being the so-called, control points). In the case of a map produced on the basis of measurements with the use of an electronic tacheometer (object *A*), the

differences of coordinates of control points, surveyed two times (following the theory of measurements in pairs) were used as true errors. With respect to other analysed methods of acquisition of location details used for creation of large-scale digital maps (objects *B*, *C* and *D*), true errors of control points were calculated basing on differences of coordinates obtained from the investigated map and coordinates determined from a new field survey.

Coordinates of analysed details of locations of the objects *A*, *B* and *D* were acquired in the form of text listings or database reports; in the case of the object *C* coordinates were acquired by means of manual vectorisation of the raster image of the orthophotomap (DOSKOCZ 2002).

Four digital maps (objects) for the cities of Olsztyn and Zielona Góra were the subject of research. The object *A* is the digital map in the scale 1:500, produced on the basis of direct survey performed at the university campus in Olsztyn in 1995–1996 by student teams with use of an electronic tacheometer (total station survey). The survey was based on the restorable 3rd order geodetic control network. 481 control points covering the area of approximately 200 ha were used for estimation of accuracy.

The object *B* is the digital base map of the City of Zielona Góra. The digital map has been produced basing on existing results of surveys, performed in the period of 1974–1999 (basing on technical traversing of the 2nd order from 1973–1974, developed in accordance with the B-III Instruction), by means of the method of orthogonal measurements, and, in the recent period, by means of the polar method, using an electronic tacheometer (in relation to the restorable 3rd order network). The map accuracy was evaluated for the area of approximately 330 ha (out of 5800 ha of the total area of the city), using 1619 control points.

The object *C* is the digital orthophotomap of the City of Olsztyn. The digital orthophotomap was produced basing on 1:5000 aerial photographs taken within the Phare Programme in 1995. Aerial photographs were processed to the digital form using a matrix scanner with the resolution of 1000 dpi; then the orthophotomap was developed at the scale of 1:2000. The orthophotomap accuracy was evaluated basing on 311 control points from the area of approximately 115 ha.

The object *D* is the digital base map of the City of Olsztyn. The digital map was produced using the method of graphical-and-digital processing of the analogue base map at the scale of 1:500 with the layers of utilities, at the scales of 1:500 and 1:1000. The base map was produced basing on technical traversing of the 2nd order from 1974. Survey of details was performed by means of a photogrammetric method, for initial conditions of October 1977. The map was updated by means of direct surveys, connected to the control network of 1974, and, after 1986 – to the newly established restorable control network of

the 3rd order. Accuracy of the digital map was estimated for the area of approximately 355 ha (out of 8800 ha, being the total area of the city), using 2282 control points.

Statistical analysis for estimation of horizontal accuracy of large-scale maps

In the course of statistical analysis for estimation of horizontal accuracy of large-scale digital maps based on sets of true errors, estimation of parameters of distribution of the random variable and verification of compliance of its distribution with theoretical models of errors were performed. It highly influenced the statistical estimation of accuracy of control objects, since – in the case when compliance between the distribution of both sets of true errors ε_X , ε_Y of the given control objects with the normal distribution is stated – the random variable ε_L^2 ($\varepsilon_L^2 = (\varepsilon_X^2 + \varepsilon_Y^2)$) – the square of the length of the shift vector of the control point) would have the χ^2 distribution with two degrees of freedom.

For the needs of surveying, the ε_L type variable is often used. That variable of two degrees of freedom, expresses the length of the vector, the components of which represent two independent random variables of normal distribution and of equal standard deviations. Some transformations of the χ^2 distribution of practical value are known from literature (CRAMÉR 1958). An example of such a variable is the linear error of the point location (NEY 1976).

The strategy of estimation of accuracy of large-scale digital maps with use of initial statistical analysis of true errors is shown in Table 1.

Determination of parameters of a random variable

Two groups of parameters, i.e. measures of location and measures of scattering are most frequently applied. The basic numerical characteristics of the distribution of the random variable are particular cases of moments of the random variable (BARAN 1983).

Some values of the basic numerical characteristics are helpful to specify (hypothetical) reasons of anomalies of distributions of empirical sets (SZACHERSKA, KURPIEWSKA 1976, WIŚNIEWSKI 1986):

- Existing skewness ($S \neq 0$) in an empirical set proves that the set was created from combination of subsets of various size and of various expected values. This also proves that a deterministic factor occurs (a factor of non-random characteristics) which is systematic with respect to the sign but variable with respect to the value.

Table 1

Stages of initial statistical analysis for estimation of horizontal accuracy of map

Statistical analysis of the sets of true errors $\varepsilon_X, \varepsilon_Y$	
I stage: Determination of parameters of the random variable	
Calculation of empirical parameters of the random variable "true error"	
II stage: Analysis of distribution of the sets of true errors	
Determination of the type of the random variable "true error" (continuous or discrete type)	
Formulation of initial assumptions on the distribution of true errors (basing on empirical parameters and determined type of the random variable)	
Verification of non-parametric hypotheses with respect to compliance of distribution of the sets of true errors $\varepsilon_X, \varepsilon_Y$ with the normal distribution	
III stage: Estimation of accuracy of control objects (independence of $\varepsilon_X, \varepsilon_Y$ errors assumed)	
<i>In the case when compliance of distribution of the sets of true errors $\varepsilon_X, \varepsilon_Y$ of the given control object with the normal distribution is stated</i>	<i>In the case when no compliance of distribution of at least one of the sets of true errors ε_X or ε_Y of the given control object with the normal distribution is stated</i>
<i>Estimation of accuracy of the control object using the χ^2 distribution (with two degrees of freedom) for the random variable ε_L^2 ("the square of length of the shift vector of the control point")</i>	<i>Estimation of accuracy of the control object with the use of statistical definition of probability, where the probability of occurrence is expressed as the relative frequency of occurrence – occurrence of a specified length of the shift vector (ε_L) in the set of control points of the given object (for the sufficient number of sample population)</i>

- Theoretical justification of $e > 0$ coefficient (slender empirical curve) is the occurrence of elements of various accuracy in a set.
- Flatteness of an empirical curve ($e < 0$) proves that systematic errors occur.
- Non-zero expected value of the error ($\bar{x} \neq 0$) indicates the occurrence of permanent errors.

In the initial statistical analysis of true errors the following values have been empirically determined: the average values $\bar{x} = \sum_{i=1}^N \varepsilon_{Xi}/N$ (expressed by its estimator – the arithmetic mean) and standard deviation of the random

variable $m = \sqrt{\sum_{i=1}^N \varepsilon_{Xi}^2/N}$ (estimated by the mean square error). Asymmetry of

the distribution has been specified by asymmetry factor (skewness) $S = \mu_3/m^3$ and the level of flattening of curves of empirical distribution with respect to theoretical models has also been determined. The factor of flattening (excess) has been calculated as $e = (\mu_4/m^4)-3$. The following quantities have also been calculated: the mean square error of the average value of the random variable

$m_{\bar{x}} = m/\sqrt{N}$, the average error of the random variable $d = \sum_{i=1}^N |\varepsilon_{Xi}|/N$, and the d/m ratio, where N is the size of the set. Parameters of random variables of control sets investigated are given in Table 2 and Table 3.

Table 2

Empirical parameters of the random variables from control objects of digital maps
of the City of Olsztyn

Control object (size)	Set of errors	Size of the set	Empirical parameters of random variables						
			\bar{x} [m]	m [m]	\bar{x} [m]	d [m]	d/m	S	e
A (200 ha)	ε_X	478	0.00	0.05	0.002	0.04	0.80	-0.23	0.04
	ε_Y	478	0.00	0.04	0.002	0.03	0.75	0.01	2.58
C (115 ha)	ε_X	311	-0.01	0.15	0.008	0.11	0.73	0.12	0.64
	ε_Y	311	-0.02	0.15	0.008	0.11	0.73	0.51	1.35
D-1 (46 ha)	ε_X	1001	0.10	0.26	0.008	0.19	0.73	-0.16	2.25
	ε_Y	1001	-0.08	0.28	0.009	0.21	0.75	0.31	1.54
D-2 (154 ha)	ε_X	549	0.10	0.31	0.013	0.23	0.74	-0.32	2.27
	ε_Y	549	-0.09	0.32	0.014	0.24	0.75	0.22	1.34
D-3 (25 ha)	ε_X	240	-0.06	0.31	0.020	0.23	0.74	0.00	0.95
	ε_Y	240	0.06	0.34	0.022	0.27	0.79	-0.03	0.34
D-4 (20 ha)	ε_X	236	0.01	0.22	0.014	0.16	0.73	-0.79	3.25
	ε_Y	236	0.05	0.25	0.016	0.17	0.64	-0.61	4.24
D-5 (100 ha)	ε_X	134	0.11	0.24	0.018	0.18	0.75	-0.60	1.26
	ε_Y	134	-0.02	0.18	0.016	0.14	0.78	0.06	1.17
D-6 (10 ha)	ε_X	115	0.10	0.29	0.027	0.23	0.79	-0.11	-0.77
	ε_Y	115	-0.08	0.25	0.023	0.19	0.76	0.14	0.22

Table 3

Empirical parameters of the random variables from control objects of digital base map
of the City of Zielona Góra

Control object (size)	Set of errors	Size of the set	Empirical parameters of random variables						
			\bar{x} [m]	m [m]	$m_{\bar{x}}$ [m]	d [m]	d/m	S	e
B-1 (92 ha)	ε_X	257	-0.04	0.11	0.007	0.08	0.73	0.14	0.70
	ε_Y	257	-0.01	0.10	0.006	0.07	0.70	0.56	1.73
B-2 (13 ha)	ε_X	217	0.00	0.14	0.010	0.09	0.64	0.77	3.46
	ε_Y	217	0.00	0.16	0.011	0.10	0.62	-0.77	9.91
B-3 (46 ha)	ε_X	209	-0.02	0.20	0.013	0.14	0.70	-0.80	2.38
	ε_Y	209	0.06	0.27	0.019	0.17	0.63	1.47	4.61
B-4 (60 ha)	ε_X	241	0.07	0.15	0.010	0.12	0.80	0.08	-0.15
	ε_Y	241	-0.06	0.15	0.010	0.11	0.73	0.15	1.30
B-5 (90 ha)	ε_X	318	0.00	0.12	0.007	0.08	0.67	1.09	13.90
	ε_Y	318	0.00	0.15	0.008	0.07	0.47	1.11	39.34
B-6 (18 ha)	ε_X	264	-0.01	0.11	0.007	0.08	0.73	1.31	4.34
	ε_Y	264	-0.01	0.09	0.006	0.06	0.67	0.03	9.59
B-7 total (7 ha)	ε_X	96	0.05	0.26	0.026	0.16	0.62	1.58	2.57
	ε_Y	96	0.15	0.31	0.032	0.20	0.64	1.15	0.39
B-7 sheet 2(2) (5 ha)	ε_X	72	0.04	0.13	0.015	0.09	0.69	0.43	0.59
	ε_Y	72	-0.06	0.16	0.019	0.12	0.75	-0.34	-0.88

Analysis of distribution of true errors

The second stage of analysis was focused on the determination of the distribution of empirical sets. At the beginning the type of the random variables “true error of increment of coordinates” ε_X and ε_Y was specified. Initially the type of the random variable was visually recognised, since in empirical sets of discrete random variables the number of elements of various values would be small (less then twenty). However, in the case of a theoretically continuous variable each element of a set has different value but the same value of variable may occur several times (NEY 1976). Finally, the type of the random variable was specified with use of the hypothesis of wave structure of errors (ADAMCZEWSKI 1961). In the case of sets of true errors ε_X , ε_Y of all control objects, the continuous function of attenuation has been stated. For example, in the case of set with greatest number of elements (Fig. 1) and set with least number of elements (Fig. 2).

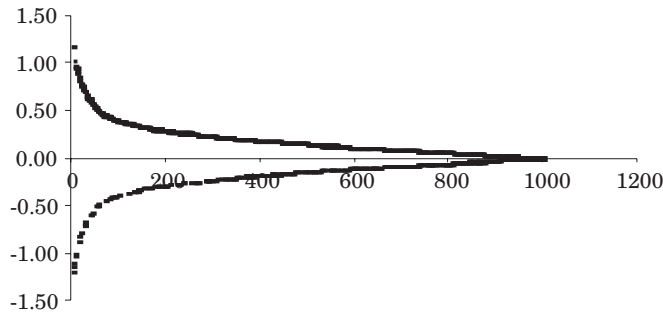


Fig. 1. Continuous function of attenuation of the empirical set ε_X of D-1 control object (set with greatest number of elements)

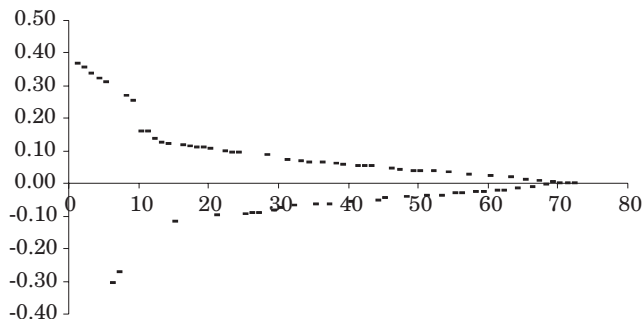


Fig. 2. Continuous function of attenuation of the empirical set ε_X of B-7 control object (set with least number of elements)

The specified type of random variable and calculated empirical parameters of the random variable (Tables 2 and 3) allowed to assume that distributions of investigated sets of true errors may belong to a family of normal distributions. Besides, basing on empirical parameters, initial specification of distribution of true errors was performed. It was noted that the majority of sets are asymmetric ($S \neq 0$) and are affected by a systematic factor ($\bar{x} \neq 0$). It was also found that, for the considerable part of sets, that obtained d/m ratio vary from its theoretical value in the normal distribution (for Gaussian distribution that ratio equals to $d/m = \sqrt{2/\pi} \approx 0,80$ (NEY 1976)). The excess values in empirical sets are almost all positive, what indicates more distinctive slenderness of empirical curves of probability density of errors than a normal curve of the variance determined in the given empirical set. Therefore, the use of modified normal distribution, in particular the Modulated Normal Distribution (MND) (ROMANOWSKI 1974, 1979) was considered. The analysis of relative frequency of true errors ε_X , ε_Y in the investigated sets indicates the similarity of their distribution with the MND distribution of the 1st-type.

The empirical sets of observation errors frequently substantially differ from the Gaussian model; it concerns asymmetry and excess (SZACHERSKA 1974, ŁYSZKOWICZ 1975b, WIŚNIEWSKI 1984, 1986). Such differences were also exhibited by the empirical sets investigated. In order to determine the empirical distribution density curves, Pearson method was applied, that requires calculating numerical coefficients β_1 , β_2 , k (basing on values of central moments of empirical sets, calculated earlier): β_1 , μ_3^2/μ_2^3 , β_2 , μ_4/μ_2^2 , $k = \beta_1 \cdot (\beta_2 + 3)^2 / 4 \cdot (2 \cdot \beta_2 - 3 \cdot \beta_1 - 6) \cdot (4 \cdot \beta_2 - 3 \cdot \beta_1)$. Those coefficients become the basis for determination the curve, out of 12 Pearson curves, that might be used for approximation of the given empirical set. Pearson distributions of I, II, IV and VII types were identified as suitable for typical surveying data (ŁYSZKOWICZ 1975a, 1975b).

The search for Pearson distributions that might be used for approximation of empirical sets was undertaken. Besides, two statistical tests, i.e. Pearson χ^2 test and Kolmogorow λ test were used for verification of non-parametric hypotheses concerning the compliance of distributions of empirical sets with theoretical distributions (Gaussian and MND 1st-type distribution characterized by the leptokurtosis index ω_t). Investigations of compliance of distribution of true errors of ε_X , ε_Y with theoretical models was performed for the standardized random variable (e.g. $\varepsilon_X' = (\varepsilon_X - \bar{x})/m$).

The χ^2 test is of higher sensitivity than λ test, but, at the same time, it requires larger set (at least above one hundred elements) (NEY 1970). The χ^2 test better characterizes the difference between the empirical distribution and the theoretical model, since it uses all class intervals of a distributive series. In the λ test the level of compliance between the empirical and theoretical

distributions is expressed by the point value D_i . The argument that supports the use of the Kolmogorow λ method is that the λ test is not sensitive on discrepancies which occur for final small class intervals of the distributive series (which often prevail in empirical sets) (HELLWIG 1998). The Kolmogorow λ method was applied when it was necessary as an auxiliary test.

Analysed the sets ε_X , ε_Y are slender (leptokurtic) in majority of cases, with respect to Gaussian distribution (except of ε_X and ε_Y sets of the object A, the ε_Y set of the object D-5 and the ε_Y set of the object B-7); prevailing discrepancies of their distribution occur in central class intervals of the distributive series. Detailed results of investigations of compliance between distributions of sets of true errors with theoretical distributions are presented in the paper (DOSKOCZ 2005).

Summary of results of analysis of distribution of true errors

In the first two stages of statistical analysis (Tab. 1) it was found that the distributions of ε_X , ε_Y sets “are governed by their own law” which makes it difficult to present them by means of known, theoretical models of errors. Only in a few cases the compliance between empirical distribution with the theoretical distribution was stated. The only set which proved the compliance between the distribution of the empirical set and the normal distribution (ND) was the empirical set ε_X of D-6 control object (Fig. 3).

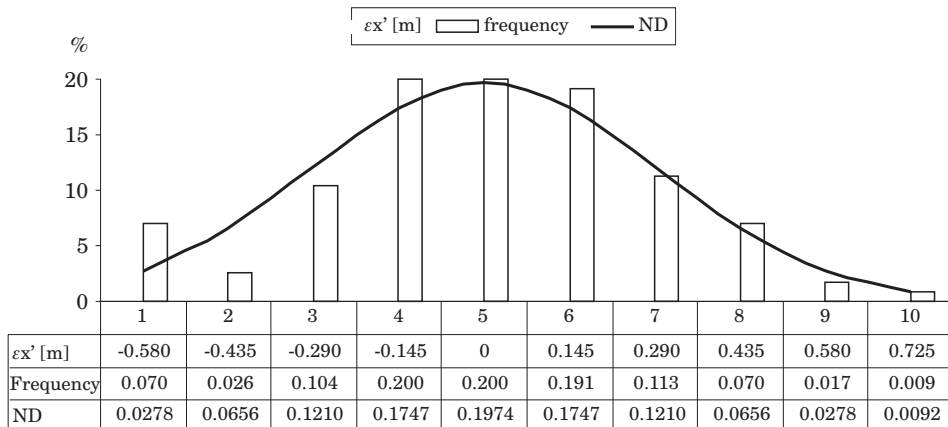


Fig 3. Compliance between the distribution of the empirical set ε_X of D-6 control object with the normal distribution

Distributions of investigated sets of true errors are, in general, not compliant with MND Romanowski distributions (DOSKOCZ 2005), what results from their skewness as it is known from literature utilisation of modulated normal distributions is not fully consistent in conditions of existing asymmetry' (WIŚNIEWSKI 1986).

Also Pearson curves, which accept the presence of asymmetry and excess in an empirical empirical set, could, to a very limited extend (ε_Y set of A, ε_Y set of B-7, ε_X and ε_Y sets of D-3, ε_Y set of D-5) approximate investigated sets of true errors (DOSKOCZ 2005).

Estimation of accuracy of investigated digital maps

Because of lack of compliance between the random variable "the square of the length of the shift vector" and the theoretical distribution χ^2 , the probability of occurrence of specified values of the point location error m_p (expressed by the length of the vector of shift of the control point ε_L) has been estimated on the basis of the relative frequency W_N of occurrence of particular values ε_L within the control objects. The required probability was determined by means of the method presented in (SMIRNOW, DUNIN-BARKOWSKI 1969). Probabilities have been estimated for the confidence level $\gamma = 0.997$ for $t_\gamma = 3$.

The confidence interval for the unknown probability may be determined by that method when the condition $N \cdot P \cdot Q > 9$ is met (N is the size of the set; P is the event probability to be determined; Q is the probability of the complementary event). This condition define sufficient size of the samples who is needed for estimating probability of an analysed event.

The limits of confidence interval for the estimated probability P are expressed as $P_1(W, N) < P < P_2(W, N)$ (SMIRNOW, DUNIN-BARKOWSKI 1969), where

$$P_1(W, N) = \frac{2 \cdot N \cdot W_N + t_\gamma \cdot \sqrt{D}}{2 \cdot (N + t_\gamma^2)}$$

$$P_2(W, N) = \frac{2 \cdot N \cdot W_N + t_\gamma \cdot \sqrt{D}}{2 \cdot (N + t_\gamma^2)}$$

$$\sqrt{D} = \sqrt{4 \cdot N \cdot W_N \cdot (1 - W_N) + t_\gamma^2}$$

Statistical estimation of the horizontal accuracy of large-scale digital maps in particular control objects is given in Tables 4 and 5. Columns 6 and 8, present probabilities that the map error does not exceed stated point location error (m_p) multiplied by factor 3 and 2, respectively, at the given control object. Column 10 presents the probability that the theoretical error will be exceeded

(m_t – determined in accordance to the accuracy standard for mapping). The symbol (*) by the confidence interval means that the probability is determined in situation when the relative frequency of the considered event in the empirical set had not ensured that the condition of the sufficient sample size was fulfilled.

Table 4
Statistical estimation of horizontal accuracy of control objects on digital maps of the City of Olsztyn

Control object	Analysed value	Size of the set	m_p [m]	Statistical characteristics of accuracy of control objects determined for the confidence level $\gamma = 0.997$					
				Estimated probabilities of occurrence of the (Δ) error in general population					
				W_N	$\Delta \leq 3m_p$	W_N	$\Delta \leq 2m_p$	W_N	$\Delta > m_t$
1	2	3	4	5	6	7	8	9	10
A	ε_L	478	0.04	0.95	$0.91 < P < 0.97$	–	–	0.02	$0.01 < P < 0.05^*$
C	ε_L	311	0.21	–	–	0.97	$0.92 < P < 0.99$	0	$0 < P < 0.03^*$
D-1	ε_L	1001	0.38	0.99	$0.98 < P < 1^*$	0.95	$0.93 < P < 0.97$	0.19	$0.16 < P < 0.24$
D-2	ε_L	549	0.45	0.99	$0.97 < P < 1^*$	0.95	$0.92 < P < 0.97$	0.27	$0.22 < P < 0.33$
D-3	ε_L	240	0.46	1	$0.96 < P < 1^*$	0.95	$0.90 < P < 0.98$	0.32	$0.24 < P < 0.42$
D-4	ε_L	236	0.33	0.98	$0.93 < P < 0.99^*$	0.96	$0.90 < P < 0.98^*$	0.15	$0.09 < P < 0.23$
D-5	ε_L	134	0.30	–	–	0.96	$0.88 < P < 0.99^*$	0.14	$0.07 < P < 0.26$
D-6	ε_L	115	0.39	–	–	0.97	$0.88 < P < 0.99^*$	0.29	$0.18 < P < 0.42$

Table 5
Statistical estimation of horizontal accuracy of control objects on the digital base map of the City of Zielona Góra

Control object	Analysed value	Size of the set	m_p [m]	Statistical characteristics of accuracy of control objects determined for the confidence level $\gamma = 0.997$					
				Estimated probabilities of occurrence of the (Δ) error in general population					
				W_N	$\Delta \leq 3m_p$	W_N	$\Delta \leq 2m_p$	W_N	$\Delta > m_t$
1	2	3	4	5	6	7	8	9	10
B-1	ε_L	257	0.15	–	–	0.97	$0.92 < P < 0.99^*$	0.004	$0 < P < 0.04^*$
B-2	ε_L	217	0.21	0.99	$0.94 < P < 1^*$	0.96	$0.90 < P < 0.98^*$	0.03	$0.01 < P < 0.09^*$
B-3	ε_L	209	0.33	0.98	$0.93 < P < 1^*$	0.92	$0.85 < P < 0.96$	0.13	$0.08 < P < 0.22$
B-4	ε_L	241	0.22	–	–	0.94	$0.87 < P < 0.97$	0.05	$0.02 < P < 0.12$
B-5	ε_L	318	0.20	0.98	$0.94 < P < 0.99^*$	0.97	$0.93 < P < 0.99^*$	0.03	$0.01 < P < 0.07^*$
B-6	ε_L	264	0.14	0.98	$0.94 < P < 0.99^*$	0.96	$0.90 < P < 0.98$	0.02	$0 < P < 0.06$
B-7 total	ε_L	96	0.41	0.98	$0.88 < P < 1^*$	0.91	$0.78 < P < 0.96^*$	0.15	$0.07 < P < 0.28$
B-7 sheet 2(2)	ε_L	72	0.21	–	–	0.97	$0.84 < P < 1^*$	0.03	$0 < P < 0.16^*$

Conclusions

Results of statistical analysis proved the lack of compliance of considered sets of true errors with the normal distribution (except ε_X set of the control object *D-6*). That is why estimation of horizontal accuracy of investigated digital maps was based on statistical definition of the probability, where the probability of an event is identified with the relative frequency of this event. Obtained results of accuracy estimation using statistical analysis are coherent with conclusions developed on the basis of classical estimation of accuracy (DĄBROWSKI, DOSKOCZ 2008).

Initial statistical analysis confirmed high accuracy of the digital map produced on the basis of survey with an electronic tacheometer (object *A*). Probability that the theoretical error (0.3 mm at the map scale) will be exceeded in the object *A* does not exceed 5% (Table 4, col. 10).

The probability of occurrence of the point location error which does not meet the accuracy standards in the case of a digital map produced on the bases of the past field surveys is relatively low (object *B*); in general it does not exceed 10% (except control objects *B-3* and *B-7*) (Table 5, col. 10).

Statistical analysis confirmed the high accuracy (in relation to well identified details of the 1st group, i.e. characteristic points of technical utilities) of a digital orthophotomap (object *C*). In the case of that object the probability of occurrence errors larger than the theoretical error does not exceed 3% (Table 4, col. 10).

The lowest accuracy was confirmed for a digital map produced by means of graphical-and-digital processing of analogue maps (object *D*). The estimated probability of occurrence of the point location error that exceeds the theoretical error value (0.3 mm at the map scale) within the object *D* equals to 20 ÷ 30% (Table 4, col. 10).

Results of performed investigations allow to formulated the general conclusions:

1) Large-scale digital maps based on data acquired from various methods do not always meet the requirements of accuracy standards specified in technical standards.

2) There is a need for estimation accuracy of large-scale digital maps to ensure an appropriate quality of the state surveying resources.

3) In author opinion of this paper, future investigations should be focused on automation process of estimation of digital map data bases with application mathematical and statistical methods.

Acknowledgments

This work is the result of own research within the frames of the university internal grant (theme) No. 522-0309-0213 “Creation and updating of databases of digital maps for the needs of surveying administration and for educational purposes”.

Accepted for print 10.01.2010

References

- ADAMCZEWSKI Z. 1961. *Hypothesis of wave structure of the errors* (in Polish). *Geodezja i Kartografia*, X (2): 151–159.
- BARAN L.W. 1983. *Theoretical bases of elaborate of results of the geodetic surveys*. PWN, Warsaw.
- BOLSTAD P.V., GESSLER P., LILLESAND T.M. 1990. *Positional uncertainty in manually digitized map data*, *Int. J. Geogr. Inf. Systems*, 4(4): 399–412.
- CRAMÉR H. 1958. *Mathematical methods in statistic*. PWN, Warsaw.
- DĄBROWSKI W., DOSKOCZ A., MRÓWCZYŃSKI T. 2007. *Utility accuracy of large-scale digital maps of the City of Zielona Góra – The city appreciated orthophoto*. *GEODETA*, 1(140): 26–28, <http://www.geoforum.pl/pages/index.php?page=edition&subpage=artykuly&id=30>
- DĄBROWSKI W., DOSKOCZ A. 2008. *Estimation of accuracy of the large-scale digital topographic map data*. *Proceeding of the 7th International Conference “Environmental Engineering” Volume III*, pp. 1293–1299. https://www.vgtu.lt/upload/leid_konf/dabrowski_et_al_estimation.pdf
- DOSKOCZ A. 2002. *Examining of accuracy of large-scale digital maps made with different methods*. Ph.D. Dissertation, University of Warmia and Mazury in Olsztyn, p. 174.
- DOSKOCZ A. 2005. *The use of statistical analysis for estimation of positional accuracy of large-scale digital maps*. *Geodezja i Kartografia*, 54(3): 131–150.
- GAZDZICKI J. 1995. *Cadastral systems*. PPWK, Warsaw–Wrocław.
- HELLWIG Z. 1998. *Elements of probability and mathematical statistic*. PWN, Warsaw.
- HUSÁR K. 1996. *Presnosť digitálnych priestorových údajov*. *Kartografické Listy*, 4: 69–78.
- ŁYSZKOWICZ A. 1975a. *Define of Pearson curves description of sets of errors of the geodetic surveys*. *Geodezja i Kartografia*, XXIV, 4: 275–282.
- ŁYSZKOWICZ A. 1975b. *Choice of mathematical models for empirical distribution of results of the geodetic surveys*. Ph.D. Dissertation, University of Warmia and Mazury in Olsztyn.
- NEY B. 1970. *Criteria of compliance of empirical distribution with models*. *Polska Akademia Nauk – Oddział w Krakowie, Prace Komisji Górniczo-Geodezyjnej, Seria Geodezja*, 7: 31–46.
- NEY B. 1976. *Statistical methods in geodesy*. AGH Uczelniane Wydawnictwa Naukowo-Dydaktyczne, 497, Kraków.
- PODOBNIKAR T. 1999. *Modelling and Visualisation of Spatial Data Error. Monte Carlo Simulations in Slovenia*, *GIM International*, 13(7): 47–49.
- ROMANOWSKI M. 1974. *Theory of modulation of the random errors in observations*. *Polska Akademia Nauk – Oddział w Krakowie, Prace Komisji Górniczo-Geodezyjnej, Seria Geodezja*, 18: 19–46.
- ROMANOWSKI M. 1979. *Random Errors in Observations and the Influence of Modulation on their Distribution*. Verlag Konrad Wittwer, Stuttgart.
- SMIRNOW N.W., DUNIN-BARKOWSKI I.W. 1969. *Course of probability and mathematical statistic in technical applications*. PWN, Warsaw.
- SZACHERSKA M.K. 1974. *Model of composition of errors of the geodetic surveys*. *Geodezja i Kartografia*, XXIII (1): 21–51.
- SZACHERSKA M.K., KURPIEWSKA A. 1976. *Accuracy of precision leveling in light of statistical investigations*. *Geodezja i Kartografia*, t. XXV, 1: 17–33.

- URBAŃSKI J. 1997. *Understand GIS – analysis of spatial information*. PWN, Warsaw.
- WIŚNIEWSKI Z. 1984. *Use of Pearson distributions II and VII types in adjustment of the geodetic networks*. Geodezja i Kartografia, XXXIII (3): 85–104.
- WIŚNIEWSKI Z. 1986. *Adjustment of geodetic networks with use of probabilistic models of errors of the surveys*. Acta Acad. Agricult. Techn. Olst. Geodaesia et Ruris Regulatio, 15, Supplementum C., University of Warmia and Mazury in Olsztyn.

QUASIGEOID FOR THE AREA OF POLAND COMPUTED BY LEAST SQUARES COLLOCATION

Adam Łyszkowicz

Chair of Land Surveying and Geomatics
University of Warmia and Mazury in Olsztyn

Key words: gravity field, geoid, collocation.

Abstract

The quasigeoid models recently computed in Poland e.g. (ŁYSZKOWICZ, KRYŃSKI 2006) and abroad e.g. (AL MARZOOQI et al. 2005) were computed from Stokes's integral by Fast Fourier Technique (FFT). At present because of significant capability of personal computers and proper strategy of computation more often for geoid/quasigeoid computation the least squares collocation is used.

In the present paper is described the first quasigeoid computation by least collocation for the area of Poland. The quasigeoid model was computed in two version, namely from the gravity data only and from the gravity and vertical deflections data simultaneously. The differences between these two versions are small and do not exceed 1–2 mm.

In order to evaluate the advantages coming from the collocation the third pure gravimetric model using Stokes's integral was computed and compared with the gravimetric model computed by collocation. The differences between these versions are significant and at the level of 20 cm, beside the collocation model is better.

WYZNACZENIE PRZEBIEGU QUASI-GEOIDY DLA OBSZARU POLSKI METODĄ KOŁOKACJI NAJMNIEJSZYCH KWADRATÓW

Adam Łyszkowicz

Katedra Geodezji Szczegółowej
Uniwersytet Warmińsko-Mazurski w Olsztynie

Słowa kluczowe: pole siły ciężkości, geoida, kolokacja.

Abstract

Wszystkie ostatnio liczone grawimetryczne modele quasi-geoidy w Polsce (np. ŁYSZKOWICZ, KRYŃSKI 2006) i na świecie (np. AL MARZOOQI et al. 2005) były liczone na podstawie całki Stokesa, do której oszacowania wykorzystywano szybką transformatę Fouriera (FFT). Obecnie ze względu na znaczne możliwości komputerów oraz odpowiednio opracowaną strategię obliczeniową coraz częściej do wyznaczenia przebiegu geoidy/quasi-geoidy wykorzystuje się metodę kolokacji.

W pracy przedstawiono pierwsze w Polsce wyznaczenie przebiegu quasi-geoidy metodą kolokacji. Model quasi-geoidy wyznaczono w dwóch wariantach, a mianowicie tylko z danych grawimetrycznych, a następnie łącznie z danych grawimetrycznych i astro-geodezyjnych odchyłeń pionu. Różnice między tymi dwoma wariantami są minimalne i wynoszą 1–2 mm.

W celu oceny korzyści wynikających z metody kolokacji grawimetryczną quasi-geoidę policzono również metodą FFT i porównano z quasi-geoidą obliczoną metodą kolokacji. Z przeprowadzonego porównania wynika, że rozbieżność między modelami jest rzędu 20 cm, z tym że quasi-geoida kolokacyjna jest lepsza.

Introduction

The potential improvement of efficiency and lowering costs of height determination technology by replacing spirit levelling with GNSS technique is one of major factors generating research interest in developing regional quasigeoid models of high quality. Research on high-resolution precise quasigeoid models is thus of great importance not only for scientific purposes, in geodesy, geodynamics, geophysics, geology but also in surveying practice.

The extensive research on precise quasigeoid modelling in Poland with the use of all available data including gravity data and deflections of the vertical, conducted in 2002–2005 resulted in generating regional quasigeoid models: gravimetric quasigeoid obtained from gravity data with the use of “remove-restore” method, and astro-gravimetric quasigeoid calculated from astro-geodetic and astro-gravimetric deflections of the vertical with the use of astronomic levelling (KRYŃSKI 2007).

The aim of the following research was to investigate the contribution of collocation method and the existing deflections of the vertical in Poland to the improvement of the quality of the regional gravimetric quasigeoid in Poland and to determine a suitable methodology of combined use of gravity data with the deflections of the vertical for quasigeoid modelling.

Quasigeoid by remove-restore technique

Geoid calculation in a regional scale by the „remove-restore” technique is realized by summation of the three terms according to the formula

$$N = N_{GM} + N_{\Delta g_{res}} + N_H \quad (1)$$

where N_{GM} is computed from geopotential model, $N_{\Delta g_{res}}$ is computed from residual Faye’s gravity anomalies and N_H express the influence of topography. The residual gravity anomalies are compute from

$$\Delta g_{\text{res}} = \Delta g_F - \Delta g_{\text{GM}} \quad (2)$$

where Δg_F is Faye gravity anomaly and Δg_{GM} is gravity anomaly computed from geopotential model.

Term N_{GM} is computed from the general formula e.g. (TORGE 2001)

$$N_{\text{GM}}(r, \phi, \lambda) = N_0 + \frac{\text{GM}}{r\gamma} \sum_{n=2}^{n_{\text{max}}} \left(\frac{a}{r}\right)^n \sum_{m=0}^n (C_{nm} \cos m\lambda + S_{nm} \sin m\lambda) P_{nm}(\sin\phi) \quad (3)$$

and the term Δg_{GM} is computed from

$$\Delta g_{\text{GM}}(r, \phi, \lambda) = \frac{\text{GM}}{r\gamma} \sum_{n=2}^{n_{\text{max}}} (n-1) \left(\frac{a}{r}\right)^n \sum_{m=0}^n (C_{nm} \cos m\lambda + S_{nm} \sin m\lambda) P_{nm}(\sin\phi) \quad (4)$$

where C_{nm} , S_{nm} are fully normalized spherical harmonic coefficients of degree n and order m , n_{max} is the maximum degree of geopotential model, GM is product of the Newtonian gravitational constant and mass of the geopotential model, r , ϕ , λ are spherical polar coordinates, a is the equatorial radius of geopotential model and P_{nm} are the fully normalized associated Legendre's functions.

The term N_0 is the zero term due to the difference in the mass of the Earth used in IERS Convention and GRS80 ellipsoid. It is computed according to the well known formula

$$N_0 = \frac{\text{GM} - \text{GM}_0}{R\gamma} - \frac{W_0 - U_0}{\gamma} \quad (5)$$

where the parameters GM_0 and U_0 correspond to the normal gravity field on the surface of the normal ellipsoid. For the GRS80 ellipsoid we have $\text{GM}_0 = 398\,600.5000 \times 10^9 \text{ m}^3 \text{ s}^{-2}$ and $U_0 = 62\,636\,860.85 \text{ m}^2 \text{ s}^{-2}$. The Earth's parameter GM used in quasigeoid computation from geopotential models and the constant gravity potential W_0 on the quasigeoid according to IERS Conventions have been set to the following values: $\text{GM} = 398\,600.4415 \times 10^9 \text{ m}^3 \text{ s}^{-2}$, $W_0 = 62\,636\,856.00 \text{ m}^2 \text{ s}^{-2}$. The mean Earth radius R and the mean normal gravity γ on the reference ellipsoid are taken equal to $6\,371\,008.771 \text{ m}$ and 9.798 m s^{-2} respectively (GRS80 values). Based on the above conventional choices, the zero degree term from equation (5) yields the value $N_0 = -0.442 \text{ m}$, which has been added to the geoid heights obtained from the corresponding spherical harmonic coefficients series expansions of geopotential model.

The numerical computations for the spherical harmonic values of N from EGM08 model have been performed with the *geocol* software program that was kindly provided by dr Gabriel Strykowski from *Danish National Space Center*. The final GM geoid heights computed from equation (3) refer to the tide free system, with respect to a geometrically fixed reference ellipsoid (GRS80).

Term $N_{\Delta g_{\text{res}}}$ can be compute from Stokes' integral or by least squares collocation method. When the geoid is computed by least squares collocation method then the term $N_{\Delta g_{\text{res}}}$ can be computed from the formula e.g. (MORITZ 1989)

$$N_{\Delta g_{\text{res}}} = \mathbf{C}_{Nl} \mathbf{C}_{ll}^{-1} \mathbf{l} \quad (6)$$

where \mathbf{l} is a vector of observations, \mathbf{C}_{ll} is autocovariance matrix of observations, \mathbf{C}_{Nl} is crosscovariance matrix between the \mathbf{l} and N .

Once the geoid is computed from gravity anomaly Δg and vertical deflection ξ, η , then vector of observations \mathbf{l} can be in the form

$$\mathbf{l} = \begin{bmatrix} \mathbf{l}_{\xi\eta} \\ \mathbf{l}_{\Delta g} \end{bmatrix} \quad (7)$$

where vector $\mathbf{l}_{\xi\eta}$ contain components of vertical deflections ξ, η , and vector $\mathbf{l}_{\Delta g}$ contains gravity anomalies from the consider region.

In order to determine the term $N_{\Delta g_{\text{res}}}$ the knowledge of the matrix \mathbf{C}_{ll} and \mathbf{C}_{Nl} is necessary, which can be computed from the proper model of covariance function. In our case the logarithmic function was used (FORSBERG 1987). This model is defined by three parameters: variance C_0 of gravity anomalies, and parameters D and T that determine the degree of damping high and low frequencies of the gravity signal, respectively.

Suitable choice of the parameters of the covariance function is obtained by its proper fit to the empirical data. Practically, parameters C_0, D and T can be determined using gravity anomalies from the area of interest, e.g. with the use of the *gpfitt* program of the *GRAVSOFT* package (TSCHERNING et al. 1992).

In the case when the sphere is approximated by the plane the Stokes' integral in two dimensional coordinate system x and y is (VANIČEK, CHRISTOU 1994)

$$N_{\Delta g_{\text{res}}}(x, y) = \frac{1}{\gamma} \Delta g_{\text{res}}(x, y) * l_N(x, y) \quad (8)$$

where

$$l_N(x, x) = \frac{1}{2\pi} (x^2 + y^2)^{-\frac{1}{2}} \quad (9)$$

is planar form of Stokes' kernel function and * denotes convolution. The equation (8) can be evaluated by direct and inverse Fourier transform. For more details see e.g. (VANIČEK, CHRISTOU 1994).

The displacement of the topographic masses in gravity reductions changes the gravitational potential and thus the geoid. Therefore the computed surface is not the geoid itself but slightly different surface cogeoid. The vertical distance between the geoid and cogeoid can be computed from (e.g. WICHEN-CHAROEN 1982)

$$N_H \approx \frac{\pi G \rho}{\gamma_m} H_P^2 \quad (10)$$

where G is gravitational constant, ρ is mass density, H_P is topographic height of the point P and γ_m is mean normal acceleration.

The transformation from geoid undulation N to the height anomaly ζ representing the quasigeoid height over the ellipsoid is realized with the use of the Bouguer anomaly Δg_B using the formula e.g. (HEISKANEN, MORITZ 1967).

$$\zeta = N - \frac{\Delta g_B}{\gamma_m} H \quad (11)$$

Data used in quasigeoid computation

Gravity data

The determination of gravimetric quasigeoid on the territory of Poland is based on gravity anomalies presented on Fig. 1, which consist of 202 403 point and mean Faye's anomalies.

Basic data set consist of gravity data from area of Poland and contains 147 530 mean $1' \times 1'$ Faye's anomalies, computed from point data, clean from outstanding observation, recomputed to the POGK99 gravity and ETRS80 system and finally corrected due to topography (KRYŃSKI 2007).

Gravity data sets from Czech, Slovakia, Hungary, Romania and Western Ukraine contain mean Faye's anomalies in blocks $5' \times 5'$ obtained from the

Bouguer anomaly maps. Remaining data sets are very different and contain point and mean data from maps or from direct measurements.

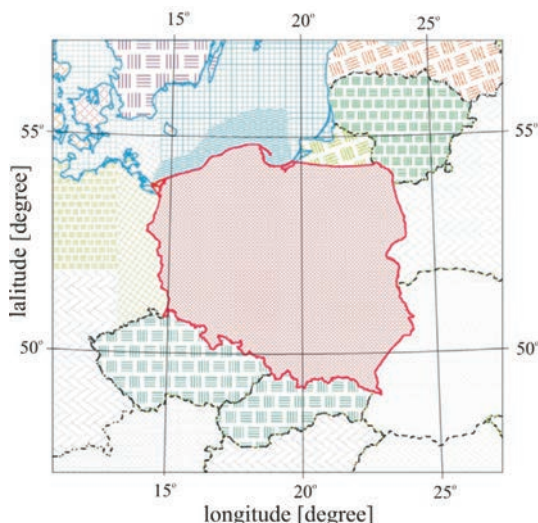


Fig. 1. Distribution of terrestrial and marine gravity data

Vertical deflections

Archival astrogeodetic data are kept in eleven catalogues calculated in years 1967–1981. They do not contain any materials from the area of Poland to 1939. Unfortunately the archival materials are not source materials and do not contain the results of astronomical observations.

Archival astronomical data kept in repository contain mean value of determined coordinates together with the epoch of observation (time). They possess also information concerning the number of observed star pairs, the method of observation, used instrument and star catalogue used to reduction of observation. Generally, observations were reduced on the bases of the catalog FK3. In ten cases the catalog FK4 was used and three observations were reduced using Chelberger catalogue.

Saved information also contains the values of the reduction to the conventional mean pole and correction to the TU1 time system according to the conventions of International Astronomical Union. These deflections were reduced on geoid (BOKUN 1961b, p. 116).

Various instruments and different methods were used in astronomical observations and coordinate computation. For latitude determination Talcott,

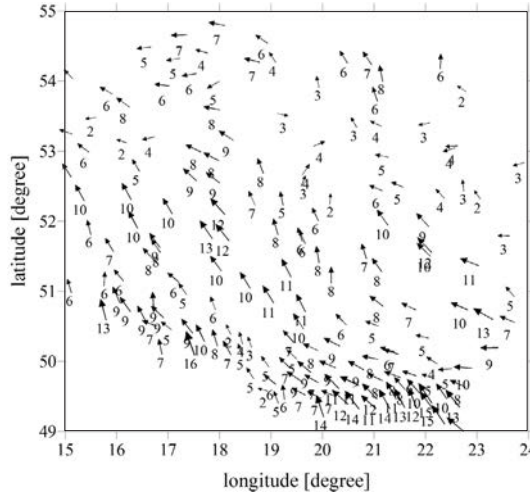


Fig. 2. Distribution of 171 astrogeodetic vertical deflections referred to GRS80 ellipsoid
(all values in second of arc)

Sterneck and Piewcow methods were used. In the case of longitude determination Zinger and Mayer methods were applied.

Existing astronomical data contain 171 points (Fig. 2). The standard error of vertical deflection of ξ and η was estimated on $\sigma_{\xi} = \pm 0.2''$ and $\sigma_{\eta} = \pm 0.3''$ (BOKUN 1961) while in (KAMELA 1975, p. 12) accuracy of both components is evaluated as $\pm 0.45''$.

Topographic data

Presently in Poland there are two available numerical terrain models, namely model DTED (*Digital Terrain Elevation Data*) and model SRTM (*Shuttle Radar Topography Mission*).

The model DTED was worked out according to the NATO standards by polish military group. As source material in this study military topographical maps in scale 1:50 000 with the contours interval 10 m in the horizontal system of coordinates called system "1942". Horizontal coordinates of the model were expressed in WGS84 system, however heights became referred the tide gauge in Kronsztad. Resolution of the model in the northern part of Poland is $1' \times 2'$, and for the southern part is $1' \times 1'$. The accuracy of the vertical component of the model on the area of Poland is estimated on $\pm 2 - \pm 7$ meters, while horizontal accuracy of the model is estimated on $\pm 15 - \pm 16$ meters.

Quasigeoid from gravity data

Stokes integral

In order to calculate the gravimetric quasigeoid, equation (1), from gravity data using Stokes integral, in the first step the geoid undulation N_{GM} and gravity anomalies Δg_{GM} from EGM08 model were computed using *geocol* software for the territory $47^{\circ} < \varphi < 57^{\circ}$, $11^{\circ} < \lambda < 27^{\circ}$ on a grid $1.5' \times 3.0'$ (Table 1).

Table 1

Statistics of computed N_{GM} , Δg_{GM} from EGM08 model

Specification	Number of points	Mean	Std dev	Min.	Max
N_{GM} [m]	128 721	34.21	6.98	19.34	52.03
Δg_{GM} [mGal]	128 721	1.18	19.93	-72.66	212.63

In the next step the residual anomalies from the area of Poland and neighboring countries (202 403 values) were computed using *geoip* software (Fig. 3). Such residual anomalies on the territory of Poland are very small, usually 2 mGal, and they do not exceed value of 4 mGal what means that the EGM08 model well represent Polish gravity field.

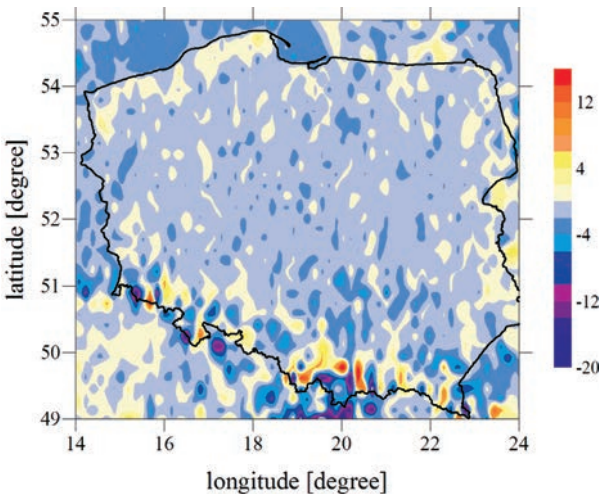


Fig. 3. Residual anomalies (isoline 2 mGal)

The evaluation of Stokes integral by FFT method require the distribution of gravity data on a regular grid. The interpolation of gravity data on a grid $1.5' \times 3.0'$ were done by least square collocation method using *geogrid* software. First the empirical covariance function of reduced due to EGM08 model mean $1' \times 1'$ for the area of Poland were computed (Fig. 4). Then the parameters of such empirical covariance function were determined. The computation were dane using *gpfit* from GRAVSOF Software.

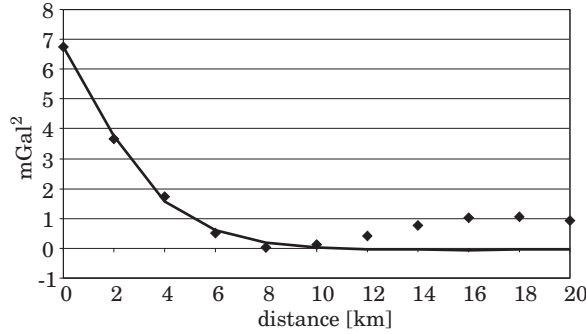


Fig. 4. Empirical covariance function of residual gravity anomalies (blue rhombus) and fitted analytical logarithmic function (red line)

The numerical value of the estimated parameters are the following: root square of the residual anomalies is $\sqrt{C_0} = \sqrt{6.76} = 2.6$ mGal, the correlation length is $\xi = 2.55$ km, the parameter D is 1 km and parameter T is equal 5 km. These parameter were used in interpolation of a mean Faye anomalies on a grid $1.5' \times 3.0'$. It yields the residual gravity data set which was used in further computation.

Next residual geoid ellipsoid undulations $N_{\Delta g_{\text{res}}}$, according to the formula (8), were computed. The term N_H was computed from formula (10) using SRTM3 topographic heights in a grid $1.5' \times 3.0'$. In this computation the density ρ was assumed equal 2.67 g cm^{-3} . The result of N_H computation are shown on Fig. 5. It is seen that cogeoid corrections for the main part of Poland do not exceed -3 mm, in the mountains is not bigger than -50 mm.

After that the geoid model was computed and then transform into the quasigeoid by adding the correction computed from the formula (11). In order to compute quasigeoid corrections the knowledge of Bouguer anomalies is necessary. The Bouguer anomalies were estimated from available Faye's anomalies by the formula

$$\Delta g_B = \Delta g_F - 0.1119 \times H \quad (12)$$

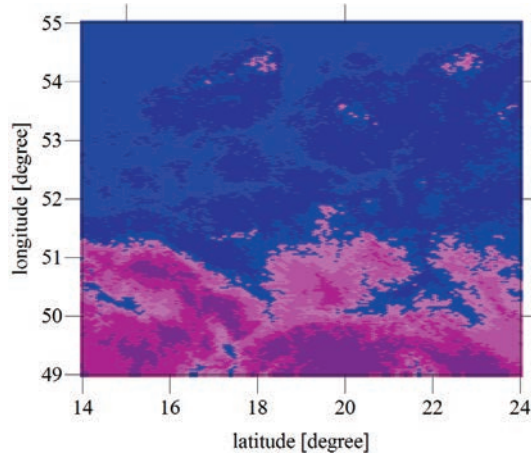


Fig. 5. Cogeoid correction N_H for the area of Poland. All correction are negative. Blue from 0 to -1 mm, dark blue from -1 to -2 mm, pink from -2 to -3 mm, dark pink from -17 to -620 mm

for the area of $47^\circ < \varphi < 57^\circ$, $11^\circ < \lambda < 27^\circ$ on a grid $1.5' \times 3.0'$, where H is a height obtained from model SRTM30 or SRTM3. The final result of computation is shown on Fig. 6.

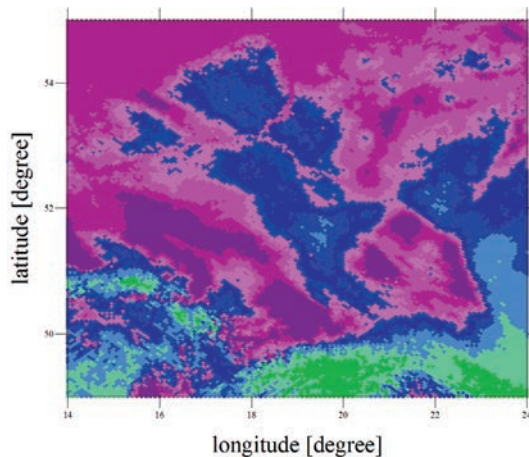


Fig. 6. Quasigeoid correction for the area of Poland. Dark pink from -11 to 0 mm, pink from 0 to 1 mm, light pink from 1 to 2 mm, blue from 3 to 6 mm, green from 17 to 766 mm

From Fig. 6 it is seen that the sign of correction depend on the sign of Bouguer anomaly and on the main part of Poland is few millimeter while in mountains can reach value even plus 80 cm.

The quasigeoid model computed in this chapter from gravity data by the FFT method was called *quasi09a*.

Collocation approach

Subsequently from the same gravimetric data the next gravimetric model of the quasigeoid was computed by the least square collocation method. Taking into account parameters of the empirical covariance function computed in previous chapter the residual geoid distances of the geoid from ellipsoid were computed by the collocation method, equation (6), using *gpcol* software. They were computed on a grid $1.5' \times 3.0'$ for the area $47^\circ - 57^\circ; 11^\circ - 27^\circ$.

Because of a large number of gravity data, computation of residual geoid heights was not possible in one step. Therefore the consider area was divided into 160 blocks $1^\circ \times 1^\circ$ each. For each block the gravity data was prepare in three data sets (Fig. 7). First set contained all accessible data for the area $1.2^\circ \times 1.4^\circ$. In the second set data were collected from the surrounding area on width $1^\circ \times 2^\circ$ on a grid $3.0' \times 6.1'$. In the third data set the data were collected for the remaining area with a mesh $9.0' \times 18.0'$ (Fig. 7).

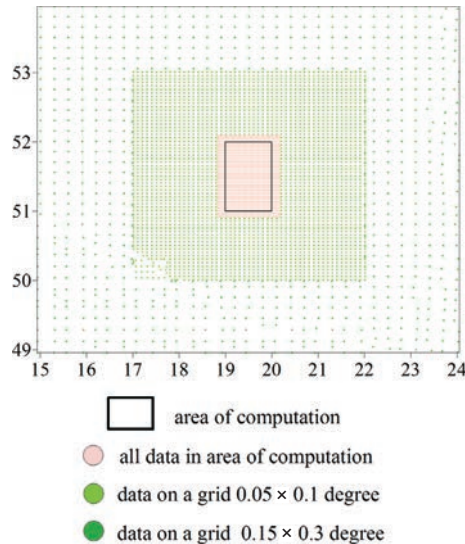


Fig. 7 The way in which gravity data for the block $51^\circ - 52^\circ; 19^\circ - 20^\circ$ was formed

From the results of computation in 160 blocks the final solution was created by adding all blocks together. The residual geoid ellipsoid separations were calculated for the area $47^\circ - 57^\circ; 11^\circ - 27^\circ$ with a mesh $1.5' \times 3.0'$. Together

with geoid computation first time in Poland the accuracy of computed residual geoid separation were estimated and the results are shown on Fig. 8. From the Fig. 8 appears that the accuracy of the term $N_{\Delta g_{res}}$ is from ± 3 – to ± 4 mm.

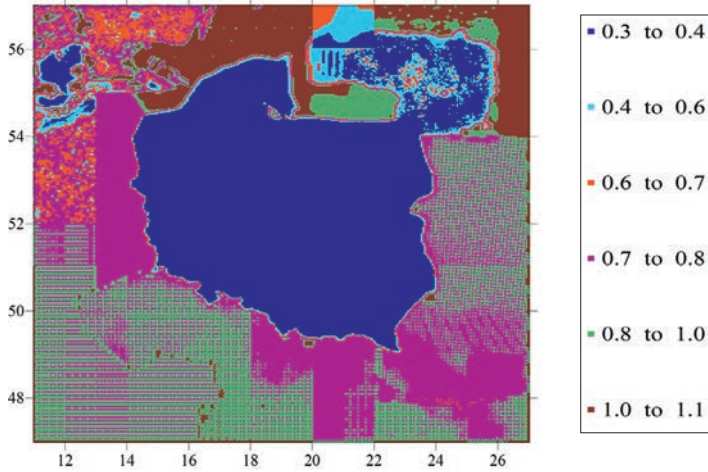


Fig. 8. Error distribution (in cm) of residual geoid ellipsoid separation $N_{\Delta g_{res}}$ computed by the least squares method from gravity data for the area of Poland

The final geoid solution was obtained applying formula (1) and then quasigeoid solution was obtained through the transformation of the geoid into quasigeoid according to the formula (11). Computed in such a way the gravimetric model of the quasigeoid was called *quasi09c*.

Quasigeoid from gravity data and vertical deflections

Combined quasigeoid from gravimetric data and astrogeodetic vertical deflection was calculated according the rules given in sec. 2. In our calculation residual gravity anomalies (Fig. 3) and residual vertical deflections ξ and η referred to EGM08 model were used. Mean value of residual gravimetric anomalies is -0.93 mGal, while mean value for the vertical deflection is -0.15' for the component ξ and 0.13' for the component η . It means that the EGM08 model well represents the gravity field of Poland.

From residual data i.e. gravity anomalies and vertical deflections, the term $N_{\Delta g_{res}}$ by the least squares collocation was computed (eq. 6). These calculation were done for each $1^\circ \times 1^\circ$ block and final residual solution was obtained by summation all computed blocks. The combined geoid was obtained by the adding indirect effect (eq. 11) and quasigeoid was obtained by transforming

geoid into quasigeoid accordingly with (eq. 11). Such computed quasigeoid model was called *quasi09b*.

Accuracy assessment and quasigeoid comparison

In the present chapter three computed models, namely:

- model *quasi09c* computed from gravimetric data by least squares collocation,
 - model *quasi09a* computed from gravimetric data by FFT method,
 - model *quasi09b* computed from gravimetric and vertical deflection data by the least squares collocation method,
- were evaluated on the satellite GPS/levelling networks.

The quasigeoid evaluation is based on the comparison the quasigeoid distances $\zeta^{\text{gps/niw}}$ computed from satellite GPS observations and levelling of the POLREF network with distances ζ^{grav} from appropriate gravimetric models.

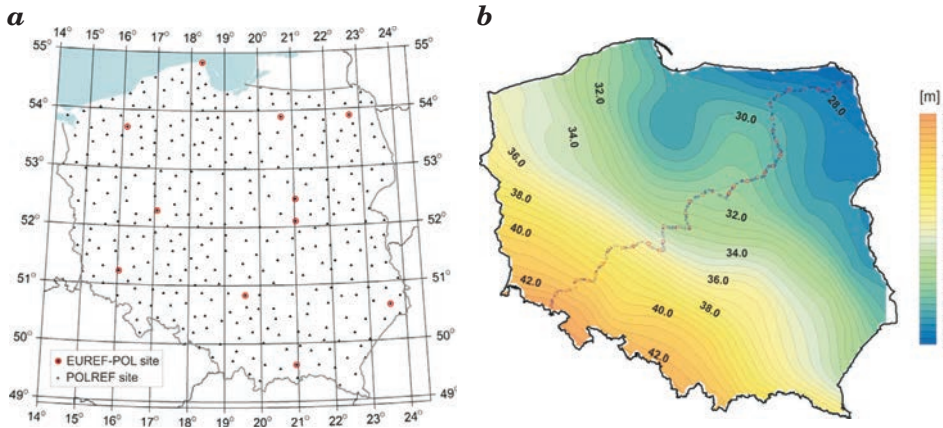


Fig. 9. EUREF-POL92 i POLREF points (a) and precise traverse (b)

For verification of quasigeoid models as well as for estimation of their accuracy and evaluation of interpolation algorithms used for application of GPS/levelling quasigeoid, a GPS/levelling control traverse has been established across Poland (KRYNSKI 2006). The traverse of 868 km surveyed in 2003–2004 consists of 190 stations (1/4.6 km) of precisely determined ellipsoidal and normal heights.

Observation strategy developed and processing methodology applied ensure accuracy of quasigeoid heights at traverse points at a centimeter level. The 49 stations of the traverse considered as the 1st order control were

surveyed in one or two 24 h sessions. The remaining 141 stations were surveyed in 4h sessions. The coordinates of 1st order control were determined using the EPN strategy with the Bernese v.4.2. Accuracy of the coordinates determined in such a way is at the level of single millimeters. The coordinates of 141 points were calculated using the Pinnacle program with the 1st order control as reference (CISAK, FIGURSKI 2005).

In order to estimate the absolute accuracy of the gravimetric model the differences

$$\varepsilon_i = \zeta_i^{\text{gps/niw}} - \zeta_i^{\text{graw}} \quad (13)$$

were computed in each point of satellite GPS network and the mean value was a valuated from

$$\hat{x} = \frac{1}{n} \sum_{i=1}^n \Delta_i \quad (14)$$

The empirical standard deviation is computed from

$$\hat{\sigma} = \pm \sqrt{\frac{\sum \varepsilon_i^2}{n-1}} \quad (15)$$

which gives the numerical description of the accuracy of the tested quasigeoid model.

Below are given the results of the accuracy evaluation of the models: *quasi09a*, *quasi09b* and *quasi09c* at the POLREF network (Table 2) and precise traverse points (Table 3).

From the results given in Table 2 it is seen that the model *quasi09c* computed by collocation method is visible (8%) more exact then the model *quasi09a* computed from the same data but by FFT method. From the Fig. 10 results that the differences between these two models are on the level of two decimeters.

Table 2

Accuracy evaluation of models *quasi09a*, *quasi09c* i *quasi09b* (in m) at 360 points of POLREF network (bias in not removed)

Specification	<i>quasi09a</i>	<i>quasi09c</i>	<i>quasi09b</i>
Mean	0.374	0.181	0.180
Std dev	0.035	0.032	0.032
Min.	0.241	0.103	0.103
Max	0.482	0.309	0.308

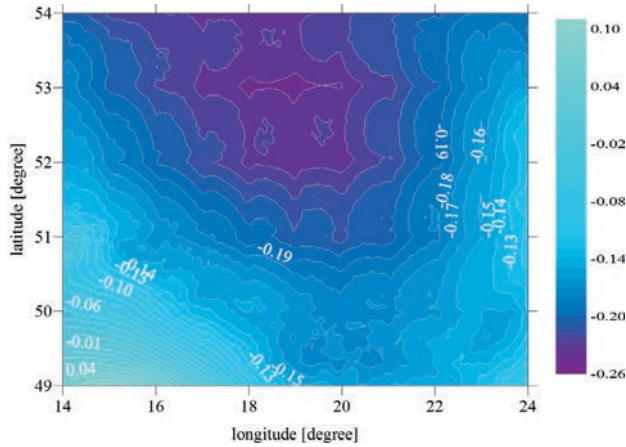


Fig. 10. Differences between the *quasi09a* and *quasi09c* models at POLREF sites (isolines 1 cm)

Considerably better accuracy of computed models was obtained when they were tested at precise traverse points (Table 4). From the quoted table results that the *quasi09c* model computed by least squares collocation method is a significantly (33%) better than model *quasi09a* computed from the same data but by FFT method. From the Fig. 10 results that the differences between these two model are 1–2 dm on the area of Poland and bias about -20 cm is visible (see Fig. 11).

Table 3
Accuracy evaluation of models *quasi09a*, *quasi09c* and *quasi09b* (in m) at the 190 points of precise traverse (bias in not removed)

Specification	<i>quasi09a</i>	<i>quasi09c</i>	<i>quasi09b</i>
Mean	0.348	0.141	0.140
Std dev	0.027	0.018	0.018
Min.	0.279	0.093	0.091
Max	0.401	0.187	0.187

Influence of additional data i.e. astro-geodetic vertical deflection on the accuracy of gravimetric quasigeoid computed by least squares method do not improve in visible way such combined solution.

Impact of vertical deflection data on the pure gravimetric solution results from -2 mm to +1 mm (see Fig. 12 and Fig. 13)

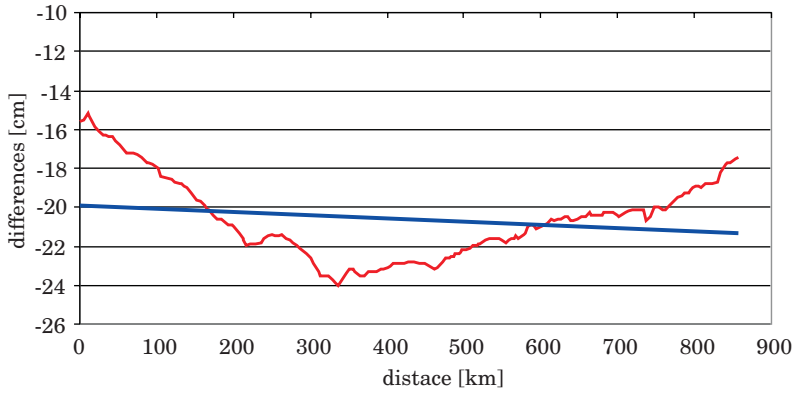


Fig. 11. Differences between the *quasi09a* and *quasi09c* models at the 190 points of precise traverse – red line, and bias – blue line

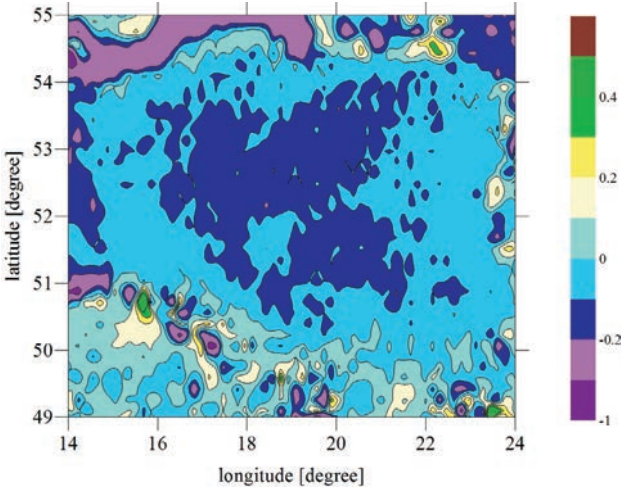


Fig. 12. Differences between the *quasi09b* and *quasi09c* models at the 360 POLREF sites (isolines 1 cm)

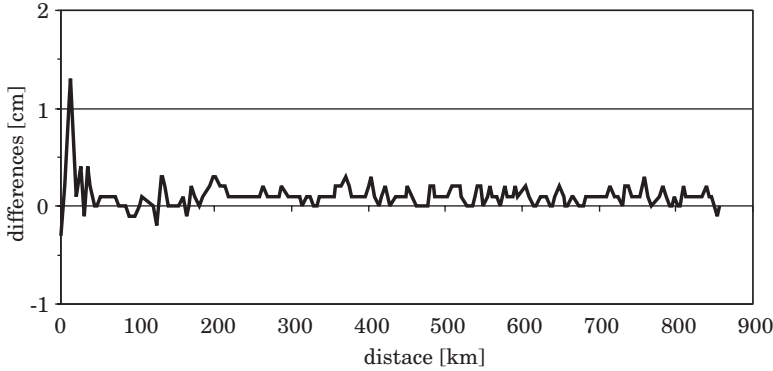


Fig. 13. Differences between the *quasi09b* and *quasi09c* models at the 190 points of precise traverse

Summary and conclusions

The gravimetric models of quasigeoid were computed using “remove-restore” technique. In this quasigeoid modelling EGM08 potential model was used since it is five time better than the last EGM96 model and can be characterized (in absolute sense) by the empirical standard deviation from ± 2 to ± 3 cm (ŁYSZKOWICZ 2009).

Gravity data used in geoid modelling comprise gravity anomalies from Czech Republic, Slovakia, Hungary, Romania, West Ukraine, Byelorussia, Lithuania, Latvia, Denmark, Germany and the main amount of gravity data was from Poland. Additionally in quasigeoid modelling the topographical data were used, namely DTED and SRTM model.

Gravimetric quasigeoid from gravity data was computed by the FFT method (*quasi09a*) and by the least squares collocation method (*quasi09c*).

Simple accuracy evaluation of *quasi09a* model at the 360 points of POLREF network gives value ± 3.5 cm, while the identical evaluation at the 190 points of precise traverse gives value ± 2.7 cm.

In order to assess the quality of the least squares collocation the quasigeoid from the same data again was computed. This model was computed using *gpcol* software, which main part is logarithmic model of covariance function proposed by R. Forsberg (FORSBERG 1987).

Logarithmic function was fitted to the mean residual gravity anomalies from the territory of Poland and then following parameters were obtained: $\sqrt{C_0}$ mGal, $D = 6$ km, $T = 30$ km. These parameters were used in *quasi09c* computation. Because of large number of the gravity data residual geoid distances were computed for the 160 block with size $1^\circ \times 1^\circ$. One estimates that the accuracy of *quasi09c* model evaluated at 360 points of POLREF network is ± 3.2 cm and evaluated at 190 points of precise traverse is ± 1.8 cm.

The third quasigeoid model *quasi09b* was computed from gravity and vertical deflection data and EGM08 geopotential model. Evaluated accuracy of this model at the POLREF network is ± 3.2 cm, while evaluated at the points of precise traverse is ± 1.8 cm.

Finally we can state that quasigeoid computed by least square collocation method gives better results then by FFT method.

In the last years a considerably progress in precision of geoid calculation from decimeters to centimeters was achieved. In case of decimeters accuracy the result of calculation by FFT or collocation method was identical. At present when the residual geoid ellipsoid separations on the area of Poland are calculated with accuracy 3 – mm (see Fig. 8) appears that local solution by collocation is better than regional solution by FFT.

Inclusion additional data i.e. components of astro-geodetic deflections of the vertical in our case gives difference of few millimeters (Fig. 12) and tests conducted at the POLREF network and precise traverse do not show, in terms of standard deviation, which solution is better.

Acknowledgement

The research was supported by the Polish State Committee for Scientific Research (grant N N526 2163 33). The author desire express thankful to dr Gabriel Strykowski from Danish National Space Center for *geocol* software program, to dr Grażyna Kloch-Główka for realization of practical geoid computation by collocation method and to prof. Jan Kryński from Institute of Geodesy and Cartography for the GPS/levelling data relating to the traverse.

Accepted for print 22.06.2010

References

- AL MARZOOQI Y., FASHIR H., SYED ILIYAS A., FORSBERG R., STRYKOWSKI G. 2005. *Progress Towards a Centimeter Geoid for Dubai Emirate*. FIG Working Week 2005 and GSDI-8 Cairo, Egypt April 16–21, 2005.
- BOKUN J. 1961. *Geoid determination in Poland on the base of astrogravimetric and gravity data*. Prace IGiK, t. VIII, 1(17).
- CISAK J., FIGURSKI M. 2005. *Control GPS/levelling traverse*. II Workshop on Summary of the project on a cm geoid in Poland, 16–17 November 2005, Warsaw (CD).
- FORSBERG R. 1987. *A New Covariance Model for Inertial Gravimetry and Gradiometry*. Journal of Geophysical Research, 92(B2): 1005–1010.
- KRYŃSKI J. 2007. *Precyzyjne modelowanie quasi-geoidy na obszarze Polski – wyniki i ocena dokładności*. Instytut Geodezji i Kartografii, Seria Monograficzna, 13.
- ŁYSZKOWICZ A. 2009. *Assessment of accuracy of EGM08 model over the area of Poland*, Technical Sciences, (12): 118–134.
- ŁYSZKOWICZ A., KRYŃSKI J. 2006. *Regional quasi-geoid determination in the area of Poland*, Proceedings of the 5th FIG Regional Conference, Accra, Ghana, March 8–11, pp. TS15/1–17.
- MORITZ H. 1989. *Advanced physical geodesy*. Second edition, Wichmann.
- TORGE W. 2001. *Geodesy*. Third edition, de Gruyter.
- TSCHERNING C., FORSBERG R., KNUDSEN P. 1992. *The GRAVSOFT package for geoid determination*. First Continental Workshop On The Geoid In Europe “Towards a Precise Pan-European Reference Geoid for the Nineties” Prague, May 11–14.
- Geoid and its geophysical interpretations*. 1994. Eds. P. Vaniček, N.T. Christou. CRS Press.

ACCURACY EVALUATION OF THE SUCCESSIVE CAMPAIGNS OF THE PRECISE LEVELLING IN POLAND

Adam Łyszkowicz¹, Anna Bernatowicz²

¹ Chair of Land Surveying and Geomatics
University of Warmia and Mazury in Olsztyn

² Chair of Land Surveying
Koszalin University of Technology

Key words: levelling networks, random errors, systematic errors.

A b s t r a c t

In the paper the evaluation of accuracy of the four successive campaigns of the precise levelling in Poland is presented. Estimation of accuracy was conducted by the: traditional, Lallemand and Vignal formulas. From the conducted evaluations results, that the successive campaigns are characterize by the more and more small random errors. It can be interpreted that better instruments and measuring methods were used in the successive campaigns. However the systematic errors remain almost the same what can be interpreted that the influence of such factors like the topography, climate (refraction) and vertical movements is always the same on the area of Poland. Considerable divergences in the evaluation of systematic errors from Lallemand's and Vignal's formulas suggest that the model of systematic errors adopted by Vignal is probably not realistic and it requires further investigations.

OCENA DOKŁADNOŚCI KOLEJNYCH KAMPANII NIWELACJI PRECYZYJNEJ W POLSCE

Adam Łyszkowicz¹, Anna Bernatowicz²

¹ Katedra Geodezji Szczegółowej
Uniwersytet Warmińsko-Mazurski w Olsztynie

² Katedra Geodezji Gospodarczej
Politechnika Koszalińska

Słowa kluczowe: wyrównywanie sieci niwelacyjnych, błędy przypadkowe, błędy systemowe.

A b s t r a k t

W pracy przedstawiono ocenę dokładności czterech kolejnych kampanii niwelacji precyzyjnej w Polsce. Dokładność oszacowano wzorami: tradycyjnymi, Lallemanda i Vignala. Z oszacowań wynika, że kolejne kampanie są obciążone coraz mniejszym błędem przypadkowym, co można

interpretować coraz lepszą dokładnością instrumentów i metod pomiarowych, podczas gdy błąd systematyczny pozostaje prawie taki sam, co można interpretować wpływem stałych na danym obszarze czynników, jak topografia, klimat (refrakcja) i ruchy pionowe skorupy ziemskiej. Znaczne rozbieżności w ocenie błędów systematycznych wzorami Lallemenda i Vignala sugerują, że model błędów systematycznych przyjęty przez Vignala jest mało realistyczny i zagadnienie to wymaga dalszych badań.

Introduction

Until now the four campaigns of the precise levelling were realized in Poland. The first campaign in years 1926–1937, the second in years 1953–1955, the third in years 1974–1982 and the last (fourth) in years 1999–2003. The evaluation of the accuracy of these campaigns was conducted using mostly the traditional formulas. The results of these estimates are spread out in many works. For example the accuracy of the first campaign, evaluated by the traditional formulas only, is given in (*Katalog...* 1939). The evaluation of the accuracy of the second campaign by the Vignal formulas is given in (WYRZYKOWSKI 1969) and the evaluation of the accuracy of the second and third campaign in the traditional way and by Lallemend's formulas is given in (WYRZYKOWSKI 1988). The evaluations of the accuracy of the campaign IV by the use of traditional formulas is given e.g. in the paper (GAJDEROWICZ 2005).

The aim of the present work is collection of scattered information concerning networks accuracy and calculation of lacking accuracy evaluation of every campaign if only it is possible. In the first step of the present work successive four campaigns of the precise levelling in Poland are characterized. Then it is given in a large shortcut the basic information relating to the traditional formulas as well as Lallemend's and Vignal's formulas. Next estimation of the accuracy of the campaign I was conducted by the Lallemend's and Vignal's formulas and then estimation of the campaign IV by the traditional, Lallemend's and Vignal's formulas. The results of these calculations, were next completed by estimates from the literature, then were taken down in a suitable tables and introduced on suitable drawings.

Description of the successive campaigns of precise levelling in Poland

The first precise levelling campaign began in 1926 and was finished in 1937. The network consists of 5 907 sections, 121 lines and 36 loops (Fig. 1). Total length of the levelling lines is 10 046 km.

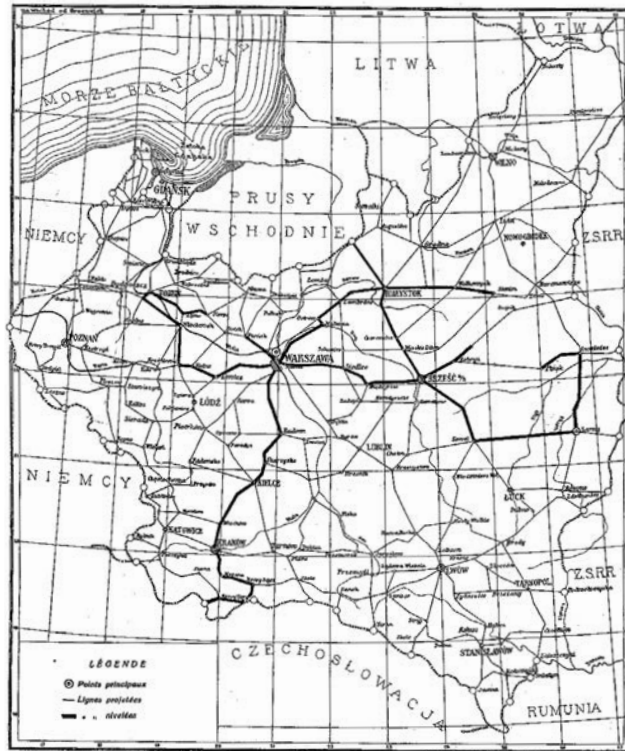


Fig. 1. The levelling network of the first campaign

The levelling lines were measured by the precise optical levels Zeiss III with parallel plate. The observed height differences were corrected due to rod scale and normal orthometric corrections. The adjustment of the levelling network was carried out by the condition method with fixed height of the benchmark in Toruń referred to Amsterdam tide gauge. After adjustment the standard deviation of height difference was $\pm 1.04 \text{ mm} \sqrt{\text{km}}$ (*Katalog...* 1939).

The second levelling campaign was carried out in two stages. The first measurements were done in 1947–1950, and the second measurements in 1953–1955. The second version of network comprises of 4 500 sections, 60 levelling lines and 12 loops. Total length of levelling lines is 5 778 km. The levelling lines were measured by precise levels Aerogeopribor NA-1 and Wild N III with parallel plates. The observed heights difference was corrected due to rod scale and normal corrections. Gravity necessary to calculate normal Molodensky corrections was referred to Potsdam Gravity System. The first adjustment of the levelling network was carried out by the parametric methods with fixed height of one benchmark in Toruń. The second and final adjustment

was carried by parametric method assuming several bench marks as fixed. The results of this adjustments gives the standard deviation of height difference equal $\pm 0.78 \text{ mm}\sqrt{\text{km}}$ (WYRZYKOWSKI 1988). The final results of the adjusted heights of benchmarks are collected in (*Katalog...* 1960) which is described e.g. in (ŁYSZKOWICZ et. al. 2003).

The third levelling campaign was measured in 1974–1982. The network consists of 15 827 sections, 371 lines and 135 loops. The total length of levelling lines is 17 015 km. The levelling lines were measured by automatic levels: Opton Ni1 and Zeiss Ni002. The following corrections were implemented to the raw data: rod scale corrections, rod temperature corrections, tidal corrections, normal Molodensky corrections. The final adjustment of the entire network was carried out in a few versions. In 1985 the accepted solution was obtained as a least square approach with stations constrains. Heights of 23 bench marks with their estimated accuracy (from new UPLN solution) was incorporated to the adjustment. After adjustment the standard deviation of height difference was $\pm 0.844 \text{ mm}\sqrt{\text{km}}$ and standard deviation of adjusted heights changes between $\pm 6.5 \text{ mm}$ and $\pm 11 \text{ mm}$ (WYRZYKOWSKI 1988). The final results of the adjusted heights of benchmarks are collected in (*Katalog...* 1982) which is described e.g. in (ŁYSZKOWICZ et. al. 2003).

The fourth precise levelling campaign started in 1999 and was finished in 2003 (Fig. 2). The network consists of 16 150 sections with average length 1.1 km, 382 lines with average length about 46 km, 135 loops, and 245 nodal points. Total length of levelling lines is 17 516 km. The levelling lines were measured with Zeiss Ni002 (66% measurements), Zeiss DiNi 11 (31% measurements), Topcon NJ (3% measurements) e.g. (PACZUS 2001). As in the case of the third campaign the rod scale corrections, rod temperature corrections, tidal corrections and normal Molodensky corrections were introduce to the raw height differences.

The first, the simplest assessment of a successful network adjustment of the fourth campaign is described in (ŁYSZKOWICZ, JACKIEWICZ 2005). The adjustment of the network was done as the minimally constrained adjustment and the standard deviation of height differences equal $\pm 0.88 \text{ mm}\sqrt{\text{km}}$ was obtained. Identical evaluation of the accuracy of the campaign IV was obtained in the network adjustment carried out in the study (GAJDEROWICZ 2005).

Discrepancies between forward and backward levelling of a section, line and the loop misclosures

In the present study we assume height differences δH of a section or height differences ΔH of a line from the forward and backward levelling as a “observations”.

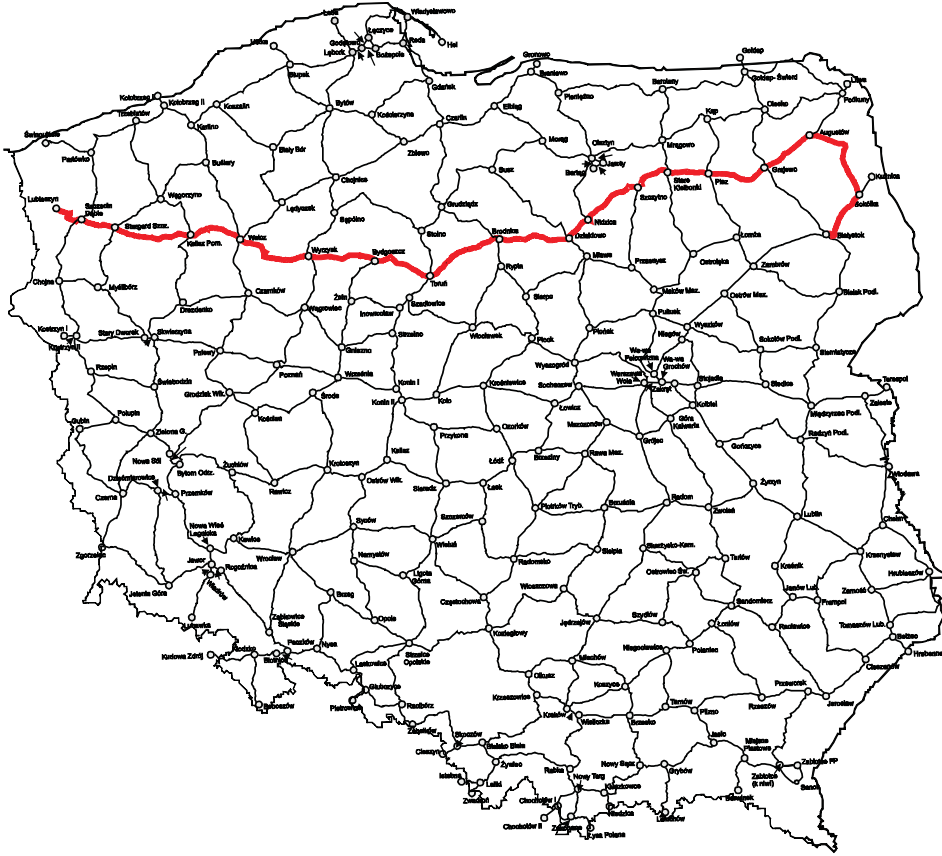


Fig. 2. The levelling network of the fourth campaign

The difference between forward and backward levelling of a section is define by the formula:

$$\rho = \delta H^g - \delta H^p \quad (1)$$

where δH^g is a height difference from the forward measurement and δH^p is a height difference from the backward measurement.

The discrepancy λ of a forward and backward levelling of a line is defined by the formula

$$\lambda = \Delta H^g - \Delta H^p = \sum_{i=1}^n \rho_i \quad (2)$$

where ΔH^g is height difference of a line from the forward levelling and ΔH^p is height difference of a line from the forward and backward levelling and n the number of section of a line.

The loop misclosures φ is compute from the formula

$$\varphi = \sum \Delta H_i^{sr} \quad (3)$$

where ΔH_i^{sr} is a mean height differences of the i line included in the loop (WARCHAŁOWSKI 1954, p. 374) and n is the number of the lines which form the loop.

In a case of the first campaign the discrepancies λ and φ are available only from (*Katalog...* 1939), while for the second campaign we did not have access to any discrepancies. In the case of the third campaign the discrepancies φ are available in (WYRZYKOWSKI 1988) and in the last case all discrepancies are available for the present study. Statistical characteristic of the discrepancies ρ , λ , φ for the successive levelling campaigns are given in Table 1.

Table 1

Statistical characteristic of the discrepancies ρ , λ , φ (in mm) of the successive levelling campaigns in Poland

	ρ	λ	φ
Campaign I			
Number	–	121	36
Mean	–	–2.18	–0.32
Std dev	–	± 14.32	± 23.56
Min	–	–56.00	–43.80
Max	–	34.50	43.20
Relevant data from campaign II are not available			
Campaign III			
Number	–	–	136
Mean	–	–	–0.39
Std dev	–	–	± 14.79
Min	–	–	–36.49
Max	–	–	30.45
Campaign IV			
Number	16 132	382	133
Mean	0.07	2.72	0.27
Std dev	± 0.78	± 6.88	± 12.54
Min	–23.83	–20.41	–31.49
Max	17.72	20.83	28.83

From the Table 1 results that the most data of the section, line and loop misclosures are available for the first and third campaign, and there is no data for the second campaign while all data are available for the fourth campaign.

From the comparison of the loop misclosures of the levelling campaigns results that the mean value of the discrepancies φ in all campaigns are comparable (the same systematic factors), however standard deviation of the discrepancies getting smaller – even twice – what means that the instruments and methods of the measurement are more and more precise.

Accuracy evaluation of the successive campaigns of the precise levelling

Traditional formulas

During the last one hundred and fifty years several methods of evaluation of accuracy of precise levelling were proposed. These methods are exactly described in the work (JORDAN et al. 1956, p. 223–255). The requirements which the precise levelling has to fulfill were defined first time during the second Surveyor Assembly in Berlin in 1897, and next were specified in 1871. As the results of these considerations to the evaluation of the accuracy of height differences from precise levelling the following formula was proposed

$$m_1^2 = \frac{1}{4n_l} \sum \frac{\rho^2}{l} \quad (4)$$

where ρ is discrepancies between forward and backward levelling of a section, n_l is a number of sections and l is the length of a section in km.

In this formula accidental and systematic errors which affect the levelling measurements are considered simultaneously.

The same accuracy evaluation can be obtained from the discrepancy λ of a forward and backward levelling of a line from the formula

$$m_2^2 = \frac{1}{4n_L} \sum \frac{\lambda^2}{L} \quad (5)$$

where L is the length of a line in km and n_L is the number of a lines.

The next information about the accuracy of the levelling network is included in the loop misclosures. The mean error of levelling can be computed from the formula

$$m_3^2 = \frac{1}{n_F} \sum \frac{\varphi^2}{F} \quad (6)$$

where φ is the loop misclosures in millimeters and F is the length of a loop in km, and n_F is a number of the loops.

The mean errors of the levelling network considered above can be evaluated before the network adjustment. After adjustment the accuracy of levelling network can be evaluated from the residuals v_i

$$m_o^2 = \frac{1}{n - u} \sum p v^2 \quad (7)$$

where m_o is a mean error computed from residuals, n is the number of observations and u is the number of unknown parameters.

To evaluate the accuracy of the network of precise levelling obtained from campaign IV 16 150 discrepancies ρ from the forward and backward levelling of a sections, 282 discrepancies from the forward and backward levelling of a lines and 133 loop misclosures were used. After applying the formulas (4), (5) and (6) it yields $m_1 = \pm 0.278 \text{ mm}/\sqrt{\text{km}}$, $m_2 = \pm 0.518 \text{ mm}/\sqrt{\text{km}}$ and $m_3 = \pm 0.826 \text{ mm}/\sqrt{\text{km}}$.

The Fig. 3 illustrates the results of the accuracy evaluation of the four national campaigns of the precise levelling counted from the above mentioned formulas. Errors evaluation of the first, second and third campaign were taken from (*Katalog... 1939*) and from monograph (WYRZYKOWSKI 1988).

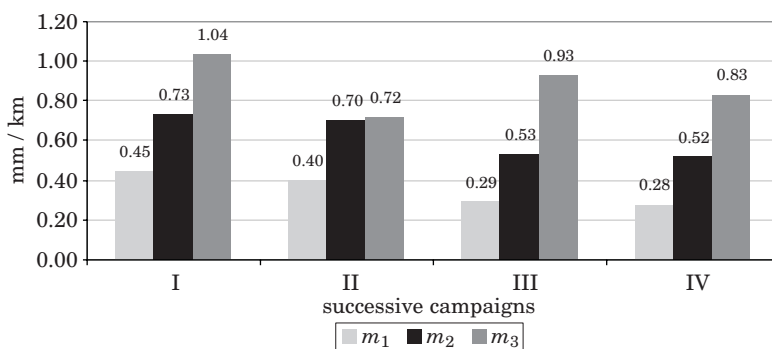


Fig. 3. Comparison of the errors m_1 , m_2 and m_3 for the four successive levelling campaigns in Poland

From the Fig. 3 also results that the error m_1 is always smaller than the error m_2 and this subsequently is smaller then the error m_3 . This regularity is fulfilled for all campaigns. This phenomenon shows the existence in the precise levelling one side acting factors which cause the growing of systematic errors. It means, that accidental and systematic errors should be considered separately in the proper way.

The value of errors m_1 , m_2 , and m_3 are getting more and more smaller in successive campaigns and it can be interpreted that instruments and methods used in the measurements are more and more exact.

For the better illustration of the accuracy evaluation of precise levelling some examples of the European levelling networks will be quoted beneath. In the case of Finnish levelling network measured in 1935–1955 we have $m_1 = \pm 0.33 \text{ mm}\sqrt{\text{km}}$, $m_2 = \pm 0.59 \text{ mm}\sqrt{\text{km}}$ and $m_3 = \pm 0.63 \text{ mm}\sqrt{\text{km}}$ (KÄÄRIÄINEN 1966). The Norwegian network measured in 1916–1953 can be characterized by $m_1 = \pm 0.84 \text{ mm}\sqrt{\text{km}}$, $m_2 = \pm 1.06 \text{ mm}\sqrt{\text{km}}$, (TROVAAG, JELSTRUP 1956), while the Dutch network has the accuracy: $m_1 = \pm 0.57 \text{ mm}\sqrt{\text{km}}$, $m_2 = \pm 0.88 \text{ mm}\sqrt{\text{km}}$ and $m_3 = \pm 1.1 \text{ mm}\sqrt{\text{km}}$ (NITTINGER, LUCHT 1971).

Lallemand formulas

The formulas for the accuracy estimation given the previous chapter, were subjected of the critical analysis on the International Conference of Surveyors in Hamburg in 1912 and finally formulas proposed by Lallemand were accepted.

Lallemand assumed that the total mean error m of the levelling is a sum of random and systematic errors and can write down by the following formula.

$$m^2 = \eta^2 L + s^2 L^2 \quad (8)$$

where η is a random error, s is a systematic error and L is the length of a line in km.

According to the Lallemand the mean random error η should be computed from

$$\eta^2 = \frac{1}{4} \left[\frac{\sum \rho^2}{\sum L} - \frac{\sum l^2}{(\sum L)^2} \sum \frac{\lambda^2}{L} \right] \quad (9)$$

where ρ is the height difference of forward and backward section levelling, λ is the height difference of forward and backward line levelling and L is the length of the line.

Mean systematic error s is computed from

$$s^2 = \frac{1}{4 \sum L} \sum \frac{\lambda^2}{L} \quad (10)$$

or using loop misclosures φ from the formula

$$s^2 = \frac{1}{\sum F^2} \left[\frac{1}{2} \sum \varphi^2 - \eta^2 \sum F \right] \quad (11)$$

where F is the length of the levelling loop.

Using the above Lallemand formulas the accuracy of the campaign IV was evaluated and for the mean random error the value $\eta = \pm 0.27 \text{ mm}/\sqrt{\text{km}}$ was received. The mean systematic error computed from λ is $s = \pm 0.08 \text{ mm}/\sqrt{\text{km}}$, while the same error computed from φ is $s = \pm 0.04 \text{ mm}/\sqrt{\text{km}}$. The total error which is the combination of accidental and systematic error, equation (8), is $m = \pm 0.28 \text{ mm}/\sqrt{\text{km}}$.

The results of accuracy evaluation of the all four campaigns of the precise levelling in Poland are presented in Table 2. The errors for first three campaigns were taken from the monograph (WYRZYKOWSKI 1988).

Table 2
Character of systematic and accidental errors of the four levelling campaigns computed by the Lallemand's formulas

Kind of error	Successive levelling campaigns			
	I 1926–1937	II 1952–1955	III 1974–1982	IV 1999–2003
Random error η	± 0.46	± 0.37	± 0.28	± 0.27
Systematic error s Estimated from λ	± 0.08	± 0.13	± 0.08	± 0.08
Systematic error s Estimated from φ	± 0.08	± 0.11	0.04	± 0.03
Total error m	± 0.47	0.40	0.29	± 0.28

On the Fig. 4 the illustration of the Table 2 is presented.

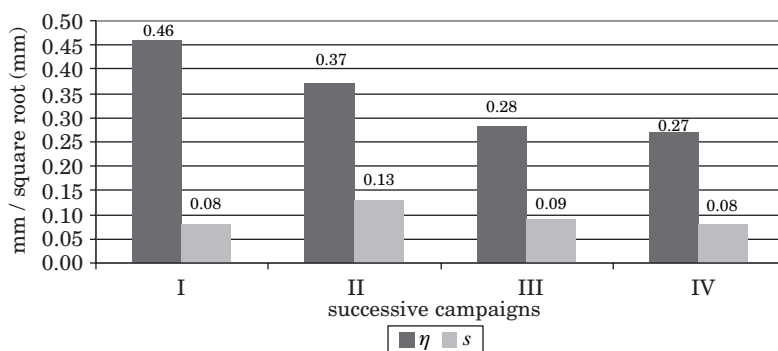


Fig. 4. The comparison of the errors η i s for the successive levelling campaigns in Poland

From the Fig. 4 result that the random error η in the successive campaigns decrease almost two times, from the value $\pm 0.46 \text{ mm}/\sqrt{\text{km}}$ to the value $\pm 0.27 \text{ mm}/\sqrt{\text{km}}$ while the systematic error remained on almost the same the

level of 0.08 mm/km. Only for the campaign II the systematic error is somewhat larger and as for now it was not possible explain this phenomenon.

Getting smaller the value of the random error is evidences about using more and more exact instruments and measuring methods. On the other hand the value of the systematic errors in all campaigns is constant what can means that these errors reflect invariable for the Polish network such conditions like topography, climate (refraction) and movements of earth crust.

The comparison of the total error m counted according to the Lallemand's formulas with the error m_1 for individual campaigns is very interesting. From Fig. 3 and the last row of Table 2 results, that between these estimates, in principle, there are not significant differences. It authorizes to stating that these evaluations are equivalent.

Vignal formulas

Since the precise levelling observations are affected by the systematic one side acting errors, therefore at the Oslo Assembly of the IAG in 1948, the levelling error formulas were again reviewed and the new resolution for the method of estimation of the levelling was adopted.

The errors were divided into two groups, random and systematic group, which were assumed independent of each others. The random errors are caused by sources which are independent in all successive observations and obey Gauss's law of error distribution. The systematic errors are due to factors acting in the similar way on the successive or neighboring levelling observations. They do not obey Gauss's law. They become random only for distance exceeding a certain limit distance Z , which is a few tens of kilometers (see Fig. 5).

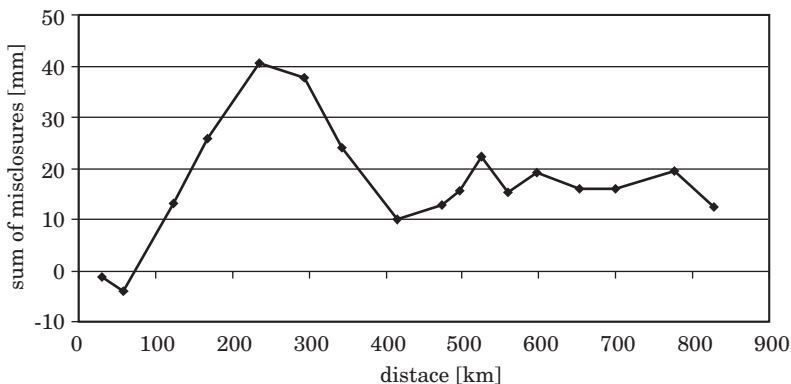


Fig. 5. Accumulation of misclosures λ for the line Szczecin-Białystok consist from 17 lines of precise levelling (see red line on Fig. 1)

From the graph shown on the Fig. 5 one clearly can see that what the value of the sum of successive misclosures λ grows up to initially distance about 220 km what means, that the on the result of the measurement has influence the systematic factor, then the sum of misclosures begins oscillate around the value of 45 mm what means that systematic errors begin to keep as accidental errors. Below are given the basic information concerning Vignal's formulas.

The mean random error limiting value of the total error τ is the limit value of

$$u_L^2 = \frac{1}{4n_L} \sum \frac{\lambda^2}{L} \quad (12)$$

where λ is a line misclosures, L is a length of a line and n_L is a number of line in the network. In the case of the campaign IV the estimation of error u_L^2 has value 0.270 mm²/km.

The mean random error is computed from

$$\eta^2 = u_r^2 - \zeta^2 \times j^2 \quad (13)$$

where u_r and j are computed from the formulas

$$u_r^2 = \frac{1}{4n_r} \sum \frac{\rho^2}{r} \quad \text{and} \quad j^2 = \frac{K}{Z} \times r_m \quad (14)$$

where ρ is a section misclosures, r is a length of a section and n_r is a number of the sections, r_m is a mean length of the section and Z , K are parameters. The value $K = 2$ and $Z = 50$ km were used here, since their values have no significance in this connection. In a case of campaign IV the error u_r^2 is 0.077 mm²/km.

The mean random limiting value of the systematic error is consequently equal

$$\zeta^2 = \tau^2 - \eta^2 \quad (15)$$

where $\tau^2 = u_L^2$. According to these formulas the total error of the fourth campaign was computed in the following way

$$\tau^2 = u_L^2 = \frac{1}{4n_L} \sum \frac{\lambda^2}{L} = 0.27 \text{ mm}^2/\text{km} \quad (16)$$

$$\tau^2 = u_F^2 = \frac{1}{n_F + 1} \left(\sum \frac{\varphi^2}{F} + \frac{\varphi_e^2}{F_e} \right) = 0.69 \text{ mm}^2/\text{km} \quad (17)$$

To determine the systematic error ζ^2 and random error η^2 the system of equations should be solved

$$\begin{cases} \eta^2 = u_r^2 - \zeta^2 \cdot j^2 \\ \zeta^2 = u_L^2 - \eta^2 \end{cases} \quad (18)$$

The solution of this system of equations was realized by the method of successive approximations. In the first approximation we found, that $\eta^2 \approx u_r^2$ and we calculated the approximate value of the systematic error ζ . Then on the basis the approximate value the error ζ we calculated second time random error η and then the systematic error ζ . The final random and systematic errors were received after three iterations i.e. $\eta = 0.26 \text{ mm}/\sqrt{\text{km}}$ and $\zeta = 0.45 \text{ mm}/\sqrt{\text{km}}$. The total error containing the random and systematic part is $\tau = \pm\sqrt{\eta^2 + \zeta^2} = 0.52 \text{ mm}/\sqrt{\text{km}}$.

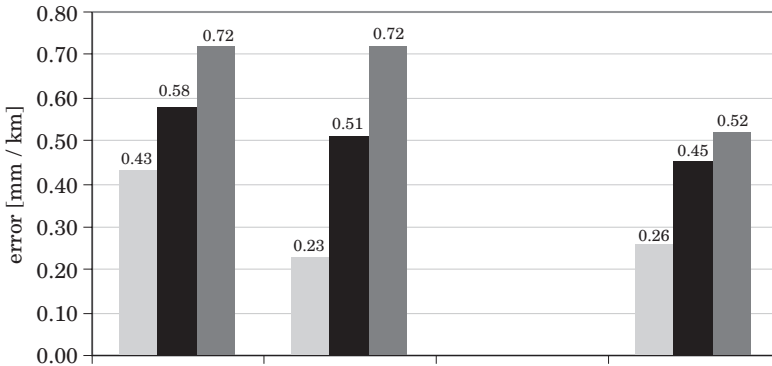


Fig. 6. Comparison of systematic and random errors computed from Vignal formulas for the successive levelling campaigns in Poland

On the Fig. 6 are presented values of the random error η , systematic error ζ and total error τ for the respective campaigns of the precise levelling in Poland. Because of the lack of data there are no evaluations for the campaign III.

From the Fig. 6 results that both the random and systematic error in the successive campaigns decrease, with the except of the random error from campaign II, which achieves exceptionally small value of $\pm 0.23 \text{ mm}/\sqrt{\text{km}}$. This evaluation was made by (WYRZYKOWSKI 1969) according to rather complicated and difficult to verifying calculations which could be incorrect.

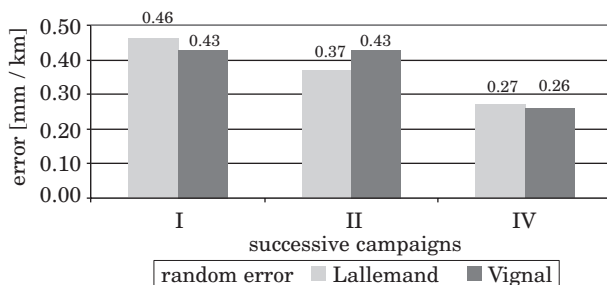


Fig. 7. Comparison of random errors computed from Lallemand and Vignal formulas for the successive levelling campaigns in Poland

On the Figs. 6 is introduced the comparison of the value of random errors counted from the Lallemand's and Vignal's formulas. It results that estimated errors from the Lallemand's formulas are somewhat larger than errors estimated from the Vignal's formulas in the case of the campaign I and II. However in the case of the campaign IV random errors computed in two different way are identical.

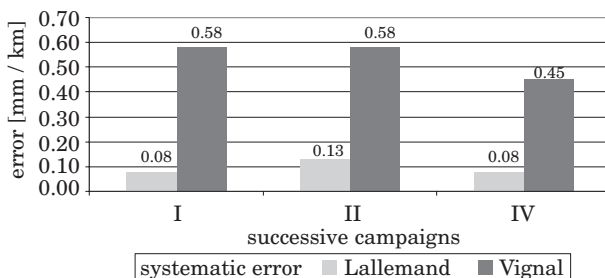


Fig. 8. Comparison of systematic errors computed by the Lallemand and Vignal formulas for the successive levelling campaigns in Poland

The comparison of systematic errors estimated from the Lallemand's and Vignal's formulas looks completely differently. From the Fig. 8 result that the systematic error computed from the Lallemand's formula is 0.08–0.13 mm/km, while the same error counted from the Vignal's formula gives four times larger value i.e. $\pm 0.45 - \pm 0.58$ mm/km. It is very difficult to say which evaluation is correct. One can affirm only, that such discrepancy proves difficulties when we trying to estimate systematic errors in the levelling networks.

Summary and conclusions

Exhausting analysis of the accuracy of the successive four campaigns of the precise levelling in Poland was described in the article. The evaluation of accuracy was conducted with utilization of traditional, Lallemand's and Vignal's formulas.

The results of the conducted evaluations confirm of the well known fact, that the error m_1 is always smaller than the error m_2 and it subsequently is smaller then the error m_3 . (Fig. 3). This regularity is fulfilled for all campaigns. This phenomenon shows the existence in the precise levelling one side acting factors which cause the accumulation of systematic errors. It means, that accidental and systematic errors should be considered separately in the proper way.

The value of errors m_1 , m_2 , and m_3 are getting more and more smaller in the successive campaigns and it can be interpreted that instruments and methods used in the measurements are more and more precise.

The random error η in the successive campaigns decrease almost two times, from the value $\pm 0.46 \text{ mm}/\sqrt{\text{km}}$ to the value $\pm 0.27 \text{ mm}/\sqrt{\text{km}}$ while the systematic error remained on almost the same level of 0.08 mm/km . Getting smaller the value of the random error is evidences about using more and more precise instruments and measuring methods. On the other hand the value of the systematic error in all campaigns is constant what can means that this error reflects invariable for the Polish network conditions like topography, climate (refraction) and movements of earth crust.

Comparison of the total error m counted according to the Lallemand's formulas with the error m_1 for each campaigns shows not significant differences. It authorizes to stating that these evaluations are equivalent.

Assessment of the value of random errors counted from the Lallemand's and Vignal's formulas shows that estimated errors from the Lallemand's formulas are almost the same than errors estimated from the Vignal formulas. However systematic error computed from these both formulas gives quite different estimations and is very difficult to say which evaluation is correct.

Accepted for print 9.08.2010

References

- GAJDEROWICZ I. 2005. *Ocena dokładności krajowej sieci niwelacji precyzyjnej I klasy pomierzonej w latach 1997–2003*. Technical Sciences, Supplement 2, UWM Olsztyn.
- GAJDEROWICZ I. 2007. *Propozycja nowego polskiego układu wysokościowego*. Geomatics and Environmental Engineering, 1(1/1).
- JORDAN W., EGGERT E., KNEISSL M. 1956. *Handbuch der Vermessungskunde*. Band III, Höhenmessung, Stuttgart.

- KÄÄRIÄINEN E. 1966, *The secon levelling of Finland in 1935–1955*, Veröffentlichungen des Finnischen Geodatischen Institute, nr. 61, Helsinki.
- Katalog wysokości reperów polskiej podstawowej sieci niwelacji (niwelacji precyzyjnej I-ego rzędu) nad poziomem morza w Amsterdamie*. 1939. Ministerstwo Komunikacji, Biuro Pomiarowe, nr PM-3a.
- Katalog punktów niwelacyjnych. Bałtycki system wysokości (zero mareografu w Kronsztadzie)*. 1960. Główny Urząd Geodezji i Kartografii M.S.W.
- Katalog*. 1982. Centralny Ośrodek Dokumentacji Geodezyjnej i Kartograficznej, Warszawa.
- ŁYSZKOWICZ A., LEWANDOWICZ E., KOWALCZYK K., OGÓREK T. 2003. *Status of the precise levelling data base*, Geodezja i Kartografija, 1: 27–30.
- ŁYSZKOWICZ A., JACKIEWICZ A. 2005. *Adjustment of polish precise levelling network using Geolab package*, Proceedings of the 6th International Conference “Environmental Engineering”, Vilnius, Lithuania.
- NITTINGER J., LUCHT H. 1971. *North west european lowlands levelling*. Deutsche Geod. Komm., Reiche B, nr 184, Munchen.
- TROVAAG O., JELSTRUP G. 1956. *Precisjonsnivellment I sjørnorge 1914–1953*. Norges Geografiske Oppmaling, Geodediske arbeider, hefte 5, Oslo.
- WARCHAŁOWSKI E. 1954. *Niwelacja geometryczna*. PPWK, Warszawa.
- WYRZYKOWSKI T. 1969. *Analiza dokładności polskiej sieci niwelacji precyzyjnej I klasy wzorami Vignala*. Prace Instytutu Geodezji i Kartografii, XVI (3/39). PPWK, Warszawa.
- WYRZYKOWSKI T. 1988. *Monografia krajowych sieci niwelacji precyzyjnej I klasy*. Instytut Geodezji i Kartografii, Warszawa.

EXPERIMENTAL SOLAR INSTALLATION WITH A SELF-ACTING CIRCULATION PUMP, POWERED BY LOCAL HEAT

Jurij Dobriański, Michał Duda

Chair of Electrics and Power Engineering
University of Warmia and Mazury in Olsztyn

Key words: solar energy, solar installation, circulation pump.

A b s t r a c t

The paper presents a diagram of an experimental solar installation with a self-acting circulation pump powered by local heat. The installation is a measuring stand which enables an assessment of this type of pumping device in terms of its practical operational efficiency. A self-acting circulation pump has been successfully tested in a laboratory.

EKSPERYMENTALNA INSTALACJA SŁONECZNA Z SAMOCZYNNA POMPĄ CYRKULACYJNĄ NAPĘDZANĄ CIEPŁEM LOKALNYM

Jurij Dobriański, Michał Duda

Katedra Elektrotechniki i Energetyki
Uniwersytet Warmińsko Mazurski w Olsztynie

Słowa kluczowe: energia słoneczna, instalacja słoneczna, pompa cyrkulacyjna.

A b s t r a k t

W pracy przedstawiono schemat eksperymentalnej instalacji słonecznej z samoczynną pompą cyrkulacyjną napędzaną ciepłem lokalnym. Instalacja ta jest stanowiskiem badawczym pozwalającym na ocenę jakości tego typu urządzenia pompującego pod względem jego praktycznej efektywności eksploatacyjnej. Samoczynną pompę cyrkulacyjną pomyślnie sprawdzono w warunkach laboratoryjnych.

Introduction

Solar systems for water heating have been used in various configurations and can operate under several systems of control (CHOCHOWSKI, CZEKALSKI 1999). The simplest and the cheapest installation for heating water is a gravitational system, also known as thermosiphon. The flow of the heating agent in such installations takes place spontaneously owing to convection movements of hot mass (LEWANDOWSKI 2006). Such circulation is also self-controlled, i.e. the intensity of the agent movement depends on the temperature difference between the upper parts of the collectors and the lower part of the tank. The absence of a circulation pump and of automatic control are undoubtedly the advantage of this solution. However, to operate effectively, particular elements of the system have to be positioned appropriately. The tank should be situated above the upper edge of the collectors, which is impractical for roof collectors. Additional load on the roof is also a problem. It is an advantage of the solution that by placing the collectors on the roof, use is made of unshaded, unused space. The inclination angle of roofs frequently makes it possible to mount a collector directly on the roof. In such cases, installations are applied with active (i.e. forced) circulation of the agent in the system of solar collectors – accumulation tank. The agent circulation is usually started by a one-phase glandless pump, whose work is controlled by a differential temperature regulator.

In areas with no electricity supply, it is possible to power the pump by energy obtained in photo-voltaic cells. Such a system is self-controlled to a certain extent, but the cost of the cell purchase is an additional expense. This can be solved by applying a circulation pump powered by part of the heat, supplied to the system by the solar collector (DOBRIŃSKI, WESOŁOWSKI 2003).

Materials and Methods

A self-acting circulation pump is known from a Ukrainian patent no. 15361A (DOBRIŃSKI 1997). It is built as a closed loop, filled partly with a liquid working agent. The device operates in cycles. In the upper part of the downward circulation conduit, the liquid heat carrier is heated, which results in an increase in its saturated vapour pressure, which in turn pushes it downwards. The agent cools down in the lower part of the loop and flows to the upward conduit. This is a result of the pressure difference in the circulation conduits. After the specified pressure difference has been achieved, the passage in the upper part of the loop opens and the vapour from the upper part of the downward conduit passes to the upward conduit. At the same time, the excess

of cooled-down liquid from the upward conduit pours down gravitationally through the intermediate conduit to the upper part of the cold conduit. There are several varieties of devices which transfer heat in this manner. In general, all the solutions have the form of a closed loop with an upward and downward conduit. The pump used in this system is based on patent PL 195 490 B1 (DOBRIŃSKI, FIEDUCIK 2000). The device consists of two vessels (cold and hot), one placed above the other. The vessels are connected with an intermediate conduit, through which liquid pours down after a cycle of operation is finished, and a hydraulic valve which controls the entire process. The work in the circulation is performed by saturated pressure of the working agent.

Solar installation – location and structure

A solar installation for operation with a self-acting circulation pump has been constructed at the Faculty of Technical Sciences of the University of Warmia and Mazury in Olsztyn. It is an active system with a liquid collector, area $F = 2.0 \text{ m}^2$, fixed to the roof of the university building (Fig. 1). The collector is connected with a 300 L water heater, installed in the building basement. Two manners of forcing the solar liquid flow have been provided for. In the first one, the circulation is forced by an electric pump. It is a traditional



Fig. 1. Experimental solar installation on the roof of building

- pressure in the self-acting circulation pump circuit.

The system operation parameter values will be collected and sent to the central unit through a module with analogue and 4-20 mA current inputs. Operation of all the devices of the system can be visualised as a graphic mask, shown in Fig. 2. It displays changes of all the measured parameters. The mask contains descriptions of the sensors which comprise the installation's measuring system:

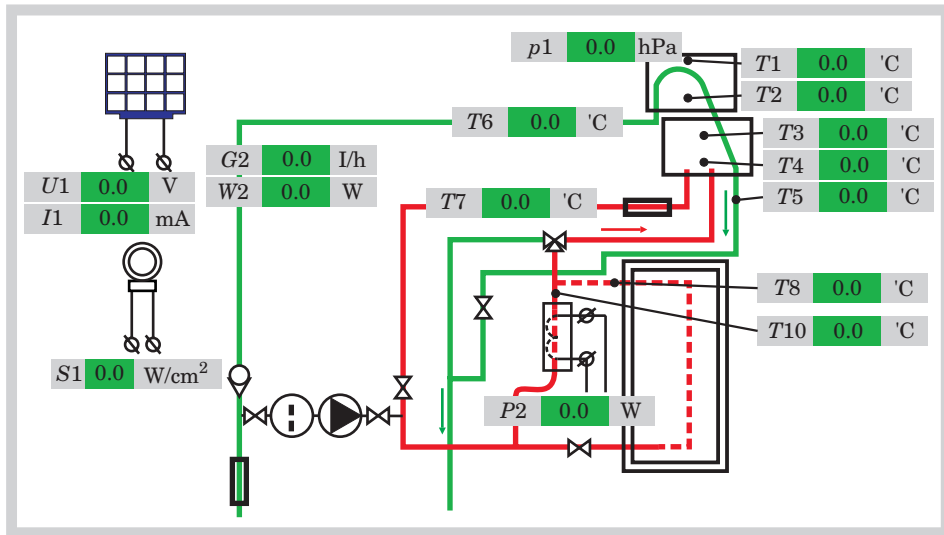


Fig. 3. Display of measured magnitudes of test solar installation with self-acting circulation pump

The method of laboratory tests of the self-acting pump

The self-acting pump was tested in a laboratory. The collector in the tested model was replaced with a 300 W electric heater with a thermostadjuster; water was used as the heat carrier. The pump forced the medium through a copper heat exchanger, placed in a 7 L insulated tank, filled with water. No heat exchange in the tank took place during the experiment. During the device operation, temperature measurements were performed in the downward and upward conduits as well as in the tank. The sensor deployment places are shown in Fig. 4.

Three calibrated resistance thermal sensors Cu 100' with an accuracy of $\pm 0.5^\circ\text{C}$ connected to visualization and data acquisition system were used to measure the temperature of water. The temperature measurements were made with the frequency of 0.1 Hz. The experiment was carried out successive-

ly for two different temperature values of source heat (35°C and 60°C) set with an accuracy of $\pm 5^\circ\text{C}$. An algorithm written in MS Excel for measurement noise reduction in periodical processes was used in empirical data processing (DOBRIŃSKI, DUDA 2007).

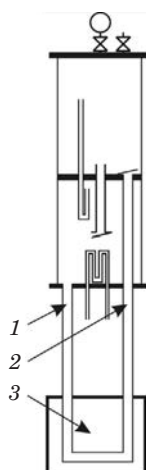


Fig. 4. Scheme of sensor layout: 1 – pump's supply conduit, 2 – pump's return tube, 3 – heat exchanger in tank-accumulator

Results

The experiment results are shown in Figs. 5 and 6. In the first case, the system was started when the liquid temperature was 17°C and the upper limit of the heat source temperature was established as 35°C. The system operation

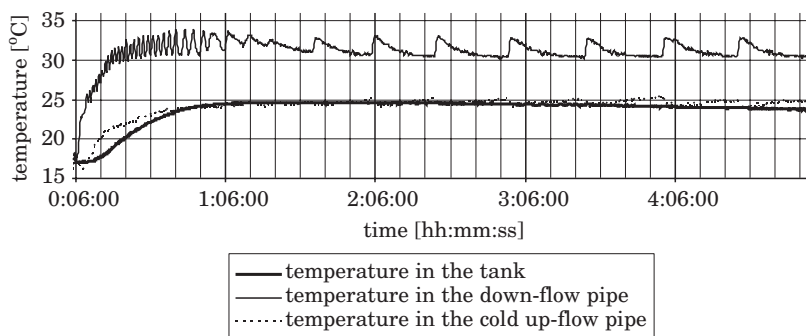


Fig. 5. Temperature diagram for different measurement points of laboratory model at heater temperature 35°C

started upon switching on the heater. The initial cycles of the medium pumping were intense, which resulted in a temperature increase at every measurement point. Subsequently, the temperature in the tank and in the upward conduit settled at 25°C, and in the downward conduit it fluctuated within the range from 31°C to 33°C. At the same time, a noticeable increase in the length of the pumping cycles was recorded. The other diagram shows the system operation at an established initial heater temperature of 60°C. As in the previous case, the temperature in each measurement point rose initially until it settled at about 47°C for the upward conduit and the tank and about 55°C for the downward conduit.

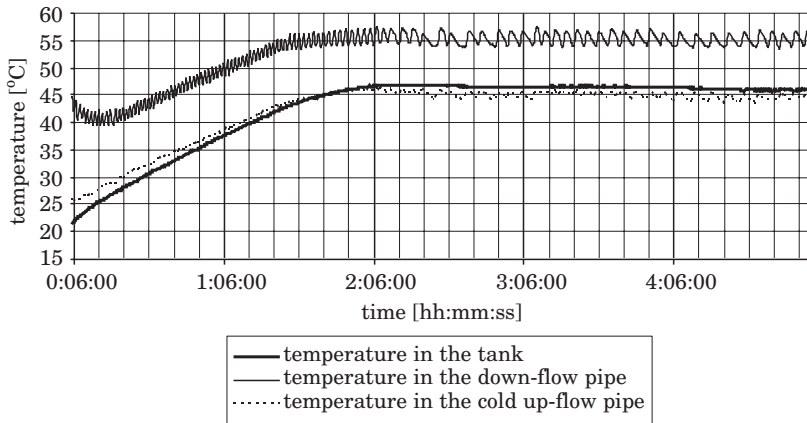


Fig. 6. Temperature diagram for different measurement points of laboratory model at heater temperature 60°C

Summary

The experiment results confirmed the periodical character of the device operation, which starts pumping the medium upon switching on the heat source. The pumping intensity depends on the source power and on the temperature difference between the source and the hot water tank. In this case, the system can be regarded as self-controlling. Thanks to successful tests of the laboratory model it was possible to build the solar installation discussed here. Subsequent tests will be related to the checking of the installation with the use of the self-acting circulation pump in the installation.

Reference

- CHOCHOWSKI A., CZEKALSKI D. 1999. *Słoneczne instalacje grzewcze*. Wyd. COIB. Warszawa.
- DOBRIAŃSKI J., DUDA M. 2007. *An algorithm for handling experimental data of periodical processes with Microsoft Excel*. Technical Sciences, 10.
- DOBRIAŃSKI YU. P. 1997. *Sposib teploperedachi i prystriy do yego zdiysnieniya*. Patent of Ukraine. UA 15361 A; MPK F 28 D 25/00.
- DOBRIAŃSKI J., WESOŁOWSKI M. 2003. *Ocena techniczno-ekonomiczna zastosowania samoczynnego obiegu cyrkulacyjnego w słonecznej instalacji grzewczej*. Problemy Inżynierii Rolniczej, 3: 71–78.
- DOBRIAŃSKI J., FIEDUCIK J. 2000. *Urządzenie do przekazywania ciepła w kierunku przeciwnym do konwekcji naturalnej*. Patent PL 195490 B1.
- LEWANDOWSKI W. 2006. *Proekologiczne odnawialne źródła energii*. WNT, Warszawa.

TORQUE OF THE OPERATOR'S UPPER EXTREMITY IN RELATION TO ITS ORIENTATION WITHIN A NORMAL WORKING SPACE

Joanna Hałacz

Department of Electrical and Power Engineering
University of Warmia and Mazury in Olsztyn

Key words: torque of the upper extremity, ergonomy, anthropometry.

A b s t r a c t

This paper presents the results of a study into the effect of some factors determining the orientation of the upper extremity within the normal working space on the torque of the muscles of this extremity. The results of this study may be useful in the anthropotechnical design of controlling devices. The paper also includes data on the torque developed by the upper extremity within the operator's normal working space which are presented in the form of centile characteristics.

MOMENT SKRĘCAJĄCY KOŃCZYNY GÓRNEJ OPERATORA W ZALEŻNOŚCI OD JEJ POŁOŻENIA W NORMALNEJ PRZESTRZENI PRACY

Joanna Hałacz

Katedra Elektrotechniki i Energetyki
Uniwersytet Warmińsko-Mazurski w Olsztynie

Słowa kluczowe: moment skręcający kończyny górnej, ergonomia, antropometria.

A b s t r a k t

W pracy przedstawiono wyniki badań dotyczących wpływu wybranych czynników określających położenie kończyny górnej w normalnej przestrzeni pracy na wartość momentu skręcającego rozwijanego przez mięśnie tej kończyny. Wyniki badań mogą być wykorzystane w antropometrycznym projektowaniu urządzeń sterujących. Przedstawiono także, w formie charakterystyk centylowych, dane dotyczące momentów skręcających rozwijanych przez kończynę górną w normalnej przestrzeni pracy operatora.

Introduction

Performing work by humans with the use of machines is made possible through controlling elements which correspond to human motory output and elements which carry information in the form of mental stimuli, corresponding to human sensory input. Machines can be controlled through various elements such as levers, pedals, steering wheels, manual wheels, rotating hand grips and knobs. The task of a designer is to select the most appropriate element in the best form for a given control, also in terms of shape and size (SŁOWIKOWSKI 2000).

Another important element is the choice of force applied by a human – operator to the controlling element.

The objective of the study was to describe the effect of some factors determining the orientation of the upper extremity within the normal working space on the torque of the muscles of this extremity.

The effect of the following factors on the mean values of the maximum torque of the upper extremity were studied: the extremity (right, left), the value of the angle determining the orientation of the extremity and the measurement plane in which the pronation and supination movements were conducted.

The results of the study are new data within the scope of the operator's biomechanical competences. The results of this study may be useful in the anthropotechnical design of controlling devices.

Method

Subject of the study

The study involved 300 persons (124 women and 176 men) aged 21-48. The majority of the subjects were young and working or students. Based on an interview it was found that they were healthy. The study excluded left-handed persons due to possible functional asymmetry of the upper extremities.

Table 1 presents a complete description of the subject of the study.

Sample size

The sample size was established according to the representation method by unlimited dependant draw (draw with no return) (GREŃ 1984, POLAŃSKI, PIETRASZEK 2001). The initial sample size was: For women $n_1 = 124$, for men $n_2 = 176$.

Table 1
Anthropometric characteristics of the studied women and men

Specification of characteristics	Statistical parameters									
	women					men				
	mean value*	standard deviation*	variation coefficient [%]	median (C ₅₀)*	range*	mean value*	standard deviation*	variation coefficient [%]	median (C ₅₀)*	range*
Age [years]	26.68	6.2471	23.42	24.0	19.0	27.14	6.2936	23.19	25.0	26.0
Height [cm]	163.53	5.3711	3.28	163.0	20.0	175.90	17.6894	10.06	177.3	126.0
Body weight [kg]	59.84	10.7927	18.04	56.7	40.2	81.72	15.0975	18.48	80.0	90.0
Right arm length [cm]	16.47	0.8434	5.12	16.3	2.9	17.97	0.8071	4.49	18.0	3.3
Left arm length [cm]	16.25	0.8918	5.49	16.1	3.6	17.89	0.8430	4.71	17.9	3.4
Right hand length [cm]	8.29	0.5428	6.54	8.3	2.2	8.88	0.6262	7.05	9.0	3.1
Left hand length [cm]	8.12	0.5067	6.24	8.1	2.2	8.87	0.5464	6.16	8.9	2.6
Right arm width [cm]	7.84	0.4038	5.15	7.8	1.5	9.00	0.4810	5.34	9.1	2.1
Left arm width [cm]	7.66	0.4013	5.24	7.7	1.5	8.82	0.4397	4.98	8.8	1.9
Right carpal bone width [cm]	5.48	0.3870	7.07	5.4	1.4	6.33	0.3905	6.17	6.3	2.1
Left carpal bone width [cm]	5.36	0.3684	6.87	5.3	1.3	6.16	0.4442	7.21	6.1	2.2
Right hand joint circumference [cm]	15.50	0.9372	6.05	15.4	4.5	17.75	0.8849	4.98	17.7	4.6
Left hand joint circumference [cm]	15.36	0.7088	4.61	15.3	3.2	17.61	0.8573	4.87	17.5	4.6
Right hand fingers thickness [cm]	3.08	0.3247	10.53	3.1	1.5	3.56	0.2896	8.14	3.6	1.4
Left hand fingers thickness [cm]	3.03	0.2809	9.26	3.1	1.2	3.52	0.2315	6.58	3.5	1.1

* – values in units of a given characteristic

For the sample sizes in the particular groups of the study that were greater than the requisite (for women $n_o = 123$, for men $n_o = 78$), they were acknowledged sufficient.

Measuring devices

The torque was measured with the use of a specially constructed prototype measuring device.

Figure 1 presents a simplified operation principle of the measuring device.

The mechanical system through the spring mechanism produces a lineary incrementing torque in the function of the rotation angle. The electronic module measures the rotation angle, the torque and displays the results on the display.

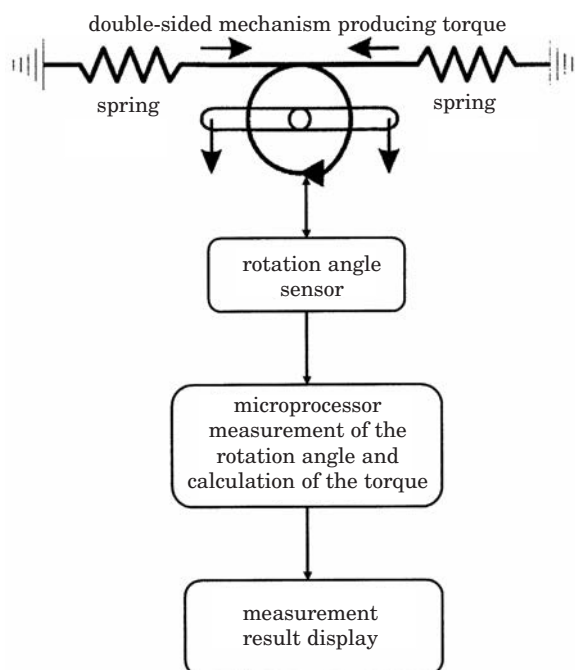


Fig. 1. Flow chart of the measuring stan

Source: own elaboration.

Scope of the study

The initial position was determined as the intersecting point of the horizontal and the vertical planes with the axis of the ulnar articulation which is the centre of the motion space. The subjects were in the imposed sitting position.

The measurements in the vertical plane were carried out at the angle $\alpha = \{+30^\circ; 0^\circ; -30^\circ\}$ (upwards „+” ; downwards „-”) (Fig. 2b)), whereas the measurements in the horizontal plane at the angle $\alpha = \{+30^\circ; 0^\circ; -30^\circ\}$ (inwards „-” ; outwards „+”) (Fig. 2a).

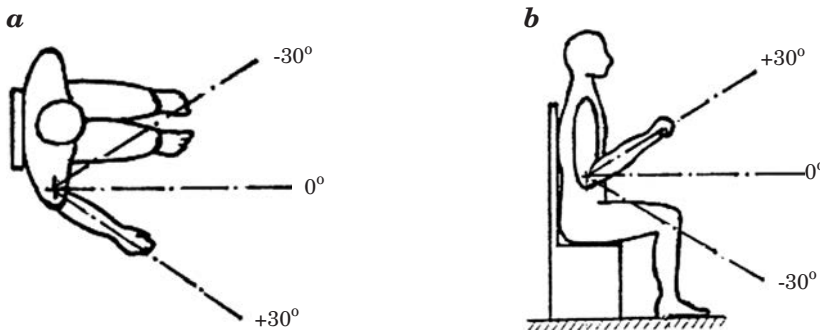


Fig. 2. Location of the upper extremity during the measurements of the torque: *a* – in the horizontal plane; *b* – in the vertical plane

Source: own elaboration.

In each of the five orientations, the subjects performed the pronation and supination movement of a continuous turn at the maximum strength which was recorded.

Statistical analysis

The experimental results were analysed with the use of the StatisticaPL and the WINSTAT software packages.

The following statistical procedures were applied:

- Basic statistical measures to determine the location and dispersion;
- Variance analysis;

The following basic measures of location and dispersion of the torque values for women and men were determined: Mean value, standard deviation, variance co-efficient, median (centile C_{50}), modal value, minimum value, maximum value, range, centile C_5 , centile C_{95} (HAŁACZ 2008).

The variance analysis was carried out by evaluating the independent effect of the following factors: the extremity (right, left), the value of the angle determining the orientation of the extremity and the measurement plane in which the pronation and supination movements were conducted on mean values of the studied torque, separately for women and men. Moreover, the interactions of these factors were taken into account.

The following hypotheses were verified:

The zero hypothesis (H_0): the assumed experimental factors (the extremity, the value of the angle determining the orientation of the extremity and the measurement plane) do not have a significant effect on the mean values of the torque for women (men) at pronation (supination).

The alternative hypothesis (H_1): the mean values of torque for women (men) at pronation (supination) differ depending on the extremity, the value of the angle determining the orientation of the extremity and the measurement plane.

Results

The variance analysis results were presented below. Due to the large amount of data, the analysis does not cover the results reflecting the interactions between the studied factors, nevertheless such analysis was performed.

Tables 2–5 presents the results of the statistical comparison of the torque in relation to the assumed factors separately for women and men and movement direction (pronation – supination).

The following marking system was assumed in this study:

Factor *A* – extremity (R – right, L – left)

Factor *B* – value of the angle determining the measuring position ($a - \alpha = -30^\circ$; $b - \alpha = 0^\circ$; $c - \alpha = +30^\circ$)

Factor *C* – measurement plane (I – horizontal plane, II – vertical plane).

Based on the results it was found that statistically significant differences in the torque values for women at pronation occurred only for the different extremities. The mean value of torque for the right extremity (6.06 Nm) was greater than for the left extremity (5.70 Nm). As far as the other factors are concerned, i.e. group *B* and group *C* factors, statistically significant differences in the mean values of torque do not occur.

For supination, statistically significant differences in the torque values occur in relation to the kind of plane of measurement. The mean value of torque for the horizontal plane (5.97 Nm) was greater than for the vertical plane (5.74 Nm).

For the other factors, i.e. the group *A* and *B* factors, statistically significant differences were not found.

Table 2

Results of statistical comparison of the torque values at pronation depending on the assumed factors
– women

Not including the <i>B</i> and <i>C</i> group factors			
Factor <i>A</i>	Mean value [Nm]	Standard deviation [Nm]	Variation coefficient [%]
R – right	6.06	0.9934	16.40
L – left	5.70	1.0868	19.06
Difference significance results (Duncan test): $P > L^{**}$			
Not including the <i>A</i> and <i>C</i> group factors			
Factor <i>B</i>	Mean value [Nm]	Standard deviation [Nm]	Variation coefficient [%]
$a - \alpha = -30^\circ$	5.84	1.1267	19.31
$b - \alpha = 0^\circ$	5.88	1.1025	18.74
$c - \alpha = +30^\circ$	5.92	0.9307	15.72
Difference significance results (Duncan test): No statistically significant differences			
Not including the <i>A</i> and <i>B</i> group factors			
Factor <i>C</i>	Mean value [Nm]	Standard deviation [Nm]	Variation coefficient [%]
I – horizontal plane	5.92	1.0312	17.42
I – vertical plane	5.84	1.0787	18.48
Difference significance results (Duncan test): No statistically significant differences			

Calculations were carried out at the significance level of $\alpha = 0.05$.

** – statistically significant differences at the significance level of $\alpha = 0.01$,

* – statistically significant differences at the significance level of $\alpha = 0.05$.

Table 3

Results of statistical comparison of the torque values at supination depending on the assumed factors
– women

Not including the <i>B</i> and <i>C</i> group factors			
Factor <i>A</i>	Mean value [Nm]	Standard deviation [Nm]	Variation coefficient [%]
R – right	5.93	0.9963	16.81
L – left	5.78	1.0636	18.40
Difference significance results (Duncan test): No statistically significant differences			
Not including the <i>A</i> and <i>C</i> group factors			
Factor <i>B</i>	Mean value [Nm]	Standard deviation [Nm]	Variation coefficient [%]
$a - \alpha = -30^\circ$	5.86	0.9407	16.05
$b - \alpha = 0^\circ$	5.72	1.1162	19.52
$c - \alpha = +30^\circ$	5.98	1.0220	17.09
Difference significance results (Duncan test): No statistically significant differences			
Not including the <i>A</i> and <i>B</i> group factors			
Factor <i>C</i>	Mean value [Nm]	Standard deviation [Nm]	Variation coefficient [%]
I – horizontal plane	5.97	1.0392	17.42
I – vertical plane	5.74	1.0146	17.67
Difference significance results (Duncan test): I > II*			

Calculations were carried out at the significance level of $\alpha = 0.05$.

** – statistically significant differences at the significance level of $\alpha = 0.01$,

* – statistically significant differences at the significance level of $\alpha = 0.05$.

Table 4

Results of statistical comparison of the torque values at pronation depending on the assumed factors
– men

Not including the <i>B</i> and <i>C</i> group factors			
Factor <i>A</i>	Mean value [Nm]	Standard deviation [Nm]	Variation coefficient [%]
R – right	8.29	0.8926	10.76
L – left	8.12	0.8590	10.57
Difference significance results (Duncan test): $P > L^{**}$			
Not including the <i>A</i> and <i>C</i> group factors			
Factor <i>B</i>	Mean value [Nm]	Standard deviation [Nm]	Variation coefficient [%]
$a - \alpha = -30^\circ$	8.41	0.9319	11.07
$b - \alpha = 0^\circ$	8.08	0.7915	9.79
$c - \alpha = +30^\circ$	8.13	0.8767	10.79
Difference significance results (Duncan test): $a > b, c^{**}$			
Not including the <i>A</i> and <i>B</i> group factors			
Factor <i>C</i>	Mean value [Nm]	Standard deviation [Nm]	Variation coefficient [%]
I – horizontal plane	8.14	0.8031	9.87
I – vertical plane	8.28	0.9456	11.42
Difference significance results (Duncan test): No statistically significant differences			

Calculations were carried out at the significance level of $\alpha = 0.05$.

** – statistically significant differences at the significance level of $\alpha = 0.01$,

* – statistically significant differences at the significance level of $\alpha = 0.05$.

Table 5

Results of statistical comparison of the torque values at supination depending on the assumed factors
– men

Not including the <i>B</i> and <i>C</i> group factors			
Factor <i>A</i>	Mean value [Nm]	Standard deviation [Nm]	Variation coefficient [%]
R – right	8.23	0.8755	10.63
L – left	8.17	0.8537	10.45
Difference significance results (Duncan test): No statistically significant differences			
Not including the <i>A</i> and <i>C</i> group factors			
Factor <i>B</i>	Mean value [Nm]	Standard deviation [Nm]	Variation coefficient [%]
$a - \alpha = -30^\circ$	8.29	0.8278	9.98
$b - \alpha = 0^\circ$	8.10	0.9688	11.95
$c - \alpha = +30^\circ$	8.21	0.7802	9.50
Difference significance results (Duncan test) No statistically significant differences			
Not including the <i>A</i> and <i>B</i> group factors			
Factor <i>C</i>	Mean value [Nm]	Standard deviation [Nm]	Variation coefficient [%]
I – horizontal plane	8.33	0.8193	9.84
I – vertical plane	8.08	0.8909	11.03
Difference significance results (Duncan test): I > II*			

Calculations were carried out at the significance level of $\alpha = 0.05$.

** – statistically significant differences at the significance level of $\alpha = 0.01$,

* – statistically significant differences at the significance level of $\alpha = 0.05$.

Based on the results, it was found that statistically significant differences in the torque values for men at pronation occurred for the different extremities. The mean value of torque for the right extremity (8.29 Nm) was greater than for the left extremity (8.12 Nm). Significant differences were also recorded for the angle determining the measurement location. The mean value of torque for $\alpha = -30^\circ$ (8.41 Nm) was greater than for the other angles. No statistically significant differences were found for the group *C* factors (plane of measurement).

For supination, statistically significant differences in the torque values occur only in relation to the kind of plane of measurement. The mean value of torque for the horizontal plane (8.33 Nm) was considerably greater than for the vertical plane (8.08 Nm). For the other factors i.e. the group *A* and *B* factors statistically significant differences were not found.

In order to complement the above study results, tables 6 and 7 present torque mean values in the horizontal and vertical planes and the values of centiles C_5 , C_{50} and C_{95} in the normal operator space. This data may serve as guidance for designers.

Table 6
Statistical parameters of torque in the horizontal plane

Specification	Women				Men			
	mean value [Nm]	centile C_5 [Nm]	median C_{50} [Nm]	centile C_{95} [Nm]	mean value [Nm]	centile C_5 [Nm]	median C_{50} [Nm]	centile C_{95} [Nm]
Torque of the right extremity at pronation in the orientation of $\alpha = -30^\circ$	6.16	5.0	5.9	7.9	8.25	6.9	8.3	9.5
Torque of the right extremity at supination in the orientation of $\alpha = -30^\circ$	6.26	4.4	6.1	8.5	8.44	7.1	8.4	10.2
Torque of the right extremity at pronation in the orientation of $\alpha = 0^\circ$	6.06	4.1	6.2	7.6	8.20	7.0	8.2	9.7
Torque of the right extremity at supination in the orientation of $\alpha = 0^\circ$	6.18	4.6	6.1	7.6	8.31	7.1	8.3	9.6
Torque of the right extremity at pronation in the orientation of $\alpha = 30^\circ$	6.16	5.0	6.1	7.6	8.18	6.8	8.2	9.7
Torque of the right extremity at supination in the orientation of $\alpha = 30^\circ$	5.93	4.8	5.9	7.1	8.27	7.3	8.3	9.5
Torque of the left extremity at pronation in the orientation of $\alpha = -30^\circ$	5.83	4.2	5.8	7.2	8.13	7.1	8.1	9.3
Torque of the left extremity at supination in the orientation of $\alpha = -30^\circ$	5.87	4.1	5.8	8.0	8.44	7.2	8.5	9.7
Torque of the left extremity at pronation in the orientation of $\alpha = 0^\circ$	5.70	3.8	5.7	7.6	7.97	6.9	7.9	9.3
Torque of the left extremity at supination in the orientation of $\alpha = 0^\circ$	5.78	4.2	5.6	7.8	8.11	7.0	8.0	9.4
Torque of the left extremity at pronation in the orientation of $\alpha = 30^\circ$	5.61	3.8	5.6	7.1	8.09	7.1	8.1	9.2
Torque of the left extremity at supination in the orientation of $\alpha = 30^\circ$	5.64	4.2	5.5	7.2	8.21	7.0	8.2	9.8

Source: HAŁACZ (2008).

Table 7

Statistical parameters of torque in the vertical plane

Specification	Women				Men			
	mean value [Nm]	centile C ₅ [Nm]	median C ₅₀ [Nm]	centile C ₉₅ [Nm]	mean value [Nm]	centile C ₅ [Nm]	median C ₅₀ [Nm]	centile C ₉₅ [Nm]
Torque of the right extremity at pronation in the orientation of $\alpha = -30^\circ$	5.76	4.2	5.4	8.3	8.67	7.3	8.5	10.5
Torque of the right extremity at supination in the orientation of $\alpha = -30^\circ$	5.53	4.0	5.4	6.9	7.75	6.3	7.7	9.4
Torque of the right extremity at pronation in the orientation of $\alpha = 0^\circ$	6.06	4.1	6.2	7.6	8.20	7.0	8.2	9.7
Torque of the right extremity at supination in the orientation of $\alpha = 0^\circ$	6.18	4.6	6.1	7.6	8.31	7.1	8.3	9.6
Torque of the right extremity at pronation in the orientation of $\alpha = 30^\circ$	6.12	5.1	6.0	7.3	8.27	6.7	8.4	9.8
Torque of the right extremity at supination in the orientation of $\alpha = 30^\circ$	6.11	4.9	6.0	7.7	8.28	7.1	8.3	9.4
Torque of the left extremity at pronation in the orientation of $\alpha = -30^\circ$	5.59	4.1	5.2	8.6	8.61	7.1	8.5	10.4
Torque of the left extremity at supination in the orientation of $\alpha = -30^\circ$	5.21	3.9	4.9	7.8	7.79	6.5	7.7	9.9
Torque of the left extremity at pronation in the orientation of $\alpha = 0^\circ$	5.70	3.8	5.7	7.6	7.97	6.9	7.9	9.3
Torque of the left extremity at supination in the orientation of $\alpha = 0^\circ$	5.78	4.2	5.6	7.8	8.11	7.0	8.0	9.4
Torque of the left extremity at pronation in the orientation of $\alpha = 30^\circ$	5.79	4.5	5.5	7.6	8.40	7.2	8.2	10.3
Torque of the left extremity at supination in the orientation of $\alpha = 30^\circ$	5.77	3.8	5.8	7.7	7.96	6.7	8.0	9.2

Source: HAŁACZ (2008).

Results

Based on the statistical analysis of the experimental results, the following conclusions can be drawn:

1. Based on the results of verification of the statistical hypotheses, the correlation between the torque and the extremity (left, right) was found only for pronation (inward motion). Both in women and men the mean torque values for the right extremity (women – 6.06 Nm, men – 8.29 Nm) were greater than for the left extremity (women – 5.70 Nm, men – 8.12 Nm). This is confirmed by a proven occurrence of functional asymmetry.

During supination (outward motion), the type of extremity did not have an effect on the torque mean values. However, based on the statistical analysis it

was found that during supination, another factor, i.e. the plane of motion, has an effect on the results. In both women and men the mean torque values obtained for the horizontal plane (women – 5.97 Nm, men – 8.33 Nm) are significantly greater than for the vertical plane (women – 5.74 Nm, men – 8.08 Nm). Such a correlation was not recorded for pronation.

According to the author, it is possible that the difference resulting from the functional asymmetry of the extremities was bridged by a more significant factor, i.e. the plane of motion. It is also significant that for both the women and the men the studied correlations are the same. It is probable that the vertical plane is more natural and convenient for conducting turning motions and for the supination, the plane type plays a more important role.

2. While verifying the statistical hypotheses it was also found that some interactions have a significant effect on the torque value.

In all the cases, except pronation in women, the combined effect of the following factors was recorded: plane of measurement and angle determining the location of measurement. At supination in both women and men the best results were obtained at the orientation of $\alpha = 0^\circ$ in the horizontal plane, which is the most natural position not requiring divergence of the extremity.

Moreover, men obtained very good results at $\alpha = -30^\circ$ both in the vertical and horizontal planes (i.e. with the extremity oriented inwards or downwards), whereas women obtained better results at supination for $\alpha = +30^\circ$ also in the vertical and horizontal planes (i.e. with the extremity oriented outwards or upwards).

Conclusion

The resulting correlations are significant for the arrangement of the controlling components and devices. Utilisation of such data at the design phase of machines and control panels may contribute to a reduction of operator's physical effort and make the controlling process safer and more precise.

Based on the analysis of the correlations found, the best location of the control components requiring the application of turning force of the upper extremity (various knobs, rotating handles) is the horizontal plane on the operator's right side at the level of upper extremity in the normal position or with a small divergence. This is particularly important when it comes to components of high importance for the control or safety and those frequently used. If it is not possible to ensure such an arrangement, the extreme locations in the vertical plane at the operator's left side should be avoided.

The ergonomics of devices, machines and stationary work posts is determined by adopting appropriate guidelines at the design phase. The study

completed may be complementary to the existing data and guidelines and could contribute to the improvement of the existing work conditions concerning process control.

Accepted for print 11.12.2009

References

- GREŃ J. 1984. *Statystyka matematyczna. Modele i zadania*. PWN, Warszawa.
- HAŁACZ J. 2008. *Badania wielkości maksymalnej momentu obrotowego kończyny górnej dla potrzeb projektowania urządzeń sterujących*. Inżynieria i Aparatura Chemiczna, 6: 91–92.
- POLAŃSKI Z., PIETRASZEK J. 2001. *Komputerowe wspomaganie planowania i analizy statystycznej doświadczalnych badań innowacyjnych*. Materiały wewnętrzne StatSoft Polska, Sp. z o.o., Kraków.
- SŁOWIKOWSKI J. 2000. *Metodologiczne problemy projektowania ergonomicznego w budowie maszyn*. CIOP, Warszawa.

THE INFLUENCE OF REPEATED HEATING AND COOLING PROCESS ON THE TRANSFORMATION CHARACTERISTICS IN Ni-Ti ALLOY

Krzysztof Kuś

Chair of Functional Materials and Nanotechnology
University of Warmia and Mazury in Olsztyn

Key words: Ni-Ti alloy, heating and cooling cycles, DSC, transformation behaviour.

Abstract

The transformation characteristics of a near-equiatomic polycrystalline Ni-Ti alloy in an annealed state (600°C/30 min/air-cooling) were determined by DSC measurements in order to investigate the effect of repeated heating and cooling process through the martensitic transformation region. It was observed that transformation profiles exhibited qualitative differences depending on the number of executed heating and cooling cycles. Due to the increasing number of thermal cycles, the forward transformation changed from a one-stage ($B2 \rightarrow B19'$) to a two-stage ($B2 \rightarrow R \rightarrow B19'$) reaction while the reverse martensitic transformation showed the one-stage character ($B19' \rightarrow B2$), independently of the number of achieved cycles. The other thermal properties were also found to change with thermal transformation cycles. Based on the calorimetric results and literature studied, it is thought that observed changes in transformation characteristics can be attributed to the modifications of the alloy microstructure. In this case the introduced defects which are accumulated during the thermal cycles play an important role.

WPLYW PROCESU WIELOKROTNEGO NAGRZEWANIA I CHŁODZENIA NA CHARAKTERYSTYKI PRZEMIAN W STOPIE Ni-Ti

Krzysztof Kuś

Katedra Materiałów Funkcjonalnych i Nanotechnologii
Uniwersytet Warmińsko-Mazurski w Olsztynie

Słowa kluczowe: stop Ni-Ti, wielokrotne nagrzewanie i chłodzenie, metoda DSC, zachowanie się stopu w zakresie przemiany.

Abstrakt

Metodą pomiarów DSC wyznaczano charakterystyki cieplne przemian fazowych w stopie polikrystalicznym Ni-Ti o składzie bliskim równoatomowemu, w stanie po wyżarzaniu (600°C/30 min/chłodzenie w powietrzu) w celu zbadania wpływu procesu wielokrotnego nagrzewania i chłodzenia w obszarze występowania przemiany martenzytycznej. Stwierdzono, że rejestrowane profile DSC przemian przejawiały jakościowe zmiany w zależności od liczby wykonanych cykli cieplnych. Wraz ze wzrostem liczby cykli przemiana z ang. „wprost” zmieniła się od jednostopniowej ($B2 \rightarrow B19'$) do dwustopniowej ($B2 \rightarrow R \rightarrow B19'$), podczas gdy przemiana odwrotna wykazywała sekwencję jednostopniową ($B19' \rightarrow B2$), niezależnie od zrealizowanej liczby cykli. Poza tym ustalono, że inne właściwości cieplne również się zmieniają. Na podstawie uzyskanych wyników kalorymetrycznych oraz przeglądu literatury można sądzić, że obserwowane zmiany w charakterystykach cieplnych mogą być spowodowane modyfikacją mikrostruktury stopu. W tym przypadku defekty oraz ich nagromadzenie się wskutek wielokrotnego nagrzewania i chłodzenia odgrywają główną rolę.

Introduction

From among many “smart/interactive” materials (WEI et al. 1998, MACKERLE 2001, MONNER 2005, WILSON et al. 2007), shape memory alloys (SMAs) still have strong interest in scientific and commercial areas. From the wide range of alloys with the reversible effect of shape memory (FREMONT, MIYAZAKI 1996, SCHWARTZ 2002, SHAW et al. 2008), it is commonly accepted that near-equiatomic Ni-Ti alloy (designated as Nitinol) exhibits the best shape memory and structural properties. In the studies of SMAs, for example, with regard to their cyclic applications, it is important to know the material response to the various thermal/mechanical treatments. There are many factors having an influence on the transformation characteristics in NiTi alloys (NURVEREN et al. 2008, PAULA et al. 2004, MEHRABI et al. 2009). One of them is the repeated heating↔cooling, i.e. thermal cycling which can lead to changes in sequences of the forward and reverse transformations (MATSUMOTO 1993, MCCORMICK, LIU 1994, WU et al. 1999, MATSUMOTO 2003). The transformation behaviour in SMAs is mostly examined using differential scanning calorimetry (DSC) method. In such experiments different types of transformations depending on the above indicated factors, therefore, can be revealed. According to (EGGELER et al. 2005), one-step transformation means that only one DSC peak is observed on cooling from the high temperature to the low temperature phase. In two- and multiple-step transformations two and multiple peaks appear. Two-step transformations, in turn, are explained by the R-phase, which forms first ($B2 \rightarrow R$), followed by the formation of $B19'$ ($R \rightarrow B19'$).

The present paper gives the DSC results of the repetition of the forward and reverse martensitic transformation during stress-free thermal cycling process, and its influence on the thermal transformation properties in an annealed Ni-Ti alloy is considered.

Experimental

A polycrystalline Ni-Ti SMA in sheet form was utilized in this study, and its composition was 50.08 nickel in atomic percent. Owing to the fact that the thermo-mechanical history of the as-received material was unknown, the alloy sample was initially annealed at 600°C for 30 minutes prior to the proper DSC measurements. It should be noted that the Ni-Ti alloy exhibited in the as-received state the presence of the R-phase, as shown elsewhere (KUŚ 2007, KUŚ, BRECKZO 2010). The annealing process of a rectangular sample with dimensions of 3x1.7x0.5 mm was carried out in a muffle furnace, followed by air-cooling to room temperature (about 22°C). In order to reduce the oxidation of the sample during heat-treatment, a continuous flow of argon gas through the furnace chamber was applied. The annealing conditions selected for this study ensured a one-step of the $B2 \leftrightarrow B19'$ reaction, i.e. without revealing the intermediate R-phase. After the annealing, the sample surface was carefully cleaned by fine abrasive paper, washed in distilled water and alcohol, and etched with a $5H_2O + 4HNO_3 + 1HF$ solution for 30 s. Following that, the sample was again washed in water and alcohol. These operations were aimed at removing the surface layer that might be slightly oxidized during heat-treatment.

A differential scanning calorimeter (DSC 204, Netzsch) system was used to characterize the transformation properties of the thermally cycled alloy. After an initial heating the sample from room temperature to +70°C, it was cooled (10 K/min) to -40°C (first cooling cycle) and kept for 2 min to obtain thermal equilibrium. Then the specimen was heated (10 K/min) to +70°C (second heating cycle) and held again for 2 min. The repeated stress-free heating and cooling was carried out up to 60 cycles.

Results and discussion

Figs. 1-2 show a set of DSC graphs of the thermally cycled Ni-Ti sample, illustrating the courses for the forward and reverse transformation, respectively. The numbers on the curves indicate the number of thermal cycles.

The repeated heating and cooling process caused that transformation behaviour of the sample tested demonstrated qualitative differences depending on the number of accomplished thermal cycles. In the early stage of thermal cycling, both the forward and reverse transitions occurred as the one-step sequence from austenite to martensite, and vice versa ($B2 \leftrightarrow B19'$). However, after achieving the first full 10 cycles, the DSC courses on cooling began to show interesting changes. With effect from an appearing small shoulder on the

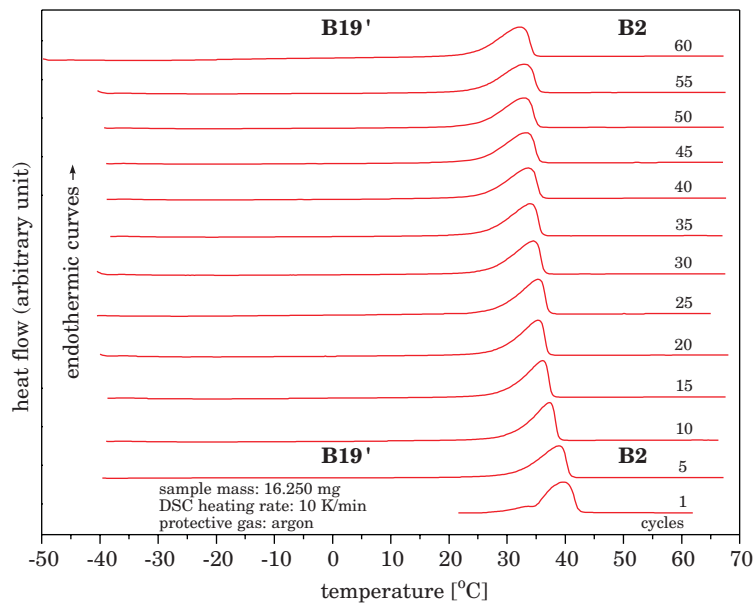


Fig. 1. DSC curves for the reverse transformation against thermal cycles

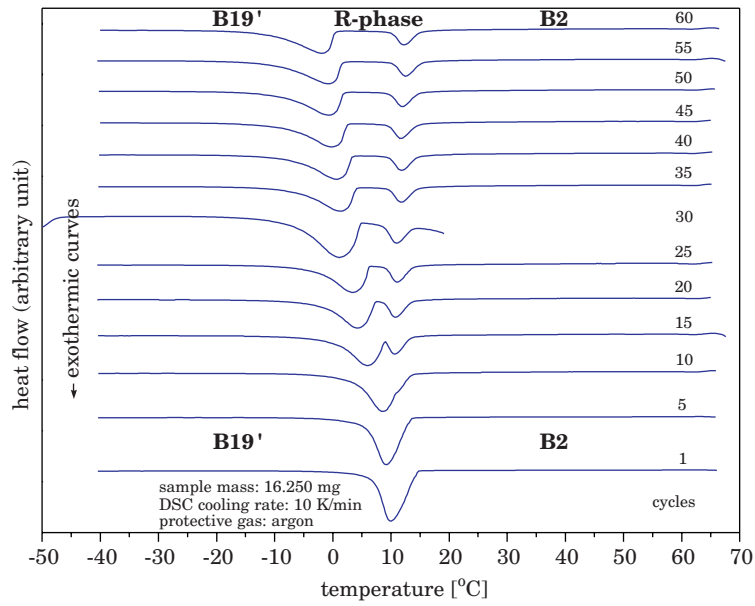


Fig. 2. DSC curves for the forward transformation against thermal cycles

exothermic peaks, two overlapping peaks were recorded in consecutive thermal cycles. It proves that the intermediate R-phase started to form prior to martensite. These heat flow peaks tended to be more distinct and separated as the number of thermal cycles increased, implying unequivocally that the forward transformation occurred in two successive steps ($B2 \rightarrow R \rightarrow B19'$). The $B2 \rightarrow R$ transformation was found to emerge clearly after eighteenth forward transformation cycles, not shown in Fig. 2. The endothermic DSC curves in Fig. 1 revealed only a single peak indicating that the reverse transformation still remained as the one-step sequence ($B19' \rightarrow B2$). It follows that the repeated heating and cooling process has a significant effect on the transformation behaviour.

The changes in other thermal properties, which can be extracted from DSC thermograms, were observed simultaneously along with the variations in peak shapes, as illustrated in Figs. 3–4. The M_p , R_p , M_p^* and A_p are defined as the temperatures of the maximum DSC peaks for the $B2 \rightarrow B19'$, $B2 \rightarrow R$, $R \rightarrow B19'$ and $B19' \rightarrow B2$ transformations, respectively. The symbols ΔH_M , ΔH_R , ΔH_{M^*} and ΔH_A mean the transformations heats corresponding to the individual transformations in order as mentioned just above. The latter parameters were estimated from the areas between the heat flow peak and the base line by means of DSC equipment software.

There was a gradual decrease in the combined values of $M_p + M_p^*$, and A_p with the repetition of the transformation by thermal cycling, as shown in Fig. 3. The temperature difference between the first and the final cycle was measured to be about 11.5 and 7°C for the ($M_p + M_p^*$) and A_p , respectively.

By observing the curve shapes during cooling, it was found the height and width of the $B2 \rightarrow B19'$ peak decreased and broadened resulting in gradually split into two separate ones (the first formed peak is due to $B2 \rightarrow R$ transition), as the number of thermal cycles increased. From the twelfth cycle, there were no distinct changes in the peak temperature of the R-phase (R_p) during the thermal cycling, though a slight tendency to increase in the value outlined. The experimental results illustrated in Fig. 3 indicate that the thermal hysteresis, defined here as the difference between the calorimetric peak temperatures of the forward and the reverse transformations, enlarged with successive thermal cycles. It was varied from ca. 30 to 34°C. It is necessary to point out that after executing a dozen cycles the thermal hysteresis was only measured between the peak temperatures of the $R \rightarrow B19'$ and $B19' \rightarrow B2$ (due to the introduction of intermediate phase).

With reference to the results presented in Figs. 1–3, it can be stated that the transformation behaviour and related thermal characteristics of the studied Ni-Ti alloy are influenced by the repeated thermal cycling. It is known that the presence of the R-phase can be revealed in Ni-Ti alloys only

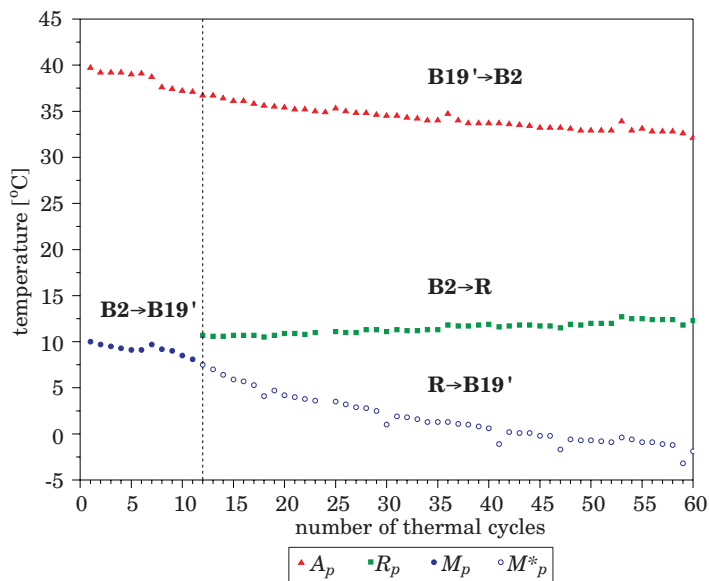


Fig. 3. Phase transformation peak temperatures against thermal cycles

if the M_s temperature is sufficiently low, so as to avoid direct $A \rightarrow M$ transformation (PAULA et al. 2004). Although the phase transformation starting and finishing temperatures were not quoted in the present paper, the changes in the DSC exothermic curves in Fig. 2 clearly show that there was a progressive fall in the M_s temperature by increasing the number of transformation cycles. Such a tendency in the critical temperature may be related to the decrease in stability of the martensite phase, thereby facilitating the formation of the R-phase (UCHIL et al. 2002). The decrease in M_s before the appearance of intermediate transition symptoms (as observed at ninth cooling cycle), was estimated to be about 3°C. The DSC results in Fig. 2 also show that the R-phase was stabilized during the repeated heating and cooling process but, only its temperature range was expanded as the number of thermal cycles increased.

The absorbed heat during reverse transformation and the released heats during forward transformation with respect to the number of thermal cycles are gathered in Fig. 4. From these data it can be seen that the heats measured for both the reverse and martensitic transformations shifted rather smoothly with increasing thermal cycles. The trend in the values of ΔH_A and ΔH_M (as absolute data) was decreasing and increasing, respectively. Basically, ΔH_M was calculated in the early stage of thermal cycling, although at the end of this range the two separate forward transitions on cooling were still combined

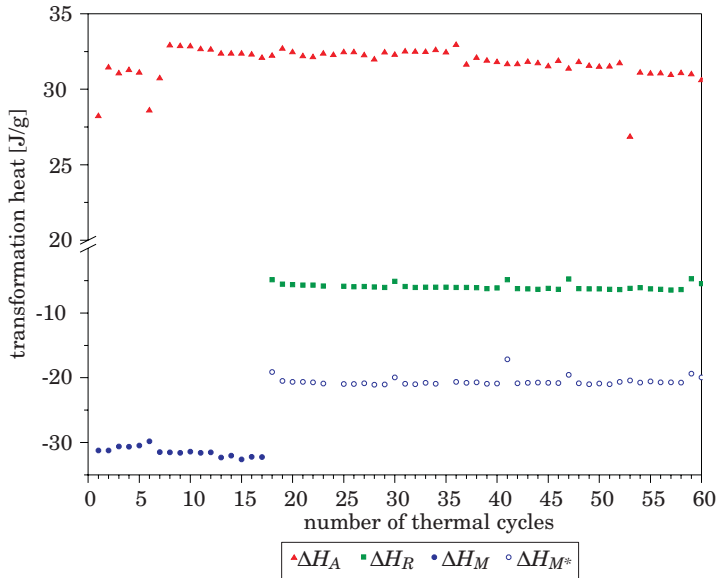


Fig. 4. Heats measured for the forward and reverse transformations against thermal cycles

together for the measurement due to the partial overlapping of the B2→R and R→B19' heat peaks. Once the two exothermic peaks were clearly separated, the values corresponding to the ΔH_R and ΔH_{M^*} were estimated. It is evident from Fig. 4 that they appeared to stay almost unchanged with respect to the number of thermal cycling.

The presented calorimetric results in this paper, showing the influence of repeated heating and cooling process on the transformation behaviour in the near-equiatomic Ni-Ti alloy, are in agreement with other studies (MATSUMOTO 1993, MCCORMICK, LIU 1994, MATSUMOTO 2003). According to them, and also Refs. (UCHIL et al. 2002, MIYAZAKI et al. 1986), observed changes in the thermal transformation characteristics can be attributed to the modifications of the alloy microstructure. In this case the introduced structural defects (dislocations) which are accumulated by the thermal cycling process are of crucial importance consequently affecting the martensitic transformation behaviour.

Summary and conclusions

The effect of repeated heating and cooling process on the transformation characteristics in Ni-Ti alloy after annealing heat-treatment was analysed

thermally using the DSC technique, and the main results received were as follows:

1. In the early stage of thermal cycling, which covered the twelfth first cycles, the specimen experienced a one-stage transformation behaviour ($B2 \leftrightarrow B19'$). With further increasing thermal cycles, it already demonstrated a two-stage ($B2 \rightarrow R \rightarrow B19'$) transformation on cooling and a single-stage ($B19' \rightarrow B2$) on heating, implying that the repeated thermal cycling has a strong influence on the transformation behaviour.

2. There was a gradual decrease in the critical transition temperatures during the thermal cycling, whereas not very discernible changes were found in the peak temperature of the intermediate R-phase. Due to the increasing number of thermal cycles, the R-phase manifested itself in stabilization although its temperature range was expanded progressively.

3. Obtained calorimetric results and literature analysed allow to think that changes in the thermal transformation properties can be related to the fact that some modifications to the alloy microstructure (mainly dislocations) are introduced and then accumulated due to the repeated heating and cooling process.

Accepted for print 2.07.2010

References

- EGGELER G., KHALIL-ALLAFI J., GOLLERTHAN S., SOMSEN CH., SCHMAHL W., SHEPTYAKOV D. 2005. *On the effect of aging on martensitic transformations in Ni-rich NiTi shape memory alloys*. Smart Materials and Structures, 14: S186–S191
- Encyclopedia of Smart Materials. 2002. (Ed) M. SCHWARTZ, John Wiley & Sons, vol. 1–2: p. 951.
- FREMOND M., MIYAZAKI S. 1996. *Shape Memory Alloys*. in CISM Courses and Lectures, Springer Wien New York, 351: 72.
- KUŚ K. 2007. Wybrane charakterystyki funkcjonalne stopu Ni-Ti z pamięcią kształtu w warunkach obciążeń termomechanicznych. Prace naukowe ITWL, 22: 231–243.
- KUŚ K., BRECZKO T. 2010. DSC-investigations of the effect of annealing temperature on the phase transformation behaviours in a Ni-Ti shape memory alloy. Materials Physics and Mechanics, 9(1): 75–83.
- MACKERLE J. 2001. *Smart materials and structures: FEM and BEM simulations. A bibliography (1997–1999)*. Finite Elements in Analysis and Design, 37: 71–83.
- MATSUMOTO H. 1993. *Transformation behaviour of NiTi in relation to thermal cycling and deformation*. Physica B, 190: 115–120.
- MATSUMOTO H. 2003. *Transformation behaviour with thermal cycling in NiTi alloys*. Journal of Alloys and Compounds, 350: 213–217.
- MCCORMICK P.G., LIU Y. 1994. *Thermodynamic analysis of the martensitic transformation in NiTi-II. Effect of transformation cycling*. Acta Metallurgica Materialia, 42(7): 2407–2413.
- MEHRABI K., BRUNCKO M., KNEISSL A. C. 2009. *Effect of thermomechanical training on the transformation temperatures and properties of NiTi melt-spun ribbons*. ESOMAT 2009, 06022: 1–6.
- MIYAZAKI S., IGO Y., OTSUKA K. 1986. *Effect of thermal cycling on the transformation temperatures of Ti-Ni alloys*. Acta Metallurgica, 34(10): 2045–2051.

- MONNER H. P. 2005. *Smart materials for active noise and vibration reduction*. Keynote Paper, Novem-Noise and Vibration: Emerging Methods, Saint-Raphaël, France, 18–21 April, pp. 1–17.
- NURVEREN K., AKDOĞAN A., HUANG W. M. 2008. *Evolution of transformation characteristics with heating/cooling rate in NiTi shape memory alloys*. Journal of Materials Processing Technology, 196: 129–134.
- PAULA A.S., CANEJO J.P.H.G., MARTINS R.M.S., BRAZ FERNANDEZ F.M. 2004. *Effect of thermal cycling on the transformation temperature ranges of a Ni-Ti shape memory alloy*. Materials Science and Engineering, A378: 92–96.
- SHAW J. A., CHURCHILL C.B., IADICOLA M.A. 2008. *Tips and tricks for characterizing shape memory alloy wire: part 1- differential scanning calorimetry and basic phenomena*. Experimental Techniques, 32: 55–62.
- UCHIL J., GANESH KUMARA K., MAHESH K. K. 2002. *Effect of thermal cycling on R-phase stability in a NiTi shape memory alloy*, Materials Science and Engineering, A332: 25–28.
- WEI Z.G., SANDSTRÖM R., MIYAZAKI S. 1998. *Review Shape-memory materials and hybrid composites for smart systems*. Part I. *Shape-memory materials*. Journal of Materials Science, 33: 3743–3762.
- WILSON S.A., JOURDAIN R.P.J., ZHANG Q., DOREY R.A., BOWEN CH.R., WILLANDER M., WAHAB Q.U., WILLANDER M., AL-HILLI S.M., NUR O., QUANDT E., JOHANSSON CH., PAGOUNIS E., KOHL M., MATOVIC J., SAMEL B., VAN DER WIJNGAART W., JAGER E.W.H., CARLSSON D., DJINOVIC Z., WEGENER M., MOLDOVAN C., IOSUB R., ABAD E., WENDLANDT M., RUSU C., PERSSON K. 2007. *New materials for micro-scale sensors and actuators. An engineering review*. Materials Science and Engineering, R56: 1–129.
- WU S.K., LIN H.C., CHENG P.C. 1999. *Multi-strengthening effects on the martensitic transformation temperatures of TiNi shape memory alloys*. Journal of Materials Science, 34: 5669–5675.

ABRASIVE WEAR OF THE AlSi12Mg WITH Al-Si ALLOY FOR CASTING MACHINE PARTS

***Tomasz Lipiński, Mirosław Bramowicz, Paweł Szabracki,
Paweł Mikołajczyk, Marcin Cudakiewicz***

Department of Materials Technology
University of Warmia and Mazury in Olsztyn

Key words: Al-Si alloys, silumin, mechanical properties, structure, abrasive wear.

A b s t r a c t

This work presents results of modification of AlSi12Mg alloy with a modifier containing Al and Si. The modifier was taken down with components Al, Al7%Si and Al12%Si. A homogeneous modifier was obtained by fast cooling of homogeneous modifiers at $V=200^{\circ}\text{C/s}$. The components were put into a crucible containing liquid Al-Si alloy and kept there for one minute. The influence of the modifier in reference to the pulp of the worked alloy on abrasive wear was introduced in a graphic mould. The analysis of the modification process of a hypo eutectic alloy AlSi12Mg with a compound modifier showed the modifying influence on structure and abrasive wear.

ZUŻYCIE ŚCIERNE STOPU AlSi12Mg PO MODYFIKACJI STOPEM Al-Si PRZEZNACZONEGO NA CZĘŚCI MASZYN

***Tomasz Lipiński, Mirosław Bramowicz, Paweł Szabracki, Paweł Mikołajczyk,
Marcin Cudakiewicz***

Katedra Technologii Materiałów i Maszyn
Uniwersytet Warmińsko-Mazurski w Olsztynie

Słowa kluczowe: stopy Al-Si, silumin, właściwości mechaniczne, struktura, zużycie ścierne.

A b s t r a k t

W pracy przedstawiono wyniki badań zużycia ściernego stopu AlSi12Mg po modyfikacji modyfikatorem homogenicznym. Modyfikator przygotowywano przez chłodzenie z prędkością 200 K/s ciekłego stopu złożonego z Al, Al-7%Si i Al-12%Si. Odpowiednio rozdrobniony modyfikator dodawano do tygla wraz z ciekłym stopem AlSi12Mg na 1 minutę. Wpływ modyfikatora w odniesieniu do masy obrabianego stopu na wagowe zużycie ścierne przedstawiono w formie graficznej. Badanie zużycia prowadzono na maszynie Shoppera. Stwierdzono, że modyfikacja modyfikatorem o składzie zbliżonym do składu obrabianego stopu wpływa na strukturę i zużycie ścierne stopu AlSi12Mg.

Introduction

Al-Si alloys despite dynamic development of constructional materials designed on part of machines are still very popular. Its popularity is mainly results the low temperature of melting and proper weight as well as resistance on corrosion. Silumins has defekt, too. Main defect raw siluminów is susceptibility to creating of coarse-grained structures with low tensile strength and elongations. For improvement its proprieties silumins are modified. The modification depends on introduction to liquid alloy of additions which not changing in principal way its chemical composition, but cause crumbling the structure, and the same rise of mechanical proprieties of alloy. For machines parts produced by industry from eutectic Al-Si alloys most often were applied the process of modification with thoroughly well-chosen mixtures with sodium and strontium. The modification process, run with the chemical elements, improves in principal way the mechanical proprieties of alloy. The problems begin on stage of recycling. The used in exploitation phase casts are as dirtied of different chemically modifiers, which in renewed processing can effect unforeseen chemical reactions. With this reason purposeful is study method of making better the mechanical propriety of Al-Si alloys which will not exert on later process of recycling the negative influence on improvement process properties of alloys (BORKOWSKI 1999, GUZIK, KOPYCIŃSKI 2006, KRUPIŃSKI, DOBRZYŃSKI, SOKOŁOWSKI 2008, LIPÍŃSKI 2000, 2008, LJUTOVA, VOLCHOK 2008, NOVA, EXNER, HOSEK, NOVAKOVA 2004, PEZDA 2007, PIETROWSKI 2001, ROMANKIEWICZ, ROMANKIEWICZ 2006, WOŁCZYŃSKI 1990).

The processing of Al-Si alloys what is fulfilling technological requirements is modification with chemical compositions consisting with basic silumin components (homogenous modifier). The eutectic Al-Si alloy after modification with homogeneous modifier has crumbled structure in comparison with raw alloy. The structure eutectic Al-Si alloy with homogenous modifier is not fibrous structure as after modification process with chemical elements. Its consists from small silicon needles on background α -phase. Apart of that the mechanical properties treatment silumin with homogenous modifiers are comparable with proprieties of alloy after modification with typical chemical elements. However the chemical elements did not were introduce to alloy come from modifier in result of modification process, different than native classic components of alloy (Al and Si) (LIPÍŃSKI 2006, 2008, 2008).

The abrasive wear is one of proprieties of alloys. It depends from a lot of number of factors. But the structural of alloy is the main factor, its effect of modification process (ELMADAGLI, PERRY, ALPAS 2007, YASMIN et al. 2004).

The abrasive wear eutectic silumin AlSi12Mg with homogenous modifier (ecological modifier) is main research problem in this work.

Aim of the study, and methods

Investigation was conducted on alloy AlSi12Mg with Al+AlSi7+AlSi12. Founding, that studied proprieties are continuous functions considered variables and its can be with sufficient exactitude represented in figure of polynomial in investigations planning experiences was applied active, applying total factorial experiment (2^3) for three independent variables (Tab. 1). The equation (1) was introduced for received plan of investigations the figure of equation of regress.

$$\hat{y} = b_0 + b_1x_1 + b_2x_2 + b_3x_3 + b_{12}x_1x_2 + b_{13}x_1x_3 + b_{23}x_2x_3 + b_{123}x_1x_2x_3 \quad (1)$$

Table 1
Chemical composition of modifier in basic plan point number

Plan point number	Chemical composition of modifier [%]		
	Al	AlSi7	AlSi12
1	0.2	0.2	0.2
2	0.3	0.2	0.2
3	0.2	0.3	0.2
4	0.3	0.3	0.2
5	0.2	0.2	0.3
6	0.3	0.2	0.3
7	0.2	0.3	0.3
8	0.3	0.3	0.3
9	0.2	0.3	0.3
10	0.2	0.3	0.3
11	0.2	0.3	0.3

The results were analyzed mathematically, which enabled to formulate the factor equation for three variables, for the parameters studied, at the level of significance $\alpha = 0.05$. The adequacy of the above mathematical equation was verified using the Fischer criterion for $p = 0.05$. The methodology of process of modification in detail was described at work (LIPIŃSKI 2006, 2008, 2008).

Abrasive wear tested using Schopper machine by corundum abrasive disk at grainy 400 for parameters:

- | | | |
|-----------------------------|----------------|--------|
| – abrasive disk diametr | $\phi = 0.158$ | m |
| – abrasive disk revolutions | $n = 14.1$ | r.p.m. |
| – sample revolutions | $n = 0$ | r.p.m. |
| – holding down | $F = 200$ | N |

- unit pressure for area of samples $N = 3.9$ MPa
- working distance $l = 400$ m
- running speed $v = 0.12$ m.p.s.

Measurment of abrasive wear practiced by weight, determine loss in total weight with accuracy ± 0.0005 g by laboratory balance WA-21 manufactured in Zakład Mechaniki Precyzyjnej. For statistical analysis of abrasive wear was taken the value of averages with five measurements.

In aim of assurance of equal surface point of contact during investigation as well as obtainment of equal roughnesses of working surface, samples designed to investigations of abrasive wear was profiled to curvature of counter-samples by polishing. Working surfaces was cleaned after polishing by alcohol.

Result and discussion

The example of AlSi12Mg alloy structure with the modifier according to point 6 plan of investigations (Tab. 1) was showed on Fig. 1. There is fine-needle of eutectic β -phase on background of dendritic α -phase.

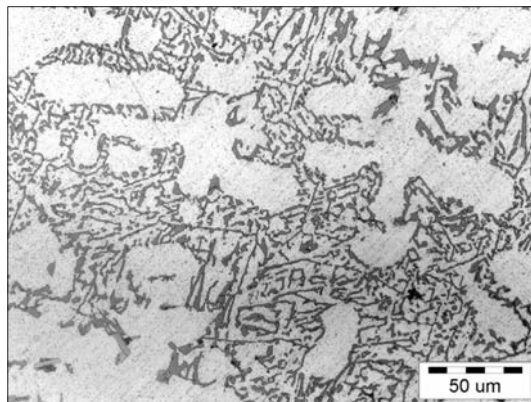


Fig. 1. Structure of AlSi12Mg alloy with 0.3% Al + 0.2% AlSi7 + 0.3% AlSi12 (point 6 of the research design – table 1)

Equation of abrasive wear regress (zs) for AlSi12Mg alloy with components: $Al \in <0.2, 0.3> [\%]$, $AlSi7 \in <0.2, 0.3> [\%]$, and $AlSi12 \in <0.2, 0.3> [\%]$ shows at (2) and its graphic mould at Fig. 2–7.

$$zs = 0.3255 + 0.003x_2 + 0.00775x_3 + 0.00325x_1x_2 + 0.0035x_1x_3 - 0.00425x_2x_3 - 0.0025x_1x_2x_3 \quad (2)$$

when: $F = 17.4$, $F_{1-p}(f_1, f_2) = 19.3$, then equation (2) is adequate.

Abrasive wear AlSi12Mg alloy with Al = 0.3%, AlSi7 \wedge AlSi12 \in <0.2, 0.3>[%] was showed at Figure 2. When the share of AlSi7 and AlSi12 was kept constant at 0.06% (Tab. 1), and when the remaining a three of factors had a 0.2% share of the mixture, abrasive wear reached $zs = 0.308$ g. This is the lowest abrasive wear for analysed plan of investigations. When the share of AlSi7 was increased to 0.3% (high level of investigation plan), abrasive wear increased by 8% to reach 0.334 g. When the also share of AlSi12 was increased from 0.2 to 0.3% (to high level of investigation plan – Tab. 1) and 0.2% AlSi7, abrasive wear increased by 7% to reach 0.330 g. When the share of Al was kept constant at 0.3%, and when the remaining two factors also had a 0.3% share of the mixture, abrasive wear reached $zs = 0.329$ g. Treatment of AlSi12Mg alloy with 0.29–0.3% AlSi12 and 0.2–0.2% AlSi7 did not reason change of level abrasive wear investigations alloy. It similar result was observed in this arrangement of variables, after use about 0.28 % AlSi7 and 0.2–0.2 % AlSi12.

When the share of Al was kept constant at 0.2%, and when the remaining two factors also had a 0.2% the abrasiwe wear of AlSi12Mg alloy was reported $zs = 0.312$ (Fig. 3). When the share of AlSi7 was increased (0.3% of the mass of the processed alloy), abrasive wear increased to reach 0.316 g. The more intensive growth of abrasiwe wear ($zs = 0.339$ g) was received after analogous increased participation of AlSi12 to the level 0.3%. There is the highest abrasive wear of AlSi12Mg alloy in analysed plan of investigations. When the share of Al was kept constant at 0.2% and about 0.265% AlSi12, the variations in the level AlSi7 does not influence on change of abrasive wear. After decrease quantity AlSi12 component AlSi7 affects on abrasive wear directly in proportion to changes its content in mixture, however after increased quantity AlSi12 inversely in proportion to its quantity. The AlSi12 is the main reason of change of analysed parameter for showed at Fig. 3 weight in weight concentration.

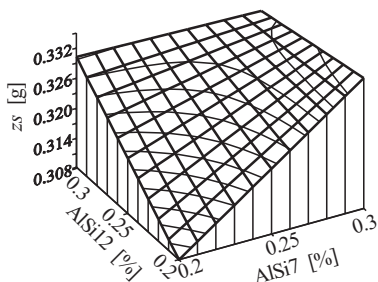


Fig. 2. Abrasive wear (zs) AlSi12Mg alloy with AlSi7 \in <0.2, 0.3> [%], AlSi12 \in <0.2, 0.3> [%], Al = 0.3%

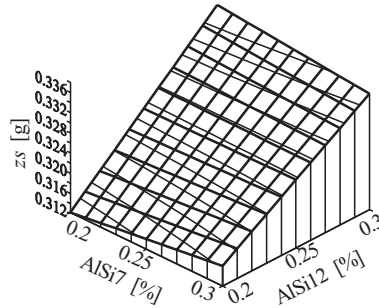


Fig. 3. Abrasive wear (z_s) AlSi12Mg alloy with AlSi7 \in <0.2, 0.3> [%], AlSi12 \in <0.2, 0.3> [%], Al = 0.2%

When the share of AlSi7 was kept constant at 0.3% and when the remaining two factors had a 0.2% share of the mixture, abrasive wear reached $z_s = 0.316$ g (Fig. 4). When the share of AlSi12 was increased from 0.2% to 0.3%, abrasive wear increased by 6% to reach 0.335 g. Increased abrasive wear was received after analogous increased in modifier contents of Al, too. For 0.3% Al abrasive wear was $z_s = 0.330$ g. For 0.3% AlSi7 i 0.3% AlSi12 and when the share of Al was increased from 0.2 to 0.3%, abrasive wear was reduced to reach 0.329 g. When the share of AlSi7 was kept at 0.3%, changes of Al i AlSi12 in range <0.265, 0.29> [%] was not change of wear (Fig. 4). When the share of both significant factors (Al or AlSi12) was kept at range about 0.28%, the resulting abrasive wear was stabilized on unchanging level.

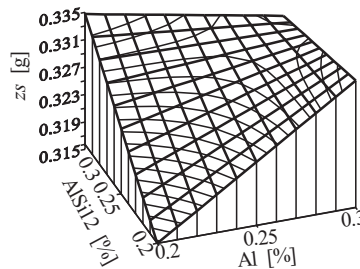


Fig. 4. Abrasive wear (z_s) AlSi12Mg alloy with Al \in <0.2, 0.3> [%], AlSi12 \in <0.2, 0.3> [%], AlSi7 = 0.3%

The abrasive wear of AlSi12Mg alloy with constant 0.2% AlSi7 and when the remaining two factors of modifier on range 0.2–0.3 % was showed on Fig. 5. When the share all of components of modifier was kept constant at 0.2%, abrasive wear reached $z_s = 0.312$ g. When the share of Al was increased, abrasive wear reduced to reach 0.308 g. After analogous introduction 0.3% AlSi12, was received opposite direction of influence. For it the change of wear is directly proportional to its content. The distribution of contour lines

indicates that AlSi12 had a more intensive effect on the analyzed parameter than Al. When the share of AlSi12 was kept constant at 0.3%, the lowest wear was reported for also a higher share of the remaining factors (0.3%), reaching $z_s = 0.329$ (Fig. 5). When the share of Al and AlSi12 was reduced to 0.2% and with 0.2% AlSi7, abrasive wear increased to reach 0.339 g. For the contents of modifier abrasive wear is the higher in this plan of investigation. Increasing content the AlSi7 in mixture strengthens influence the Al.

The changes of abrasive wear AlSi12Mg alloy with constant range at 0.2% AlSi12 was showed at Fig. 6. The above suggests that changes in the AlSi7 from 0.2 to 0.3% share of the mixture affect with less effect on the abrasive wear of

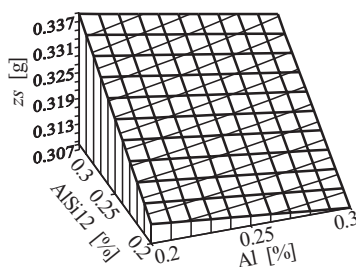


Fig. 5. Abrasive wear (z_s) AlSi12Mg alloy with $Al \in <0.2, 0.3> [\%]$, $AlSi12 \in <0.2, 0.3> [\%]$, $AlSi7 = 0.2\%$

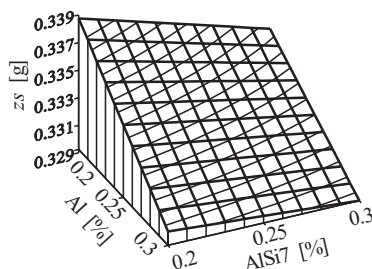


Fig. 6. Abrasive wear (z_s) AlSi12Mg alloy with $AlSi7 \in <0.2, 0.3> [\%]$, $Al \in <0.2, 0.3> [\%]$, $AlSi12 = 0.3\%$

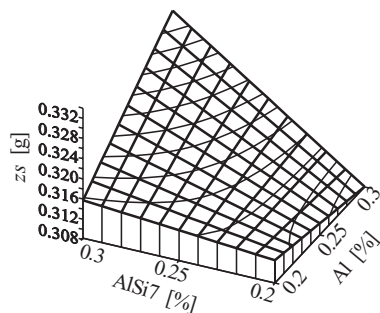


Fig. 7. Abrasive wear (z_s) AlSi12Mg alloy with $AlSi7 \in <0.2, 0.3> [\%]$, $Al \in <0.2, 0.3> [\%]$, $AlSi12 = 0.2\%$

the AlSi12Mg alloy then analogous change of Al. The intensity of abrasive wear, in this arrangement, dynamically increases with concurrent increased in modifier quantity of Al and AlSi7.

A comparison of the effect of Al and AlSi7 and with AlSi12 on constant range 0.3% on the abrasive wear of the AlSi12Mg alloy indicates that Al is capable of inducing more intensive changes (Fig. 6). However, for 0.2% AlSi12 more intensive changes was affirmed for AlSi7 (Fig. 7). Then, the effect of mixture components on the range of abrasive wear in AlSi12Mg alloy depends of their percentage. This facts speaks about co-operation of analysed factors.

Conclusions

The largest gradient of changes was received for 0.3% Al and $\text{AlSi7} \in <0.2, 0.3 > [\%]$. For participation 0.2 % Al, similarly how for 0.2 % AlSi7, change suitably AlSi7 or Al does not cause the large change of abrasive wear.

Summing up analyze influence the applied to processing of alloy AlSi12Mg of components on base of Al with variable of content Si, the growth of abrasive wear was affirmed for AlSi12Mg alloy treatment with growth of part of silicon in homogenous modifier.

Minimal abrasive wear $z_s = 0.308 \text{ g}$ may be achieved by using 0.3% Al, 0.2% AlSi7 and 0.2% AlSi12.

Accepted for print 18.08.2010

References

- BORKOWSKI S. 1999. *Quality controll of cast constructional materiale for example cast iron*. WNT, Warsaw.
- ELMADAGLI M., PERRY T., ALPAS A.T. 2007. *A parametric study of the relationship between microstructure and wear resistance of Al-Si alloys*. Wear, 262: 79–92.
- GUZIK E., KOPYCIŃSKI D. 2006. *Modeling Structure Parameters of Irregular Eutectic Growth: Modification of Magnin-Kurz Theory*. Metallurgical and Transactions 37A: 3057–3067.
- KRUPIŃSKI M., DOBRZYŃSKI L.A., SOKOŁOWSKI J.H. 2008. *Microstructure analysis of the automotive Al-Si-Cu casting*. Archives of Foundry Engineering, 8: 71–74.
- LIPIŃSKI T. 2000. *Analysis of influence exothermal mixtures on AlSi7Mg alloy*. Mińsk, pp. 87–89.
- LIPIŃSKI T. 2006. *Ekological modification AlSi7Mg alloy*. Archives of Foundry Engineering, 6/18: 91–96.
- LIPIŃSKI T. 2008. *Improvement of mechanical properties of AlSi7Mg alloy with fast cooling homogenous modifier*. Archives of Foundry Engineering, 8: 85–88.
- LIPIŃSKI T. 2008. *Modification of the Al-Si Alloys with the use of a Homogenous Modifiers*. Archives of Metallurgy and Materials, 53(1): 193–197.
- LJUTOVA O.V., VOLCHOK I.P. 2008. *Increase of foundry properties of secondary silumins*. Archives of Foundry Engineering, 8: 89–91.
- NOVA I., EXNER J., HOSEK Z., NOVAKOVA I. 2004. *Crystallization of Al-Si alloys in the course of high pressure die-casting*. Archives of Foundry, 4(14): 325–332.

- ORŁOWICZ A.W., TUPAJ M., MRÓZ M. 2008. *Mechanical properties of AlSi7Mg with sodium*. Archives of Foundry Engineering, 8.
- PEZDA J. 2007. *Continuous modification of AK11 silumin with multicomponent salt on base of NaCl*. Archives of Metallurgy and Materials, 4: 151–154.
- PIETROWSKI S. 2001. *Silumins*, University of Łódź.
- ROMANKIEWICZ F., ROMANKIEWICZ R. 2006. *The influence of modification for structure and morphology fractures of alloy AlSi132*. Archives of Foundry Engineering, 6(22): 436–440.
- WOŁCZYŃSKI W., CYPRUŚ R. 1999. *The analysis of the influence of the gibbs free energy onto the lamella-rod transition in Al-Si alloy*. Archives of Metallurgy, 44(3): 339–353.
- YASMIN T., KHALID A.A., HAQUE M.M. 2004. *Tribological (wear) properties of aluminum-silicon eutectic base alloy under dry sliding condition*. Journal of Materials Processing Technology, 153–154: 833–838.

INFLUENCE OF PROCESSING MULTIPLICITY ON VALUES OF MASS FLOW RATE AND MELT VOLUME RATE OF POLYCARBONATE

Piotr Mazur, Daniel Jasiukiewicz

Chair of Materials and Machines Technology
University of Warmia and Mazury in Olsztyn

Key words: polymers, mass flow rate, volume rate, recycling.

A b s t r a c t

Both the mass flow rate and melt volume rate are the basic technological indicators of the polymers injection moulding. During material recycling, which is the injection moulding of recyclates, awareness of the values of the above mentioned indicators is crucial. It enables setting up the optimal values of an injection moulding machine and if necessary suggests using other type of recycling.

WPŁYW KROTNOŚCI PRZETWÓRSTWA NA WARTOŚĆ MASOWEGO I OBJĘTOŚCIOWEGO WSKAŹNIKA SZYBKOŚCI PŁYNIĘCIA POLIWĘGLANU

Piotr Mazur, Daniel Jasiukiewicz

Katedra Technologii Materiałów i Maszyn
Uniwersytet Warmińsko-Mazurski w Olsztynie

Słowa kluczowe: polimery, masowy i objętościowy wskaźnik szybkości płynięcia, recykling.

A b s t r a k t

Masowy i objętościowy wskaźnik szybkości płynięcia to podstawowe wskaźniki technologiczne wtryskowego przetwórstwa tworzyw polimerowych. W czasie recyklingu materiałowego polegającego na wtryskiwaniu recyklatów istotna jest znajomość wartości tych wskaźników. Umożliwia to optymalne ustawienie parametrów pracy wtryskarki, a w skrajnych przypadkach należy zastosować inny rodzaj recyklingu.

Introduction

Both the mass flow rate and melt volume rate are the basic technological indicators of the polymers injection moulding. Their values are directly connected with the viscosity of plastics, whereas the viscosity is dependent on the length of a polymer chain and its branching. During material recycling, which is the injection moulding of recyclates, awareness of the values of the above mentioned indicators is crucial. It enables setting up the optimal values of an injection moulding machine and if necessary suggests using other type of recycling.

Obtaining Polycarbonate

Polycarbonates are received in the polycondensation reaction of alcohols or phenols with phosgene or esters of the carbonic acid. The reaction can proceed on the phase boundary or in a solvent (PIELICHOWSKI, PUSZYŃSKI 1998).

Polycarbonate Properties

The polycarbonate is received by phosgening of the dian (just that was used in the research). It is a thermoplastic polymer of the very high softening temperature, linear constitution, with no branches. The polycarbonate macromolecules characterize with the high rigidity, which is limited by the rotation of the aromatic rings, and relatively long segments having no polar units. It results from the constitution that polycarbonate has small tendency to crystallization, relatively high vitrification temperature, high melting temperature and high viscosity in the melted state. Clean polycarbonate products are colorless and transparent because of the low crystallization ability. The light transmittance is comparable with that of glass. The polymer characterizes with the smooth glossy surface. It can be easily colored (PIELICHOWSKI, PUSZYŃSKI 1998, SEACHTLING 1999, ŻUCHOWSKA 2000).

Polycarbonate belongs to not numerous polymers which join good mechanical and thermal properties with electric and optic ones. It is distinguished by the high rigidity, strength, and particularly the impact strength in the range of 150°C to 135°C. The maximal short-term use temperature is 150°C. The range of long-term use is 40°C do 130°C. The range qualifies polycarbonate to the thermal resistant materials. Polycarbonate is one of not numerous thermoplastic polymers of the high resistance to the impact fatigue (with no notch). However, it is fragile for a notch, which is obviously visible at the long-term

fatigue strength. There is a risk of the strain cracking. In the abrasion activity conditions its application is limited. Polycarbonate characterizes with the creep resistance and the small water absorbing capacity. Humidity has no influence on the dielectric properties of that polymer. The chemical resistance of polycarbonate is limited, especially in case of the organic solvents, as: chloroform and dichloromethane. CO₂ permeability is relatively high. That is why in the production of bottles for the carbonated drinks the protective layers of PET or PBT should be applied. Polycarbonate does not show neither the poisonous properties nor harmful influence on the human body. It is hydrolysis resistant. It can be sterilized and used in medicine (it is physiologically neutral). It is a self-extinguishing polymer after removal of the source of fire (PIELICHOWSKI, PUSZYŃSKI 1998, SEACHTLING 1999, ŻUCHOWSKA 2000).

Polycarbonate Processing

Polycarbonate is processed by all the methods typical for the thermoplastics, e.g. injection, drawing, etc. It is a polymer difficult in processing. In spite of that its flow temperature is 220°C, its processing temperature (because of the low heat conduction) is high and it is equal to 280–320°C at injection, and while drawing – 240–280°C. In the melted state polycarbonate has big adhesion to a metal what considerably makes the processing more difficult. High viscosity of the polymer requires much injection power or small ratio between the flow distance and wall thickness. The preliminary drying at the temperature of 120°C of the polymer prior to processing is necessary within 4 to 24 hours to decrease the humidity under 0.01–0.02%. The processing shrinkage is 0.6–0.8%, the after – shrinkage is not crucial (SEACHTLING 1999, ŻUCHOWSKA 2000, SZLEZYNGIER 1998).

Methodology of Processing Properties Research

The precise determination of the plastics viscosity curves, i.e. the dependence of the viscosity on the shear rate, is expensive and time consuming. That is why the MFR and MVR characterize polymers flow in the machines and devices canals during processing. These are the quantities defining mass or volume of a polymer drawn for 10 minutes through the nozzle with a specified diameter, under a specified load and at a specified temperature. The essence of determining the flow rate is the measurement of the mean flow rate of the plastic at the specified basic parameters of the processing. The flow rate is a measure of the liquidity of a material, therefore it is opposite to the viscosity.

It represents one point of the viscosity curve of the examined material, determined at the measurement temperature. It does not define unequivocally the examined material and it can be the same for plastics with different viscosity characteristics.

The standard measurement conditions (ISO 1133 norm) concern the capillary tube and piston geometry, load of a piston, time and temperature of the measurement. The load of the piston and measurement temperature are selected in dependence on a type of the examined plastic, and to be precise, they are conditional on the properties of the plastic. Results of the measurements are given either in g/10 min (MFR) or in cm³/10 min (MVR). Evaluation of the Mass Flow Rate and Melt Volume Rate consists in the plasticization of a plastic sample in a heated cylinder, drawing of the plasticized material through the nozzle situated in the lower part of the cylinder and determining of the drawn mass or the cylinder displacement. Prior to the beginning of the research the cylinder and plastometer piston are heated to the proper temperature, which is maintained ($\pm 0.5^\circ\text{C}$) over 15 min before the measurement and during the measurement.

The research was carried out with the REO-100 plastometer, at the temperature of 280°C and under the load of 2160 g; the density of the investigated polycarbonate was $\rho = 1.20 \text{ g cm}^{-3}$.

Basic technical parameters of the REO-100 plastometer:

- max. heating power of a heater – 1050 W,
- range of measured temperature – $30\text{--}300^\circ\text{C}$,
- temperature stabilization – $\pm 0.2^\circ\text{C}$,
- accuracy of time measurements – 10 μs ,
- accuracy of distance measurements – 5 μm ,
- range of measured distance – 100 mm.

The initial plastic had a form of granulate. After going through the plastometer the plastic was mechanically shredded (cut). The regranulate obtained that way was investigated in the plastometer.

Results

The research results of the Mass Flow Rate (Fig. 1) and Melt Volume Rate (Fig. 2) are presented in the diagrams. The curve presenting changes of the Mass Flow Rate can be circumscribed with the equation (1):

$$y = 14.587e^{0.6927x} \quad (1)$$

where $R^2 = 0.9589$.

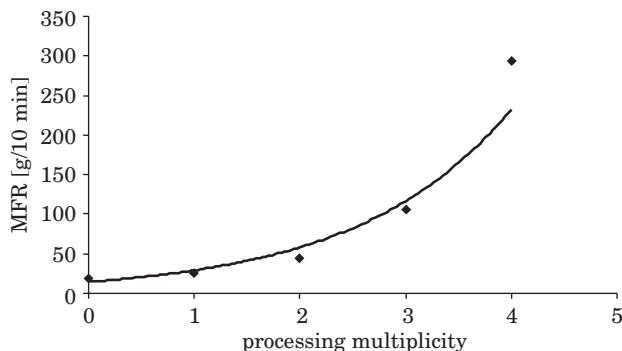


Fig. 1. Changes of Mass Flow Rate in dependence on processing multiplicity

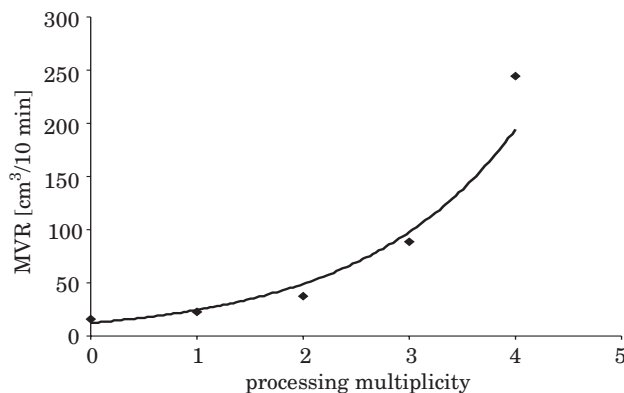


Fig. 2. Changes of Melt Volume Rate in dependence on processing multiplicity

The curve presenting changes of the Melt Volume Rate can be circumscribed with the equation (2):

$$y = 12.381e^{0.6883x} \quad (2)$$

where $R^2 = 0.9601$.

Conclusions

The MFR and MVR are closely related with each other. This fact is confirmed by the similarity of the regression curves and similarity of their equations. Their analysis shows degradation and destruction of the investigated polymer (shortening of chains) (KOSZKUL, MAZUR 2003). It is connected

with the influence of the temperature (processing) and mechanical shredding (recycling). The degradation proceeds so fast that it was impossible to carry out the measurements after the fourth processing, because the polymer was leaking through the not loaded nozzle. That limits using the material recycling (up to the fourth processing) in case of the polymer. On the other hand, that rather suggests application of the raw material recycling, which gives many more possibilities of reuse of the depolymerization products.

Accepted for print 19.08.2010

References

- KOSZKUL J., MAZUR P. 2003. *Kompozyty z recyklatu poli(tereftalanu etylenu) z krótkim włóknem szklanym*. Kompozyty, 8: 349–352, Politechnika Częstochowska.
- PIELICHOWSKI J., PUSZYŃSKI A. 1998. *Technologia tworzyw sztucznych*. WNT, Warszawa.
- SAECHTLING H. 1999. *Tworzywa sztuczne*. Poradnik. WNT, Warszawa.
- SZLEZYNGIER W. 1998. *Tworzywa sztuczne*. Rzeszów.
- ŻUCHOWSKA D. 2000. *Polimery konstrukcyjne*. WNT, Warszawa.

INFLUENCE OF PROCESSING MULTIPLICITY ON VALUES OF MASS FLOW RATE AND MELT VOLUME RATE OF PPS

Piotr Mazur, Piotr Smoleński

Chair of Materials and Machines Technology
University of Warmia and Mazury in Olsztyn

Key words: polymers, mass flow rate, volume rate, recycling.

A b s t r a c t

Both the mass flow rate and melt volume rate are the basic technological indicators of the polymers injection moulding. During material recycling, which is the injection moulding of recyclates, awareness of the values of the above mentioned indicators is crucial. It enables setting up the optimal values of an injection moulding machine and if necessary suggests using other type of recycling.

WPŁYW KROTNOŚCI PRZETWÓRSTWA NA WARTOŚĆ MASOWEGO I OBJĘTOŚCIOWEGO WSKAŹNIKA SZYBKOŚCI PŁYNIĘCIA PPS

Piotr Mazur, Piotr Smoleński

Katedra Technologii Materiałów i Maszyn
Uniwersytet Warmińsko-Mazurski w Olsztynie

Słowa kluczowe: polimery, masowy i objętościowy wskaźnik szybkości płynięcia, recykling.

A b s t r a k t

Masowy i objętościowy wskaźnik szybkości płynięcia to podstawowe wskaźniki technologiczne wtryskowego przetwórstwa tworzyw polimerowych. W czasie recyklingu materiałowego polegającego na wtryskiwaniu recyklatów istotna jest znajomość wartości wymienionych wskaźników. Umożliwia to optymalne ustawienie parametrów pracy wtryskarki, a w skrajnych przypadkach należy zastosować inny rodzaj recyklingu.

Introduction

Both the mass flow rate and melt volume rate are the basic technological indicators of the polymers injection moulding. Their values are directly connected with the viscosity of plastics, whereas the viscosity is dependent on the length of a polymer chain and its branching. During material recycling, which is the injection moulding of recyclates, awareness of the values of the above mentioned indicators is crucial. It enables setting up the optimal values of an injection moulding machine and if necessary it suggests using other type of recycling.

Obtaining PPS

Production of polyphenylene sulfide for needs of plastics processing is based mainly on two technological processes. Polycondensation of dichlorobenzene with sodium sulfide is first of them. Thermal modification of PPS is the second one.

Properties of PPS

At present the most familiar form of polyphenylene sulfide is a polymer known in the market as Ryton, which is manufactured by the Phillips Petroleum Company in the USA. Also German and Japan companies manufacture the chemical compound. PPS is produced in several varieties, which differ in the degree of the physical modification and types of the fillers (JURGA 1994). The characteristic feature of PPS is change of the properties during heating in the presence of oxygen. Polyphenylene sulfide heated to the temperature of over 320°C behaves as a thermohardening polymer. However, the hardening process proceeds very slowly and does not make difficult processing by the injection moulding (HAŁASA, HENECZKOWSKI 2007).

The perfect utility properties of PPS, and especially PPS hardened by the glass fiber (HAŁASA, HENECZKOWSKI 2007), are:

- High rigidity and hardness,
- High mechanical strength, thanks to the huge adhesion of PPS to the glass fiber,
- Dimension stability,
- Low creep,
- High resistance to chemicals and solvents,
- Self-extinguishing properties,

– Very good dielectric properties, practically independent neither on the humidity rate of environment nor frequency.

PPS is a fragile thermoplastic and in the not-filled form it is seldom used in the injection moulding processing. However, PPS can be used for the production of foils and fibers. The injection moulding method is applied to manufacture mixtures hardened by the fibers, the mineral fillers or their combinations. For the purposes there are used the glass fibers, carbon fibers, aramid fibers and as a filler is used calcium carbonate, calcium sulfate, kaolin, mica, talc and quartz. The mechanical properties are mostly dependent on kinds and quantity of additives (SZLEZYNGIER 1998). Polyphenylene sulfide, except for the good thermal resistance, characterizes with very satisfactory chemical resistance. It is also resistant to the hydrolysis. PPS is not UV resistant. This feature might be improved by adding some dark pigment (HAŁASA, HENECZKOWSKI 2007).

PPS processing

PPS and its composites processing is carried out by the ordinary machines used for processing of the typical thermoplastics but after the necessary modifications. The basic differences concern higher limitation temperature of a cylinder, nozzle and mould (HAŁASA, HENECZKOWSKI 2007).

The main parameters of the injection moulding process are as follows (HAŁASA, HENECZKOWSKI 2007):

- mould temperature – 130–160°C – it decides on crystallization degree, which means it decides on the polymer properties,
- injection temperature – recommended in the range of 305–345°C.

Polyphenylene sulfide is not hygroscopic but the fillers are. This is why the filled polymer prior to processing has to be dried to the humidity level of 0.03%. The granulated PPS is dried in the temperature of 150–160°C over 2–3 hours. PPS can be processed by injection moulding, pressing or sintering.

Research Methodology of Processing Properties

Precise determining of the viscosity curves for plastics, that is the dependence of the viscosity on the shear rate, is expensive and time consuming. That is why the MFR and MVR indexes characterize polymers flow in machines and devices canals during processing. These are the quantities defining mass or volume of a polymer drawn for 10 minutes through the nozzle with a specified diameter, under a specified load and at a specified temperature. The essence of

determining the flow rate is measurement of the mean flow rate of a plastic at the specified basic parameters of processing. The flow rate is a measure of the liquidity of a material, therefore it is opposite to the viscosity. It represents one point of the viscosity curve of an examined material, determined at the measurement temperature. It does not define unequivocally the examined material and it can be the same for plastics with different viscosity characteristics. The standard measurement conditions (ISO 1133 norm) concern the capillary tube and piston geometry, load of a piston, time and temperature of the measurement. The load of the piston and measurement temperature are selected in dependence to a type of the examined plastic, and to be precise, they are conditional on the properties of a plastic. Results of the measurements are given either in g/10 min (MFR) or in cm³/10 min (MVR). Evaluation of the Mass Flow Rate and Melt Volume Rate consists in the plasticization of a plastic sample in the heated cylinder, drawing of the plasticized material through the nozzle situated in the lower part of the cylinder and determining of the drawn mass or the cylinder displacement. Prior to the beginning of the research the cylinder and plastometer piston are heated to the proper temperature, which is maintained ($\pm 0.5^{\circ}\text{C}$) over 15 min before the measurement and during the measurement.

The measurements were carried out using the REO-100 plastometer characterizing the following parameters:

- max. heating power of a heater – 1050 W,
- range of measured temperature – 30–300°C,
- temperature stabilization – $\pm 0.2^{\circ}\text{C}$,
- accuracy of time measurements – 10 μs ,
- accuracy of distance measurements – 5 μm ,
- range of measured distance – 100 mm.

The literature does not present the influence of the processing multiplicity on values of the MFR and MVR. In the paper there was made an effort to determine the above mentioned dependence. The granulated PPS was the initial material and each processing was followed by the mechanical shredding to the form of regranulate.

The process temperature was equal to 300°C and the load equaled 5000 g.

Research Results and their Analysis

The results of the investigation of the Mass Flow Rate (Fig. 1) and Melt Volume Rate (Fig. 2) were presented in the diagrams. The curve presenting changes of the Mass Flow Rate can be circumscribed with the equation (1):

$$y = 0.0002x_3 - 0.0142x_2 - 0.5386x + 47.838 \quad (1)$$

where $R^2 = 0.8747$.

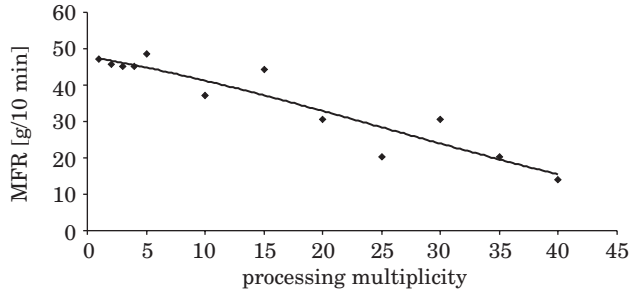


Fig. 1. Changes of Mass Flow Rate in dependence on processing multiplicity

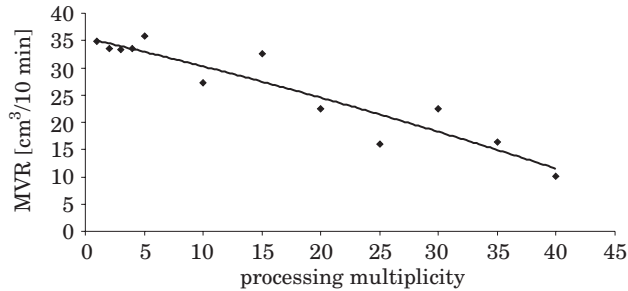


Fig. 2. Changes of Melt Volume Rate in dependence on processing multiplicity

The curve presenting changes of the Melt Volume Rate can be circumscribed with the equation (2):

$$y = -0.0026x_2 - 0.4968x + 35.477 \quad (2)$$

where $R^2 = 0.8801$.

Conclusions

The MFR and MVR are closely related with each other. This fact is confirmed by the similarity of the regression curves and similarity of their equations. Their analysis shows the increase of the polymer viscosity which is connected with either elongation of the chain or its branches growth (flanks).

It is caused by the temperature during the following processing multiplicities (KOSZKUL, MAZUR 2003). It creates huge possibilities for material recycling of the polymer.

Accepted for print 18.08.2010

References

- HAŁASA E., HENECZKOWSKI M. 2007. *Wprowadzenie do inżynierii termoodpornych materiałów polimerowych*. Rzeszów.
- JURGA J. 1994. *Dynamika i struktura molekularna polisiarczku fenylu modyfikowanego termicznie do celów przetwórstwa*. Politechnika Poznańska. Poznań.
- KOSZKUL J., MAZUR P. 2003. *Kompozyty z recyklatu poli(tereftalanu etyleny) z krótkim włóknem szklanym*. Kompozyty, 8: 349–352, Politechnika Częstochowska. Częstochowa.
- SZLEZYNGIER W. 1998. *Tworzywa sztuczne*. Rzeszów.

AN ATTEMPT TO IMPROVE THE AXISYMMETRIC MODEL OF A PNEUMATIC TIRE

Józef Pelc

Chair of Mechanics and Machine Design
University of Warmia and Mazury in Olsztyn

Key words: tire, cord-rubber composite, deformation modeling, finite element method.

Abstract

The existing method of a tire cord-rubber ply modeling involved the determination of effective material constants relative to ply thickness. This paper investigates the use of the same method in reference to plies with the thickness of a cord. Cord-rubber plies with orthotropic properties were separated by layers of isotropic rubber to maximize the composite susceptibility to deformation. When the improved model was applied in the simulations of tire pumping to nominal pressure, an increase was observed in the displacements of the tire characteristic points, maximum equivalent stress in rubber layers located between cord-rubber plies and the shear strain of rubber.

PRÓBA DOSKONALENIA OBROTOWO-SYMETRYCZNEGO MODELU OPONY PNEUMATYCZNEJ

Józef Pelc

Katedra Mechaniki i Podstaw Konstrukcji Maszyn
Uniwersytet Warmińsko-Mazurski w Olsztynie

Słowa kluczowe: opona, kompozyt kodowo-gumowy, modelowanie deformacji, metoda elementów skończonych.

Abstrakt

Dotychczasowy, powszechnie stosowany sposób modelowania warstwy kord-guma w oponie polegał na wyznaczaniu stałych efektywnych materiału w odniesieniu do grubości warstwy. Zbadano możliwość zastosowania tego samego sposobu, ale w odniesieniu do warstwy o grubości nici kordu. Warstwy kordu o właściwościach ortotropowych rozdzielono warstwami gumy izotropowej, co wpłynęło na zwiększenie podatności kompozytu na odkształcenia. Wykorzystując udoskonalony model do symulacji pompowania opony testowej do ciśnienia o wartości nominalnej, zaobserwowano wzrost wartości przemieszczeń jej punktów charakterystycznych, maksymalnych naprężeń zredukowanych w gumie między warstwami oraz odkształceń postaciowych w gumie.

Introduction

In axisymmetric computational models of pneumatic tires based on the finite element method, the rubberized cord ply is usually discretized in such a way that one of the finite element dimensions is equal to the thickness of that ply (KAGA, OKAMOTO, TOZAWA 1977, TSENG et al. 1991, PELLE 1994, PELC 1995, PELC 2000). In this case, the mechanical properties of a layer comprising cords, the rubber between cords and two rubber layers covering the cord-rubber layer are averaged in the area of the finite element and are presented in the form of effective constants of the composite ply (JONES 1975). This material is characterized by greater rigidity than the material of the rubber layers (referred to as separators) isolating cord-rubber plies with the thickness of a cord (i.e. steel or textile yarn). The finite elements of adjacent plies share nodes along their boundary, therefore, the relative displacement of those plies is blocked despite the existence of compliant rubber separators. The method for the cord-rubber composite material modeling with rubber separators has been indicated by WALTER (1978) and used by CEMBROLA and DUDEK (1985) in modeling of deformations of a plane composite specimen. This study investigates the effect of separators in modeling of deformation of a truck tire subjected to internal pressure.

Constants for cord-rubber plies and for rubber materials

Effective (averaged) constants of the cord-rubber composite ply may be calculated based on the equations proposed by HALPIN and TSAI (1969) which take on the following form on the assumption that cords have a much higher shear modulus than rubber:

$$\begin{aligned}
 E_1 &= E_c v_c + E_r (1 - v_c) \\
 E_2 &= \frac{E_r (1 + 2v_c)}{1 - v_c} \\
 \nu_{12} &= v_c v_c + v_r (1 - v_c) \\
 G_{12} &= G_r \frac{1 + v_c}{1 - v_c}
 \end{aligned} \tag{1}$$

where: letters $E/G/\nu$ – indicate Young modulus, Kirchhoff modulus and the Poisson ratio, indices c/r denote cord and rubber. Axis 1 is parallel to the cord, and axis 2 is the perpendicular axis in the layer plane. At constant density of

cord e_p with cross-section area A_c , the values of the above constants are determined by the ply thickness t and the ply cord volume fraction:

$$v_c = \frac{e_p A_c}{t} \quad (2)$$

When rubber layers covering the cord on both sides are included in the cord-rubber composite ply, the value of parameter v_c decreases in comparison with that corresponding to the cord-rubber ply with the thickness of a cord.

The tire purely rubber elements (tread, sidewall, etc.) are considered to be incompressible, and their properties are described with the use of a one-parameter, neo-Hookean model.

Characteristic of an axisymmetric tire model

The model has the features of an axisymmetric system if only internal pressure is applied to the tire. In this case, only the tire cross-section is discretized, and the problem has class 2.5D. The analyzed tire cross-section and the standard mesh of elements with one finite element at the thickness of the rubber/cord-rubber/rubber composite ply are presented in Figure 1a and Figure 1b, respectively. The mesh is also used to generate 3D tire models.

To eliminate the effect of the discretization degree on the results, a refined mesh of finite elements was generated and used in both the standard model of cord-rubber composite plies (Fig. 2a) as well as in the improved model, i.e. a model accounting for rubber separators between reinforcement layers, when cord-rubber plies have the thickness of a cord (Fig. 2b). It has been assumed that the nodes of tire beads that come into contact with the rim are fully fixed, therefore, the tire contact with the rim has been disregarded as insignificant for the needs of this analysis. The nodes located in the tire plane of symmetry (yz) may be displaced only in the radial direction. Internal pressure was applied to the tire (Fig. 1b).

The problem was solved using the MARC program with user subroutines supporting the description of the composite specific properties. The composite geometric parameters in the tire are determined based on the properties of the non-vulcanized, raw layer on the tire building drum, the geometric parameters of the drum and the vulcanization mold. In the FEM model, the element overlaying technique was used to improve the model numeric properties (PELC 2002). Cord-rubber composite plies and bead wire were modeled with four-noded axisymmetric solid elements, while five-noded incompressible Hermann elements were applied to model rubber layers and purely rubber elements. The number and type of elements are presented in Table 1.

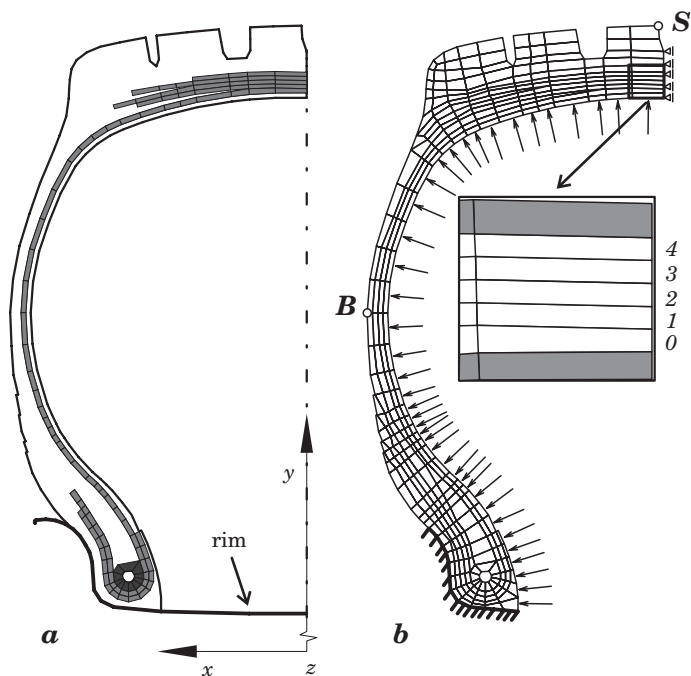


Fig. 1. Axisymmetric model of a truck tire: *a* – cross-section with an indication of plies, *b* – typical finite elements mesh: 0 – body ply; 1, 2, 3 and 4 – successive belt plies

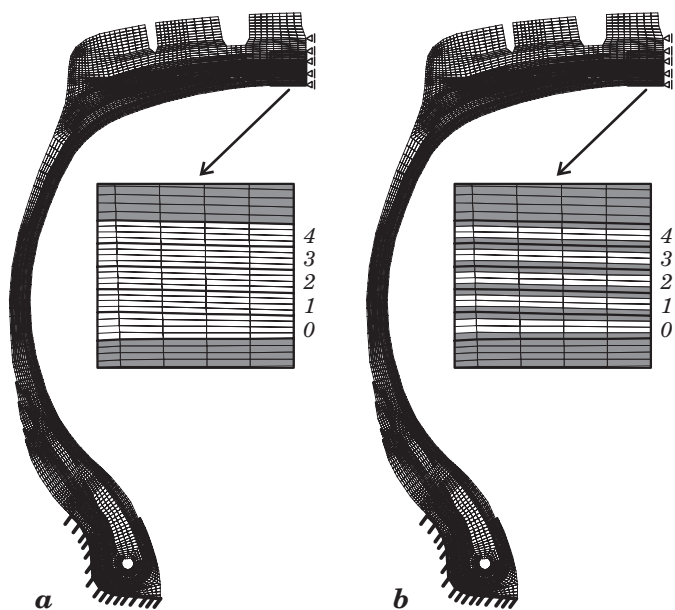


Fig. 2. Axisymmetric model of a truck tire: *a* – standard model, *b* – improved model: 0 – body ply; 1, 2, 3 and 4 – successive belt plies

Table 1

Number of elements in every tire zone

Zone	Number of elements		
	typical model (Fig. 1b)	standard model (Fig. 2a)	improved model (Fig. 2b)
Cord-rubber plies	96	1536	768
Rubber under plies	96	1536	768
Bead wire (steel)	11	176	176
Pure rubber	227	3632	3632
Rubber between plies	0	0	768
Total	430	6880	6112

Calculation results

Due to the model non-linear character, the Newton-Raphson method was selected to calculate the solution. The tire was subjected to incremental load by increasing internal pressure to nominal pressure of 800 kPa.

Displacement components of the tire two characteristic points, point *B* and point *S* (Fig. 1b), are presented in Table 2. In the improved model, maximum axial and radial displacement of the two points increased by 8% and 3%, respectively, in comparison with the standard model.

Table 2

Displacement components of the tire characteristic points

Tire model	Point located in tire profile	<i>B</i>		<i>S</i>	
	Displacement [mm]	<i>x</i>	<i>y</i>	<i>x</i>	<i>y</i>
Standard		2.11	1.05	0	4.32
Improved		2.28	1.19	0	4.44
Displacement difference [%]		8.3	13.3	0	2.8

Percent changes in the maximum values of Cauchy stress in rubber located between reinforcement layers are given in Table 3.

Table 3

Changes in the maximum values of Cauchy stress in rubber

Ply	Change in Cauchy stress in rubber [%] ← between plies →	Ply
Body	10	belt No. 1
Belt No. 1	11	belt No. 2
Belt No. 2	-5	belt No. 3
Belt No. 3	-8	belt No. 4

The greatest changes in the maximum equivalent stress values in rubber reached 10% and were observed between the body ply and the first belt ply, and between the first and the second belt.

The presented isoline maps of shear strain E_{xy} indicate that the separation of cord-rubber plies with isotropic rubber layers produces higher shear strain values in rubber in comparison with the model where rubber separators were not applied (Fig. 3). In the improved model, the maximum strain values were 18% higher than in the standard model.

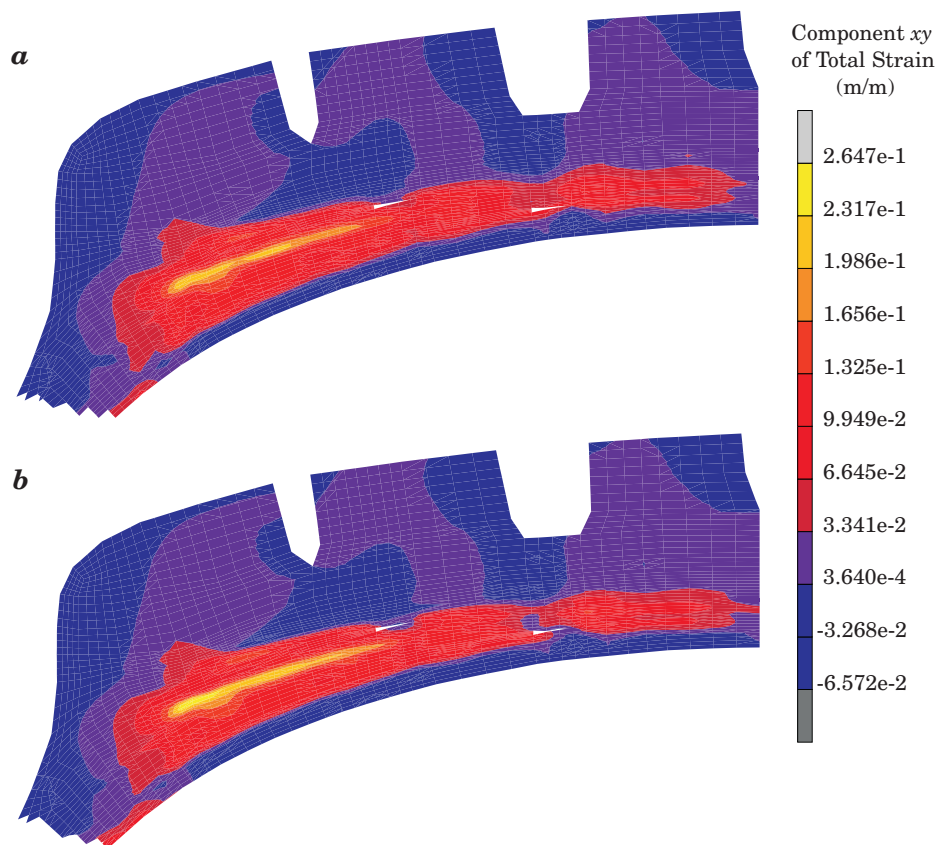


Fig. 3. Isoline maps of shear strain E_{xy} in rubber in the tread zone of an inflated tire: *a* – standard model, *b* – improved model

Conclusions

This study analyzed the effect of improved modeling of pneumatic tire plies in the axisymmetric model of a test tire subjected to nominal pressure

of 800 kPa. In the improved modeling technique, cord-rubber plies were separated with rubber layers. The axial displacement of the characteristic point on the sidewall increased by 8%, and the radial displacement of the point situated at the apex of the tire increased by 3% in comparison with the results yielded by the standard model. The discussed technique for modeling of layered materials significantly enhances the system flexibility. Cord-rubber plies are more readily deformed – they are separated by layers of isotropic rubber, and finite elements representing layers of the cord-rubber composite do not have shared nodes.

The presented approach to the cord-rubber plies modeling may seem natural, but to date, it has not found any applications in deformation modeling of tires. The discussed model requires a drastic increase in the number of the finite elements in the mesh (14-fold in the analyzed tire) to preserve the right proportions between the length of the sidewalls. In view of the computing power of contemporary computers, attempts should be made to use the improved method of layered composite material modeling, which gives a more reliable computational model of a tire. Unfortunately the suggested approach requires the generation of two finite elements meshes for tire cross-section: one (refined) for axisymmetric analyses and the other, with a reduced number of elements, for 3D tire analyses.

Accepted for print 11.05.2010

References

- CEMBROLA R.J., DUDEK T.J. 1985. *Cord/rubber material properties*. Rubb. Chem. Technol. 58(4): 830–856.
- HALPIN J.C., TSAI S.W. 1969. *Effects of environmental factors on composite materials*. AFML-TR 67–423.
- JONES R.M. 1975. *Mechanics of composite materials*. McGraw-Hill, London.
- KAGA H., OKAMOTO K., TOZAWA Y. 1977. *Stress analysis of a tire under vertical load by a Finite Element Method*. Tire Sci. Technol., 5(2): 102–118.
- PELC J. 1995. *Pomiary i analiza metodą elementów skończonych opony całostalowej do samochodów ciężarowych podczas pompowania*. Acta Acad. Agricult. Tech. Olst. Aedificatio et Mechanica, 26: 15–27.
- PELC J. 2000. *Material Modelling in Cord-Rubber Structures*. Kautsch., Gummi Kunstst. 53(10): 561–565.
- PELC J. 2002. *Static three-dimensional modelling of pneumatic tyres using the technique of element overlaying*. Proc. Instn Mech. Engrs, Part D: J. Automobile Engineering.
- PELLE R.G. 1994. *FEM Simulation of the Tire/Rim Seating Process*. Tire Sci. Technol., 22(2): 76–98.
- TSENG N.T., PELLE R.G., CHANG J.P., WARHOLIC T.C. 1991. *Finite element simulation of destructive tire testing*. Tire Sci. Technol., 19(1): 2–22.
- WALTER J.D. 1978. *Cord-rubber tire composites: theory and applications*. Rubb. Chem. Technol., 51(3): 524–576.

JET PUMPS – NUMERICAL MODELING POSSIBILITIES UPON THE BIFURCATION PHENOMENA

Wojciech Sobieski

Chair of Mechanics and Machine Design
University of Warmia and Mazury in Olsztyn

Key words: flow bifurcation, jet pumps, CFD.

A b s t r a c t

This paper presents the results of numerical simulations for modeling the air-air jet pump in 2D canal. The conducted simulation studies indicate the possibility of presence of strong bifurcations in jet pumps with the degree of intensity depending on geometric indicators and thermodynamic parameters of the system. Appearance of bifurcation in the mixing chamber causes periodic appearance of free spaces between the bifurcating liquid jet flowing out of the working nozzle and the walls of the chamber in which compression of the medium sucked and transport of it to the diffuser occurs. The paper presents and discuss the results of earlier works on bifurcation phenomenon in the systems of “nozzle – mixing chamber” type and qualitative results of computer simulation of sample ejector operation. The paper also contains the analysis of the influence of various factors on the results of computations. The goal of the work was confirmation of the possibility of numerical modelling jet pumps based on the bifurcation phenomena.

MOŻLIWOŚCI NUMERYCZNEGO MODELOWANIA STRUMIENIC Z WYKORZYSTANIEM ZJAWISKA BIFURKACJI

Wojciech Sobieski

Katedra Mechaniki i Podstaw Konstrukcji Maszyn
Uniwersytet Warmińsko-Mazurski w Olsztynie

Słowa kluczowe: przepływy bifurkacyjne, strumienice, CFD.

A b s t r a k t

W artykule przedstawiono wyniki symulacji numerycznych dotyczących modelowania strumienicy powietrzno-powietrznej w przestrzeni 2D. Wyniki badań symulacyjnych wskazują na możliwość występowania w strumienicach silnych bifurkacji, o stopniu intensywności zależnym od

wyróżników geometrycznych oraz parametrów termodynamicznych układu. Wystąpienie bifurkacji w komorze mieszania powoduje okresowe pojawianie się przestrzeni – między wypływającym z dyszy roboczej bifurkującym dżetem płynu a ściankami komory, w których następnie dochodzi do sprężenia zasysanego czynnika i transportowania go do dyfuzora. Przedstawiono również wyniki wcześniejszych prac dotyczących zjawiska bifurkacji w układach typu „dysza – komora mieszania” oraz jakościowe wyniki symulacji komputerowych pracy przykładowej strumienicy. Przeanalizowano wpływ różnych czynników na wyniki obliczeń. Celem badań było sprawdzenie możliwości modelowania numerycznego strumienia bazującego na zjawisku bifurkacji.

Introduction

Currently three basic mixing mechanisms in jet pumps are identified:

1. impact mixing – this mixing mechanism assumes presence, along a certain section of the mixing chamber, of the parallel flow of the working medium (in the form of central, compact stream) and the suction medium (in the form of a cylinder between the working stream and the walls), which next, in a rapid way, transforms into the vertical flow. After the mixing zone the liquid is the major fraction while the gas is present in it in the form of bubbles. The impingement model was developed for liquid-gas jet pumps in the algebraic form (WHITTE 1969).

2. friction mixing – this mixing mechanism assumes that as a consequence of friction (increased by turbulent movement) direct transfer of kinetic energy from the feeding stream to the suction stream occurs. That means balancing of velocities of both phases although there is no mixing of them. That model was developed for any type of jet pump in the form of differential equations (SPALDING 1992).

3. pulsation mixing – while the two preceding mechanisms were related to the stationary phenomenon of mixing, the pulsation mixing mechanism is based on dynamic phenomena occurring locally in the area of the catching nozzle and the mixing chamber. That mechanism contains certain elements identical with the mechanism of impingement mixing (no influence of viscosity) or friction mechanism (non-stationary nature of multiscale turbulence) (CUNNINGHAM 1974, FLÜGEL 1951). In the pulsation model, side surfaces of bifurcating mainstream substitute for the blades of the traditional compressor (Fig. 1).

This paper mainly refers to the third model. Further in the paper simulation results are presented in case of which the suction effect on passive inlets was achieved resulting from flow bifurcation phenomenon only. In those simulations where bifurcations did not appear there was also no suction of passive medium. The presented analysis represents a continuation of earlier studies on appearance of bifurcations in systems of “nozzle – mixing chamber” type (BADUR, SOBIESKI 2001, BADUR, SOBIESKI 2005) and it is not based on

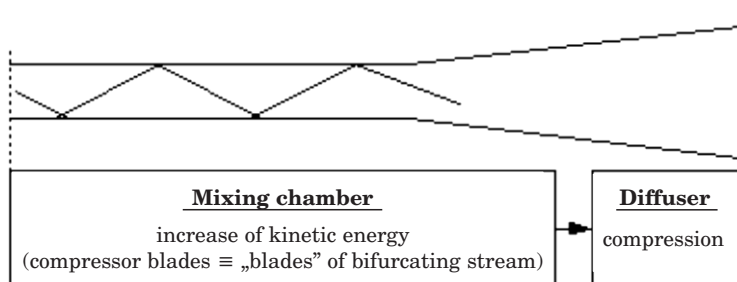


Fig. 1. Nature of pulsation model functioning

a specific, actual jet pump. The general nature of the paper is a consequence of the fact that so far a correct jet pump simulation model has not been developed and the literature does not offer appropriate publications.

Introduction to bifurcation theory

In mathematical terms bifurcation is a phenomenon of the abrupt change of mathematic model characteristics resulting from a small change in its parameters (e.g. initial conditions of the process or the boundary conditions). That notion is particularly important and frequently met during solving differential equations and studies on fractals (and chaos theory). In the model with parameter λ , λ_0 is the bifurcation point if, in every surrounding of it, two points exist for which the characteristics of the model are not identical. In case of differential equations bifurcation occurs when the solution of the nonlinear differential equation:

$$\frac{dx}{dt} = f(x, \lambda)$$

changes qualitatively its character with the change of the active parameter λ (Fig. 2).

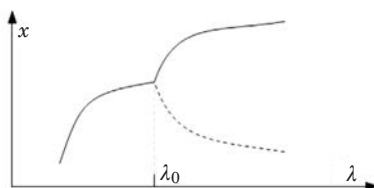


Fig. 2. Visualization of the nature of bifurcation
Source: MELLIS (2006), TRYBULEC (2006), WILSON (2006).

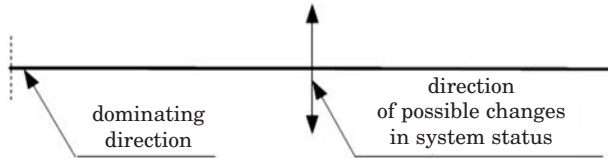


Fig. 3. Conditions for appearance of bifurcation

In case of passing the critical value the behavior of the system can be of two types (BADUR, SOBIESKI 2001, KURNIK 1997):

- the system will change its status into another one of stationary character – this type of bifurcation is referred to as stationary or divergent bifurcations,
- the system will change its status periodically – this type of bifurcation is referred to as non-stationary or oscillatory bifurcations.

The critical value is usually a specific parameter characterizing a given system. In case of flow system that role can be played by, e.g. Mach number or Reynolds number. Examples of the bifurcation phenomena in a solid-body and in a fluid flow are presented on Fig. 4.



Fig. 4. Examples of bifurcation in a solid (left) [Lega] and liquid (right)

Source: MANASSEH et al. (2006).

Types of bifurcation in flow systems

The issue of bifurcation in mechanics of liquids is a frequent subject of scientific studies and analyses. Authors of papers indicate the possibilities of appearance of different bifurcation types in flow systems characterized by a specific type of geometry. The examples are:

a) flow takes place in a channel with a sudden widening – Hopf bifurcations possible (BADUR et al. 1999, BATAGLIA et al. 1997, ROSENFELD 1995, SOBIESKI 2009a, SOBIESKI 2009b),

b) flow takes place in a channel with a perpendicular branch – Hopf bifurcations possible (KHODADADI 1991, SCHINAS and MATHIOULAKIS 2000),

c) flow takes place as a result of convection – Rayleigh-Benard bifurcations possible (HARAMINA 2005, MANNEVILLE, ZHANG 2001),

d) flow takes place between rotating cylinders – Taylor vortices possible (BAIER 1999, GREBE 2004, YOUNG).

The goal of the studies described in the paper was to find the basic relations between the geometry of a “nozzle – mixing chamber” system and its parameters and the intensity of bifurcations appearing in the flow. The system in which Hopf bifurcations occur was assumed as the optimal.

Conditions for development of Hopf bifurcations

Hopf bifurcations are a type of oscillatory bifurcations in which changes of system state occur in a periodic pattern. Such bifurcations can occur, e.g. during outflow of the liquid jet from a nozzle to a larger space that is limited by walls. Such a situation occurs, inter alia in jet pumps in the area of outflow of liquid from the working nozzle into the mixing chamber. In literature papers can be found concerning analysis of bifurcations in the flow systems of that type. It is found that the major parameters influencing the behavior of the main liquid stream are the geometrical conditions (BATAGLIA et al. 1997, DYBAN et al. 1971, SOBIESKI 2009a, SOBIESKI 2009b). The ratio between channel or mixing chamber width D and the width of the working nozzle outlet d is the basic parameter characterizing the system in this case (the symbols D and d are from (BATAGLIA et al. 1997)). With the increase of that parameter consecutive recirculation zones larger in size and with the progressively larger flow oscillations amplitude appear (Fig. 5) (BATAGLIA et al. 1997). The second parameter influencing the behavior of the system in considered case is the flow velocity (Fig. 6). Depending on it, symmetrical or asymmetrical (bifurcation) forms can appear (BATAGLIA et al. 1997). The importance of other parameters, such as e.g. viscosity, seems to be lower (DYBAN et al. 1971).

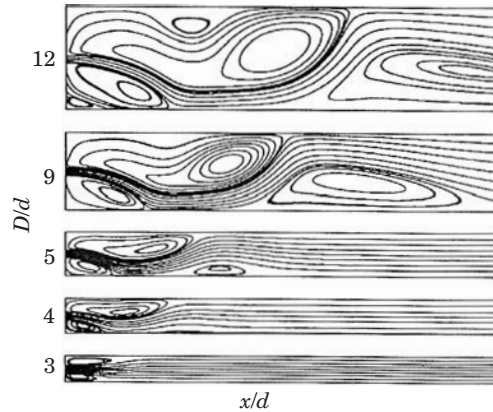


Fig. 5. Current contour lines for $D/d = 3, 4, 5, 9, 12$, $c = 15$ m/s, $x/d = 50$ i $Re = 60$
Source: BATAGLIA et al. (1997).

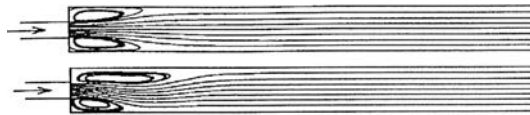


Fig. 6. Current contour lines for $Re = 53$ (upper) and $Re = 67$ (lower)
Source: BATAGLIA et al. (1997).

Types of bifurcations in nozzle – mixing chamber systems

Earlier completed own simulation studies based on laboratory experiments of other authors (DYBAN et al. 1971 resulted in identification of several flow structure types (BADUR and SOBIESKI 2001, BADUR and SOBIESKI 2005, ŚWIĄTECKI 2004):

- TYPE A – oscillations of the stream along the entire length of the channel, by the closing wall separation into two parts and symmetrical or alternating return towards side channels (Fig. 7-A),
- TYPE B – after reaching the closing wall, asymmetrical, cyclic return of the flow towards the side channels (Fig. 7-B),
- TYPE C – asymmetric return in the central part of the channel with characteristic, periodically changing reflections of the stream (regular or not) (Fig. 7-C),
- TYPE D – symmetrical return of the stream at the specific distance from the main nozzle outlet (ca. 1 – 1.5 width of the nozzle). In the other part of the channel no clear flow structures (Fig. 7-D),
- TYPE E – symmetrical return of the stream at the wall closing the channel (Fig. 7-E).

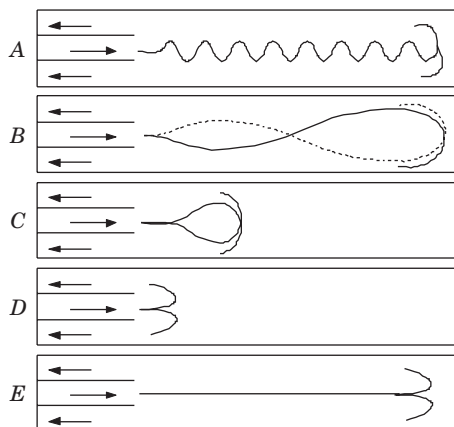


Fig. 7. Bifurcation types present in a flat, dead end channel

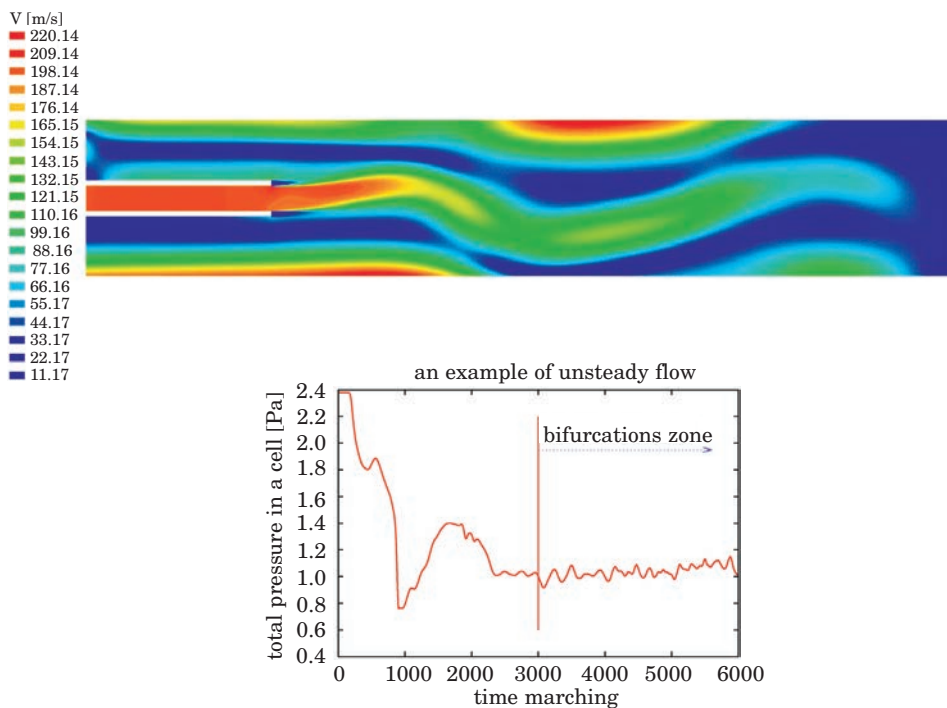


Fig. 8. Total velocity in the channel for $b/B = 0.16$, $H/B = 4.4$, $p_{in} = 120\,000$ [Pa] (upper) and record of total pressure in a selected cell (lower)

Source: ŚWIĄTECKI (2004)

The results of simulations obtained in the study (BADUR, SOBIESKI 2001, BADUR, SOBIESKI 2005) were consistent with the description of the laboratory experiment and allowed revealing of a new type of flow (type E) not mentioned

by the authors of the paper (DYBAN 1971). All numerical simulation series were performed in the Multi Flower 2D version 3.0 software package and some of them were then processed in FLUENT 6.1 software. During the studies the technique of thermodynamic parameters tracing in selected cells of the computation net was applied, which facilitated classification of the type of bifurcation present. Figure 8 presents an example of such analysis with Hopf bifurcations evidently present. The symbols in the description: H – channel length [m], B – channel width [m], b – working nozzle width [m], p_{in} – inlet pressure [Pa].

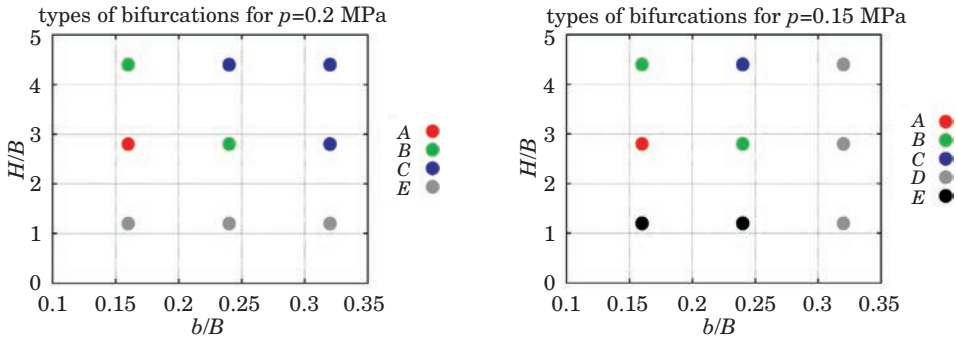


Fig. 9. Areas in which individual types of bifurcation were present at different values of pressure in the working nozzle

The simulations carried out allowed development of generalized characteristics providing graphic presentations of areas of individual types of bifurcation appearance depending on two geometric parameters, H/B and b/B (Fig. 9). The generalized characteristics were developed for a narrow range of pressures in the working nozzle (linked to the parameters of the laboratory experiment), for 0.12, 0.15 and 0.2 MPa. The developed characteristics also allowed determining the behavior of the system with elongation of the channel (Fig. 10).

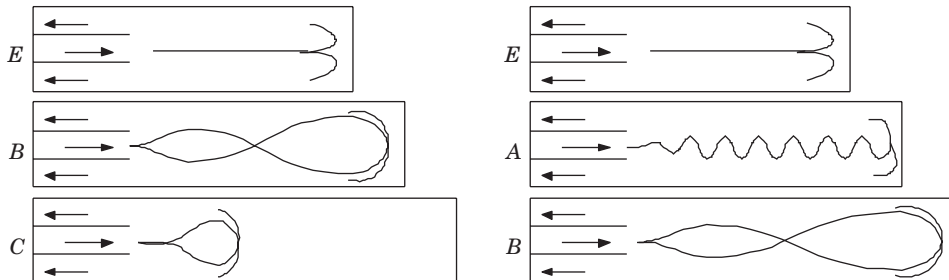


Fig. 10. Transitions of bifurcation types with increasing the parameter H/B for: $p = 0.15$ MPa and $b/B = 0.24$ (left), $p = 0.20$ MPa and $b/B = 0.16$ (right)

Possibilities of bifurcations appearance in jet pumps

The simulation analysis example presented in the preceding point covered the channel, the end of which was closed with a wall that made further flow impossible. In case of liquid-gas jet pumps the role of the wall limiting the flow is assumed by the impact mixing zone characteristic for those devices.

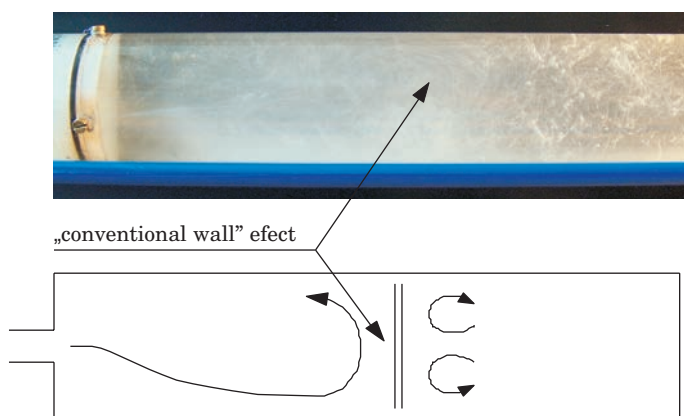


Fig. 11. Example of cavitation flow with stream bifurcation

The effect of the “conventional wall” is also encountered in other types of flows. Figure 11 presents a photograph from own studies on visualization of cavitation phenomenon (SOBIESKI 2004, SOBIESKI 2005), in which zones of different velocities are clearly visible.

Analyzing the results of numerical simulations the following conclusions can be reached:

- in jet pumps possessing no mixing zone or the mixing zone is positioned relatively far from working nozzle outlet, the oscillation bifurcations, including Hopf bifurcations, can occur (in Fig. 7 cases A, B or intermediate),
- in jet pumps possessing mixing zone (in particular when it is situated close to the working nozzle outlet) the effect of “conventional wall” and oscillation or divergent bifurcation can occur (in Fig. 7 cases B, C or intermediate).

The presented analogy leads to the question, if Hopf bifurcations can appear in real jet pumps and, if yes, then how these bifurcations influence operation of the jet pump. An attempt at solving that issue will be presented further in the paper.

Numerical modeling of air-air jet pumps

Aiming at verification of the possibility of bifurcation occurrence in flow devices a series of numerical simulations was completed. The following assumptions were made for the study:

- simulation will be done in 2D space for the example of air-air jet pump,
- jet pump geometry will be selected on the basis of Fig. 9, for the zone in which the Hopf bifurcations occurrence probability is the highest (that case seems to be the most interesting one),
- the influence of viscosity is dismissed from the computations.

The computer model parameters were as follows:

- geometric indicator b/B : 0.16, 0.20, 0.24 ($b = 4$ mm),
- mixing chamber length H : 400, 600, 800, 1000 mm,
- operational medium: air, water steam, 293 K (ideal gas model),
- medium sucked in: air, 293 K (ideal gas model),
- total pressure p_{in} at working inlet: 150, 200, 250 kPa (Mach Number in all cases under 0.3),
- static pressure of the medium sucked in: 101.3 kPa,
- static pressure p_{out} on the outlet: 105, 110, 115, 120 kPa,
- grid type: structured, 52 600 cells,
- numerical scheme: TVD (Total Variation Diminishing),
- time scheme: implicit,
- CFL number: 10,
- minimum number of iterations: 10 000.

Sample results of computer simulation are presented in Fig. 12. It was found out that in the area of the assumed geometric discriminants and pressures in the working nozzle appearance of bifurcations, including Hopf bifurcation is very typical. In such cases the main stream, after leaving the working nozzle, was subject to periodic deviations from jet pump axis in part or along the entire length of the mixing chamber. Those deviations caused appearance of characteristic, alternating zones (air-chambers) forming at both walls of the mixing chamber. The consequence of development of those “chambers” as well as oblique sections of the main stream was that the medium was sucked into the side channels of the jet pump. It should be highlighted that the suction appeared only in case of appearance of bifurcation. In other cases the backward flow occurred on the external sides of the main stream (the pressure on the outlet was slightly higher than on the passive inlet).

During the simulation tests of the influence of individual parameters of the jet pump on the effect of passive stream suction were conducted. The results of studies (Figures 13, 14 and 15) indicate that the geometric discriminant

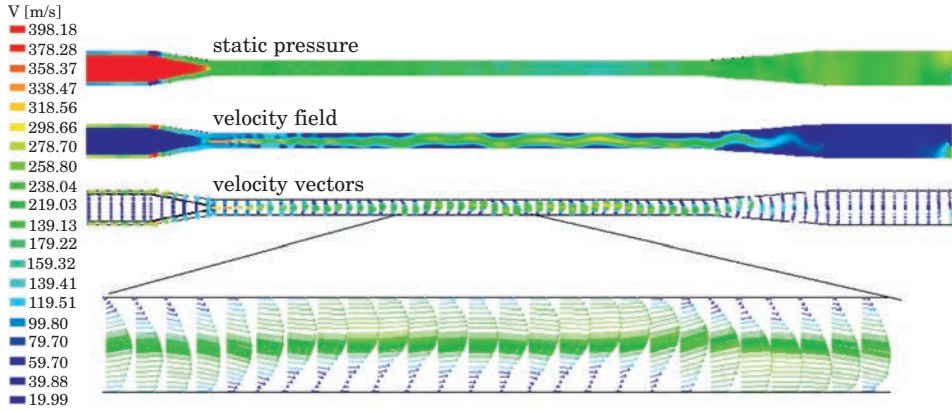


Fig. 12. Example of working stream bifurcation for $b/B = 0.16$, $H = 800$ [mm], $p_{in} = 150$ [kPa], $p_{out} = 110$ [kPa]

Source: CUDAKIEWICZ (2005).

b/B and inlet pressure p_{in} in the working nozzle had a large influence on jet pump operation. In case of small discriminants and low pressures regular bifurcations (including Hopf bifurcations) are achieved. With the increase of the difference between working nozzle width and channel width b/B and the inlet pressure p_{in} , bifurcations became increasingly irregular and the suction speed decreased almost to zero. The highest suction speed was achieved for the jet pump with the following parameters: $p_{in} = 150$ [kPa], $b/B = 0.16$, $p_{out} = 110$ [kPa].

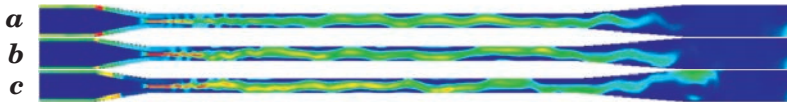


Fig. 13. Distribution of total velocity for: a) $p_{in} = 150$ [kPa], $b/B = 0.16$, $p_{out} = 110$ [kPa]; b) $p_{in} = 200$ [kPa], $b/B = 0.16$, $p_{out} = 110$ [kPa]; c) $p_{in} = 250$ [kPa], $b/B = 0.16$, $p_{out} = 110$ [kPa]
Source: CUDAKIEWICZ (2005).

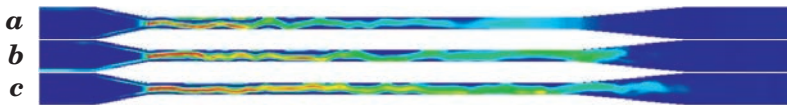


Fig. 14. Distribution of total velocity for: a) $p_{in} = 150$ [kPa], $b/B = 0.20$, $p_{out} = 110$ [kPa]; b) $p_{in} = 200$ [kPa], $b/B = 0.20$, $p_{out} = 110$ [kPa]; c) $p_{in} = 250$ [kPa], $b/B = 0.20$, $p_{out} = 110$ [kPa]
Source: CUDAKIEWICZ (2005).

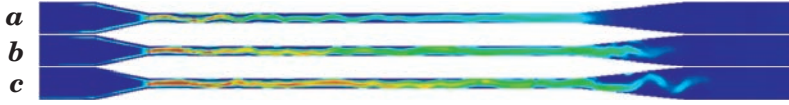


Fig. 15. Distribution of total velocity for: a) $p_{in} = 150$ [kPa], $b/B = 0.24$, $p_{out} = 110$ [kPa]; b) $p_{in} = 200$ [kPa], $b/B = 0.24$, $p_{out} = 110$ [kPa]; c) $p_{in} = 250$ [kPa], $b/B = 0.24$, $p_{out} = 110$ [kPa]
Source: CUDAKIEWICZ (2005).

The influence of mixing chamber length on jet pump operation was another aspect considered during studies. For that purpose analysis was carried out on jet pumps with four lengths of the mixing chamber: $H = 400, 600, 800, 1000$ [mm], with the feeding nozzle inlet pressure $p_{in} = 150$ [kPa], jet pump outlet pressure $p_{out} = 110$ [kPa] and geometric discriminant $b/B = 0.16$.

The studies showed that in case of mixing chamber short length ($H = 400$ [mm]) the stream bifurcation occurs still in the diffuser, where it should be extinguished (Fig. 16a). With the change of the mixing chamber length to 600 [mm], bifurcation becomes regular, but it is still not extinguished before the diffusers (Fig. 16b). Further elongation of the mixing chamber to 800 [mm] causes regular bifurcations along the entire length of the mixing chamber and their extinction in the diffuser area (Fig. 16c). Another change of chamber length to 1000 [mm] causes that bifurcation is irregular and ends in the end part of the mixing chamber (Fig. 16d). The higher suction velocity was obtained in the jet pump with the mixing chamber of $H = 800$ [mm].

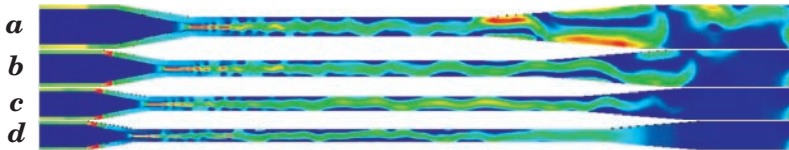


Fig. 16. Distribution of total velocity for: a) $H = 400$ [mm], b) $H = 600$ [mm], c) $H = 800$ [mm], d) $H = 1000$ [mm] (the figures are not in the same scale)
Source: CUDAKIEWICZ (2005).

Next the influence of static pressure on the diffuser outlet on jet pump operation was investigated. For that purpose cases of four pressure values: $p_{out} = 105, 110, 115$ and 120 [kPa] were analyzed. The total pressure on feed nozzle inlet was constant at 150 [kPa]. For that series of tests the jet pump with geometric discriminator $b/B = 0.16$ and mixing chamber length of $H = 800$ [mm] was selected.

The completed series of numerical simulations showed that the most developed bifurcations (occurring along the entire mixing chamber length) appeared at the pressure of around 110 kPa (Fig. 17b). Lower values of the

outlet pressure cause a significant shortening of the bifurcations area and deterioration of the effect of suction on passive inlets (Fig. 17a). Increasing the outlet pressure on the other hand caused appearance of increased pressure resistance and damping of bifurcation. In case of higher pressures the clearly visible backward flows in the area of passive nozzle also appeared (Fig. 17c and d).

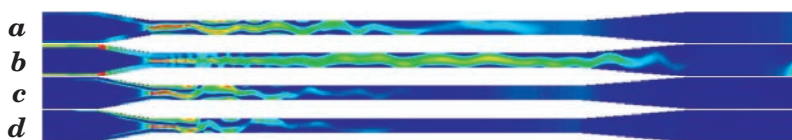


Fig. 17. Distribution of total velocity for: a) $p_{\text{out}} = 105$ [kPa], b) $p_{\text{out}} = 110$ [kPa], c) $p_{\text{out}} = 115$ [kPa], d) $p_{\text{out}} = 120$ [kPa]

Source: CUDAKIEWICZ (2005).

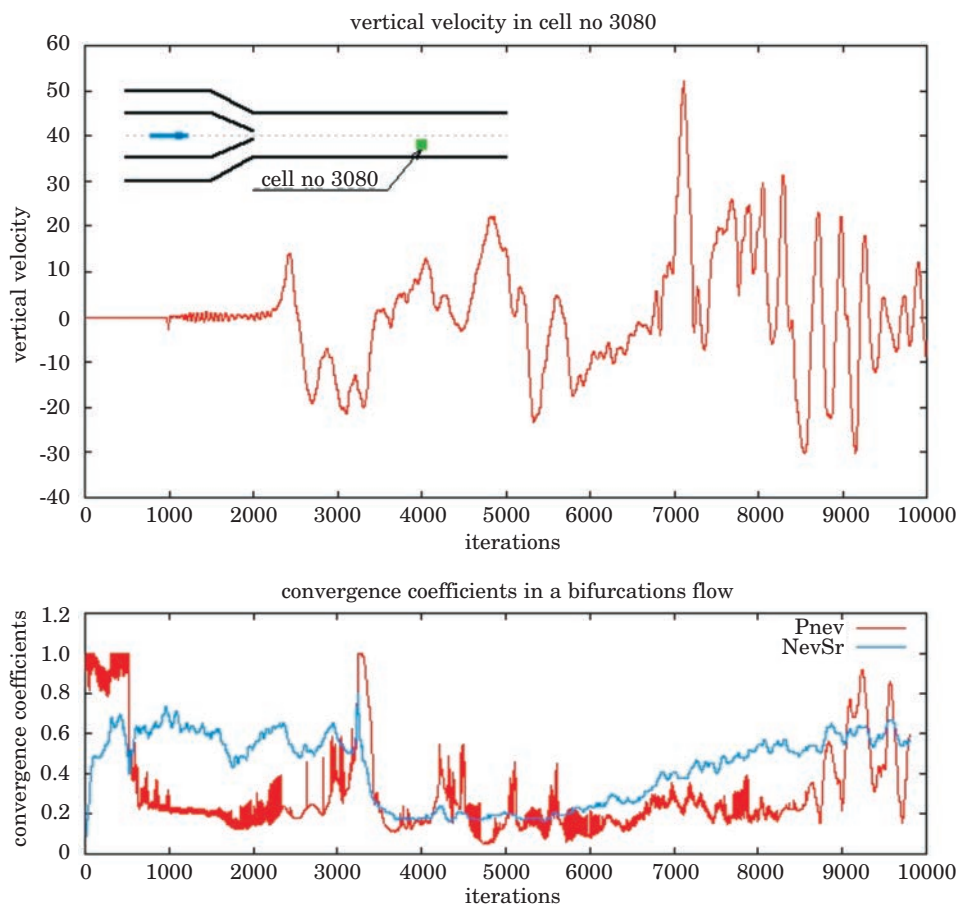


Fig. 18. Record of velocity x component in a selected computation grid cell and the computations convergence process (lower)

The studies completed so far indicate that the highest velocities of the sucked medium could be obtained in a jet pump possessing the following parameters: $p_{\text{in}} = 150$ [kPa], $b/B = 0.16$, $H = 800$ [mm] and $p_{\text{out}} = 110$ [kPa]. Changes of static pressure and velocities in directions x and y over time in one of jet pump cells were analyzed to further analyze that case and determine the type of bifurcation. The cell was selected in such a way that it was not positioned on the mixing chamber axis and at the same time it was not too close to chamber wall. The record of jet pump parameters was made as of the beginning of the iteration process. During the first part (up to ca. 8000 iterations) the process of convergence of computations is observed (Fig. 18). The results in that range are not “physically” reasonable and only after stabilization of the processes of numerical computations they become consistent with physics and reasonable for analysis. Figure 18 allows to observe the changes in the position of the main stream. That phenomenon can also be followed to a certain extent by observing the progress of computations convergence process.

Generally the studies carried out showed that the more regular the bifurcation the more efficient the process of medium suction is.

Summary

Results of numerical studies allow assuming that the pulsation model can be applicable to any type of jet pump on condition of appropriate configuration of the geometry and thermodynamic parameters. The following conclusions can be formulated on the basis of the studies completed:

1. numerical modeling allows qualitative determination of the influence of various factors, mainly thermodynamic parameters and geometric discriminants on operation of the studied steam-air jet pump;

2. assuming rightness of bifurcational jet pump operation model, it is possible to determine the range of parameters at which the jet pump operation is the most effective (the velocity in the inlet section of the suction medium was assumed to be the measure of effectiveness: the higher it is the more favorable the jet pump operation conditions are);

3. jet pumps based on bifurcational model should possess the following characteristics:

- a. the jet pump should have the appropriate relation of the feeding nozzle width and the mixing chamber width; in the studies the best suction was obtained for $b/B = 0.16$, which resulted directly from conditions of the bifurcation phenomenon,

b. the inlet pressure should be selected in such a way that bifurcation should occur and that it should have a possibly regular character; within the tested range the pressures of 150 000 [Pa] were the most favorable,

c. the outlet pressure should not be too high because of the resistance of flow; in the studies the best suction occurred at around 110 000 [Pa],

d. the chamber length should be selected in such a way that bifurcation should end at the diffuser inlet, the effect of the “blades” of the working stream is experienced the best at that case and no additional motion resistance (excessively long chamber) or irregularity in mixing of streams and pulsation operation of the jet pump (to short chamber) occur in that case;

4. simulations concerning the influence of outlet pressure on jet pump operation showed the necessity of presence of certain resistance facilitating “breaking” the stability of stream and development of bifurcation phenomenon;

5. presentation of the results of studies on bifurcation in the form of collective results proved to be very useful as it facilitated selection of jet pump geometry and preparation of the computer model;

6. the study does not exhaust the subject of jet pumps modeling; in future work the number of cases investigated should be increased and they should be verified using other numerical codes or, at best, experimentally.

Accepted for print 28.06.2010

References

- BADUR J., SOBIESKI W. 2001. *Numerical simulation of Hopf bifurcations in a turning off flow*. Research of the Chair of Mechanics and Machine Design, pp. 63–98, Olsztyn.
- BADUR J., SOBIESKI W. 2005. *Nicht stationäre Durchflussformen im 2-D Kanal*. GAMM, Luksemburg.
- BADUR J., YERSHOV S., RUSANOV A., KARDAS D., KUDRYŃSKI A., OCHRYMIUK T. 1999. *An imperfed time marching method for Hopf bifurcation in inviscid flow*. Research Report IMP PAN, No 298/97, Gdańsk.
- BATAGLIA F., TAVENOR S. J., KULKARNI A.K., MERKLE CH.L. 1997. *Bifurcation of Low Reynolds Numbers Flow in Symmetric Channel*. AIAA Journal, 35(1).
- BAIER G. 1999. *Liquid-liquid extraction based on a new flow pattern: two-fluid Taylor-Couette flow*. PhD Thesis, University of Wisconsin-Madison, Department of Chemical Engineering.
- CUDAKIEWICZ M. 2005. *Numerical Modelling of the Work of Jet Pump Devices concerning Flugel-Cunningham Method*. MSc Thesis, University Of Warmia And Mazury In Olsztyn, The Faculty of Technical Sciences.
- CUNNINGHAM R.G. 1974. *Gas Compression with the liquid jet pump*. Trans. ASME, J. Fluids Engineering, 94, 203–215.
- DYBAN E.P., MAZUR A.I., EPIK E.J. 1971. *Osobennosti istecenia plaskoj woedyszczoj strui w tupik*. Teplofizika i Teplotekhnika, 19: 41-45.
- FLÜGEL G. 1951. *Berechnung von Strahlapparaten*. 2 Aufl. A4, S. II+21. VDI-Verlag, Düsseldorf.
- GREBE T. 2004. *Simulation und Modellierung des Mischverhaltens von Taylor-Couette-Reaktoren*. PhD Thesis, Fakultät für Naturwissenschaften, Department Chemie, Universität Paderborn.

- HARAMINA T. 2005. *Coherent structures in turbulent Rayleigh-Benard convection*. PhD Thesis, Göttingen.
- KHODADADI J.M. 1991. *Wall Pressure and Shear Stress Variation in a 90-Deg Bifurcation During Pulsatile Laminar Flow*. Journal of Fluids Engineering, 113.
- KURNIK W. 1997. *Bifurkacje dywergentne i oscylacyjne*. Wydawnictwo Naukowo-Techniczne. Warszawa.
- LEGA J. *Instability of Pulse-like Deformations of an Elastic Filament* [on-line]. Access: <http://math.arizona.edu/~lega/Filaments.html> (21.06.2006).
- MANASSEH R., MERRELL J., DUNSTAN B., YOSHIDA S. *Bubble trajectory bifurcation in crossflow* [on-line]. Access: <http://resources.hightett.cmit.csiro.au/RManasseh/a9163/a9163.html> (21.06.2006).
- MANNEVILLE P. *Rayleigh-Beenard convection, thirty years of experimental, theoretical, and modeling work* [on-line]. Access: <http://www.ladhyx.polytechnique.fr/people/pops/benard.pdf> (19.10.2006).
- MELLIS D. A. 2006. *Introduction to Chaos Theory* [on-line]. Access: <http://alumni.imsa.edu/~stendahl/chaos/chaos.html> (27.06.2006).
- ROSENFELD M., EINAV S. 1995. *The Effect of Construction Size on the Pulsatile Flow in a Channel*. Journal of Fluids Engineering, 117.
- SCHINAS D., MATHIOULAKIS D.S. 2000. *Pulsating Flow in a 90 Degree Bifurcation*. Journal of Fluids Engineering, 122.
- SOBIESKI W. 2004. *Test Stand for Research of Cavitation Phenomena by Vibroacoustic Method*. Diagnostyka, 32: 37–42.
- SOBIESKI W. 2005. *Test Stand for Visualization of Cavitation Phenomena*. “Modelling of Multiphase Flows in Thermo-Chemical Systems – Advanced Measurement Techniques”, Stawiska 2005, PPW05-35.
- SOBIESKI W. 2009a. *Numerical Analysis of Flow Bifurcations in a Closed-Off Channel*. Technical Sciences, 12: 272–285.
- SOBIESKI W. 2009b. *Numerical And Experimental Analyses of Hopf Bifurcations in a Locally Expanded Channel*. Technical Sciences, 12: 259–271.
- SPALDING D.B. , HEWITT G.F. 1992. *Computer code Description*. Multiphase Science and Technology, 6: 721–808.
- ŚWIĄTECKI A. 2004. *Numerical Analysis of Hopf bifurcations in a 2D geometry*. MSc Thesis, University Of Warmia And Mazury In Olsztyn, The Faculty of Technical Sciences.
- TRYBULEC Z. *Bifurkacje Feigenbauma* [on-line]. Access: <http://www.zftik.agh.edu.pl/mof/lab/trybulec.html> (27.06.2006).
- WITTE J.H. 1969. *Mixing shocks in two-phase flow*. Journal of Fluid Mechanics, 36: 639–655.
- WILSON G. *Nonlinear Dynamical Systems as a Paradigm for International Relations Theory* [on-line]. Access: <http://www.garretwilson.com/essays/internationalrelations/complexworld.html> (27.06.2006).
- YOUND A. *Taylor-Couette Flow* [on-line]. Access: <http://www.students.ncl.ac.uk/a.j.yound/tcf/tcf.html> (28.06.2006).
- ZHANG S., MORITA K., FUKUDA K., SHIRAKAWA N. 2001. *Simulation of Three-dimensional Convection Patterns in a Rayleigh-Benard System Using the MPS Method*. Memoirs of the Faculty of Engineering, Kyushu University, 66(1).

EXAMPLES OF USING THE FINITE VOLUME METHOD FOR MODELING FLUID-SOLID SYSTEMS

Wojciech Sobieski

Chair of Mechanics and Machine Design
University of Warmia and Mazury in Olsztyns

Key words: CFD, Porous Media Model, Eulerian Multiphase Model, fluid-solid systems.

Abstract

The article presents two mathematical models designed for the numerical modeling of fluid flow through stationary and non-stationary porous beds, so called Porous Media Model and Eulerian Multiphase Model. After a brief description, both models are illustrated with several examples of their use. All examples were made in the package ANSYS Fluent. All cases come from studies on the actual objects, usually various laboratory stands. This article aims to show the differences and determinants of both approaches. Motivation stemmed from own experience of the author, indicating that in some cases the choosing of appropriate model is not obvious.

PRZYKŁADY ZASTOSOWANIA METODY OBJĘTOŚCI SKOŃCZONYCH DO MODELOWANIA OŚRODKÓW TYPU FLUID-SOLID

Wojciech Sobieski

Katedra Mechaniki i Podstaw Konstrukcji Maszyn
Uniwersytet Warmińsko-Mazurski w Olsztynie

Słowa kluczowe: CFD, Porous Media Model, Wielofazowy Model Eulera, ośrodki fluid-solid.

Abstrakt

W artykule zaprezentowano dwa modele matematyczne – Porous Media Model oraz Eulerian Multiphase Model, służące do numerycznego modelowania przepływów płynów przez stacjonarne i niestacjonarne złoża porowate. Oba modele, po krótkim ich przedstawieniu, zilustrowano kilkoma przykładami praktycznymi. Wszystkie przedstawione w pracy wyniki symulacji numerycznych bazują na rzeczywistych obiektach, zazwyczaj na konkretnych stanowiskach laboratoryjnych i zostały wykonane w pakiecie obliczeniowym ANSYS Fluent. Celem artykułu było przedstawienie podstawowych różnic dotyczących zastosowań obu modeli oraz uwarunkowań ich stosowania. Motywacją do napisania artykułu były doświadczenia autora, wskazujące, że wybór odpowiedniego modelu może w pewnych przypadkach nie być oczywisty.

Introduction

In industry there exist many systems in which a fluid flows through a bed consisting of particles with similar characteristics (density, shape, surface properties and other). From the standpoint of analysis of such systems it is very important, whether under the influence of forces arising from the motion of fluid, the particles of solid body are on the movement or not. If not, there is a typical case of fluid flow through a porous bed (Fig. 1a). If yes, there is a case with non-stationary porous bed (Fig. 1b). Both types of flows usually require use of different mathematical model. The situation is not so simple, because the boundary between the two systems can be very thin. One type may change into the second type after even relatively minor change in parameters, e.g. in the so called filtration velocity. In next sections are described two models dedicated for stationary and non-stationary porous beds, respectively.

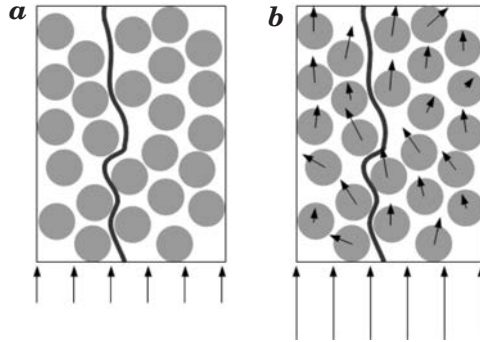


Fig. 1. Stationary (a) und non-stationary porous bed (b)

Porous Media Model

Porous Media Model (PMM), dedicated for stationary porous beds, is an extension of a basic system of mass (1) and momentum balance (2) equations intended for one phase flow (Fluent User Guide 2006, Fluent Tutorial Guide 2006:

$$\frac{\partial}{\partial t} \rho + \nabla \cdot (\rho \vec{v}) = 0 \quad (1)$$

$$\frac{\partial}{\partial t} (\rho \vec{v}) + \nabla \cdot (\rho \vec{v} \otimes \vec{v}) = -\nabla p + \nabla \cdot \vec{\tau} + \vec{S}_f \quad (2)$$

where: ρ – density [kg m^{-3}], \vec{v} – velocity [m s^{-1}], p – static pressure [Pa], τ – total stress tensor [Pa], \vec{S}_f – source of forces [N m^{-3}]. In general case the energy equation can be added to the equations (1) and (2).

In PMM the medium resistance – resulting from the presence of solid fraction – is treated as the additional source in momentum balance equation (2). To calculate a value of this resistance the very popular Forchheimer law (1901) can be used (HELLSTRÖM, LUNDSTRÖM 2006, EWING et al. 1999, ANDRADE et al. 1999) or other similar law. The Forchheimer law, taking into account losses due to viscosity and inertia, can be written in 3D domain as follow

$$S_{mf,i} = - \sum_{j=1}^3 A_{ij} \cdot \mu \cdot v_j - \sum_{j=1}^3 B_{ij} \cdot \frac{\rho \cdot |v| \cdot v_j}{2} \quad (3)$$

Symbol $S_{mf,i}$ denotes source of mass forces for the i^{th} space dimension (x, y and z), μ – dynamic viscosity coefficient [$\text{kg (m s}^{-1})$], v_j – the j^{th} component of velocity [m s^{-1}], $|v|$ – absolute value of velocity [m s^{-1}]. A_{ij} and B_{ij} are constant diagonal matrices, with diagonal terms equal to the inverse of permeability coefficient κ [m^2] and doubled value of Forchheimer coefficient β [$1/\text{m}$] respectively. Off-diagonal terms in both matrices are null. If the matrix B_{ij} will be equal to zero, the formula (3) will be simplified to the Darcy law (1856) (SAWICKI et al. 2004, NAŁĘCZ 1991) which is very known too. In general case, both A_{ij} and B_{ij} can be functions of coordinates, time, temperature and other factors. This means in practice that the flow resistance can change over time and space.

In PMM only the accurate value of resistance is important. It does not matter which medium generates these resistances and how it happens. In the literature many mathematical formulas describing the permeability coefficient κ and Forchheimer coefficient β can be found (SAWICKI et al. 2004, NAŁĘCZ 1991, MITOSEK 2007, PAZDRO, BOHDAN 1990, BELYADI A. 2006, BELYADI F. 2006, LORD et al. 2006, AMAO 2007). All of them are usually functions of particle diameter, porosity, tortuosity or other geometrical parameters. These models also contain many of constants. The application of these formulas in practice is severely limited because they are often correct only for very specific cases. The best way to obtain a correct value of model parameters (that mean κ and β) for a specific medium is to perform an own experiment. If appropriate values are already known, numerical simulations for this medium can be freely created.

Figure 2 shows an example of using the PMM. It is a water flow through a pipe filled by glass beads. The average diameter of particle was 1.95 [mm]. Experimental data were derived from own measurements performed on an existing laboratory stand, located in the Department of Mechanics and Ma-

chine Design at the University of Warmia and Mazury in Olsztyn. The aim of this study was to select of the best methods of determining the permeability coefficient and the Forchheimer coefficient. It turned out that in this case the best is so called Forchheimer Plot Method (SOBIESKI 2009d). The selection was made using a method described in the work of SOBIESKI (2010). The sensitivity of numerical model to changes in the selected parameters was also examined. It is worth adding that the use of the PMM is quite simple if only high quality experimental data are available. In the described case differences between measurements and calculations were always less than 3% (SOBIESKI and TRYKOZKO submitted). Similar accuracy on this laboratory stand was obtained for a few other porous media.

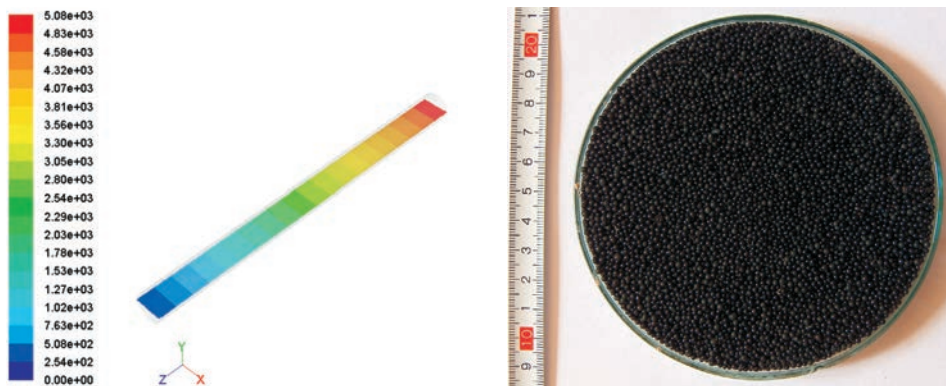


Fig. 2. Static pressure distribution in a porous column

Source: own calculations.

The second example is shown in Figure 3. There is a ground heat exchanger described in the work (NALEPA et al. 2008). This time the working medium was the air. The calculation domain consists of three parts: inlet zone (on the left), porous zone filled with gravel (the large section in the center) and outlet zone (on the right). The flow resistance was included only in the porous zone. The result presented here refers to an existing test stand, but the accurate experimental data are not yet available. After obtaining appropriate experimental data the numerical model can be further developed. The laboratory stand is located in the Department of Electrical and Power Engineering at the University of Warmia and Mazury in Olsztyn.

Another example with air flow through a porous bed is shown in Figure. 4. Presented results refer to the laboratory stand which was designed and constructed specifically for the validation of the numerical model. The device is located in the Department of Biosystems Engineering at the University

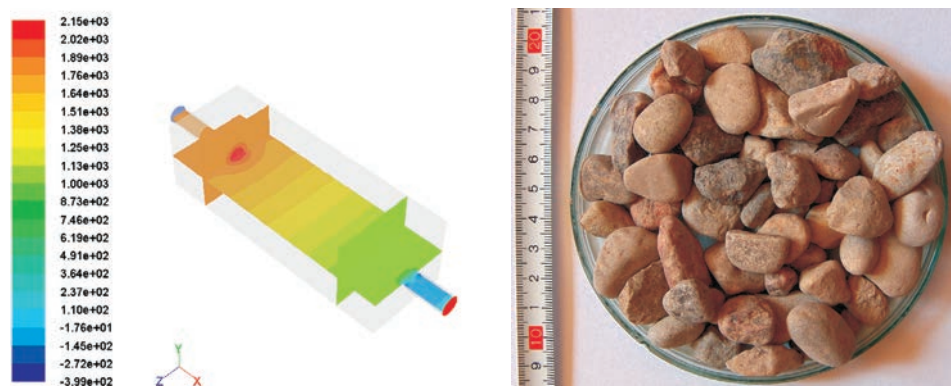


Fig. 3. Static pressure distribution inside a ground heat exchanger

Source: own calculations.

of Manitoba in Winnipeg. In this case soybean seed was the porous medium. The average diameter of grain was equal to 6.2 [mm]. The aim of the project was to study the impact of the spatial structure on the flow resistance in three directions. In this case all needed mathematical models were made in ANSYS Fluent, too, but by using so called User Defined Function and User Defined Memory. The Forchheimer law, Ergun Equation and Carman-Kozeny equation were used. In addition the porosity was defined as a function, not as a constant value. A new method for calculation of the tortuosity, needed for the Kozeny-Carman equation, was developed (SOBIESKI, LIU, ZHANG, submitted). In this example the errors are in most cases less than 1%.

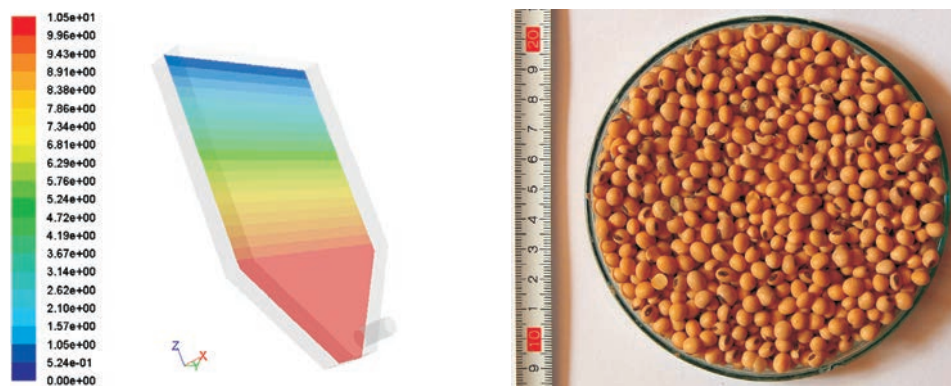


Fig. 4. Static pressure distribution inside a grain tank

Source: own calculations.

Eulerian Multiphase Model

Eulerian Multiphase Model (EMM), dedicated for flows with particle motion, is intended for description of mixtures consisting of any number of phases: gases, liquids and particles of solids. In a general case a separate system of mass, momentum and energy equations is solved for each of the phases. Coupling of phases occurs through pressure and the so-called inter-phase mass, momentum and energy exchange coefficients. Those coefficients are a characteristic feature of the model and play the key role in it. The description of interactions between individual phases depends mainly on whether just liquid or simultaneously liquid and solid phases are present in the flow. In this model, the Eulerian treatment is used for each phase. In literature other names of this model: Two-Fluid Model or Multi-Fluid model are also found. The equations of mass (4) and momentum (5) for q^{th} phase in the flow are as follow (Fluent User Guide 2006, Fluent Tutorial Guide 2006):

$$\frac{\partial}{\partial t} (\varepsilon_q \rho_q) + \nabla \cdot (\varepsilon_q \rho_q \vec{v}_q) = S_{m,q} \quad (4)$$

$$\frac{\partial}{\partial t} (\varepsilon_q \rho_q \vec{v}_q) + \nabla \cdot (\varepsilon_q \rho_q \vec{v}_q \otimes \vec{v}_q) = -\varepsilon_q \nabla p - \nabla p_q + \nabla \cdot \vec{\tau}_q + \vec{R}_q + \vec{S}_{f,q} \quad (5)$$

where: ε_q – volume fraction of component q [-], ρ_q – density of phase q [kg m^{-3}], \vec{v}_q – velocity of phase q [m s^{-1}], $S_{m,q}$ – source of mass of phase q [$\text{kg m}^{-3} \text{s}^{-1}$], p – static pressure of the mixture [Pa], p_q – granular pressure of component q [Pa], \vec{R}_q – source of momentum for phase q exchanged between phases during movement [N m^{-3}], $\vec{S}_{f,q}$ – source of mass forces influencing phase q [N m^{-3}].

Modeling the flow dynamics requires precise definition of mass and momentum exchange between flow components

$$S_{m,q} = \sum_{p=1}^n (\dot{m}_{pq} - \dot{m}_{qp}) \quad (6)$$

$$\vec{R}_q = \sum_{p=1}^n (\vec{R}_{pq} \dot{m}_{pq} \vec{v}_{pq} - \dot{m}_{qp} \vec{v}_{qp}) \quad (7)$$

where: \dot{m}_{pq} – mass transfer from phase p to phase q [$\text{kg m}^{-3} \text{s}^{-1}$], \dot{m}_{qp} – mass transfer from phase q to phase p [$\text{kg m}^{-3} \text{s}^{-1}$], \vec{R}_{pq} – force of interaction between phases p and q [N m^{-3}], \vec{v}_{pq} – interphase velocity [m s^{-1}]. The value of interphase velocity depends on the direction of mass transfer:

$$\text{if } \dot{m}_{pq} > 0 \text{ then } \vec{v}_{pq} = \vec{v}_p \quad (8)$$

$$\text{if } \dot{m}_{pq} < 0 \text{ then } \vec{v}_{pq} = \vec{v}_q \quad (9)$$

The interphase momentum exchange coefficient β_{pq} [$\text{kg (m}^{-3} \text{ s}^{-1})$] plays the key role in the model. It describes the forces of interaction between phases in the following way

$$\sum_{p=1}^n \vec{R}_{pq} = \sum_{p=1}^n \beta_{pq} (\vec{v}_p - \vec{v}_q) \quad (10)$$

where the additional dependences $\beta_{pq} = \beta_{qp}$ and $\vec{R}_{qq} = \vec{0}$ must be satisfied. The interphase momentum exchange coefficient β_{pq} may be calculated from many formulas.



Fig. 5. Solid phase distribution in a spouted bed grain dryer

Source: own calculations.

Figure 5 shows an example of modeling a spouted bed grain dryer. The interphase momentum exchange coefficient was described by the Gidaspow model, with a few own extensions. The model was made on the basis of previous experiments performed at the Department of Agricultural Process Engineering, University of Warmia and Mazury in Olsztyn. During the study a very good agreement between experiment and the numerical model was obtained (SOBIESKI 2008). In the first stage the sensitivity of EMM to the change in value of experimental data was investigated. In the next stages

dozens of “closures” for momentum exchange (SOBIESKI 2009b), switch function and sphericity coefficient in the Gidaspow model (SOBIESKI 2009a) and the influence of changing the drag coefficient were tested.

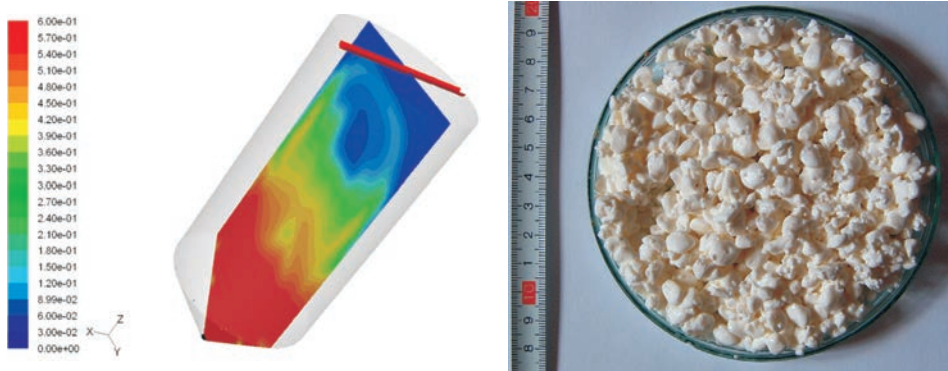


Fig. 6. Solid phase distribution in a washer cooler

Source: own calculations.

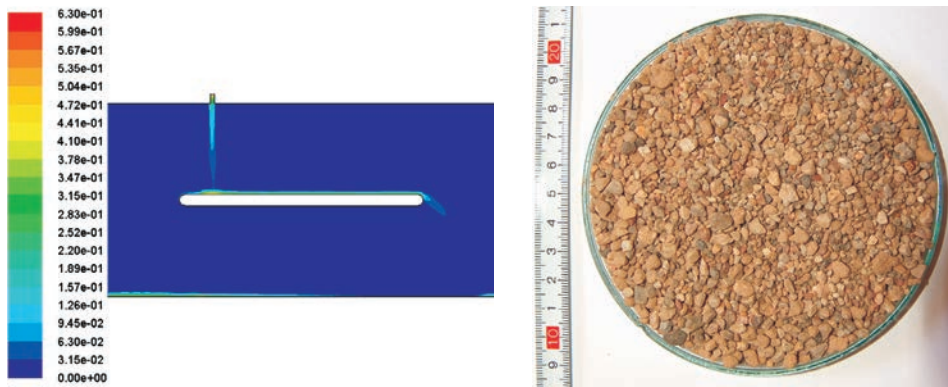


Fig. 7. Solid phase distribution in a conveyor belt

Source: own calculations.

Another example relates to an actual device used in the production process of cottage cheese (Fig. 6) (SOBIESKI 2009c). The first phase was water and the second cottage cheese mentioned above. The average diameter of particle was equal to 9 [mm]. The goal of the research was the qualitative identification of flow structures in the reservoir of the washer cooler. Such data were not previously known. In this case the validation of numerical model was not possible due to costs of an appropriate experiment. Nevertheless, the simulation results remain consistent with the available knowledge about the work of this type of equipment. A characteristic feature of this example is a different

medium. Grains of cottage cheese are indeed relatively soft and delicate. The research was conducted jointly with the TEWES-BIS company from Barczewo.

Figure 7 shows third example of using the EMM. In this case the possibilities to model transport of granular media with using a conveyor belt were investigated. In the first stage an appropriate numerical model was developed. For the second stage a simple experimental stand was designed and built (KOWALEWSKI 2009). The first phase was air and the second phase was gravel with fraction 2–8 [mm]. So far, a qualitative compliance has been obtained. In the future, further studies in this direction are planned.

Conclusions

Following conclusions related to Porous Media Model and Eulerian Multi-phase Model can be formulated:

- In PMM the shape and location of the porous zone must be defined rigid on the building stage of the numerical model. Subsequent developments in this area require rebuilding the model. In EMM those elements are only the initial conditions and may change in calculation time.

- The local values of flow resistance in EMM are different and depend on current distributions of the parameters: porosity (or volume fraction), filtration velocity and other. In the PMM the resistance value is constant in space (for one direction), unless calculations were made with using distribution functions (i.e. for porosity).

- In both models mass transfer (i.e. dissolution, drying), heat transfer (i.e. heating or cooling) and other phenomena can be added, but mathematical approach for the description is different. In the PMM all “closures” must be defined “globally” for whole porous zone. In the EMM all phenomena must be defined “locally”, on the level of interaction between particles and surroundings.

- If there is a confidence that the modeled system is stationary, it is recommended to use the PMM. The EMM is more complicated than the PMM. The EMM is also more difficult to use.

Accepted for print 29.09.2010

References

- AMAO A. M. 2007. *Mathematical Model For Darcy Forchheimer Flow With Applications To Well Performance Analysis*. MSc Thesis. Department of Petroleum Engineering. Texas Tech University.
- ANDRADE J.S., COSTA U.M.S., ALMEIDA M.P., MAKSE H.A., STANLEY H.E. 1999. *Inertial Effects on Fluid Flow through Disordered Porous Media*. Physical Review Letters, 82(26) 28 June 1999.

- BELYADI A. 2006. *Analysis Of Single-Point Test To Determine Skin Factor*. PhD Thesis. Department of Petroleum and Natural Gas Engineering, Morgantown, West Virginia.
- BELYADI F. 2006. *Determining Low Permeability Formation Properties from Absolute Open Flow Potential*. PhD Thesis. Department of Petroleum and Natural Gas Engineering, Morgantown, West Virginia.
- EWING R., LAZAROV R., LYONS S.L., PAPAVALASSIOU D.V., PASCIAK J., QIN G.X. 1999. *Numerical Well Model For Non-Darcy Flow*. Computational Geosciences, 3(3–4): 185–204.
- Fluent 6.3 Tutorial Guide. Fluent Inc., September 2006.
- Fluent 6.3 User's Guide. Fluent Inc., September 2006.
- HELLSTRÖM J.G.I., LUNDSTRÖM T.S. 2006. *Flow through Porous Media at Moderate Reynolds Number*. International Scientific Colloquium, Modelling for Material Processing, Riga, June 8–9.
- KOWALEWSKI K. 2009. *A stand for tests of dynamics of loose material in the model belt conveyor*. MSc Thesis, University Of Warmia And Mazury In Olsztyn, The Faculty of Technical Sciences.
- LORD D.L., RUDEEN D.K., SCHATZ J.F., GILKEY A.P., HANSEN C. W. 2006. *DRSPALL: Spallings Model for the Waste Isolation Pilot Plant 2004 Recertification*. SANDIA REPORT SAND2004-0730, Sandia National Laboratories, Albuquerque, New Mexico 87185 and Livermore, California 94550. February 2006.
- MITOSEK M. 2007. *Fluid Dynamics in Engineering and Environmental Protection*. Publisher Warsaw University of Technology, Warszawa, Poland.
- NALEPA K., NEUGEBAUER M., SOŁOWIEJ P. 2008. *The concept and construction of a ground heat exchanger as part of the ventilation system of a residential building*. Agricultural Engineering, 2(100): 203–208.
- NAŁĘCZ T. 1991. *Laboratory of Fluid Mechanics – exercise*. ART Publishing House, Olsztyn.
- PAZDRO Z., BOHDAN K. 1990. *General Hydrogeology*. Geological Publisher, Warsaw, Poland.
- SAWICKI J., SZPAKOWSKI W., WEINEROWSKA K., WOŁOSZYN E., ZIMA P. 2004. *Laboratory of Fluid Mechanics and Hydraulics*. Technical University of Gdańsk Publisher, Gdańsk, Poland.
- SOBIESKI W. 2008. *Numerical analysis of sensitivity of Eulerian Multiphase Model for a spouted bed grain dryer*. Drying Technology, 26(12): 1438–1456.
- SOBIESKI W. 2009a. *Switch Function and Sphericity Coefficient in the Gidaspow Drag Model for Modeling Solid-Fluid Systems*. Drying Technology, 27(2): 267–280.
- SOBIESKI W. 2009b. *Momentum Exchange in Solid-Fluid System Modeling with the Eulerian Multiphase Model*. Drying Technology, 27(5): 653–671.
- SOBIESKI W. 2009c. *Opportunities and strategies for numerical modeling of flow dynamics and thermal phenomena in the washing-cooling column*. Research report 1/2009 for TEWES-BIS Company, Barczewo, Poland.
- SOBIESKI W. 2009d. *Application of simulation methods to validate the results of the experiment*. Chapter in book “Knowledge Engineering and Expert Systems”, pp. 113–124. EXIT Publisher, Warsaw 2009.
- SOBIESKI W. 2010. *Use of Numerical Models in Validating Experimental Results*. Journal of Applied Computer Science, 18(1): 49–60.
- SOBIESKI W., LIU C., ZHANG Q. (submitted). *Calculating tortuosity in a porous bed consisting of spherical particles with known sizes and distribution in space*. Transport in Porous Media.
- SOBIESKI W., TRYKOZKO A. (submitted). *Sensitivity analysis of Forchheimer law*. Transport in Porous Media.

THE COMPUTER ANALYSIS SHAPE OF REFLEXES XRD ON THE BASIS OF X2CrNiMoN25-7-4 STEEL

Paweł Szabracki, Mirosław Bramowicz, Tomasz Lipiński

Department of Materials and Machines Technology
University of Warmia and Mazury in Olsztyn,

Key words: XRD diffractometry, XRD, Pearson VII, Gauss, Cauchy.

Abstract

This paper was introduced the author's program to the analysis of the shape of XRD reflexes. The analysis was subjected results fittings of numerical models to data got during measurements. The method of the smallest squares of mistakes was used in the analysis of the fitting. The written application lets describe peak using one from popular functions. Parameters of the diffractive reflex appointed with the program let determine lattice parameters, volumetric phase participation and determine the quantity of crystallites and network distortions.

KOMPUTEROWA ANALIZA KSZTAŁTU REFLEKSÓW XRD NA PRZYKŁADZIE STALI X2CrNiMoN25-7-4

Paweł Szabracki, Mirosław Bramowicz, Tomasz Lipiński

Katedra Technologii Materiałów i Maszyn
Uniwersytet Warmińsko-Mazurski w Olsztynie

Słowa kluczowe: dyfrakcja rentgenowska, XRD, Pearson VII, Gauss, Cauchy.

Abstrakt

W artykule przedstawiono autorski program do analizy kształtu refleksów XRD. Przeanalizowano wyniki dopasowania modeli numerycznych do wyników uzyskanych podczas pomiarów rzeczywistych. W analizie dopasowania wykorzystano metodę najmniejszych kwadratów błędów. Aplikacja pozwoliła opisać pik za pomocą jednej z dostępnych funkcji. Wyznaczone za pomocą programu parametry refleksu dyfrakcyjnego pozwalają na określenie parametrów sieciowych, objętościowych udziałów fazowych oraz wyznaczenie wielkości kryształitów i zniekształceń sieciowych.

Introduction

X-ray diffractometry (XRD – eng: X-Ray Diffraction) delivers a lot of valuable information about the structure and proprieties of materials. She lets e.g.: the precise measurement of lattice parameters, determining phase participation, determine of the size of crystallites and the measurement of stresses and network deformation. The result of XRD measurements are registered as dependencies of the intensity of the bent X-ray bundle, subjected to the right according Bragg law of diffraction on the atoms of the crystalline lattice, in the function of the angle of deflection (2θ), so-called diffraction patterns (BOJARSKI, ŁAGIEWKA 1988, BOJARSKI, BOLD 1970, CULLITY 1964, OLESZAK, OLSZYNA 2004, SENCZYK 1995).

In the present work analyzed the influence of the shape of the diffractive peak profile circumscribed the functions: Gauss, Cauchy and Pearson VII, on their basic parameters, such as: the location of the centre of gravity, total and integral intensity, half-value width.

In this aim it was created in the Delphi the application designed to the numeric analysis diffraction patterns whose working was proved on example registered diffraction patter (Fig. 1) the sample of steel X2CrNiMoN25-7-4 submitted earlier annealing in temp. 1100°C for 30 min., and then saturated in water to the temperature of surroundings.

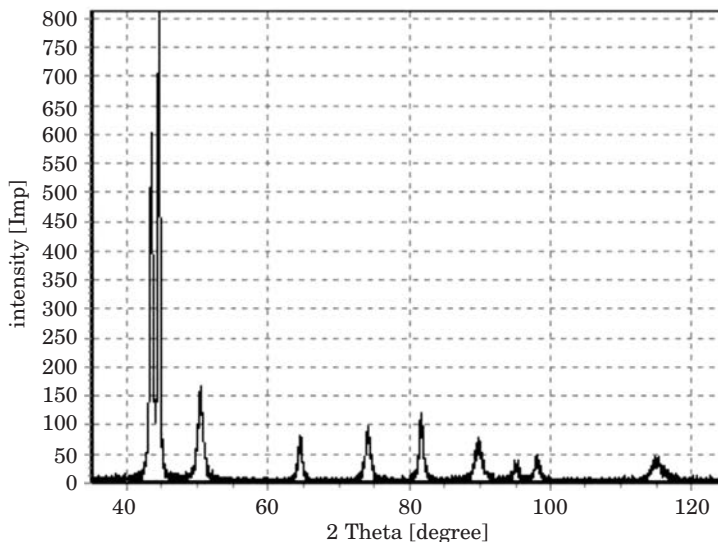


Fig. 1. Diffraction pattern of X2CrNiMoN25-7-4 steel after annealing 30 minutes at temperature 1100°C, cooling in water

The measurements were conducted on the diffractometer X-ray X'Pert PRO with focusing according to Bragg-Brentano and the prostate registration of impulses. In investigations applied radiance of characteristic CuK_α about the weighted average of the length of the wave $\lambda = 1,541783$. The measurements were conducted in range of angle 2Θ from 35 to 125° , value power of the measuring step carried out 0.02° , meanwhile time of counting impulses 2 sec.

Parameters characterizing the profile of the diffraction line

Every diffraction reflex is characterizes a few of the parameters to which belongs the location of the diffraction line, total intensity the half-value and integral width. These quantities can be assigned on the basis of function circumscribing the profile of the diffraction line (BOJARSKI, ŁĄGIEWKA 1988, CULLITY 1964, SENCZYK 1995).

The gauge of the total intensity of the diffraction line is the surface bounded curve expansion of intensity in the diffraction line and the line of the background taken by horizontal intervals the side branches of the diffraction line. It is defined as (BOJARSKI, ŁĄGIEWKA 1988, CULLITY 1964, SENCZYK 1995):

$$I_c = \int_{\Theta_1}^{\Theta_2} I(\Theta) d(\Theta) \quad (1)$$

where:

$I(\Theta)$ – the function of the expansion of the intensity of the diffraction line,
 Θ_1, Θ_2 – points, where diffraction line is equal to background.

The half-value width $\beta_{1/2}$ of diffraction line according to Sherrer is defined as width of the reflex in the half of his maximum intensity (BOJARSKI, ŁĄGIEWKA 1988, CULLITY 1964, SENCZYK 1995).

The integral width (2) according to Maxa von Laue is defined as quotient of total intensity of the diffraction line to maximum intensity (SENCZYK 1995):

$$\beta_c = \frac{I_c}{I_{\max}} \quad (2)$$

where:

I_c – total intensity of the diffraction line (1),
 I_{\max} – maximum intensity of diffraction line.

The position of the diffraction line is defined as position of top or the centre of gravity of the diffraction line. Assignment of the position of the top is easier to the execution, but less exact and shouldn't be applied to the precise measurements of the crystalline lattice or the measurements of stress. Defining the position of the diffraction line through the assignment of the the centre of gravity of the analyzed reflex is recommended to exact analysis.

Necessary diffraction pattern is not in the analysis of got results, as the integer, but position and sizes characterizing individual reflexes. SENCZYK (1995) gives the equations of functions used to the description of the expansion of the intensity of the diffraction line. As first, author exchanges circumscribed the formula (3) Gauss function (BOJARSKI, ŁĄGIEWKA 1988, CULLITY 1964, SENCZYK 1995):

$$I(x) = I_0 e^{-kx^2} \quad (3)$$

where:

I_0 – intensity in top of function,

k – coefficient circumscribing course of the function.

The coefficients I_0 and k has influence on the shape of the function Gauss. Established maximum intensity $I_0 = 0,8$ for all analyzed models will let eliminate the changes the function shape resulting from the change of this value. The solid values of coefficients circumscribing the background ($y(x) = ax + b$, where $a = 0$, $b = 0,05$) were accepted in the aim of the qualification of the homogeneous conditions of the analysis of the results of investigations. The influence of the change of the coefficient value on the course of the Gauss function was introduced at Fig. 2.

As follow from Fig. 2. together with the growth of the k coefficient value, the shape of profile Gauss function changes. Profile this becomes narrower more and more and simultaneously the radius of the profile curvature diminishes at the basis. The radius of curvature in the top of the function diminishes together with the growth of the k coefficient value. Growth of the value of the analyzed parameter causes faster achievement by the profile of the function level of the background.

Following described by Senczyk function is Cauchy (BOJARSKI, ŁĄGIEWKA 1988, CULLITY 1964, SENCZYK 1995) function described by formula (4):

$$I(x) = I_0 \frac{1}{1 + kx^2} \quad (4)$$

where:

I_0 – intensity in top of function,

k – coefficient circumscribing course of the function.

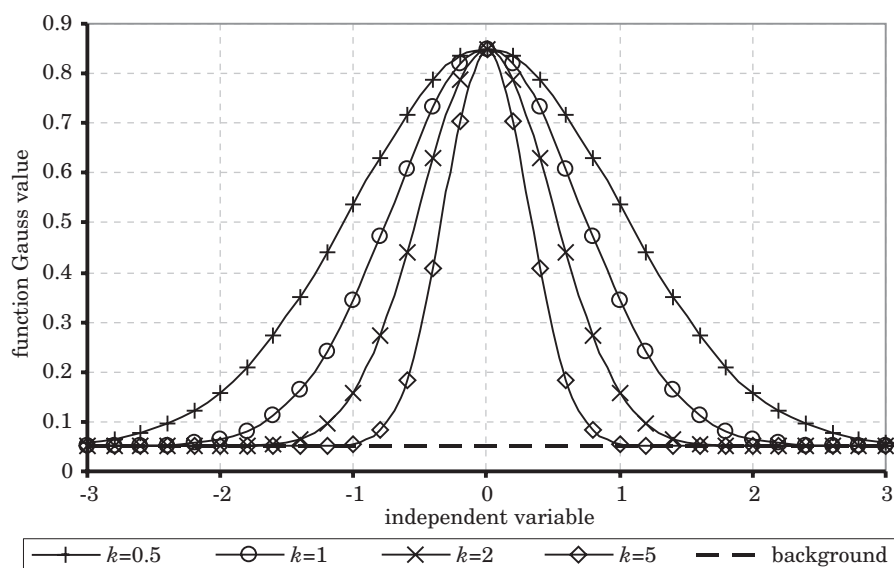


Fig. 2. The expansion of Gauss function in dependence from the value of the coefficient k

Graphic interpretation of influence of coefficient k value change (Fig. 3) was created in the aim of the view the influence parameters of model on the shape of the curve circumscribed by model Cauchy (4) on the course of the function Cauchy.

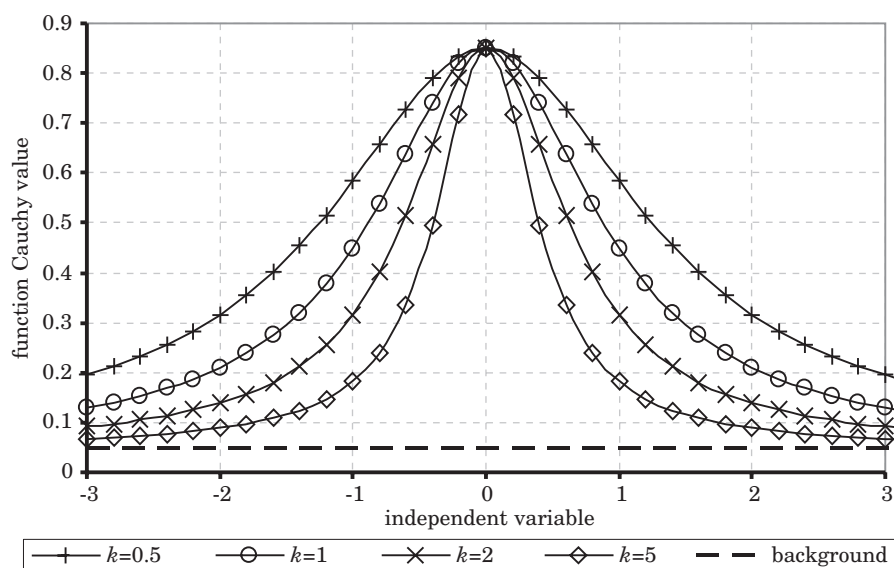


Fig. 3. The expansion of Cauchy function in dependence from the value of the coefficient k

The course of the Cauchy (Fig. 3) function differs from course of function Gauss considerably. Considerably larger radius of the curvature of the function profile near basis (passage to the value of the background) visible is than in case of Gauss function (Fig. 2). The profile of the function is also considerably wider on these same values of the coefficient k . Similarly as the Gauss, radius of the profile curvature the function near the top grows together with the fall of the value of the coefficient k . Profile of the function Cauchy brings nearer more considerably slowly oneself to the background.

Another, used in practice function to describe diffraction peaks is function Pearson VII (BOJARSKI, ŁĄGIEWKA 1988, CULLITY 1964, SENCZYK 1995) described by formula (5):

$$I(x) = I_0 \left[1 + \frac{x^2}{ma^2} \right] \quad (5)$$

where:

I_0 – intensity in top of function,

m, a – coefficients circumscribing course of the function.

In aim of qualification of influence coefficients m, a of equation (5) on course of function (5) was analyzed separately influence every one of coefficients from on the foundation of the solid value the not analyzed at the moment coefficient. Influence of coefficient m value change on course of function (5) was introduced on the solid value of the coefficient $a = 0.5$ at Fig. 4.

The growth of the value of coefficient m causes decrease of the radius of curvature of the profile Pearson VII (5) at the basis (near passage to the level of the background Fig. 4). The growth of the value of the coefficient m causes quicker simultaneously you will reach the value of the background by the profile. Obtainment of the smaller half-value width of the profile of the function is the effect of this. In the distinction from circumscribed earlier situations, when one parameter and changed profile of the function both at the basis as and in the top, parameter m of the function Pearson VII (5) influences only the profile of the function at the basis, that is the dynamics of achieving the level of the background.

Next case analyzed according to formula (5), then the influence of the change of the value of the coefficient a (5). The influence of the change of the power of the coefficient a was introduced at fig. 5. on course of function Pearson VII (5) on the constant value of the coefficient $m = 1$.

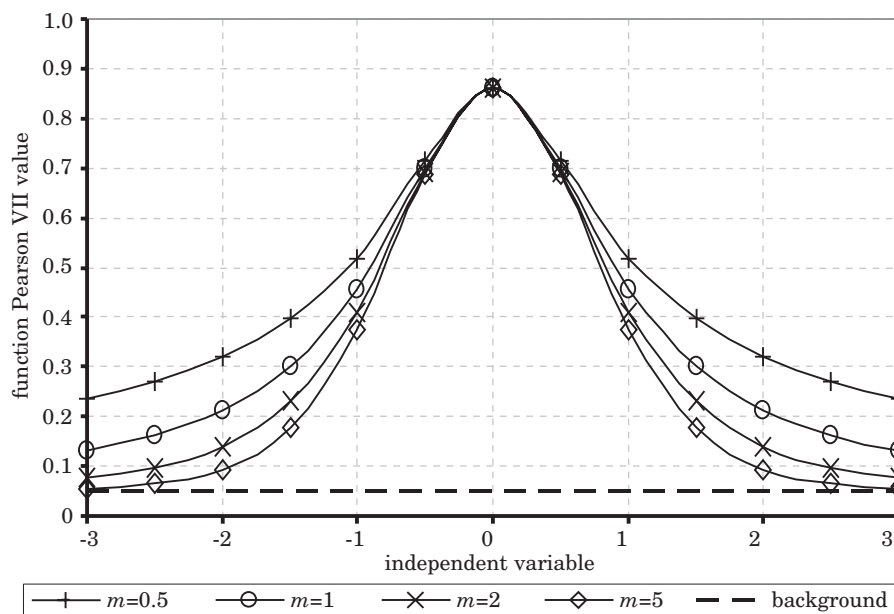


Fig. 4. The expansion of Pearson VII function in dependence from the value of the coefficient m for $a = 0.5$

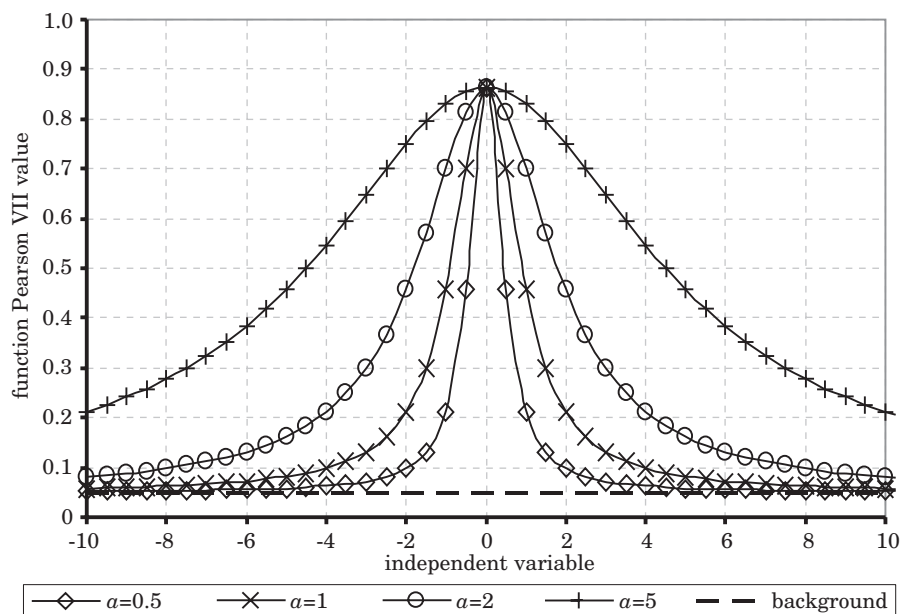


Fig. 5. The expansion of Pearson VII function in dependence from the value of the coefficient a for $m = 1$

The change of the parameter a of Pearson VII function (5) causes the change of the profile in top of function (Fig. 5). But growth of the value of the coefficient a is causes enlargement of the radius of the curve of the section of the function in the top. This change also attracts for her the change of the radius of the curvature of profile in the bottom part of the profile obviously. The bottom part of profile we can additionally control by the coefficient m of equation Pearson VII.

Composition of cases analyzed at Fig.4 and Fig.5 was introduced at Fig. 6 in the aim of demonstrating of considered situations. The composition profiles of the function Pearson VII (5) was introduced at Fig. 6. for the combination of coefficients $a = 0,5, a = 1$ and $m = 0,5, m = 2$. He results from them, that after the change of the coefficient a , the bottom parts of the profile of function for constant value of the coefficient m are not parallel in relation to themselves (the lines $a = 0,5, m = 2$ and $a = 1, m = 2$).

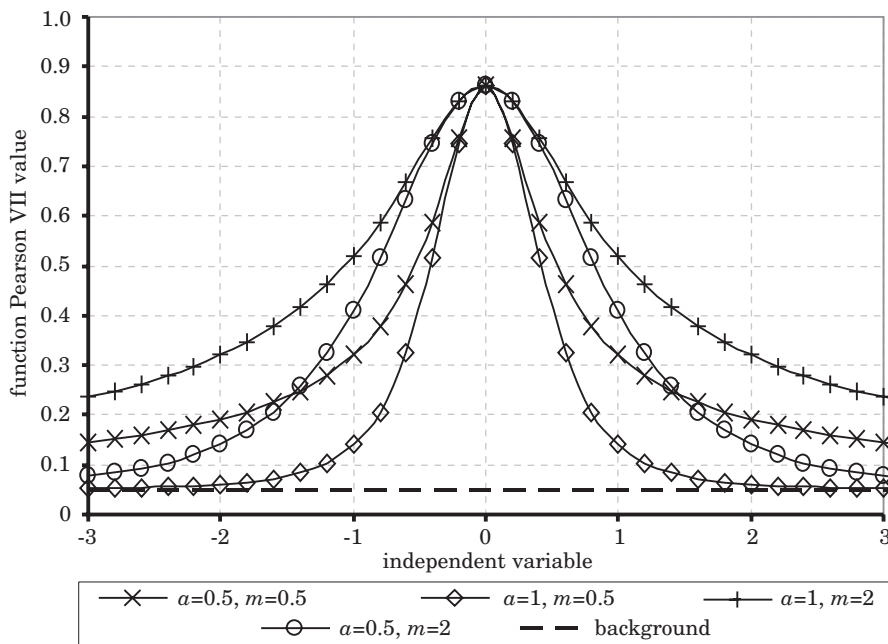


Fig. 6. Expansion of the function Pearson VII for $a = 0,5, a = 1$ and $m = 0,5, m = 2$

Because of this fits the coefficients of mathematical model to measuring data should complex be held.

In the aim of the efficient analysis of reflexes, computer program enabling obtainment of the parameters of diffraction lines in easy way and first of all quick was created. The program fits mathematical model to experimental data

with utilization of the method of the smallest squares of mistakes according to formula (6).

$$B = \sum_{\Theta_1}^{\Theta_2} [(I(\Theta) - F(\Theta))^2] \quad (6)$$

where:

$I(\Theta)$ – intensity measured for Θ angle,

$F(\Theta)$ – intensity calculated for Θ angle,

$(\Theta)_1, (\Theta)_2$ – range of angles Θ .

The correctness of the work of the individual moduluses of program and application as integral was verified with utilization of different accessible tools enabling the homothetic analysis (Mathcad) and through the analysis standard, circumscribed data. The sequence of moduluses being responsible for delimitation of individual parameters was created on the basis of the analysis of parameters circumscribing diffraction reflexes. As the determinant of the adjustment experimental data to mathematical model coefficient of line correlation (IGNATCZYK, CHROMIŃSKA 1999, TAYLOR 1999) was used:

$$r_{xy} = \frac{\text{cov}(xy)}{\sigma_x \sigma_y} \quad (7)$$

where:

$$\sigma_x = \sqrt{\frac{\sum_{i=1}^n (x_i - \bar{x})^2}{n}} \quad (8)$$

$$\sigma_y = \sqrt{\frac{\sum_{i=1}^n (y_i - \bar{y})^2}{n}} \quad (9)$$

Figure 7 introduced informative card of created application. Program wrote in Delphi 7 Personal (BORLAND SOFTWARE CORPORATION) and he can be used for non commercial usage.

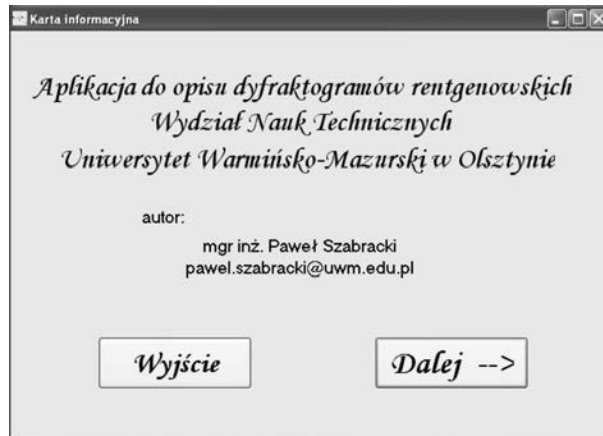


Fig. 7. The informative card of created program

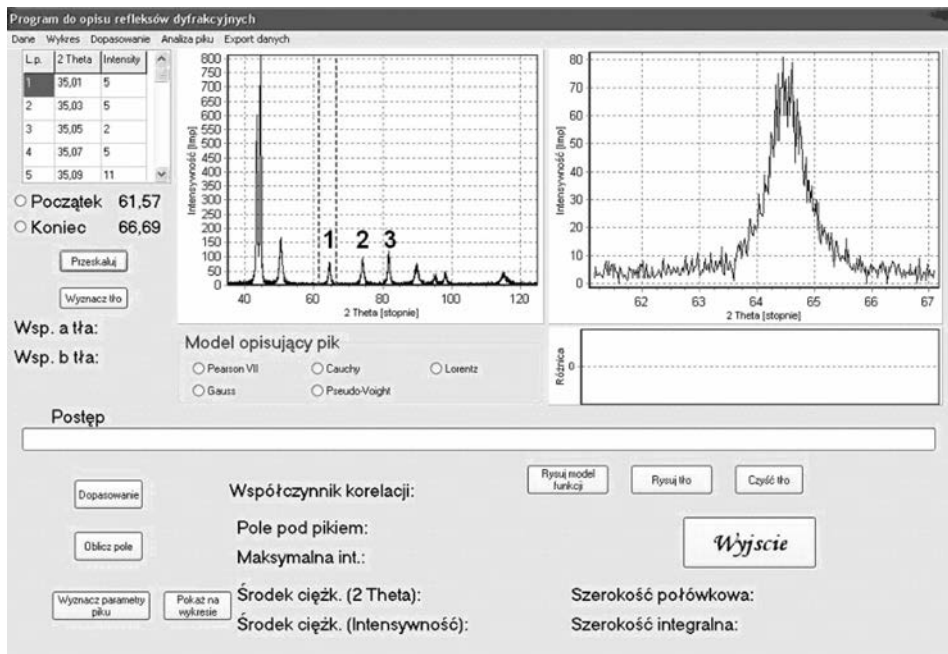


Fig. 8. Program interface

The interface of the application was introduced at Fig. 8 after reads diffraction pattern (left graph) and scaling analyses peak (right upper graph). The mark analysis peak is holds through clicking on the read diffraction pattern of points defining beginning and the end of analyzed reflex near

suitable choice fields of type radio-button for beginning and the end of the range. The right graph representing is enlarged the analyzed reflex about 20 measuring points before the indicated point as beginning and 20 measuring points behind the final point. Mine this on the aim qualification of adjustment of background and function circumscribing beyond the borders of the analyzed range. Additional points on beginning and the end of the range are not taken under the attention near guided calculations.

The comparison of models circumscribing diffraction reflexes

In the aim of proving the correctness of the rule the created application, the qualification the grade adjustment of individual curves to experimental data and proving the influence of the choice of function circumscribing the shape of the reflex on his basic parameters remembered in pkt.1 was used diffraction pattern of the sample X2CrNiMoN25-7-4 steel after the thermal processing. Three (marked at Fig. 8) were chose to the more far analysis the peaks whose profile were circumscribed individual functions. Adjustment of model Gauss (3) to analysis peak was introduced at Fig. 9.

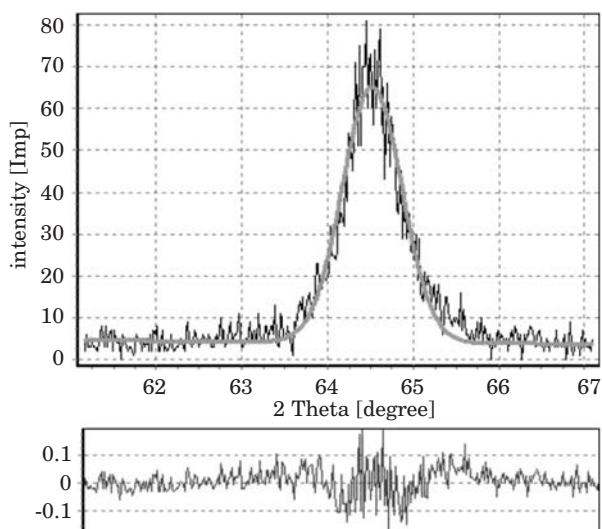


Fig. 9. Fitting Gauss model (3) to experimental data

Figure 10 introduced graphical fitting Cauchy model (4) to the same range of experimental data as for Gauss model (3).

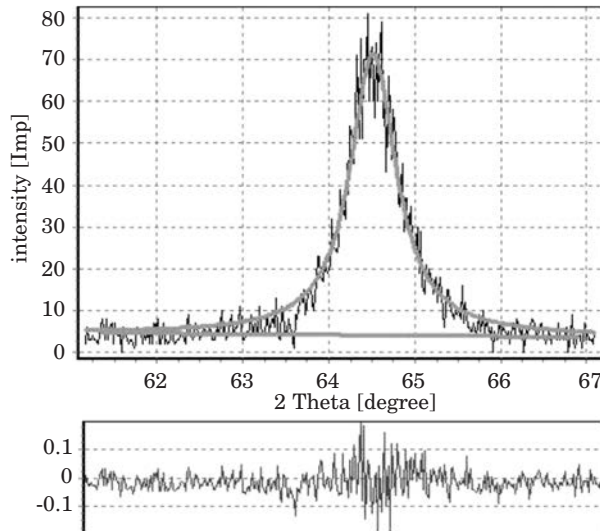


Fig. 10. Fitting Cauchy model (4) to experimental data

Figure 10 except the fitting of mathematical model, the graphic introduction of the background which is marked to consider in the calculations of the individual parameters of the reflex was also introduced.

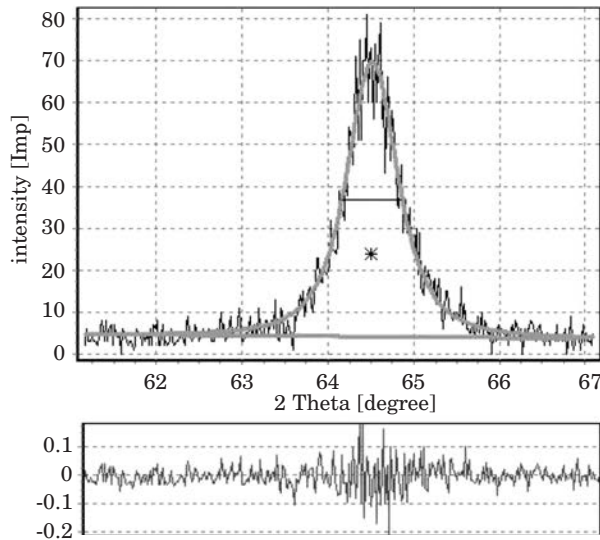


Fig. 11. Fitting Pearson VII model (5) to experimental data

The adjustment of Pearson VII model (5) was introduced graphical at Fig. 11. to experimental data. The position of the the centre of gravity (star) and line defining position and size of the half-value width $\beta_{1/2}$ were introduced graphical additionally. The analysis of the adjustment of above mentioned models was conducted for the uniform values of coefficients circumscribing the background. In table 1 was introduced the composition of parameters characterizes the reflex no. 1 appointed at Fig. 8, appointed using exchanged mathematical models.

Table 1
The comparison of circumscribing parameters the diffraction reflex (no. 1 at Fig. 8) from analyzed diffraction pattern

Specification	Model Gauss	Model Cauchy	Model Pearson VII
Total intensity	53.09	63.39	58.60
Max. intensity	61.13	67.30	65.67
Centre of gravity (2Θ)	64.52	64.474	64.507
Half-value width $\beta_{1/2}$	0.82	0.660	0.7
Integral width β_t	0.868	0.942	0.892
Correlation coefficient	0.971	0.976	0.977
Range of angles (2Θ)	61.57 – 66.69		
Function of background	$f(2\Theta) = 0.01458 \cdot 2\Theta + 4.1067$		

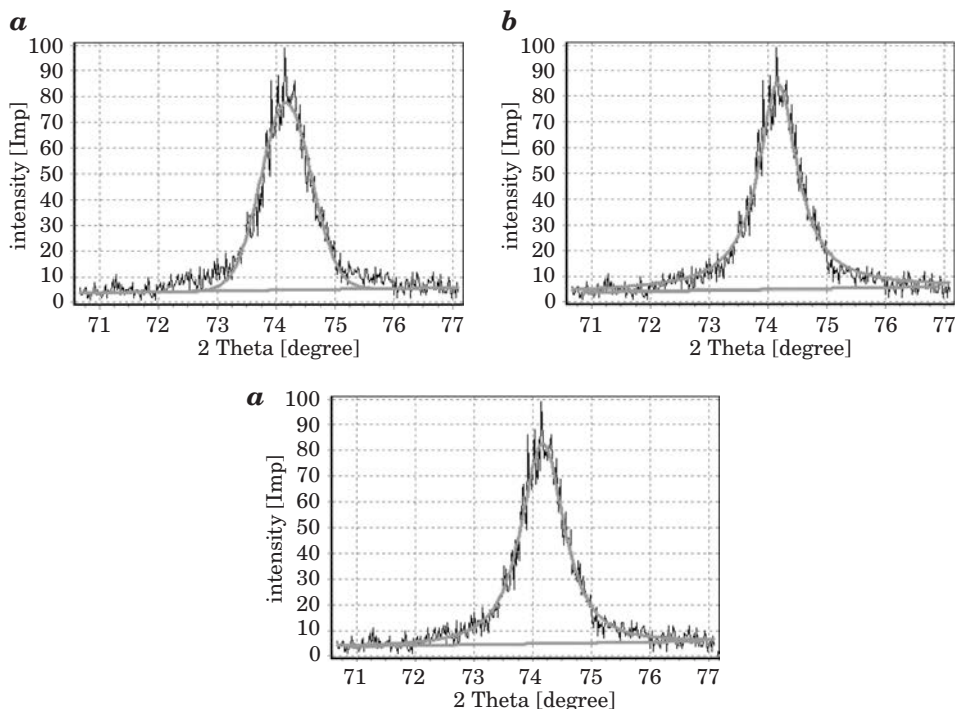


Fig. 12. Fitting models: Gauss (a), Cauchy (b), Pearson VII (c) to experimental data (peak 2 fig. 8)

Fitting of mathematical models: Gauss (*a*), Cauchy (*b*) and Pearson VII (*c*) to experimental data describing peak 2 (Fig. 8.) introduced at Fig. 12. Values of coefficients describing this peak compared in table 2.

Table 2
The comparison of circumscribing parameters the diffraction reflex (no. 2 at Fig. 8) from analyzed diffraction pattern

Specification	Model Gauss	Model Cauchy	Model Pearson VII
Total intensity	77.95	92.39	87.45
Max. intensity	72.76	79.99	77.71
Centre of gravity (2θ)	74.173	74.1354	74.160
Half-value width $\beta_{1/2}$	1	0.8	0.880
Integral width β_c	1.071	1.155	1.125
Correlation coefficient	0.978	0.98	0.982
Range of angles (2θ)	71.07 – 76.69		
Function of background	$f(2\theta) = 0.3267 \cdot 2\theta + 4.8609$		

Fitting of mathematical models: Gauss (*a*), Cauchy (*b*) and Pearson VII (*c*) to experimental data describing peak 3 (Fig. 8.) introduced at Fig. 13.

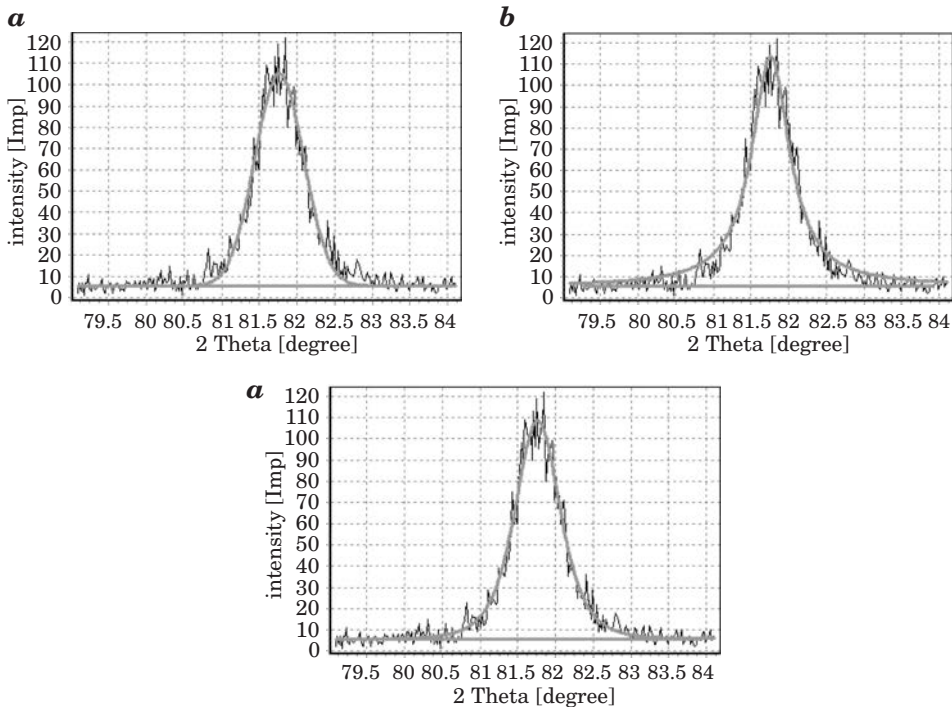


Fig. 13. Fitting models: Gauss (*a*), Cauchy (*b*), Pearson VII (*c*) to experimental data (peak 3 Fig. 8)

Graphical interpretation of fitting numerical models to experimental data introduced on fig. 13. Values of coefficients describing peak 3 (Fig. 8) introduced in table 3.

Table 3

The comparison of circumscribing parameters the diffraction reflex (no. 3 at Fig. 8) from analyzed diffraction pattern

Specification	Model Gauss	Model Cauchy	Model Pearson VII
Total intensity	80.50	95.03	85.74
Max. intensity	99.54	108.1	103.18
Centre of gravity (2Θ)	81.765	81.736	81.762
Half-value width $\beta_{1/2}$	0.76	0.62	0.7
Integral width β_c	0.809	0.879	0.831
Correlation coefficient	0.983	0.98	0.984
Range of angles (2Θ)	79.49 – 83.71		
Function of background	$f(2\Theta) = 0.0488 \cdot 2\Theta + 5.49$		

Summary

Applied in the program mathematical models are applied functions to the description of diffraction reflexes the most often. Each of them lets circumscribe the profile peak with the various grade of the adjustment, which the coefficient of the correlation characterizes.

Function Pearson VII (5) gives the best adjustment of model to experimental data (the highest value of the coefficient of the line correlation). This is caused the independent description of the individual fragments of the curve by the successive parameters of the equation.

The got high values of the coefficients of correlation for individual mathematical models circumscribing the profile of the diffraction line testify about the built correctly algorithm of the program and confirm his usefulness in the numeric analysis of results got by methods XRD. The appointed for the help of the program parameters of the diffractive reflex allow to the qualification of the parameters of lattice structure, volumetric phase participation and marking the size of crystallites and network deformation by the methods: Gauss-Gauss, Cauchy-Gauss, Cauchy-Cauchy (BOJARSKI, BOLD 1970, OLESZAK, OLSZYNA 2004).

Accepted for print 18.08.2010

References

- BOJARSKI Z., ŁĄGIEWKA E. 1988. *Rentgenowska analiza strukturalna*. Państwowe Wydawnictwa Naukowe, Warszawa.
- BOJARSKI Z., BOŁD T. 1970. *Rentgenograficzne metody wyznaczania wielkości zniekształceń sieciowych i wielkości bloków materiałów polikrystalicznych*. Prace Instytutów Hutniczych, 3: 115.
- BORLAND SOFTWARE CORPORATION. Licencja produktu Borland Delphi 7 Personal. Cullity B.D. 1964. Podstawy dyfrakcji promieni rentgenowskich. Państwowe Wydawnictwa Naukowe, Warszawa. http://www.borland.pl/licencje_produktyw/Delphi_7_Personal/licencja_pl.pdf
- IGNATCZYK W., CHROMIŃSKA M. 1999. *Statystyka teoria i zastosowanie*. Wydawnictwo Wyższej Szkoły Bankowej, Poznań.
- OLESAK D., OLSZYNA A. 2004. *Określanie wielkości krystalitów i odkształceń sieciowych w nanokompozycie NiAl-Al₂O₃ na podstawie poszerzenia rentgenowskich linii dyfrakcyjnych*. KOMPOZYTY (COMPOSITES), 4: 11.
- SENCZYK D. 1995. *Dyfraktometria rentgenowska w badaniach stanów naprężenia i własności sprężystych materiałów polikrystalicznych*. Wydawnictwo Politechniki Poznańskiej. Poznań.
- TAYLOR J.R. 1999. *Wstęp do analizy błęd pomiarowego*. Państwowe Wydawnictwa Naukowe, Warszawa.

vacat

Reviewers

Janusz Badur, Stanisław Borkowski, Jarosław Bosy, Stefan Cacoń,
Romana Cielątkowska, Tadeusz Juliszewski, Zbigniew Kacprzyk,
Roman Kadaj, Józef Koszkul, Barbara Krzysztofik, Danuta Leśniewska,
Bogusława Łapczyńska-Kordon, Stanisław Maciejewski, Marek Molenda,
Ryszard Myhan, Marian B. Nantka, Mykhaylo Pashechko,
Leonard Runkiewicz, Ziemowit Suligowski, Jędrzej Trajer,
Robert Ulewicz, Jerzy Weres